Interface engineering and absorber with composition gradient for high-efficiency Kesterite solar cells

Yunhai Zhao

COLLEGE SCIENCES DE LA MATIERE
DOCTORAL DES MOLECULES
BRETAGNE ET MATERIAUX

Université de Rennes

THESE DE DOCTORAT DE

L'UNIVERSITE DE RENNES

ECOLE DOCTORALE N° 638
Sciences de la Matière, des Molécules et Matériaux
Spécialité : *Sciences des matériaux*

Par
Yunhai ZHAO

Interface engineering and absorber with composition gradient for high-efficiency Kesterite solar cells

Thèse présentée et soutenue sur le Campus de Beaulieu à Rennes, le 9 Octobre 2024
Unité de recherche : UMR 6226 Institut des Sciences Chimiques de Rennes

Rapporteurs avant soutenance :

Marie GUEUNIER-FARRET	Maître de Conférences	Université de Bordeaux
Nicolas BARREAU	Professeur	Nantes Université

Composition du Jury :

Président :			
Examinateurs :	Marie GUEUNIER-FARRET	Maître de Conférences	Université de Bordeaux
	Nicolas BARREAU	Professeur	Nantes Université
	Jean-Jacques SIMON	Professeur	Aix-Marseille Université
Co-Dir de thèse :	Guang-Xing LIANG	Professeur	University of Shenzhen
Dir. de thèse :	Xianghua ZHANG	Directeur de Recherche	CNRS- Université de Rennes
Co-encadrant :	Michel CATHELINAUD	Ingénieur de Recherche	CNRS- Université de Rennes
Invité(s)			
	Zheng-Hua SU	Professeur	University of Shenzhen

ACKNOWLEDGE

The research works presented here are accomplished in the College of Physics and Energy of Shenzhen University in China and the Laboratoire de Verres et Céramiques of Université de Rennes in France. I was helped by many people during the period of completing my research.

First of all, I would like to express my heartfelt thanks to my doctoral supervisors, Prof. Xianghua Zhang and Prof. Ping Fan, for their guidance and assistance in experimental exploration and thesis writing. Prof. Zhang has a rigorous scientific research attitude and always points out the problems in the experiments for us. Thanks to Prof. Guangxing Liang for mentoring me in solar cell research and recommending me to the University of Rennes. Prof. Leung is able to keep a constant eye on the recent developments in the field of solar cells, and I need to continue to learn from him. I am very grateful for the support, encouragement, helpful discussions, great patience and careful guidance they gave me. I would like to thank the judges for accepting to judge the thesis. I would like to express my sincere gratitude to Prof. Marie Gueunier FARRET and Prof. Nicolas BARREAU for accepting me as a reporter for my dissertation and to Prof. Jean Jacques SIMON for participating in the defense of my doctoral degree. I would also like to thank Prof. Jean-Francois HALET and Prof. Zhongkuan LUO for reviewing my reports every year. I would like to thank Dr. Michel Cathelinaud for helping me with experimental manipulation and thesis revision. Also, I would like to thank Thierry JOUAN and Antoine GAUTIER for their help in my experiments.

During my stay in China, I would like to thank Prof. Zhenghua Su, Prof. Shuo Chen, Prof. Juguang Hu, and Dr. Jun Zhao, with their help, my experiments could be conducted so smoothly. Prof. Zhenghua Su gave me great guidance and help in experimental operation, data analysis and paper writing. I would also like to thank Xingye CHEN, Yandi LUO, Tong WU, Meng Wei, Zixuan YU, and Guojie CHEN for their companionship and support. Thanks to Mingdong CHEN, Jinhong LIN, Chuanhao LI, Ping LUO, Yi FU, Zi WANG, Xuerui LI and Yuao YE for their care and help. I am grateful for the time we spent together at SZU, and I wish you all successful experiments and good luck with graduation.

I still remember the moment when Yandi and I left our homeland and came to Rennes, Ms. Hongli

MA, who came to pick us up, made me feel the warmth of a foreign country. She helped me a lot when I first enrolled at the University of Rennes and gave me a lot of useful advice about living and working in Rennes. I would also like to thank my Chinese compatriots, Zheng WANG, Hongjiao WANG, Lilin WU, Zheyu GE and Jiajie ZHANG for their help and for the wonderful time we had in Rennes.

Last but not least, I would like to thank my family for their tolerance and affirmation all along, for sharing my joy when I am harvesting, for comforting me when I am down, and for always supporting me when I am lost.

A time will come to ride the wind and cleave the waves to cross the sea. May our path be clear.

SOMMAIRE

RÉSUMÉ DÉTAILLÉ EN FRANÇAIS

1. Introduction

Pour atteindre l'objectif de neutralité carbone, il est urgent de développer des sources d'énergie propres, renouvelables et à faible teneur en carbone. L'énergie solaire est l'une des sources d'énergie renouvelable qui peut réduire ou même remplacer les sources d'énergie traditionnelles à l'avenir. La technologie photovoltaïque (PV) est une technologie propre qui convertit l'énergie solaire directement en électricité. Les cellules solaires photovoltaïques en couches minces présentent les avantages suivants par rapport à la technologie silicium : légèreté, compatibilité avec les substrats souples et économie de la matière. Par ailleurs, le PV en couche mince présente aussi les avantages d'un processus de préparation simple et d'un faible coût, pouvant avoir une certaine transparence, ce qui permet de les utiliser pour des applications spécifiques à grande échelle telles que les bâtiments. Dans ce domaine, les cellules solaires à base de CdTe et de Cu(in,Ga)(S,Se)$_2$ (CIGS) ont démontré des rendements supérieurs à 20 % et une stabilité à long terme, et sont commercialisées depuis plus d'une décennie.

Figure 1 *(a) Photovoltaïque à couche mince, (b) cellules solaires en couche mince à substrat flexible et à substrat rigide, et (c) cellules solaires en couche mince translucide.*

Toutefois, leur part de marché est en quasi constante diminution notamment en raison de la baisse rapide du coût des PV à base de silicium et aussi de l'utilisation des éléments rares (In,Ga) ou toxiques (Cd), qui ont soit limité les réductions de coûts, soit suscité des préoccupations environnementales. Il est donc nécessaire de développer des nouveaux absorbeurs en couches minces présentant de bonnes performances photovoltaïques, et utilisant des éléments abondants et respectueux de l'environnement. Les cellules solaires à base de $Cu_2ZnSn(S,Se)_4$ (CZTSSe) sont considérées comme ayant un potentiel commercial en raison de leur band-gap modifiable (entre 1.0-1.5 eV en ajustant le rapport S/Se), de l'abondance des éléments constituants, de leur bonne stabilité et de leur non-toxicité.

2. Propriétés fondamentales des matériaux CZTSSe

Comme sa structure cristalline est dérivée du CIGS très bien étudiée, deux cations du groupe III du CIGS sont remplacés par un cation du groupe II (Zn) et un cation du groupe IV (Sn), et cette substitution permet ainsi l'incorporation d'éléments abondants sur terre. À ce jour, les méthodes de préparation des cellules solaires en couche mince en CZTSSe comprennent la pulvérisation magnétron, la co-évaporation, le dépôt électrochimique et les méthodes en solution avec des précurseurs moléculaires. Cette dernière méthode présente les avantages d'un procédé simple, d'une préparation facile à grande échelle, d'un faible coût de fabrication et d'une stœchiométrie contrôlable.

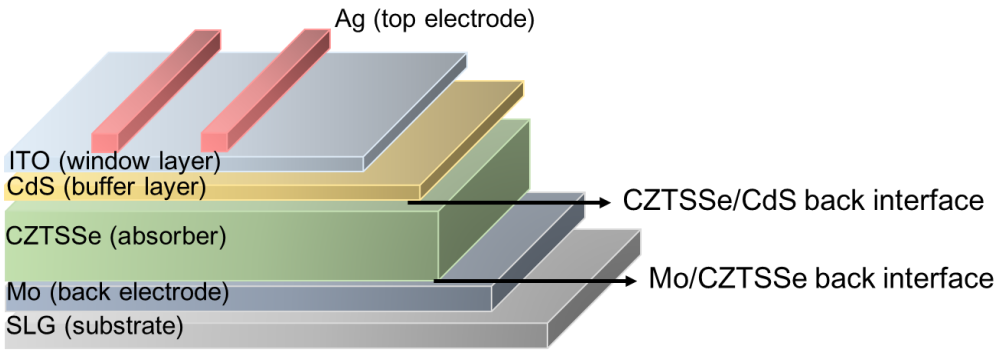

Figure 2 *Structure d'une cellule solaire en couches minces en CZTSSe.*

Ces dernières années, les progrès de la recherche dans la préparation de cellules solaires en CZTSSe avec cette méthode en solution ont permis d'obtenir des rendements très intéressants. La kesterite a été utilisée avec la même architecture de cellule solaire que le CIGS (c'est-à-dire une configuration de substrat, avec le Mo comme contact arrière et le CdS comme couche tampon pour les électrons). Ceci a facilité les premiers progrès rapides de cette technologie photovoltaïque avec un rendement dépassant les 14 %, ce qui reste bien inférieure à celle de leurs homologues en CIGS. Les principales difficultés pour accroître ce rendement résident actuellement dans l'amélioration de la tension en circuit ouvert (Voc) et le facteur de forme.

La recombinaison des porteurs de charge aux interfaces des dispositifs PV en CZTSSe est un paramètre clé pour l'amélioration du rendement. Elle est influencée par plusieurs facteurs, tels que l'alignement des bandes d'énergie, la présence des défauts et des phases secondaires. Par conséquent, l'ingénierie des interfaces joue un rôle clé dans la minimisation des recombinaisons des porteurs de charge aux interfaces afin d'améliorer le Voc et le FF des dispositifs CZTSSe. Pour cela, il est essentiel de disposer des informations pertinentes.

Les dispositifs PV performants à base de CZTSSe sont obtenus avec la méthode en solution et la transformation des couches précurseurs amorphes en absorbeurs cristallins nécessite un procédé de sélénisation rapide à haute température. Ce procédé induit une diffusion rapide des éléments pour obtenir une distribution élémentaire uniforme, ce qui rend difficile la régulation fine d'un gradient de composition. Par conséquent, il est difficile, avec cette méthode, d'obtenir une couche absorbante à double gradient de composition, comme celle obtenue dans les cellules à base de CIGS. On rappelle que ce type de gradient est favorable à la séparation et le transport des porteurs de charge.

3 Ingénierie de l'interface arrière Mo/CZTSSe

La structure des dispositifs PV à base de CZTSSe, étudiés dans ce travail, est largement inspirée des cellules solaires en CIGS. Des études ont montré que le contact en Mo a un effet néfaste sur les performances des dispositifs de CZTSSe. En effet, les réactions suivantes se produisent à l'interface entre l'électrode arrière et la couche absorbante:

$Cu_2ZnSn(S,Se)_4 + Mo \rightarrow Cu_2(S,Se) + Zn(S,Se) + Sn(S,Se) + Mo(S,Se)_2$

$Mo + S(Se)_2 \rightarrow MoS(Se)_2$

Lors de la sélénisation à haute température, des phases secondaires telles que ZnS(Se), $Cu_2S(Se)$, $SnS(Se)_2$, etc. formées par la décomposition du CZTSSe à l'interface augmentent la recombinaison des porteurs de charge à cette interface arrière. En plus ces réactions conduisent également à une couche de $MoS(Se)_2$ excessivement épaisse, qui entrave le transport des porteurs et augmente la résistance série du dispositif.

En outre, des études ont aussi montré que la présence de l'électrode arrière en Mo joue un rôle crucial dans la nucléation de l'absorbeur à l'interface, de sorte que la croissance cristalline se produit à la fois à la surface et à l'interface arrière. Au fur et à mesure que le temps de sélénisation augmente, la croissance cristalline se produit simultanément en haut et en bas de l'absorbeur avec une compétition de composition. Cette compétition conduit inévitablement à une inhomogénéité de l'absorbeur. Ce processus de croissance bidirectionnelle des grains conduit typiquement à une structure bicouche avec une faible cristallinité, ce qui se traduit par une courte longueur de diffusion des porteurs de charge minoritaires dans les dispositifs en CZTSSe. En outre, au cours du processus de recuit à haute température, le S(g) ou le Se(g) diffusé à haute température réagit avec l'électrode métallique en molybdène pour générer une couche interfaciale arrière en $MoS(Se)_2$ excessivement épaisse, dont la formation modifie l'alignement des bandes d'énergie à l'interface et forme une barrière aux porteurs de charge.

Afin de résoudre ces problèmes à l'interface Mo/CZTSSe, nous avons introduit une couche intermédiaire de WO_3 sur la surface de l'électrode arrière de Mo par évaporation thermique. Les effets de cette couche intermédiaire sur la microstructure, les propriétés électriques et les défauts électroniques du CZTSSe ont été systématiquement étudiés. Cette couche de WO_3 empêche le contact direct entre l'absorbeur de CZTSSe et l'électrode arrière de Mo et donc la réaction interfaciale indésirable entre eux. Par conséquent, l'absence du $Mo(S,Se)_2$ et de phase secondaire contribue à l'obtention d'une bonne qualité de l'interface arrière, ce qui augmente considérablement la longueur de diffusion des porteurs de charge minoritaires et réduit la barrière de contact. En outre, il a été constaté que cette couche intermédiaire améliore également la croissance cristalline de l'absorbeur, qui donne une surface dense, lisse et bien cristallisée, ce qui se traduit par une meilleure qualité de contact de l'hétérojonction avec le CdS et une plus faible densité de défauts interfaciaux. Cette stratégie, facile à mettre en œuvre, a permis d'obtenir un rendement de 12.66% pour le dispositif PV de CZTSSe, avec notamment le facteur de remplissage bien amélioré.

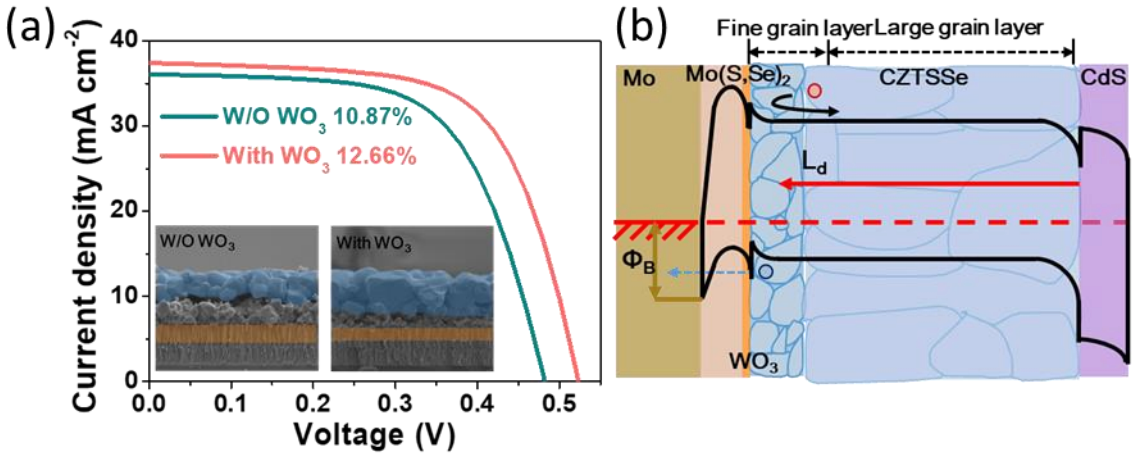

Figure 3 *(a) Courbes JV des dispositifs PV avec et sans couche intermédiaire de WO_3, les encarts sont des images MEB des composants PV, (b) Structure des bandes du dispositif PV avec WO_3, L_d est la longueur de diffusion du porteur minoritaire, et Φ_B est la hauteur de la barrière de contact arrière..*

4 Ingénierie de la jonction CZTSSe/CdS

La forte recombinaison de porteurs de charge à la jonction CdS/CZTSSe dans les cellules solaires CZTSSe est une autre raison importante de la perte de Voc, qui provient principalement de trois aspects: un alignement non optimisé des bandes d'énergie à l'interface ; une interface à haute densité de défauts générés par des défauts des réseaux cristallins et la présence de phases secondaires. Par conséquent, l'ingénierie des bandes d'énergie, la passivation des défauts d'interface et l'élimination des phases secondaires à la jonction sont essentielles pour l'amélioration du rendement des dispositifs PV.

La sulfuration des couches absorbantes en CZTSSe s'est avérée être une méthode efficace pour optimiser la qualité de l'hétérojonction. Cependant, il semble difficile d'obtenir à la fois la passivation des défauts et l'élimination des phases secondaires par cette méthode. De ce fait, nous proposons une méthode de traitement simple et efficace, capable d'améliorer la qualité de la surface et de l'intérieur de l'absorbeur. Cette méthode de sulfuration repose sur l'utilisation de vapeur de sulfure d'ammonium ($(NH_4)_2S$) comme source de soufre. Le sulfure d'ammonium est un sel, qui se décompose thermiquement à 280 ℃ pour libérer du H_2S comme suit:

$$(NH_4)_2S \leftrightharpoons NH_3+H_2S$$

Par rapport au procédé de sulfuration par immersion dans une solution, la libération de H_2S à 280 ℃ devrait permettre d'obtenir une plus grande réactivité, tandis que la température de sulfuration de 280 ℃ favorise la diffusion des S, ce qui peut efficacement passiver les défauts à l'interface ainsi qu'à l'intérieur. Par conséquent, la sulfuration à l'aide du sulfure d'ammonium devrait simultanément inhiber la recombinaison interfaciale et bien contrôler la distribution des éléments, améliorant ainsi la qualité et l'efficacité de la jonction p-n. Le procédé est le suivant : La solution du sulfure d'ammonium est enduite sur la couche absorbeur de CZTSSe et laissée pendant 2 minutes, puis par spincoating, une couche du sulfure d'ammonium est

obtenue sur la surface. Un traitement thermique à 280 °C sous atmosphère inerte est ensuite effectué. Cette méthode permet d'obtenir simultanément l'effet du décapage de la surface et de la sulfuration. Après le traitement, la teneur en S de la surface a légèrement augmenté avec une passivation de la surface, réduisant ainsi la probabilité de recombinaison des porteurs de charge. Une augmentation significative du Voc et du FF a été constatée, donnant un rendement de 13.19%.

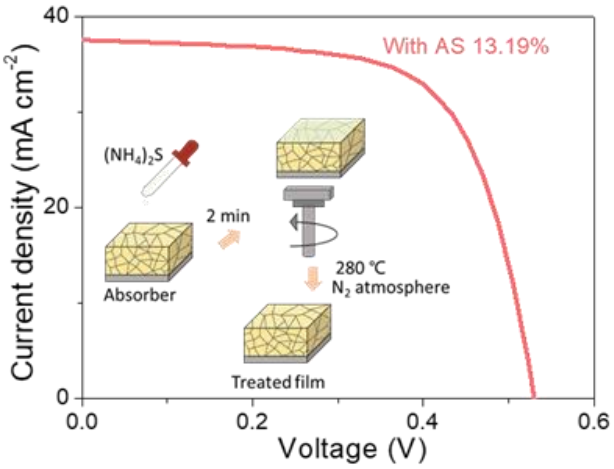

Figure 4 *Courbe J-V pour une cellule solaire après sulfuration.*

5 Mise au point d'une couche absorbeur à gradient de band-gap

Lors de la préparation de l'absorbeur CIGS, les taux d'évaporation des différents éléments peuvent être finement ajustés, pendant la co-évaporation, pour obtenir un double gradient de band-gap entre l'électrode de Mo et l'hétérojonction. Ce double gradient est constitué d'un band-gap qui diminue d'abord et augmente en suite, formant ainsi un profile de double gradient de type V. Le rétrécissement du band-gap entre l'électrode arrière et l'absorbeur, crée un champ favorable au transfert d'électrons vers la jonction p-n. Il réduit la possibilité de recombinaison des porteurs de charge à l'électrode Mo et augmente ainsi la densité du courant de court-circuit. Un band-gap minimal au milieu de l'absorbeur favorise une meilleure absorption de la lumière et par conséquent le J_{SC}. Une augmentation progressive du band-gap vers la jonction p-n

assure permet d'obtenir un V_{OC} plus élevé. Nous avons utilisé cette conception de double gradient de band-gap, développée pour les cellules solaires de CIGS pour le CZTSSe.

A ce jour, les cellules solaires CZTSSe les plus efficaces ont été obtenues en utilisant la méthode en solution, où la transformation d'une couche précurseur amorphe en un absorbeur cristallin, nécessite un processus de sélénisation rapide à haute température. La diffusion rapide des éléments au cours de la sélénisation à haute température pour obtenir une distribution uniforme des éléments pose un défi majeur pour contrôler finement un double gradient de composition.

Nous avons mis au point une méthode inédite, non toxique et facile à mettre en œuvre, qui permet d'obtenir des absorbeurs à double gradient de composition, et donc de band-gap. En plus ce procédé favorise également la croissance des grains. Cette méthode consiste à déposer une couche de K_2S, par spin-coating, à de différentes profondeurs de la couche absorbeur. Cette stratégie permet de préparer des absorbeurs avec un profil de gradients modifiable en ajustant la position et même l'épaisseur de la fine couche de K_2S. Il a été démontré que les performances de transport des porteurs de charge dans les absorbeurs CZTSSe ont été bien améliorées. En même temps, la présence de cette couche de K_2S minimise les défauts électroniques profonds, grâce vraisemblablement à l'introduction supplémentaire de S.

L'analyse SIMS montre que les échantillons optimisés présentent bien un double gradient de compositions. Différentes caractérisations ont confirmé que l'ajout de K_2S a permis d'améliorer le transport des porteurs de charge, la qualité cristalline de l'absorbeur, conduisant ainsi à diminuer la densité de défauts électroniques. La formation d'une phase liquide, le K_2Se_3, pendant la sélénisation améliore la cristallinité de l'absorbeur. La présence des ions K^+ dans la couche absorbeur peut stabiliser la teneur en Sn en augmentant le taux de diffusion de cet élément, réduisant ainsi les

défauts liés au Sn et supprimant les fluctuations de la composition et donc les fluctuations du potentiel électrostatique. En plus, pendant la sélénisation, le K_2S réagit avec le Sn pour former du $K_2Sn_2S_5$ à large bad-gap, ce qui réduit la recombinaison des porteurs aux joints de grains. En caractérisant l'absorbeur à différentes épaisseurs, la distribution du band-gap dans l'absorbeur a été visualisée pour la première fois pour des cellules solaires de CZTSSe. Cette nouvelle méthode a permis d'obtenir des cellules solaires avec le plus haut rendement de conversion d'énergie (13.70%) pour les dispositifs CZTSSe grâce aux absorbeurs avec un double gradient de band-gap. Ces résultats sont résumés dans la figure ci-dessous.

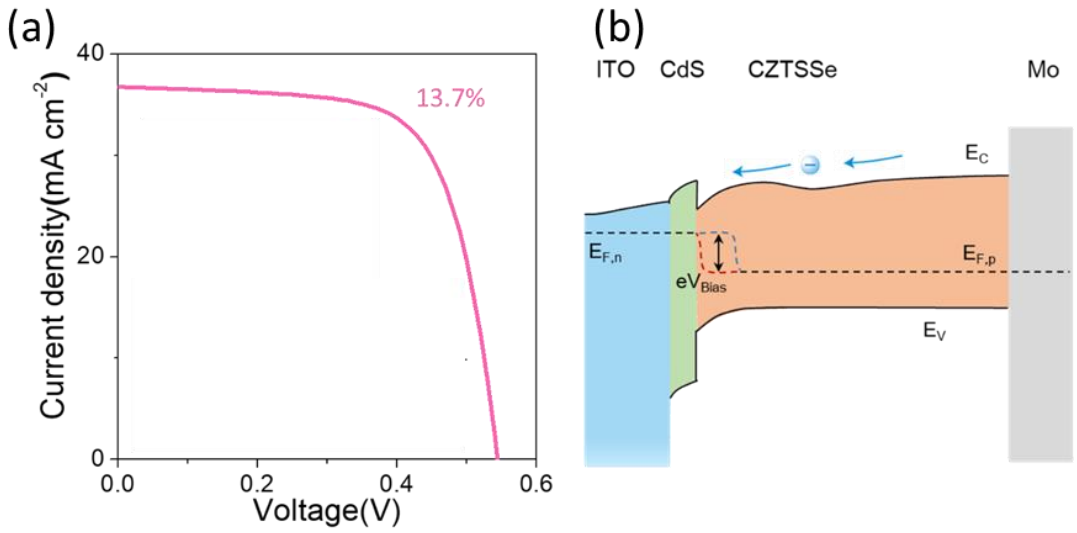

Figure 5 *(a) Courbes J-V d'une cellule solaire de CZTSSe avec une structure de double gradient de band-gap, (b) illustration de la structure à double gradient de band-gap.*

6 Conclusions

L'objectif de ce travail de doctorat était d'optimiser des couches minces de CZTSSe pour obtenir des cellules solaires performantes. Pour atteindre l'objectif, les interfaces Mo/CZTSSe et CZTSSe/CdS ainsi que la structure band-gap de la couche absorbeur de CZTSSe ont été optimisées. Afin de réduire l'important déficit de tension en circuit ouvert de ces cellules PV, l'accent a été mis sur la compréhension du mécanisme de croissance cristalline des grains de l'absorbeur en couche mince, sur l'amélioration des

propriétés de transport des porteurs de charge et sur la modulation des propriétés électroniques de l'absorbeur. Une méthode de préparation très reproductible et très simple a permis d'obtenir des couches de CZTSSe de haute qualité, conduisant à des cellules solaires de CZTSSe ayant un rendement de 13.70%.

GENERAL INTRODUCTION

In order to achieve the goal of carbon neutrality strategy, the development of low carbon and clean renewable energy generation become an urgent task. Solar energy is one of the most attractive renewable energy sources. As the first-generation solar cells are constantly approaching the theoretical limit, thin film solar cells provide more space for development and broader application prospects. $Cu_2ZnSn(S,Se)_4$ is a non-toxic, stable direct band-gap (E_g) semiconductor material with earth-abundant elements and a suitable band-gap, which can be prepared by solution method. The current world record efficiency of CZTSSe solar cells is 14.9%, which is much lower than the highest photovoltaic conversion efficiency (PCE) of its predecessor, $Cu(In,Ga)Se_2$ (CIGS) solar cells (23.35%), mainly due to the lower open-circuit voltage (V_{OC}).

The main reason for the low Voc in CZTSSe devices is the interface and bulk dominated carrier recombination. Severe non-radiative recombination at the Mo/CZTSSe interface, the CZTSSe/CdS interface and the CZTSSe bulk are the significant limiting factors for device improvement: (i) The undesirable Mo/CZTSSe back interface leads to decomposition reaction, formation of secondary phases and voids, which severely deteriorates the quality of the absorber and the interface. The excessively thick $Mo(S,Se)_2$ significantly reduces the thickness of the Mo electrode, which significantly increases the series resistance and the contact barrier height of the device. (ii) Interface and bulk defects lead to increased trap-assisted recombination, which inevitably results in larger open-circuit voltage deficit. Meanwhile, a series of secondary phases are inevitably generated during the selenization process. Those secondary phases affect the attachment between the buffer layer and the absorber, and reduce the filling factor. Besides, the Sn(S,Se) is commonly used to suppress Sn loss during the selenization process and excess Sn(S,Se) may condense on absorber surface during the cooling. (iii) The undesirable performance of CZTSSe devices compared to CIGS also results from

the obvious bulk band and potential fluctuations as well as short minority carrier lifetime. In addition, due to poor band matching at the heterojunction interface and weakened electron diffusion to ITO in the quasi-neutral region (QNR) near the back interface, the excitons are prone to recombine at the front and back interface, resulting in significant V_{OC} loss.

Based on these analyses, this PhD work was focused on back interface engineering, CZTSSe/CdS front interface engineering, and double gradient band-gap absorber construction by using the ethylene glycol methyl ether precursor solution method. Controllable synthesis of high-quality CZTSSe film, significant reduction of front and back interface recombination, enhancement of carrier transport property and effective suppression of harmful defects were achieved. Ultimately, the efficiency of the CZTSSe solar cell reported in this work reaches 13.7%, which is the highest efficiency of CZTSSe devices prepared in non-vacuum condition. The main achievements are summarized as follows:

(1) Back interface engineering: A WO_3 intermediate layer was introduced to solve the problem of poor crystallinity quality of CZTSSe absorber and the unfavorable back interface contact, thus the diffusion length of minority carrier is improved, and the contact barrier height is reduced. We systematically investigated the effects of WO_3 intermediate layer on the microstructure, electrical and defects property of CZTSSe for the first time. This intermediate layer prevents direct contact of CZTSSe with back electrode. Hence, CZTSSe decomposition and $Mo(S,Se)_2$ formation are inhibited, which is beneficial for obtaining good absorber crystallinity and better back contact, leading to significantly increased minority carriers diffusion length and reduced back interface contact barrier height. Besides, due to the improvement of crystal growth process, the dense absorber with good crystallization has a smoother surface, which gives better contact quality of CZTSSe/CdS interface and lower interface defect density.

This method not only improves interface and bulk carrier transportation, but also reduces the deep acceptor defect density, resulting in reduced non-radiative recombination. This yields a CZTSSe device efficiency of 12.66% with significant enhanced V_{OC}.

(2) Front interface engineering: A new effective strategy is proposed to simultaneously improve the front interface and suppress the CZTSSe absorber defects by introducing a thin ammonium sulfide layer on the absorber surface by a pre-soaking and spin-coating-annealing method. Through this strategy, the absorber surface is optimized by adding S and by remove the secondary phase. At the same time, the diffusion of S into the bulk transforms the dominant deep V_{Se} defect into shallower Cu_{Zn} defect, which effectively reduces carrier recombination in the CZTSSe bulk and at the CZTSSe/CdS interface, prolongs minority carrier lifetime, facilitates carrier collection, and reduces charge loss. The optimized sulfurization treatment significantly improves V_{OC} and FF to the point that device efficiency increases to 13.19%.

(3) Gradient band-gap engineering: The double gradient band-gap absorber has the potential to enhance carrier collection and to improve light collection efficiency. However, achieving the double gradient band-gap structure is challenging due to the similar diffusion rates of cations during high temperature selenization in kesterite $Cu_2ZnSn(S,Se)_4$ films. Here, a double gradient band-gap is successfully achieved in CZTSSe absorber by spin-coating the K_2S solution during the preparation process of the precursor film. The K_2S insertion serves as an additional S source for the absorber, and the high affinity energy of K-Se causes the position of the K_2S layer locally Se rich and S poor. More importantly, the position of the band-gap minimum (notch) and the depth of the notch can be controlled by varying the concentration of K_2S solution and the position of the K_2S layer, thereby avoiding the electronic potential barrier produced by an inappropriate notch position and depth. In addition, the K-Se liquid phase

expedites the selenization process to eliminate the fine grain layer. The champion CZTSSe device achieved an efficiency of 13.70%, indicating the potential of double gradient band-gap engineering for future development of high efficiency kesterite solar cells.

Chapter I: Photovoltaic materials and solar cells

1.1 Introduction

The continued growth of the world's population creates great demands for food, water and energy, while traditional fossil energy sources are facing major challenges in terms of sustainability, security and market price fluctuation. In addition, growing environmental awareness and the limited reserves of fossil energy have guided the scientific community towards the development of new sustainable alternative energy sources. Realizing the transition from the period of fossil energy to new green energy sources is a key process and a necessary path for the future development of the world's energy resources.

Among the many new renewable energy sources, solar energy has received widespread attention due to its large amount, wide distribution, safety and non-pollution. Solar cells convert solar energy directly into electricity based on the photovoltaic effect. Over the past few decades, photovoltaic power generation has made considerable progress, and solar cells are bound to play a crucial role in the future of global electricity production. The International Energy Agency found that solar PV alone accounted for three-quarters of renewable capacity additions worldwide in 2023. And as shown in **Figure 1-1**, the IEA predicts that solar power will account for more than 60% of renewable energy generation in 2028.[1] The data suggests that the future development of the solar PV industry will show a sustained and rapid growth trend, and solar energy will assume a more important responsibility in fulfilling the world's future energy needs.

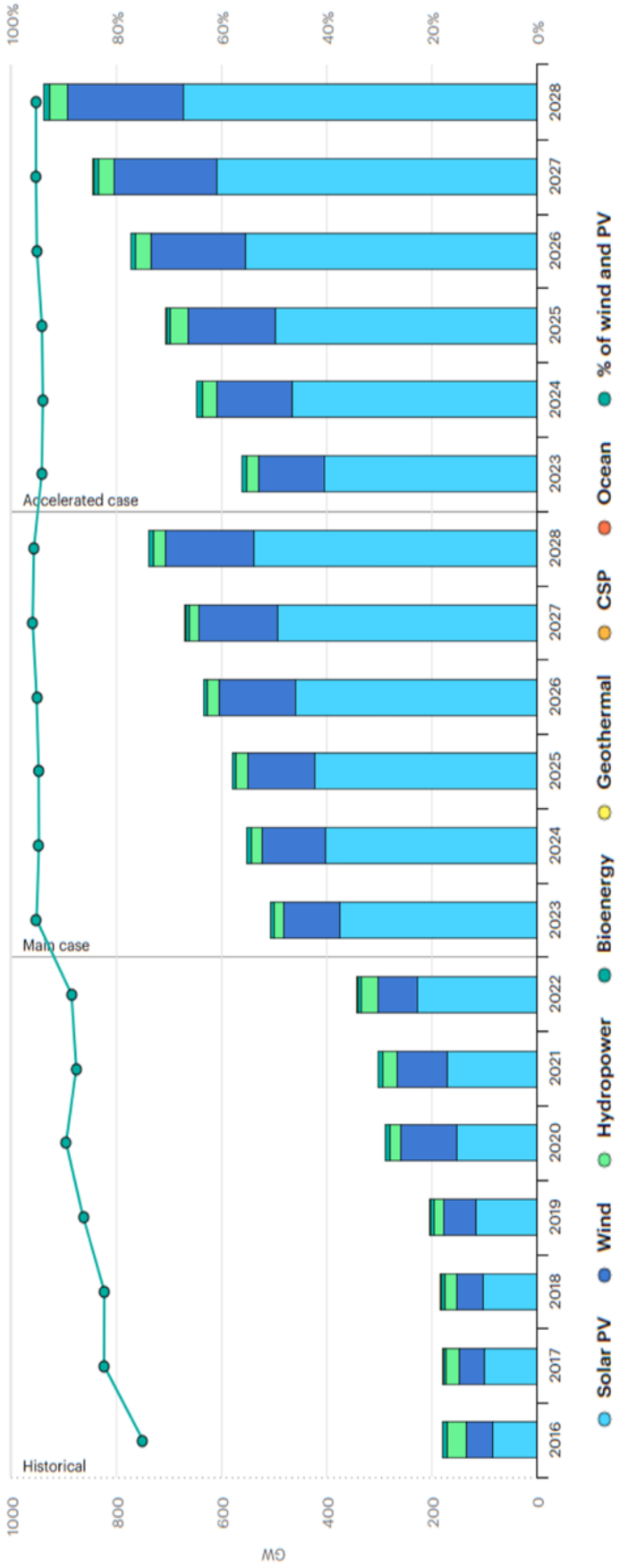
100%
80%
60%
40%
20%
0%
2028
2027
2026
2025
2024
2023
Accelerated case
2028
2027
2026
2025
2024
2023
Main case
2022
2021
2020
2019
2018
2017
2016
Historical
1000
800
600
400
200
0
GW
Solar PV
Wind
Hydropower
Bioenergy
Geothermal
CSP
Ocean
% of wind and PV

Figure 1-1 *Renewable electricity capacity additions by technology and segment, 2016-2028.*[1]

1.2. Introduction of solar cells

Through more than seventy years of development, there are many types of solar cells. Based on different materials, solar cells can be divided into the following groups: silicon-based solar cells, dye-sensitized solar cells, organic solar cells, perovskite solar cells, and inorganic thin film solar cells, and so on. As shown in Figure 1-2, the United States Renewable Energy Laboratory (NREL) summarizes the development trend of the highest certified photovoltaic conversion efficiency of different types of solar cells from 1976 to April 2024.[2] Thanks to the joint efforts of researchers, the development of various types of solar cells is gaining momentum, and the realization of the transition to a new era of green energy is just around the corner.

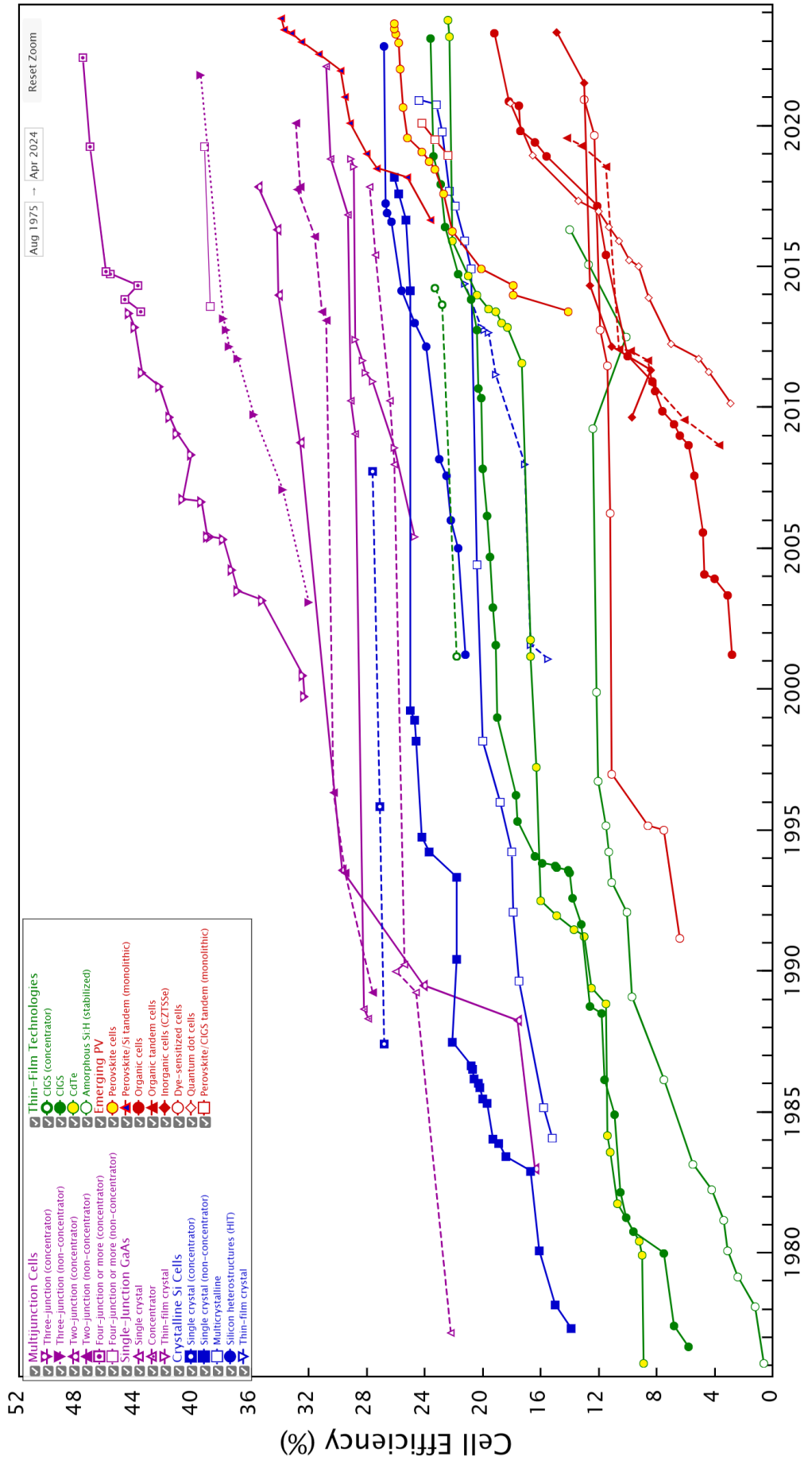
Cell Efficiency (%)
0
4
8
12
16
20
24
28
32
36
40
44
48
52
1980
1985
1990
1995
2000
2005
2010
2015
2020
Aug 1975 → Apr 2024
Reset Zoom
Multijunction Cells
Three–junction (concentrator)
Three–junction (non–concentrator)
Two–junction (concentrator)
Two–junction (non–concentrator)
Four–junction or more (concentrator)
Four–junction or more (non–concentrator)
Single–Junction GaAs
Single crystal
Concentrator
Thin–film crystal
Crystalline Si Cells
Single crystal (concentrator)
Single crystal (non–concentrator)
Multicrystalline
Silicon heterostructures (HIT)
Thin–film crystal
Thin–Film Technologies
CIGS (concentrator)
CIGS
CdTe
Amorphous Si:H (stabilized)
Emerging PV
Perovskite cells
Perovskite/Si tandem (monolithic)
Organic cells
Organic tandem cells
Inorganic cells (CZTSSe)
Dye–sensitized cells
Quantum dot cells
Perovskite/CIGS tandem (monolithic)

Figure 1-2 *The chart displays record research cell efficiencies for five major technologies: crystalline silicon cells, single-junction gallium arsenide cells, multijunction cells, thin films, and emerging PV. Efficiencies have increased across all technologies over the last 50 years.*[2]

1.2.1 The working principle of PV solar cells

A solar cell absorbs incident sunlight and generates both current and voltage. Many cells are connected in series to form an assembly that can output voltage and power. The basic process of solar cell operation includes: light shining on the cell generates photogenerated carriers; collecting the photogenerated carriers to generate current; generating a large photogenerated voltage; and distributing the generated power to the load. Solar energy is renewable, and there are no greenhouse gas emissions such as carbon dioxide during the solar power generation process, so it can basically be considered as not polluting the environment except for the fabrication process.

Currently, the main solar cells are based on semiconductor materials, so the following section describes how semiconductor-based solar cells work. The materials for the light absorbing layer usually have the following characteristics. First, since the solar spectrum is mainly concentrated in the visible wavelength band (380-780 nm), the band-gap of semiconductor materials should be in the range of 1.0-1.5 eV in order to optimally utilize the energy of sunlight.[3] Secondly, semiconductor materials should preferably be direct band-gap materials with high absorption coefficients ($>10^{-4}$ cm^{-1}), which can reduce the cost of raw materials and the difficulty of material preparation. When a photon is absorbed by light absorbing layer, a pair of charged carriers (electrons and holes) is generated. Without external intervention, these photogenerated carriers rapidly recombine or relax energy into heat through lattice vibration. The purpose of building a solar cell is to efficiently separate these electrons and holes and transport them separately into an external circuit to accomplish the conversion of light energy to

electrical energy. The working principle of solar cells is based on the photovoltaic effect. Typically, semiconductors exhibit n type or p type behavior due to their own characteristics or doping, n type semiconductors have a larger electron concentration and p type semiconductors have a larger hole concentration. When the two types of semiconductors are contacted with each other, mutual diffusion due to different carrier concentrations results in the loss of holes near the p type semiconductor interface leaving negatively charged centers, and positively charged centers near the n type semiconductor interface, thus creating a built-in electric field (**Figure 1-3**). The built-in electric field causes the holes/electrons to drift toward the p/n region, and the drift movement hinders the diffusion movement. When both of them reach equilibrium, a stable space charge region is formed at the interface where the two semiconductors are in contact, meaning that a p-n junction is formed.

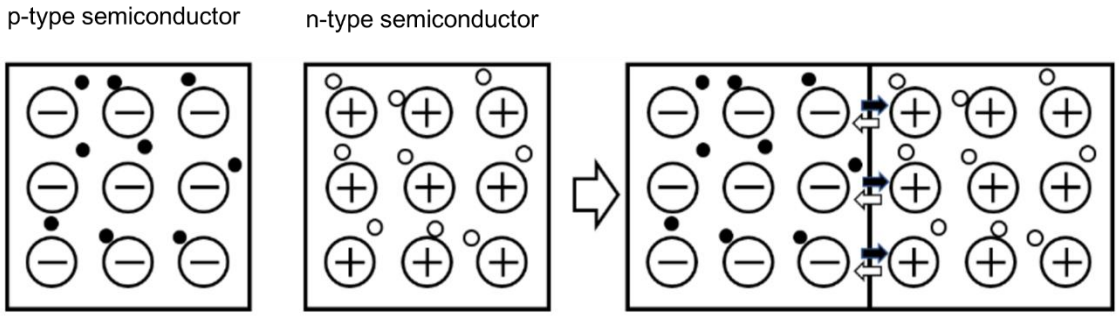

Figure 1-3 *Schematic diagrams of p-n junction.*

Photons with energy greater than the band-gap in sunlight will be absorbed by the light absorbing layer of the solar cell and produce electron-hole pairs. Under the action of the built-in electric field, the holes flow to the p region, and the potential is higher than that in the n region, thus forming a photogenerated electromotive force, which provides a current to the external circuit.

1.2.2. Classification of solar cells

Solar cells can be divided into three generations according to their respective periods of budding development. The first generation of solar cells are represented by Silicon (Si) cells and Gallium Arsenide (GaAs) cells.[4, 5] After a long period of development, their performance are now close to the theoretical limit, and they are playing an important role for both civil and military applications. The development of the second generation of solar cells is mainly civilian-oriented. The main purpose is to solve the problems of too thick light absorbing layer in Si solar cells and the high cost of GaAs preparation. For this reason, second generation solar cells generally follow the route of inorganic thin film solar cells, simplifying the preparation process as much as possible. The main representatives of the second generation solar cells are copper indium gallium selenide (CIGS) and cadmium telluride (CdTe) solar cells.[6] Third-generation solar cells have been developed to further address the high cost of raw materials or toxicity of elements in second-generation solar cells, including dye-sensitized solar cells, organic solar cells, perovskite solar cells, and $Cu_2ZnSn(S,Se)_4$ (CZTSSe) solar cells.[5]

The development of the first generation of solar cells started in the 1950s, represented by Si solar cells and GaAs solar cells (**Figure 1-4**).[6] Among them, Si is an indirect band-gap semiconductor, which requires a thickness of several hundred microns to fully absorb sunlight. Growing such a thick absorber layer imposes very high requirements on the quality of the silicon crystals grown, the purity of the crystals, and the accuracy of the doping. Si solar cells have high conversion efficiency and good temperature characteristics.[7] Si is abundant, non-toxic and has good stability as well as other good characteristics. However, the preparation of high efficiency Si-based solar cells requires the purity of more than 99.9999% of the silicon. This purity of silicon usually needs to be prepared at high temperatures (about 1400 °C), which greatly increases the cost of preparation. Si cells occupy the majority of the market share, while the more efficient

GaAs solar cells are pivotal in a variety of specialized application scenarios, especially in aerospace and military applications. The highest single junction GaAs solar cell efficiency has reached 29.1%.[8] GaAs has a direct band-gap of 1.42 eV, which is very close to the theoretical optimal band-gap. Because of its ultra-high light absorption coefficient, the thickness of the cell can be controlled at about 2 μm. Chemical vapor deposition (CVD) is currently the mainstream preparation method. However, the preparation cost as well as the raw materials cost have always been the main issues. Therefore, although GaAs solar cells have outstanding performance, their applications have been limited to the military and aerospace fields.[9]

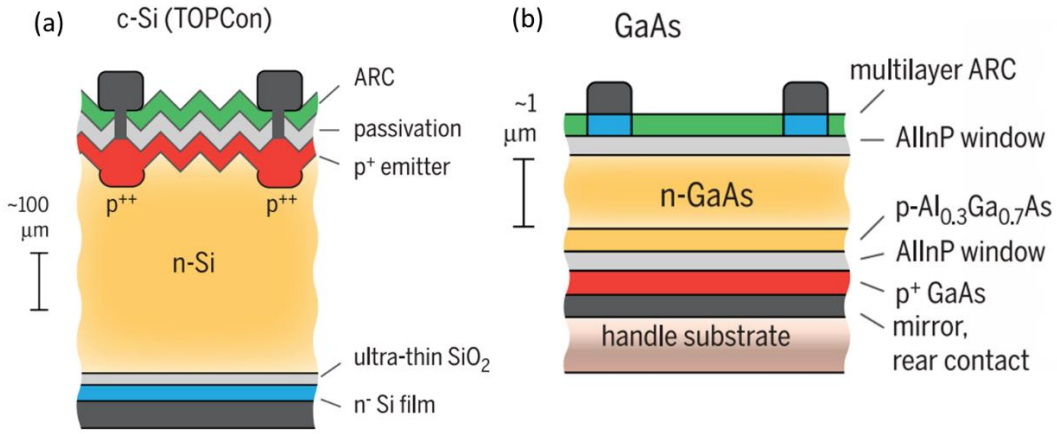

Figure 1-4 *Device structure of the first generation photovoltaics: (a) TOPCon single-crystal Sisolar cell and (b) GaAs solar cell.*[6]

The second generation of solar cells is represented by CdTe and CIGS solar cells (**Figure 1-5**).[6] After entering the 20th century, these two types of cells have rapidly improved their efficiency. At the same time, they have been industrialized and commercialized, and currently they are the two types of cells with the largest market share apart from Si. Both of these cells are thin film cells compared to crystalline silicon cells. Thinner cells mean less raw material consumption and more application scenarios. CdTe solar cells contain the toxic element Cd, so recycling of Cd and the impact of Cd on the environment must be considered in the industrialization process. The current

mainstream CdTe absorber preparation method is the near-space sublimation method, the biggest advantage of this method is that it can realize the rapid deposition of large area films.[10] CIGS solar cells use polycrystalline $CuIn_{1-X}Ga_XSe_2$ films as the light absorber. The cost of In accounts for most of the cost of CIGS materials. The preparation methods of the light absorber mainly include ternary co-evaporation and post selenization in industrial scale.[11]

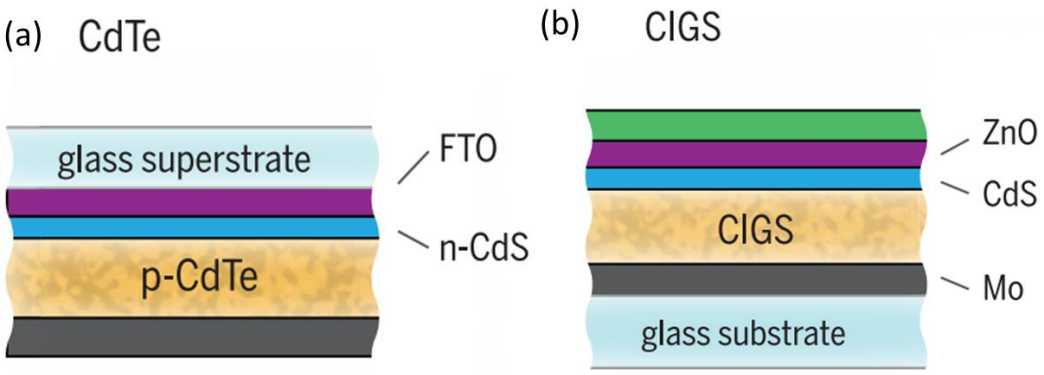

Figure 1-5 *Device structure of the second-generation photovoltaics: (a) CdTe solar cell and (b) CIGS solar cell.*[6]

Third generation solar cells encompass a wide range of cell types, including dye-sensitized solar cells, organic solar cells, perovskite solar cells, CZTSSe solar cells and others (**Figure 1-6**).[6] The development of the third generation solar cells is aims at further reducing the cost of solar cell power generation. Therefore, the raw materials used in third generation solar cells are relatively inexpensive, and their technical route shows a trend of transformation from vacuum process to solution process.

(1) Dye-sensitized solar cells (DSCCs) are one of the typical photovoltaic devices. The most important feature of DSCCs is the separation of light absorption and carrier transport. In the conversion process from light energy to electric energy, the photoexcited dye injects electrons into the conduction band of the photoanode semiconductor. Then the redox pairs in the electrolyte return the lost electrons to the

ground state. Finally, the photo-anode is used to regenerate the redox pairs with the electrons transferred from the photoanode through the external circuit, completing a cyclic process. Although a large number of organic dyes have been developed and used in the past, the efficiency of DSCCs is still low. How to further improve the efficiency of these cells is the focus of future development.[12]

(2) The core part of organic solar cells (OSCs) is organic material, and these cells have the advantages of light weight, good flexibility and low toxicity. The organic active layer based on the intrinsic heterojunction has a good network interpenetration structure, which can realize effective charge separation, and the efficiency of single-junction OSCs has exceeded 18%. In the last two decades, organic solar cells have received more and more attention from researchers as one of the important low cost sources of electricity production.[13]

(3) Perovskite cells is a rapidly developing type of solar cell with outstanding advantages. The high absorption capacity, large carrier diffusion length (>1 μm), high mobility (>10 $cm^2\ V^{-1}\ s^{-1}$), and low cost indicate that perovskite materials are well suited for photovoltaic device applications.[14] The main issues with these solar cells are the presence of the toxic Pb and the sensitivity to moisture. It is also imperative to realize large-area high-efficiency and high-stability perovskite solar modules in order to go further on the road to commercialization.

(4) CZTSSe is a direct band-gap semiconductor with outstanding advantages of ultra-high absorption coefficient and good water-oxygen stability, which is an ideal material for light absorber. Meanwhile, the band-gap can be continuously adjusted in the range of 1.0-1.5 eV by adjusting the ratio of S/Se, and the maximum band-gap can be increased to 2.0 eV after the introduction of Ge/Sn substitutions.[15] The constituent elements of CZTSSe are abundantly available on the earth, which significantly reduces its raw material cost. At the same time, these elements are environmentally friendly,

which also reduces the cost of environmental protection. In recent years, CZTSSe solar cells based on environmentally friendly solution methods have shown rapid development.[16]

Several thin-film solar cells described above have made great progress in terms of photovoltaic conversion efficiency, but none of them are perfect photovoltaic products due to the use of rare or toxic elements or to the device stability issue. Under these conditions, CZTSSe materials have attracted interest essentially because of the use of earth-abundant elements. The crustal content of Zn and Sn is 20,000 and 500 times that of In, respectively.[17] The band-gap and light absorption capacity also meet the standards of photovoltaic devices. Currently, the certified efficiency of this cell has exceeded 14%, which still has great potential for future development.[8]

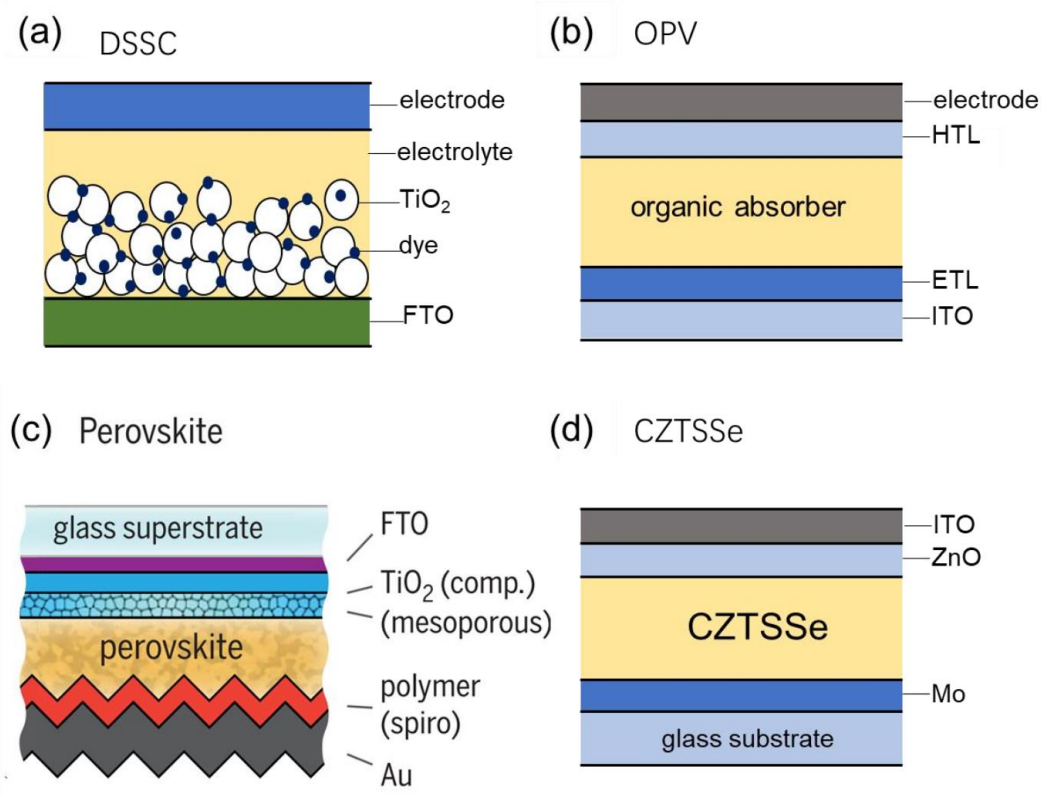

Figure 1-6 *Device structure of the third-generation photovoltaics: (a) dye-sensitized solar cell, (b) organic solar cell, (c) perovskite solar cell and (d) CZTSSe solar cell.*[6]

1.3. Development and research status of CZTSSe thin film solar cells

1.3.1. CZTSSe material

Kesterite CZTSSe solar cells are evolved from CIGS solar cells by replacing the rare elements In and Ga atoms in CIGS with Zn atoms (group II) and Sn atoms (group IV), respectively. It has attracted extensive interest from researchers in the field of thin film solar cells due to its high absorption coefficient, abundant elemental reserves, and low environmental impact. The kesterite semiconductor family includes the pure sulfide Cu_2ZnSnS_4 (CZTS), the pure selenide $Cu_2ZnSnSe_4$ (CZTSe), and the selenosulfide $Cu_2ZnSn(S,Se)_4$ (CZTSSe), as well as other Kesterite structure-based derivatives ($Cu_2CdSn(S,Se)_4$, $Cu_2BaSn(S,Se)_4$, $Ag_2ZnSn(S,Se)_4$, etc.).[18] **Figure 1-7** shows the schematic diagram of the atomic structure of CZTS, CZTSe and CZTSSe. CZTSSe materials have three main crystal structures: kesterite, stannite and wurtzite. Kesterite, stannite are both cubic sphalerite structures, the difference between the two being the different arrangement of Cu and Zn atoms. First principle calculations and experimental studies have confirmed that the Kesterite structure is the most thermodynamically stable structure, so CZTSSe mainly exists in the form of Kesterite, and it has been confirmed that this crystal structure has the highest photovoltic conversion performance. CZTSSe solar cell absorber material has the following advantages: First, it is inexpensive, low toxicity and low environmental pollution. Second, it is a direct band-gap semiconductor material with a theoretical photoelectric conversion efficiency of 32.8%.[19] Thirdly, its band-gap range is adjustable (when the ratio of Se/(Se+S) varies from 1 to 0, the band-

gap value varies from 1.0 to 1.5 eV), which is very close to the optical band-gap of an ideal solar cell. Fourth, in the UV-visible wavelength band, CZTSSe semiconductor material absorbs very strongly, with an absorption coefficient greater than 10^4 cm^{-1}. In addition, the degradation of CZTSSe semiconductor under light illumination is extremely weak, confirming the stability of CZTSSe thin film solar cells.[20]

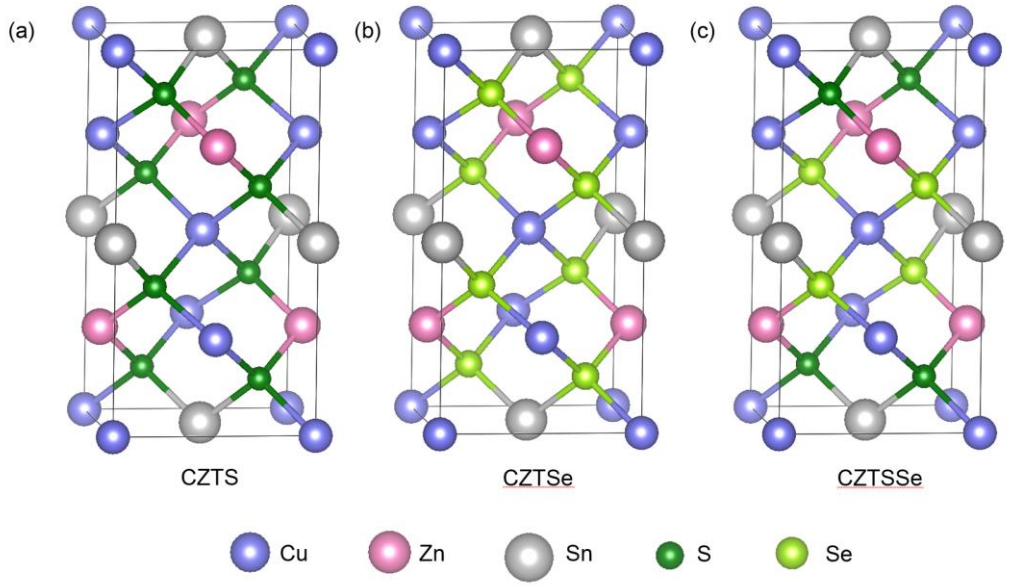

Figure 1-7 *Schematic diagram of the atomic structure of kesterite materials: (a)CZTS; (b)CZTSe; (c)CZTSSe*

The density of CZTS is 4.564 g cm^{-3} at room temperature, and the density of CZTSe increases to 5.675 g cm^{-3} after the substitution of S by Se, which has a larger relative atomic weight.[21] By high-temperature melting, Hiroaki Matsushita synthesized many single-phase Cu-III-IV-Se_4 and Cu_2-II-IV-Se_4 quaternary compounds, and the melting point of CZTSe was measured to be 805 °C by differential thermal analysis. The melting point of CZTS was even higher, reaching 962°C. The band-gap of CZTS and CZTSe calculated by density function theory (DFT) are 1.0 eV and 1.5 eV, respectively. The band-gap of $Cu_2ZnSnS_xSe_{4-x}$ has the following relationship with x, which is in good

agreement with the experimental results, in which the bending coefficient (b) is of the order of 0.07 eV:[22]

$$E_g(x)=(1-x)E_g(CZTS)+xE_g(CZTSe)-bx(1-x) \quad (1\text{-}1)$$

1.3.2 The development process

The research of CZTSSe thin film solar cells began in the 1980s. In 1988, Ito and Nakazawa firstly discovered the photovoltaic effect of CZTS materials and successfully prepared CZTS thin films by sputtering, which opened the door of CZTS research.[23] In 1996, Katagiri's group in Japan used coated Mo glass as the substrate and successfully prepared CZTS thin film solar cells with a photovoltaic conversion efficiency of 0.66% by electron beam evaporation.[24] In 1997, Professor Friedlmeier used thermal evaporation to produce CZTS device with a photovoltaic conversion efficiency of 2.3%.[25] Two years later, Katagiri's group broke this record by improving the vulcanization process and by increasing the efficiency of CZTS devices to 2.62%.[26] Subsequently, the group continued to optimize the quality of the absorber and achieved efficiency as high as 5.45% in 2003 and 6.7% in 2008.[27] At this stage, there were fewer studies and reports on CZTS, and researchers mainly used the vacuum method to prepare CZTS devices with lower efficiency.

CZTSSe experienced a period of rapid growth from 2008-2013. During this period, researchers developed some non-vacuum methods, and the development of non-vacuum methods played a pivotal role in the later development of CZTS solar cells. In 2009, Qijie Guo et al. at Purdue University successfully prepared CZTSSe solar cells for the first time using synthesized CZTS nanoparticles, achieving a PCE of 0.74%.[28] In 2010, they continued to optimize the elemental ratio and film-making process to increase the PCE of the device to 7.2%.[29] In the same year, Mitzi et al. successfully prepared CZTSSe solar cells with photovoltaic conversion efficiencies up to 9.6% using the precursor solution method with hydrazine as solvent.[30] In 2011, Mitzi et al.

continued to optimize the experimental conditions and obtained CZTSSe solar cells with a PCE of 10.1%.[31] In 2012, Mitzi et al. successfully increased the PCE of CZTSSe thin film solar cells to 11.1% by adjusting the film annealing temperature.[32] In 2013, Mitzi et al. deposited magnesium fluoride (MgF_2) on the top layer of the device, which reduced the reflection of sunlight and improved the PCE of the device to 12%. In the same year, they further improved the V_{OC} of the device and produced a CZTSSe device with a certified photovoltaic conversion efficiency of 12.6%, which was the record for seven years.[33] At this stage, a series of high efficiency cells were obtained by non-vacuum methods using hydrazine as solvent, but the inherent flammability and toxicity of hydrazine limited its long-term use. To address the limitations posed by the hydrazine solvent, researchers continued to develop numerous solution methods based on non-hydrazine solvents.

In 2019, Son et al. of Daegu Gyeongbuk Institute of Science and Technology prepared 12.62% CZTSSe solar cells based on magnetron sputtering and post-selenium sulfurization, which is on par with the record efficiency of the IBM team.[34] Subsequently, Wang et al. obtained an efficiency as high as 13.14% by directly introducing a thin GeO_2 layer on a Mo substrate.[35] The team of Hao Xin from Nanjing University of Posts and Telecommunications significantly suppressed interface recombination through Ag cation substitution and heterojunction heat treatment, realizing a CZTSSe solar cell with an efficiency of 13.5%.[36] Guangxing Liang's team of Shenzhen University obtained a device with a PCE of 13.7% by constructing a double gradient band-gap CZTSSe absorber to minimize carrier recombination.[37] The team of Qingbo Meng obtained a cell efficiency of 14.9%, which is the highest efficiency for CZTSSe.[8] In addition, pure sulfide CZTS and pure selenide CZTSe solar cells with efficiencies of 11.0% and 12.5%, respectively, are both reported by the team of Xiaojing Hao at the University of New South Wales.[38, 39]

1.3.3 The device structure

CZTSSe cells consist of several different functional layers of material. The typical cell structure consists of a substrate (soda-lime glass, SLG), a back-contact layer (Mo), a p type light absorbing layer (CZTSSe), an n type buffer layer (CdS), a window layer (ZnO/ITO), and a top electrode (Al/Ag), as shown in **Figures 1-8**. Each of these constituent materials has different physical and chemical properties, and each affects the overall performance of the device in some way. The various interfaces between the different functional layers are particularly important. Since each functional layer has different properties such as microscopic morphology, crystallographic structure, carrier concentration, carrier lifetime, energy band structure, thermodynamic stability, and binding force. Interface contact may induce stresses, defects, interface barriers, interfacial recombination centers, light scattering/reflection/transmission, and composition changes accompanied by changes of photoelectric properties.

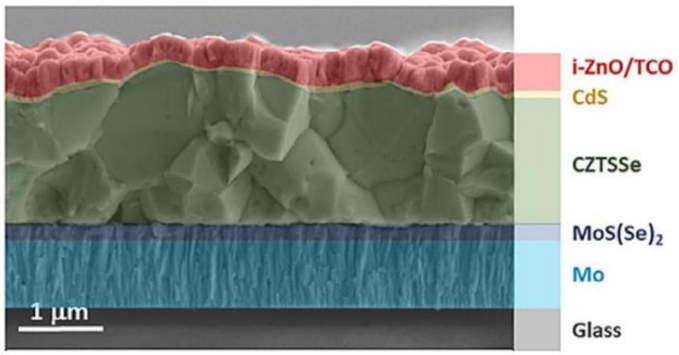

Figure 1-8 *The typical CZTSSe cell structure image.*[40]

CZTSSe thin film solar cell substrates can be rigid or flexible, rigid substrate is mainly soda-lime glass, high temperature resistant, low cost. In addition Na in soda-lime glass can be diffused into the absorber during the high temperature selenization process. Flexible substrate mainly includes polyimide, stainless steel and other materials, and it can be better used for the "roll to roll" industrial production.[41]

Mo is sputtered on SLG substrates as a back electrode material, which has high melting point and high chemical stability. The commonly used Mo back electrodes are prepared by a DC sputtering process, where the density of Mo can be controlled by adjusting the power and argon gas flow rate during sputtering. The Mo used as back electrode has a bilayer structure, with the bottom layer being looser in order to increase the adhesion with the substrate and to solve the problem of stress, and the top layer being denser in order to obtain a better electrical conductivity.[42] Molybdenum can also be used as a reflective layer to reflect unused light back to the absorber.

The P type CZTSSe absorber layer is the main part that absorbs sunlight, where photogenerated carriers are generated. CZTSSe absorber layer is an excellent semiconductor material due to the adjustable and suitable band-gap and high absorption coefficient.[43] As the core of the solar cell, the quality of the CZTSSe absorber layer has a great impact on the performance of the final device, which will be discussed in detail later on.

CdS is known as the transition layer or buffer layer. Dense CdS film covering the surface of the absorber layer can effectively prevent short-circuit and reduce leakage current. Zn (O,S), In_2S_3 and other materials for replacing Cd and for larger band-gap are also used as a buffer layer material.[44, 45]

The window layers include high-resistance layers (i-ZnO, ZnMgO, etc.) and transparent conducting oxide layers (ITO, AZO, BZO, etc.). The high-resistance i-ZnO layer can reduce the leakage current and increase the shunt resistance, and its large band-gap (3.2 eV) does not absorb a large amount of visible light, which minimizes the waste of light. Highly doped ITO can promote the collection of photogenerated carriers.[46]

A metal electrode, typically silver or nickel-aluminum, is evaporated onto the window layer in order to effectively collect the charges. The metal electrode will block the light and reduce the utilization of sunlight, so the electrode is generally designed as grid

shape. It can effectively collect charges to increase the fill factor, and reduce the shading area to effectively utilize the sunlight.

1.3.4 The device preparation method

Up to now, numerous methods for the preparation of CZTSSe thin film solar cells have emerged. They can be divided into two main categories: physical (i.e., vacuum method) and chemical (i.e., non-vacuum method). Vacuum methods mainly include magnetron sputtering, evaporation, pulsed laser ablation, etc. Non-vacuum methods include molecular precursor solution, electrodeposition and nanocrystalline ink printing.

The basic principle of sputtering (Sputtering technique) is to deposit atoms or clusters of atoms escaping from the surface of the raw material by bombardment with high energy ions to form a thin film on a substrate. This technique was invented by the British scientist William Robert Grove.[47] The sputtered metal precursor film can be alloyed by thermal treatment, which improves the density of the selenide film and acts as a Se barrier to inhibit the growth of molybdenum selenide. Direct sputtering with alloy targets is also a promising approach. The Tsinghua University team used Cu-Zn-Sn-Se ternary targets to prepare the precursor film, selenated it with hydrogen selenide H_2Se/Ar mixture, and optimized the selenization temperature to obtain a device with a PCE of 11.95%.[48] Thermal evaporation technique has a long history. Both high purity monomers and compounds are used as raw materials in the preparation of CZTS films by thermal evaporation.[49] Among them, S and Se evaporate at a fast rate, and their evaporation is often controlled independently and efficiently by a heater chamber structure. The substrate temperature has a large effect on the growth of thin films, and increasing the temperature can reduce the secondary phases in the film and decrease the number of holes in the film.

In the development process of CZTSSe thin film solar cells, the equipment cost of the vacuum method is a major factor restricting its industrialization and application. In

2009, Guo et al. of Purdue University prepared CZTS nanocrystals with stoichiometric ratio by oleylamine solution, and selenization resulted in CZTSSe thin film solar cells with 0.80% efficiency.[28] Subsequently, through process optimization, Guo et al. prepared Cu-poor Zn-rich CZTS nanocrystals by the same method in 2010 and selenized them at 500 °C to obtain CZTSSe solar cells with an efficiency of 7.2%.[29] After that, various non-vacuum preparation processes have been rapidly developed. The advantages of the non-vacuum method over the vacuum method are in its low cost, low energy consumption, high throughput, and ease of large-scale production. Molecular precursor solution is the most widely developed non-vacuum method. Its advantages are: the process is simple and low cost; second, the composition can be controlled and adjusted, and the defects in the film can be passivated or regulated by composition tuning. Molecular precursor solution method mainly includes hydrazine solution method and non-hydrazine solution method.

Hydrazine is an ideal carbon-free and oxygen-free solvent, which can effectively dissolve metal compounds and singlet sulfur compounds and remove impurities that are harmful to the film by decomposing them into clean N_2, NH_3 and H_2. Another important feature of hydrazine is its strong reducing effect, which prevents oxidation and deterioration of metals. The hydrazine solvent method for the preparation of CZTSSe thin film solar cells originated at IBM in the United States, and based on this method they successfully prepared CZTSSe devices with a certified efficiency of 12.6%.[33] However, the hydrazine solution is highly toxic and explosive, and all processing needs to be done in a glove box with an inert atmosphere. These limitations of hydrazine solvents have been a major incentive for the rapid development and widespread use of non-hydrazine solvent systems. The common non-hydrazine solvent systems can be divided into the following categories: water/alcohol system,[50] dimethyl sulfoxide (DMSO) /dimethyl formamide (DMF) system,[51] amine-carbon disulfide /thiol /mercaptoacetic acid system,[52] and ethylene glycol methyl ether (2-Me) system.[53]

Among them, 2-Me can be used in atmosphere with high solvency capacity and has the advantage of non-toxicity and non-pollution.

1.3.5 Experimental method based on solution system

The process for preparing CZTSSe devices based on solution system consists of four main steps: spin-coating to prepare CZTSSe precursor films; chemical bath deposition to prepare CdS buffer layer films; magnetron sputtering to prepare ITO window layer films; and thermal evaporation to prepare Ag top electrodes.

(1) Spin-coating

Spin-coating method is a convenient way to prepare thin films. It consists of two processes: low-speed drop coating of the solution (or static drip coating) and high-speed spin coating to prepare the thin film (**Figure 1-9**). During the high-speed spinning process of the spin coater, the acceleration of the centrifugal acceleration causes the solution on the surface of the substrate to quickly homogenize, and the excess solution is thrown away from the substrate, forming a uniform film over the entire substrate. There are two main factors that affect the thickness and other characteristics of the film: the solution itself (concentration, surface tension, speed of solution drying, etc.) and the final speed of the spin.

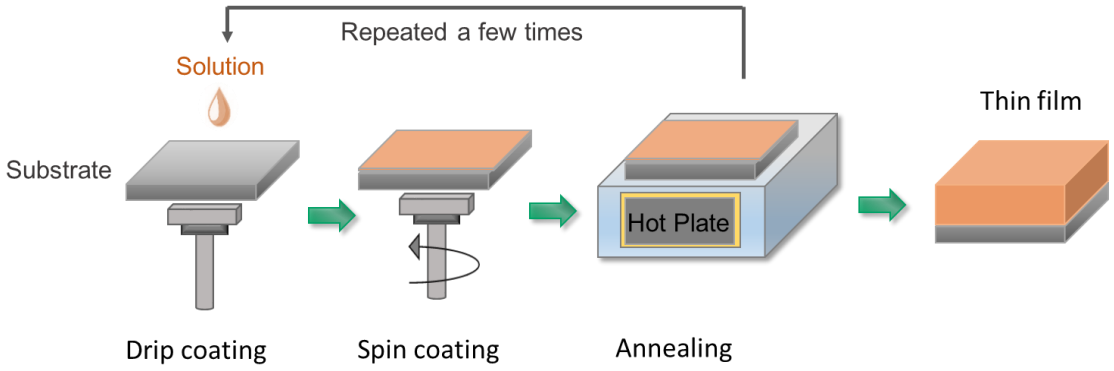

Figure 1-9 *Schematic diagram of spin coating process.*

The films prepared directly by the spin-coating method contain solvent and are therefore called wet films. Wet films need to be annealed and dried to remove solvent residues. This coating and annealing procedure was repeated several times till the desired film with certain thickness was obtained. In the experiments for CZTSSe, the CZTSSe solution was spin-coated on a soda-lime glass substrate, dried and scraped off the glass substrate for thermal gravimetric analyzer (TGA) analysis. The TGA is an instrument that uses thermogravimetry to detect the temperature-mass relationship of materials. Thermal Gravimetric Analyzer is an instrument that measures the temperature (or time) dependence of the mass of material under a programmed temperature control. The mass of the measured material changes when it sublimates, vaporizes, decomposes into gases, or loses water of crystallization during the heating process. The thermogravimetric curve is not straight but decreases. By analyzing the thermogravimetric curve, it is possible to know at what degree the measured material changes, and according to the weight loss, it is possible to calculate how much material is lost.

Figure 1-10 presents the TGA curve for the mixed CZTSSe precursor.[43] The TGA sample was prepared from the CZTSSe precursor solution by preheating at 100 ℃ for 20 min to remove the low-boiling-point molecules. It was found that the CZTSSe precursor exhibited a relatively fast weight loss between 130 and 280 ℃, which may be ascribed that the extensive N−H ··S hydrogen bonding existed in the precursor solution was broken and the CZTSSe nanocrystal formed at this temperature. Thereby, CZTSSe nanocrystal thin films were fabricated by spin coating of CZTSSe precursor solution, followed by heating on a hot plate around 300 ℃ for 2 min usually. It is noteworthy that in order to form a dense CZTSSe absorbing film, the preheating procedure for removing the organic solvents after each spin coating was essential.

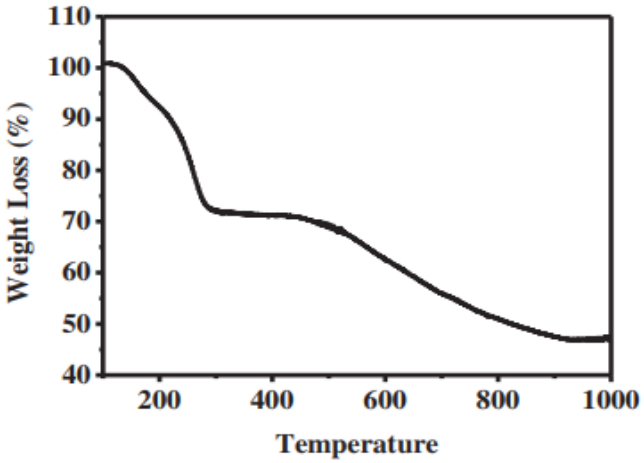

Figure 1-10 *Typically TGA curve of CZTSSe precursor with the target ratios.*[43]

(2) Chemical bath deposition

Chemical bath deposition (CBD) is a common method for preparing CdS buffer layer (**Figure 1-11**). CBD is a chemical reduction process that uses a suitable reducing agent to reduce metal ions in the plating solution and deposit them on the surface of the substrate. The CBD reaction process does not require vacuum equipment, the reaction temperature is low, and the substrate can be selected from a wide range. At the same time, CBD requires less purity of the raw materials for the reaction, so the raw materials for the reaction are highly selectable and inexpensive.

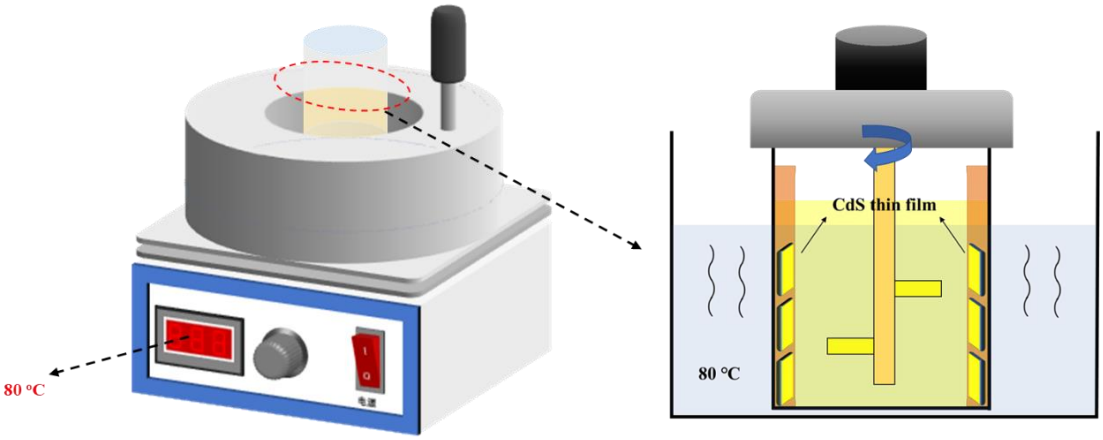

Figure 1-11 *Schematic diagram of the chemical bath deposition process for CdS thin films.*

In our experiments, the growth process of chemical water bath deposited CdS thin films consists of four stages:[44]

Cd^{2+} and NH_3 in the solution combine to form $Cd(NH_3)_n^{2+}$ coordinated ions and accumulate near the substrate:

$$Cd^{2+}+nNH_3 \rightarrow Cd(NH_3)_n^{2+} \quad (1\text{-}2)$$

Reversible adsorption process of $Cd(OH)_2$ occurs on the substrate surface:

$$Cd(NH_3)_n^{2+}+2OH^-+site \rightarrow [Cd(OH)_2]_{ads}+nNH_3 \quad (1\text{-}3)$$

Thiourea and $Cd(OH)_2$ again undergo an adsorption reaction to form a substable $Cd(OH)_2SC(NH_2)_2$ complex:

$$[Cd(OH)_2]_{ads}+SC(NH_2)_2 \rightarrow [Cd(OH)_2SC(NH_2)_2]_{ads} \quad (1\text{-}4)$$

Further decomposition of $Cd(OH)_2SC(NH_2)_2$ produces CdS, which is continuously deposited to form a thin film:

$$[Cd(OH)_2SC(NH_2)_2]_{ads} \rightarrow CdS+CN_2H_2+2H_2O+site \quad (1\text{-}5)$$

(3) Magnetron sputtering

The indium tin oxide (ITO) window layer is usually prepared using magnetron sputtering technology (**Figure 1-12**). In a high vacuum environment, the target is bombarded by accelerated argon ions (Ar^+) through the combined action of electric and magnetic fields, causing the atoms or molecules on the surface of the target to gain sufficient kinetic energy to detach from the target surface. These neutral target atoms or molecules are then deposited on the substrate to form the desired thin film.

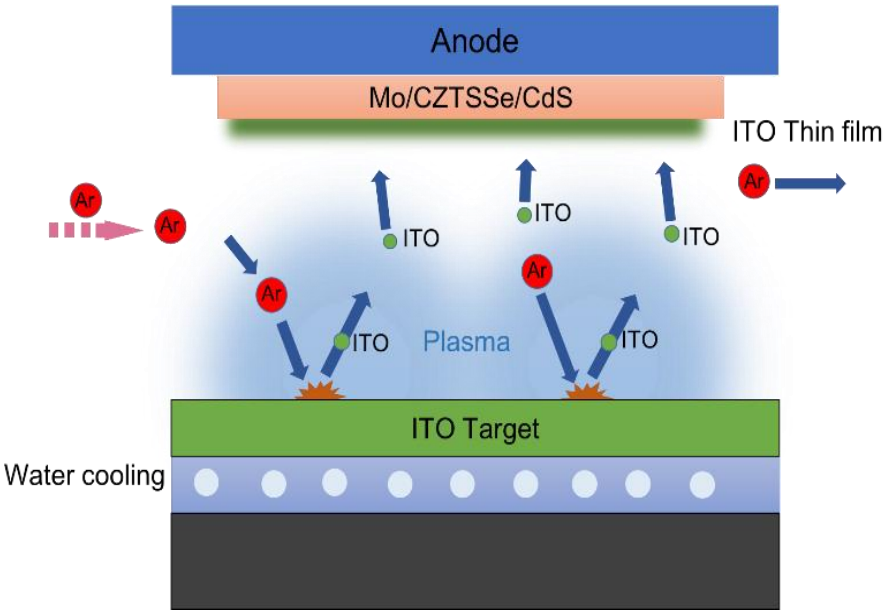

Figure 1-12 *Schematic diagram of magnetron sputtered ITO film*

The electrons fly towards the substrate in the presence of an electric field, but in the process of flying towards the substrate, the electrons collide with argon atoms, resulting in ionization of the electrons with a large number of argon ions and new electrons. These new electrons fly to the substrate, while the argon ions continue to bombard the target under the action of the electric field. In magnetron sputtering technology, the path of the electrons can be controlled by introducing a magnetic field. The electrons are bound in the plasma region close to the target material under the action of the magnetic field, so that the movement path of the electrons becomes very long, increasing the collision opportunities with the argon atoms, thus generating more argon ions to bombard the target material and improving the sputtering efficiency. At the same time, due to the circular motion of the electrons on the surface of the target, the plasma density is high near the target, further increasing the sputtering rate. With the increase in the number of collisions, the energy of the secondary electrons is gradually depleted and they eventually move away from the target surface and are deposited on the substrate under the action of the electric field. Due to the low energy of these electrons, they

transfer less energy to the substrate, resulting in a small temperature increase of the substrate.

When Sn is doped into In_2O_3, the Sn element can replace the In element in the In_2O_3 lattice and exist in the form of SnO_2. Because the In element in In_2O_3 is trivalent, the formation of SnO_2 will contribute an electron to the conduction band while generating oxygen holes in a certain oxygen-deficient state.[5] Generally speaking, the preparation of ITO films to obtain different layer thickness is relatively easy. By adjusting the film deposition deposition rate and deposition time to obtain the required thickness of the film layer, and through the corresponding process methods can be accurate control of the thickness and uniformity of the film.

The resistivity of the ITO film is the key factor in the ITO film preparation process, and resistivity is also an important indicator of the performance of ITO films. When the carrier concentration and carrier mobility is larger, the resistivity of the film is smaller, and vice versa. And the carrier concentration is related to the composition of the ITO film material, that is, the composition of the ITO film itself tin content and oxygen content. In order to get a higher carrier concentration can be achieved by adjusting the tin content and oxygen content of the ITO deposition material. The carrier mobility, on the other hand, is related to the crystalline state of the ITO film, the crystal structure and the defect density of the film. In order to obtain a high carrier mobility, factors such as deposition temperature, sputtering voltage and conditions of film formation during film deposition can be reasonably adjusted.

(4) Thermal evaporation

The principle of vacuum thermal evaporation is to evaporate or sublimate the deposited materials (e.g., metals or compounds) by heating in a high vacuum environment (**Figure 1-13**). The material vaporizes into gaseous particles such as atoms, molecules, or clusters of atoms, which fly rapidly and collisionlessly to the surface of the substrate

in a vacuum environment and coalesce and nucleate on the substrate, gradually growing to form a solid thin film. The formation of thin films during vacuum evaporation includes several key steps: evaporation or sublimation of the deposited material, transport of gaseous particles to the substrate, nucleation and growth of the gaseous particles on the substrate, and reconfiguration or chemical bonding of the thin film atoms. Thermal vacuum evaporation has the advantages of a simple film formation method, high film purity and densification, and unique film structure.

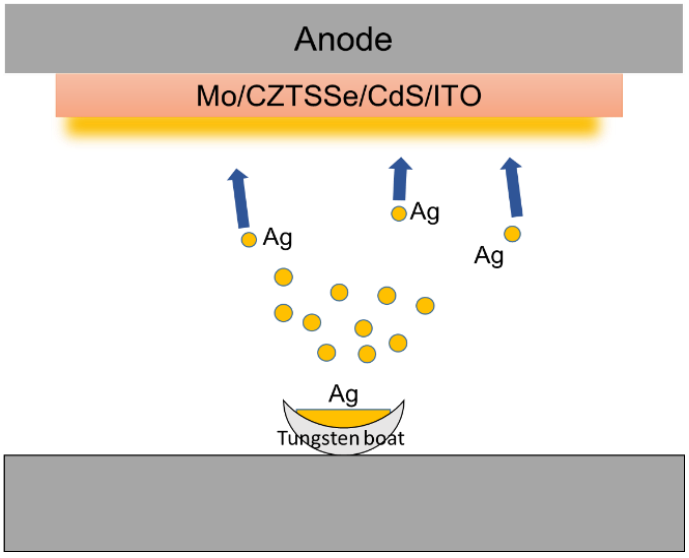

Figure 1-13 *Schematic diagram of Ag top electrode prepared by thermal evaporation.*

1.3.6 The current status

A cell efficiency of 14.9% was obtained by Qingbo Meng's team at the University of Chinese Academy of Sciences in May 2023, which is the highest efficiency for the CZTSSe solar cells.[8] However, this is still far below that of CIGS. The main obstacle limiting the performance of CZTSSe solar cells is the large V_{OC}-SQ deficit (defined as the difference in V_{OC} voltage relative to the Shockley-Queisser limit). At the same time, the fill factor of the CZTSSe is also far from the SQ limit. Large open-voltage losses and low filling factors lead to the current maximum efficiency of CZTSSe still being

less than 50% of the SQ limit. In order to break through this bottleneck, researchers have made unremitting efforts to conduct in-depth studies on the thin film grain growth mechanism, cation doping, and passivation of the front and back interfaces of CZTSSe solar cells.

(1) Interface engineering

The commonly used CdS/CZTSSe heterojunction structure, inherited from CIGS solar cells, has greatly contributed to the rapid development of CZTSSe solar cells in the past decade. However, theoretical calculations and recent characterizations have shown that the CdS buffer layer is not suitable for high band-gap CZTSSe solar cells because the "cliff-like" conduction band offset (CBO) at the heterojunction interface exacerbates the interface recombination.[54] In addition, the large photocurrent loss caused by the parasitization of the CdS buffer layer results in a considerable efficiency loss. Therefore, it is necessary to select alternative buffer layers with suitable conduction band edges in order to further improve the V_{OC}, especially for pure sulfide CZTS solar cells. Recently, in order to optimize the heterojunction interface, Xu et al. proposed a new Zn doping strategy to deposit ternary $Zn_xCd1\text{-}_xS$ buffer layers with gradient composition (**Figure 1-14**a).[55] The suppression of heterojunction interface recombination contributes to the improvement of V_{OC} and device performance, and the efficiency of the CZTSSe solar cell based on the gradient-composition $Zn_xCd_{1-x}S$ buffer layer is 12.35%. Meanwhile, the quest for "low toxicity" has motivated researchers to develop Cd-free buffer layers. In this regard, atomic layer deposition (ALD)-treated (Zn,Sn)O (ZTO) buffer layers have been proposed, with efficiencies up to 11% to date.[56] In addition to the optimization of the buffer layer, modulation of the CdS/CZTSSe heterojunction interface is also one of the feasible ways to enhance the device performance. Wang et al. proposed a synergistic optimization strategy for the bulk heterojunction interface consisting of atomic layer-deposited alumina (ALD-Al_2O_3) and $(NH_4)_2S$ treatment (Fig.

1-14b).[57] The V_{OC} deficit is reduced from 0.607 V to 0.547 V and the average FF increased from 64.2% to 69.7%, resulting in the CZTSSe solar cells with an efficiency of 13.0%.

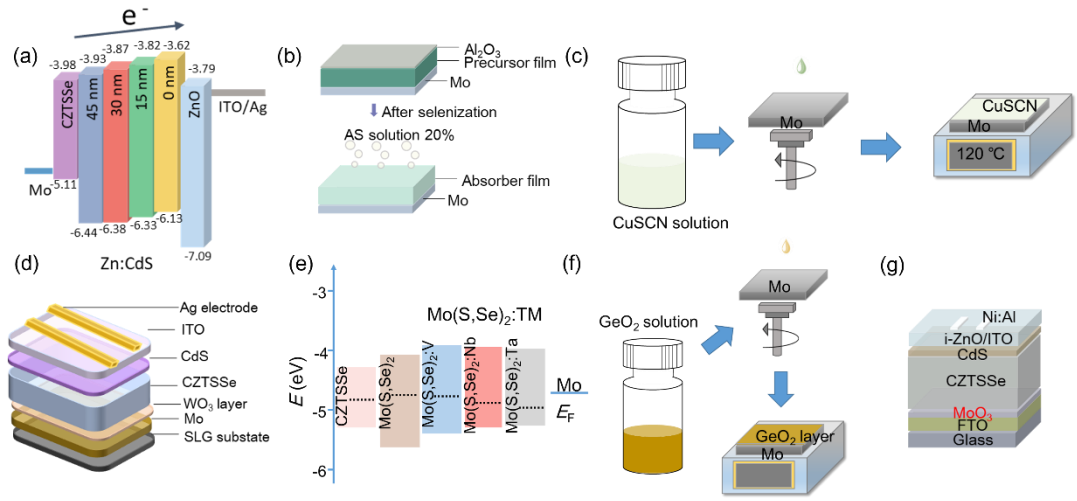

Figure 1-14 *Efficient interface engineering schematic: (a) Gradient energy levels at the gradient $Zn_xCd_{1-x}S$/CZTSSe interface;[55] (b) Schematic diagram of atomic layer deposition of alumina and $(NH_4)_2S$ treatment experiments;[57] (c) Schematic structure of spin-coated CuSCN on Mo glass;[58] (d) Structure of CZTSSe devices with WO_3 intermediate layer;[59] (e) The schematic diagrams of energy band alignment at Mo/CZTSSe(S,Se)$_2$/Mo back contact;[52] (f) Schematic structure of the CZTSSe device with GeO_2 layer derived from spin-coating GeO_2 precursor solutions;[60] (g) Schematic structure of CZTSSe device with MoO_3 interface layer and FTO transparent electrode.[61]*

The optimization of the back contact interface is also crucial to improve the performance of CZTSSe thin film solar cells. The poor Mo/CZTSSe backinterface leads to decomposition reaction and the formation of secondary phases and voids, which seriously deteriorate the crystallinity of the absorber layer and the quality of the back interface. Ji et al. introduced a self-depleted CuSCN layer at Mo/CZTS interface in order to improve the back contact (Figure 1-14c).[58] The carrier recombination was

reduced and an efficiency of 11.1% was attained. Zhao et al. effectively suppressed the undesirable interface reaction between the absorber layer and the back electrode during the selenization process by introducing a WO_3 intermediate layer at the back interface (Figure 1-14d).[59] The PCE of the device reached 12.66% due to the increase of the minority carrier diffusion length, the decrease of the contact barrier height at the back interface, and the reduction of the deep level acceptor defects. An electrically benign back interface field was established by in situ doping of the Mo back electrode with the VB group elements (TM = V, Nb, and Ta), $Mo(S,Se)_2$, according to Fu et al. The shallow V_{Mo}, Nb_{Mo} or Ta_{Mo} acceptors can convert the weak n-type conductivity of $Mo(S,Se)_2$ into p-type conductivity and increase hole concentration (Figure 1-14e).[52] Wang et al championed a device with an efficiency as high as 13.14% by introducing a thin GeO_2 layer directly on a Mo substrate (Figure 1-14f).[60] In addition, Zhou et al. conducted a study on transparent electrodes for FTO substrates, and the experimental results demonstrated that the introduction of a MoO_3 interface layer was able to increase the device efficiency of transparent substrates from 7.02% to 9.56% (Figure 1-14g).[61]

(2) Cation substitution

Cation substitution can effectively reduce the deep level defects and defect clusters in CZTSSe devices, reduce cation disorder, and enhance device performance. The characteristics of high efficiency devices obtained by the cation substitution process is displayed in **Table 1-1**. The silver (Ag) substitution is recognized as an effective method for mitigating Cu/Zn-related defects, electrostatic fluctuations, and recombination centers in CZTSSe solar cells. However, the introduction of excessive Ag into the CZTSSe bulk leads to lower carrier concentration and poorer conductivity. Cui et al. utilized AgF post-deposition treatment (PDT) to dope high concentration Ag into the absorber layer surface to increase the band bending near the p-n junction. As a result, the AgF-PDT device finally achieves a maximum efficiency of 12.34%.[62] Enkhbat et

al. proposed a method of localized replacement of Ag into the CZTSSe at the front and back interfaces to avoid the negative effects caused by the introduction of excess Ag. The PCE of the Ag-substituted device reached 12.43% by using a double interface Ag passivation method.[63] Gong et al. doped Ag into the absorber layer based on dimethyl sulfoxide (DMSO) solution system, which could promote the direct phase transition grain growth and form CZTSSe absorber layer with uniform grain size and less defects. The champion device efficiency was 13.5%, achieving a record low open-circuit voltage deficit (64.2% of the Queisser limit).[36] More interestingly, Sun et al. demonstrated a strategy to achieve a surface-modified CZTSSe absorber layer through the use of n-type Ag_2ZnSnS_4.[64] Ag acts as a surface inversion and frontier gradient distribution in the CuZnSnSe thin film device. The efficiency of the champion solar cell was as high as 12.55%. Yin et al. introduced La^{3+} on the basis of Ag doping, resulting in the high cell efficiency (13.9%).

In addition to Ag, Germanium (Ge) substituted Sn is also an effective method to suppress deep level Sn_{Zn} defects.[65] Deng et al. demonstrated that the energy level and concentration of Sn_{Zn} defects in CZTSSe absorber layer were significantly reduced by Ge substitution. The device efficiency was enhanced to 11.48%.[66] Zhang et al. found that the $GeSe_2$ post-deposition treatment on the absorber was able to passivate the deep level defects and the heterojunction band-tailed states, which significantly reduced the severe interface nonradiative carrier recombination in CZTSSe photovoltaic devices.[67] Kim et al. introduced elemental Ge by co-evaporation while adding $GeSe_2$, $SnSe_2$, and Se to control the selenide environment, obtaining a device efficiency of 12.3%.[68] He et al. obtained an efficiency of 11.6% by incorporating a small amount of Ge and Cd into a CZTSSe absorber.[69]

Table 1-1 *The summary of CZTSSe solar cells based on cation doping.*

Reference	Cation	Source	J_{SC} (mA/cm^2)	V_{OC} (mV)	FF (%)	PCE (%)
[62]	Ag^+	AgF	36.64	0.496	67.89	12.34
[63]	Ag^+	$AgNO_3$	37.93	0.502	65.31	12.43
[36]	Ag^+	$AgNO_3$	34.6	0.540	72.3	13.50
[64]	Ag^+	$AgNO_3$	35.0	0.526	68.2	12.55
[65]	Ag^++ La^{3+}	AgCl	35.8	0.550	71.0	13.90
[66]	Ge^{4+}	Ge	34.77	0.491	67.23	11.48
[67]	Ge^{4+}	$GeSe_2$	37.17	0.470	69.95	12.22
[68]	Ge^{4+}	Ge+$GeSe_2$	32.3	0.527	72.7	12.3
[69]	Ge^{4+}+Cd^{2+}	Ge+ $CdSO_4$	36.80	0.479	66.10	11.60
[70]	Li^+	LiCl	34.00	0.484	64.20	10.70
[71]	Li^+	LiTFSI	40.10	0.477	69.00	13.20
[72]	Ga^{3+}	Ga	34.78	0.515	68.55	12.30
[73]	Ti^{4+}	$TiCl_4$	39.43	0.505	61.45	12.07
[74]	Ag^++Ti^{4+}	AgCl+ $TiCl_4$	37.49	0.530	64.04	12.73

The experience of CIGS development proves that alkali metals play a crucial role in efficiency enhancement and that heavy alkali metals work better, but researchers have found that the introduction of light alkali metals is more effective in improving the performance of CZTSSe. The sodium (Na) diffusion into the absorber layer during selenization in SLG substrate can improve the crystal quality, and Lithium (Li) doping in CZTSSe has also been experimentally proven to be effective in improving the electrical performance of photovoltaic devices. He et al. demonstrated that Li-PDT can

enable Li to be uniformly incorporated into the grains, and p type doped CZTSSe absorber can be obtained.[70] Zhou et al. introduced the organic lithium salt LiTFSI into the preparation of CZTSSe solar cells for the first time, in response to the problem of low solubility of conventional lithium ion salts and the difficulty of introducing them into the precursor solution directly.[71] Du et al. utilized Ga doping to solve the problems of large open-circuit voltage deficit and low efficiency due to the presence of Sn_{Zn} antisites and [$2Cu_{Zn}$+Sn_{Zn}] defective clusters.[72] Farooq et al. found that the introduction of Ti into the CZTSSe can significantly improve the film grain size.[73] Meanwhile, Chen et al. proposed to use Ag and Ti bications to replace Cu and Sn, respectively.[74] Under the condition of dual cation substitution, a 12.73% efficiency was obtained for the champion device. These cation substitution results provide new ideas to further improve the efficiency of CZTSSe solar cells.

(3) Annealing process

The high-temperature selenization annealing process is a decisive factor for the crystallinity of the absorber layer, and many researchers have conducted detailed studies on the annealing process, the grain growth mechanism, and the resulting optimization of the device performance. Cui et al. proposed a new strategy to achieve large grains in a single layer of CZTSSe by using the synergistic optimization of the Cu^{2+}+Sn^{2+} redox system and the pre-annealing temperature (**Figure 1-15**a).[75] In addition to pre-selenization, researchers have found that two-step selenization and a two-step cooling process after selenization are also helpful for grain growth and efficiency enhancement. Yin et al. synergistically utilized high and low temperatures for selenization in promoting the formation of the CZTSSe phase to achieve a cell efficiency of 12.5% (Figure 1-15b).[76] Geng et al. reported a convenient two-step cooling strategy for selenization (Figure 1-15c), which can simultaneously suppress Cu_{Zn} and Sn_{Zn} defects and defect clusters.[77] These results illustrate the significance of

controlling the crystalline growth of CZTSSe for improving device performance. In addition Guo et al. achieved the gradient band-gap by annealing after selenization (Figure 1-15d), and this annealing process promoted the solid-state ion-exchange reaction between Cu^{+} and Cd^{2+} at the heterojunction interface, and the n type CdS was partially converted into the p type Cu_2S.[78] While Gong et al. concluded that the low-temperature annealing of kesterite/CdS junctions was able to reduce the interface recombination, achieving a 12.96% certified efficiency.[79] Zhou et al. modulated the phase transition dynamics of Ag alloyed CZTSSe by applying a over pressure inside the reaction chamber at the initial stage of the annealing process (red part in Figure 1-15e, 300-800s).[80] CZTSSe crystals were formed at relatively higher temperatures compared to the conventional selenization method, and kesterite films with high crystallinity and fewer defects were obtained with a device efficiency of 14.1%.

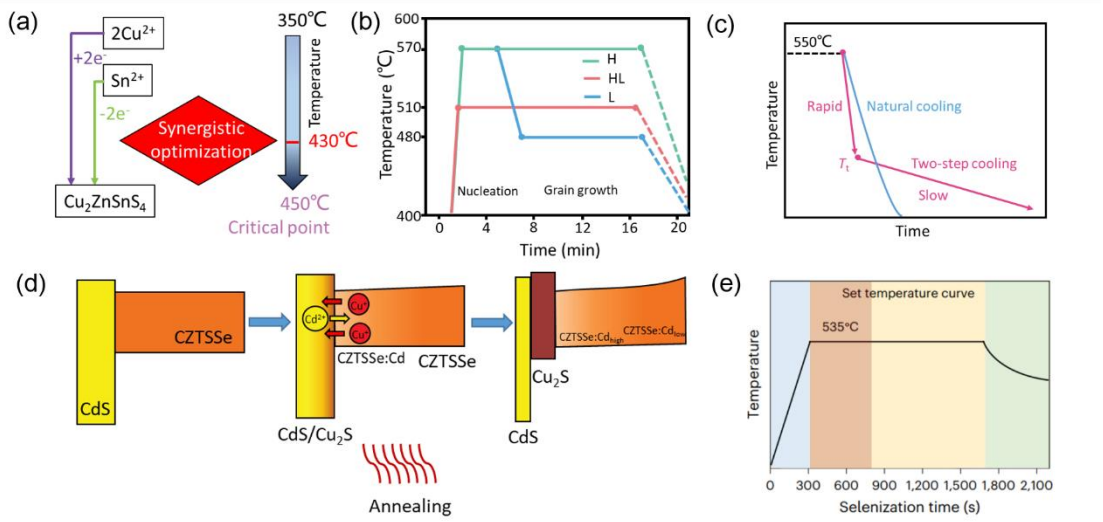

Figure 1-15 *(a) Schematic of synergistic optimization of redox reaction and pre-annealing temperature;*[75] *(b) The schematic temperature profile of the three different selenization processes;*[76] *(c) The temperature profile of the cooling process of the selenization;*[77] *(d) The energy band diagrams of CdS/CZTSSe, Schematic of the diffusion of* Cu^{+} *and* Cd^{2+} *ions during heterojunction annealing, The energy band diagrams of* $CdS/Cu_2S/CZTSSe:Cd_{high}/CZTSSe:Cd_{low}$;[78] *(e)*

Diagram of applying over pressure (300-800s) at the annealing stage of the annealing process.[80]

1.4 Problems in CZTSSe solar cells

Figure 1-16 shows the optimal photovoltaic parameters and band-gap of the CZTSSe solar cell device versus the Shockley-Queisser (SQ) limit.[6] Figure 1-16a shows the short-circuit current and product of open-circuit voltage and fill factor relative to the maximum achievable values, based on the SQ detailed-balance limit, for the most efficient solar cell made with each photovoltaic material. The main obstacle that limits the performance of these solar cells is the large V_{OC}-SQ deficit. Cells that show a Jsc lower than the S-Q limit suffer from incomplete light absorption or incomplete collection of generated carriers, whereas a reduced Voc or fill factor (FF) reflects unwanted bulk or interfacial carrier recombination, parasitic resistance, or other electrical nonidealities. The FF is also far from the SQ limit, which result in the current maximum efficiency still less than 50% of the SQ limit. CZTSSe devices have poor carrier management compared to CIGS devices. This is usually attributed to poor front and back interfaces as well as severe bulk recombination.

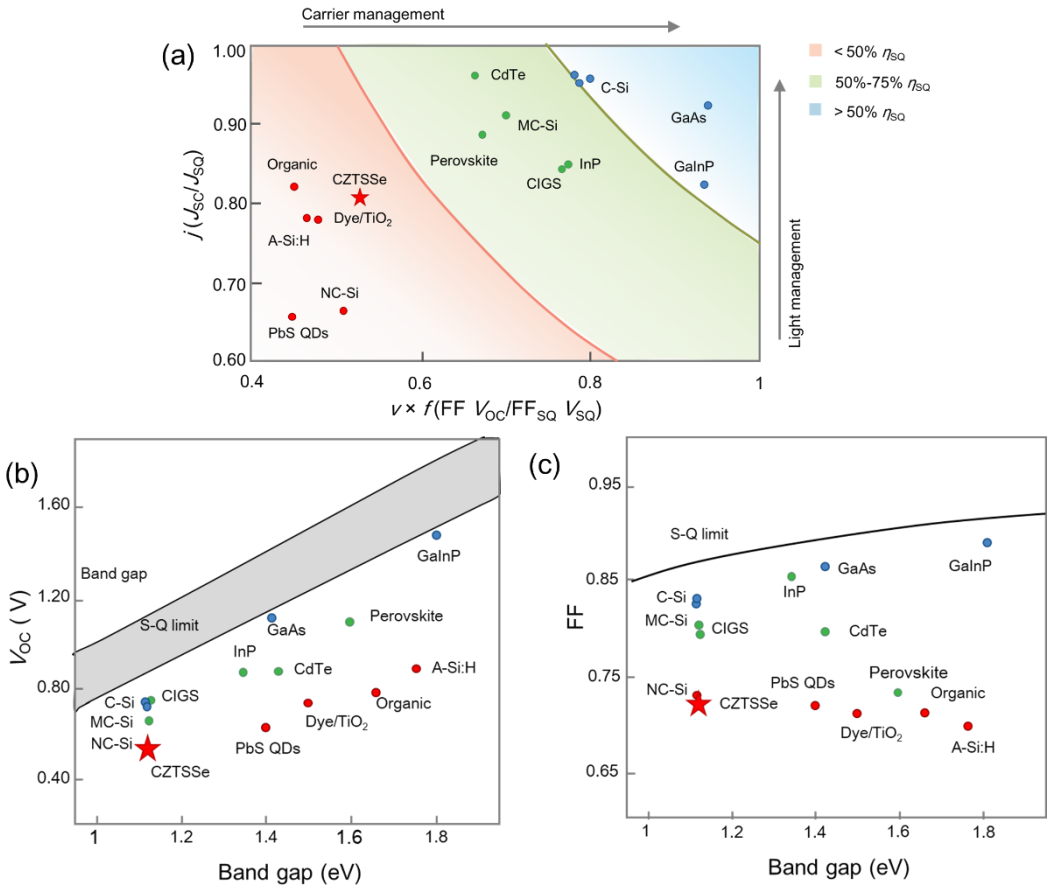

Figure 1-16 *(a) The percentage of J_{SC}, V_{OC}×FF and corresponding S-Q limit achieved by the battery device is partially recorded, (b), (c) the correspondence between the V_{OC} and FF of the world record battery and its S-Q limit.*[6]

1.4.1 The back interface recombination

In CZTSSe solar cells, the recombination at the back interface (Mo/CZTSSe) limits the Voc. The quasi-neutral region of the Mo/CZTSSe interface creates an electrostatic field that drives the diffusion of electrons into the p-n junction, and reduces the recombination of electrons and holes. Typically, the thickness of the absorber layer in CZTSSe solar cells is about 1-2 μm, and the electron-hole recombination at the back contact interface far exceeds the depletion region width of the p-n junction and the diffusion length of the minority carriers. During the high-temperature annealing process of CZTSSe absorber layer, a $Mo(S,Se)_2$ layer is usually formed between the Mo layer

and the CZTSSe absorber layer.[52] The $Mo(S,Se)_2$ layer with a suitable thickness (~100 nm) is able to enhance the bonding strength and electrical conductivity between the back electrode and the absorber layer, realizing the ohmic contact, which greatly improves the performance of the photovoltaic device by enhancing the Jsc and FF [81] However, an excessively thick $Mo(S,Se)_2$ layer increases the series resistance of the PV device, hinders charge transfer, causes electron and hole recombination, and reduces the utilization of long-wavelength incident light, which adversely affects the performance of the solar cell.[59]

(1) Unfavorable interface reaction generating secondary phases and voids

Molybdenum (Mo) metal was widely used as the back electrode of CIGS solar cells, mainly for the following characteristics: high-temperature stability, good adhesion with SLG and CIGS materials, and the formation of ohmic contacts between $Mo(S,Se)_2$ and CIGS, which is conductive to carrier transport and inhibition of interface recombination.[82] The CZTSSe solar cell device structure is completely inherited from the CIGS solar cell structure, without considering the differences between the two materials. It is still not yet conclusive whether Mo film is the best back electrode material for CZTSSe solar cells. Some reports have demonstrated that Mo back electrodes have a detrimental effect on CZTSSe device performance. Scragg et al. studied in detail the chemical reactions present at the contact of the back electrode with the following equations:[83]

$$Cu_2ZnSn(S,Se)_4 + Mo \rightarrow Cu_2(S,Se) + Zn(S,Se) + Sn(S,Se) + Mo(S,Se)_2 \quad (1\text{-}6)$$

$$Mo + S(Se)_2 \rightarrow Mo(S,Se)_2 \quad (1\text{-}7)$$

Unlike CIGS, the Mo/CZTSSe interface is not stable. During high-temperature selenization, secondary phases such as $Cu_2(S,Se)$, Zn(S,Se), Sn(S,Se), which are formed by the decomposition of CZTSSe at the interface, increase the carrier

recombination at the back contact, and also lead to an excessively thick $Mo(S,Se)_2$ layer, which hinders carrier transport and increases the series resistance of the device.[84]

(2) Undesirable interface reactions deteriorate the absorber crystallinity

Due to the relatively high Se partial pressure during selenization, the nucleation process of CZTSSe usually starts from the surface. However, related studies have shown that the presence of Mo back electrode plays a crucial role in inducing nucleation at the bottom of the absorber, so that the grain growth occurs at both the surface and back interface. The reaction (1) occurs during selenization process due to its negative Gibbs energy at high temperatures and pressures.[85] This reaction can lead to the decomposition of the precursor film into a number of secondary phases [$Cu_2(S,Se)$, $Zn(S,Se)$, $Sn(S,Se)$] and the formation of $Mo(S,Se)_2$. Then the $Cu_2(S,Se)$ compound reacts with $Sn(S,Se)$ to form $Cu_2Sn(S,Se)_3$; and $Cu_2Sn(S,Se)_3$ reacts with Zn(S, Se) to form $Cu_2ZnSn(S,Se)_4$.

$$Cu_2(S,Se)+Sn(S,Se)\rightarrow Cu_2Sn(S,Se)_3 \quad (1\text{-}8)$$

$$Cu_2Sn(S,Se)_3+Zn(S,Se)\rightarrow Cu_2ZnSn(S,Se)_4 \quad (1\text{-}9)$$

Liquid-phase Cu-SSe promotes liquid-phase-assisted grain growth, and thus the formation of $Cu_2(S,Se)$ at the back interface induces and promotes back interface crystallization.[86] The initial nucleation occurs at the surface of the absorber and at the back interface. As the selenization time increases, the top and bottom grain nuclei grow together with compositional competition. Component competition between multilayers during grain growth inevitably leads to component inhomogeneity.[85] This bidirectional grain growth process leads to a typical bilayer structure with poor crystallinity, resulting in a short minority carrier diffusion length in CZTSSe devices.

(3) Over-thick $Mo(S,Se)_2$ forming back interface barrier

In the process of high-temperature selenization, the diffused Se reacts with the Mo back electrode to generate an excessively thick $Mo(S,Se)_2$ layer, forming a non-ohmic contact at the back electrode.[87] The formation of this interface layer will change the alignment of the band at the interface and form unfavorable energy barriers. Earlier, researchers have tested the surface of the back interface of CZTSSe devices by X-ray photoelectron spectroscopy (XPS) and obtained its composition as $Mo(S,Se)_2$. Further studies indicated that the chemical reactions occurring at the back interface are spontaneous and cannot be avoided. Thinner $Mo(S,Se)_2$ layer have smaller depletion region widths, which greatly increases the probability of electron tunneling at the contact interface and facilitates the formation of good ohmic contacts. Excessively thick $Mo(S,Se)_2$ layer increases the depletion region width, which inevitably weakens the carrier drift momentum and increases the chance of recombination, ultimately leading to poor conductivity and deterioration of the device performance.

1.4.2 The front interface recombination

The front interface (CZTSSe/CdS heterojunction interface) is a mandatory pathway for carriers and thus critical for photogenerated charge separation and collection. Severe interface recombination in CZTSSe solar cells is an important cause of open-circuit voltage deficit in the device, which has at least three origins: 1) the presence of low band-gap secondary phases at the surface, 2) undesirable band alignment at the interface, and 3) high defect density generated by complex lattice defects. As a result, band design, interface defect passivation, and secondary phase elimination of heterojunctions to reduce the interface recombination loss are essential for the improvement of device efficiency.

(1) Secondary phase

CZTSSe belongs to the genus Sulfur compounds with a narrow single phase stability region (as shown in **Figure 1-17**).[16] Small composition deviation from the

stoichiometry will produce secondary phases, such as Zn(S,Se), $Cu_2Sn(S,Se)_3$, $Cu_2(S,Se)$, Sn(S,Se), or $Sn(S,Se)_2$, which appear in the absorber bulk as well as at the interfaces of CZTSSe/CdS and Mo/CZTSSe. If the band-gap of the secondary phases (e.g., Cu_2S, SnS, and Cu_2SnS_3) at the interface is lower than that of the absorber layer, they introduce electrostatic potentials in the band-gap of the absorber layer, leading to carrier recombination and limiting the V_{OC} of the solar cell. If the band-gap of the secondary phases at the interface is higher than that of the absorber layer (e.g., ZnSe), they will affect the light absorption and increase the series resistance, decreasing J_{SC} and FF.[88]

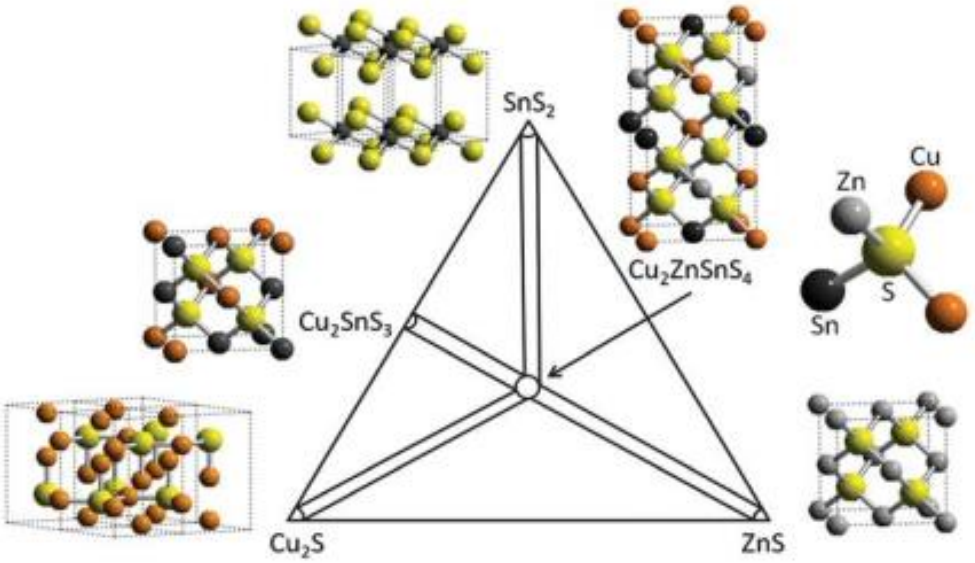

Figure 1-17 *The pseudoternary phase diagram to form the CZTS phase and other secondary phases along with their crystal structures.[16]*

(2) Band alignment

Figure 1-18 shows two band alignments at the interface of the CZTSSe/CdS heterojunction: One is a cliff-like negative conduction band offset (CBO< 0) band alignment. The conduction band edge of CZTSSe is higher than the conduction band edge of CdS, and this structure can induce the carriers to recombine at the interface when passing through the P-N junction.[89] The other is a spike-like positive conduction

band offset (CBO>0) band alignment. The conduction band edge of CZTSSe is higher than that of CdS, and this structure can effectively reduce the probability of recombination when passing through the P-N junction, but may form a potential barrier to hinder carrier transport.[90] It is shown that the ideal energy band alignment is flat or small spiky, when the CBO is in the region of 0-0.4eV, which can avoid the carrier recombination induced by the negative shift of the conduction band, and at the same time does not affect the transport of carriers at the interface. An excessively large spike-like CBO will hinder the transport of minority carriers and adversely affect the J_{SC} and FF of the device.[91]

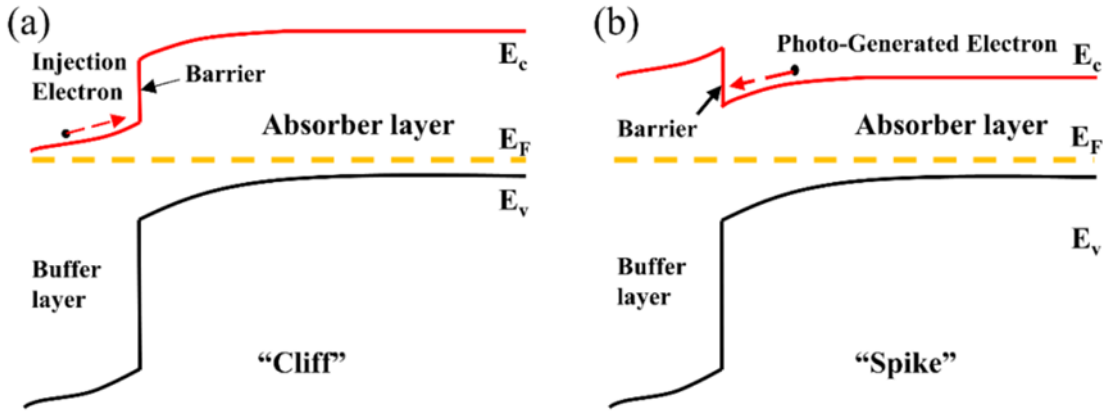

Figure 1-18 *Cliff -like band alignment heterojunction (a); Spike -like band alignment (b).*

(3) Interface defects

As a polycompound, CZTSSe contains a variety of elements with similar atomic sizes, but different degrees of oxidation, which significantly increases the probability of atomic substitutions and vacancies within CZTSSe crystals. This is more evident on the surface of CZTSSe films. Typically, the surface activity of the material is much higher, with a large number of dangling and misaligned bonds, which favors defect formation. **Figure 1-19** gives the positions of the various defect levels between the bands within CZTS and CZTSe.[92]

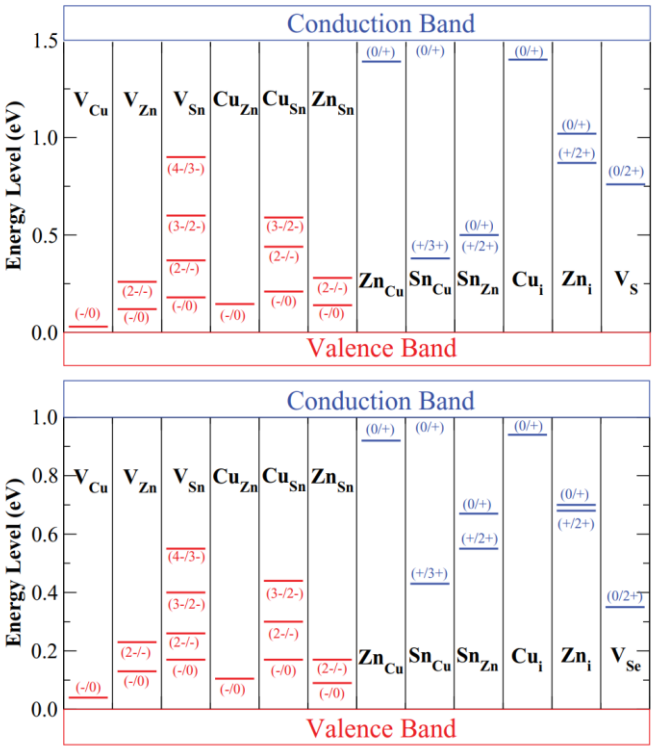

Figure 1-19 *The ionization levels of intrinsic defects in the band-gaps of Cu_2ZnSnS_4 (top) and $Cu_2ZnSnSe_4$ (bottom).*[92]

Among them, the vacancy (V_{Cu}) is the defect with the shallowest energy level, which is generally considered to provide p type carriers inside CZTSSe. The Cu/Zn antisite defect, on the other hand, is the defect with the lowest formation energy and is present in large quantity. It creates fluctuations in the band edges and reduces the effective band-gap of the material. The high concentration of Cu_{Zn} defects leads to pinning of the Fermi energy levels at the CZTSSe/CdS interface, which reduces the band bending at the interface leading to smaller Fermi energy level splitting and consequently V_{OC} losses. Sn_{Zn} defects are deep level defects and are generally considered to be the most dominant carriers within the absorber layer recombination center. Especially when this defect forms a complementary defect pair with the Cu_{Zn} defect, it generates a huge carrier capture cross section, which can drastically reduce the V_{OC}. In addition, V_{Se} defects also have a significant impact on the CZTSSe crystal quality. These defects

usually appear at grain boundaries or surfaces and have a large impact on the interface charge transport properties of CZTSSe. The main reason for their occurrence is the presence of insufficient localized selenium concentration in the selenization reaction.

1.4.3 Construction of gradient band-gap absorber

Band-gap engineering of CIGS is one of the key technologies to gain efficiency improvement, mainly by regulating the distribution of Ga or S elements in the perpendicular direction from the Mo back electrode to the CdS buffer layer to regulate progressively the band-gap width to form a gradient.[93, 94] Currently widely used gradient band-gap structure was first realized through a three-step co-evaporation method (**Figure 1-20**a).[95] The first step is to the evaporation of the elements In and Ga at a lower substrate temperature (340 ℃); then the substrate temperature is increased to 450 ℃ to evaporate Cu. In this stage, the evaporation rate of In and Ga decreases by about an order of magnitude while evaporating Cu until the overall composition reaches Cu-rich; in the last stage, the supply of Cu stops, and only In and Ga are deposited on the substrate, finally obtaining the overall Cu-poor film, avoiding the carrier recombination that could result from Cu-rich conditions. The selenium (Se) was continuously supplied throughout the evaporation process. In addition, in each sub-stage of the three-step co-evaporation, the evaporation rates of In and Ga are different, as shown by the blue lines (Ga) in Figure 1-20a, and their evaporation rates need to be carefully regulated to produce the desired gradient profiles. For example, the evaporation rates of In and Ga are controlled to decrease and decrease differently when the second stage starts, forming a back gradient with gradually decreasing Ga content from the back electrode to the middle of the absorber layer (Figure 1-20b).[96] In the third stage, the evaporation rate of In is kept constant while the evaporation rate of Ga is increased, forming a gradually increasing Ga gradient on the front surface. Similarly,

the band-gap size can be modulated by controlling the distribution of S in the absorber layer by similar means.

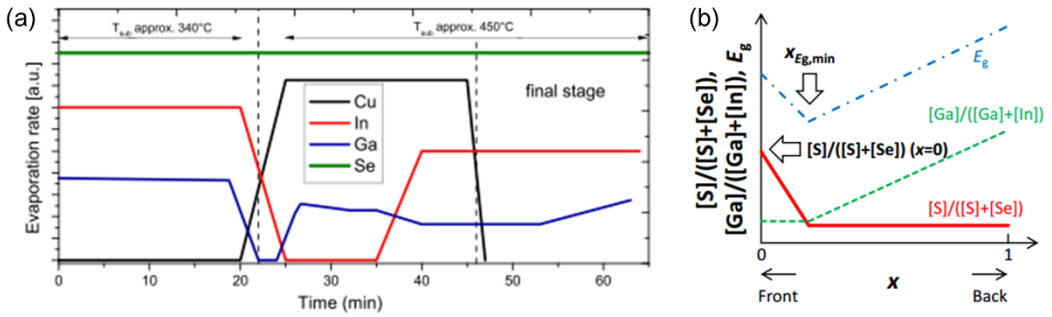

Figure 1-20 *(a)Schematic diagram of the three-step co-evaporation process;[95] (b) V-shaped double gradient band-gap structure for S/(S+Se), Ga/(Ga+In) and Eg for CIGS.[96]*

The band-gap width is positively correlated with the Ga and S content, with higher Ga content [GGI, i.e. Ga/(Ga+In)] and S content [SSe, i.e. S/(S+Se)] resulting in larger band-gap widths. Figure 1-20b shows the distribution of the Ga and S content, with the corresponding band-gaps having a similar gradient shape. This double gradient band-gap structure from the Mo back electrode to the front surface of the CdS decreases and then increases the band-gap width, which is called the "V-shaped double gradient band-gap structure". The shrinking E_g from the back electrode to the absorber forms a back surface field (BSF), assisting electron transport to the p-n junction. It diminishes the probability of recombination of carriers at Mo electrode and boosts the short-circuit current density (J_{SC}). The minimum value of E_g (the notch) in the middle of the absorber can ensure the light absorption of CIGS and promote the J_{SC}. The gradually increasing E_g from the notch to the p-n junction can ensure a large E_g value at the heterojunction interface, so as to obtain high V_{OC}.[97] It has been shown that the appropriate notch location and depth are crucial for efficiency improvement. A large front gradient (the gradient band-gap structure from the notch position to the CdS front interface) forms

an electron barrier, and the electrons generated inside the notch and deep in the absorber do not have enough thermal energy to overcome this barrier, resulting in carrier recombination that reduces V_{OC} and FF.

Till now, the most efficient CZTSSe device are obtained by solution method, a rapid high temperature selenization process is required to convert amorphous precursor film into crystalline absorber. This high-temperature selenization process exhibits a rapid element diffusion to obtain a uniform elemental distribution, making it challenging to finely regulate the element flux and to obtain a gradient band-gap structure as in CIGS.[78] At the same time, the fine grain layer caused by residual organic impurity during the process of selenization is an inherent shortcoming of the solution process. Recently, researchers have observed the gradient band-gap of CZTSSe, signifying that CZTSSe absorber films with single gradient band-gap (either in the front or back) can be achieved through the selenization-sulfurization process.[64, 98] However, the selenization-sulfurization process generally requires the simultaneous supply of sulfur and selenium powders, with different reactivities and therefore it can be difficult to control the gradient.

1.5. Approaches for improving CZTSSe solar cells

1.5.1. Back interface engineering

Back interface engineering is one of the important directions to obtain high absorber and interface quality. A WO_3 intermediate layer was introduced to solve the problem of poor crystallinity of CZTSSe absorber and the unfavorable front and back interface contact, thus the diffusion length of minority carrier is improved, and the contact barrier height is reduced. The effects of WO_3 intermediate layer on the microstructure, electrical and defects property of CZTSSe have been systematically investigated for the first time in this work. This intermediate layer initially prevents direct contact of

CZTSSe with back electrode. Hence, CZTSSe decomposition and $Mo(S,Se)_2$ formation were inhibited, which was beneficial to obtain good absorber crystallinity and better back contact, leading to significantly increased minority carriers diffusion length and reduced back interface contact barrier height. Besides, due to the improvement of crystal growth process, the dense absorber with good crystallization has a smoother surface, which makes better contact quality of CZTSSe/CdS interface and lower interface defect density. This method not only improves interface and bulk carrier transportation, but also reduces the deep acceptor defect density, resulting in reduced non-radiative recombination. Our simple and convenient strategy achieved a CZTSSe device efficiency of 12.66% with significantly improved V_{OC}.

1.5.2 Front interface engineering

In this work, we proposed an effective and simple solution treatment method that can be able to adjust simultaneously the surface property as well as the internal defect of the absorber. An ammonium sulphide solution was coated on the CZTSSe absorber and stayed for 2 min, then spinning was performed to obtain thin ammonium sulphide layer on the absorber surface, finally sintered at 280 °C under inert atmosphere. The synergistic effect of surface etching and surface sulfurization can be obtained simultaneously by this method. After the surface sulfurization treatment, the sulfur content of absorber was slightly increased, carrier separation efficiency was enhanced and the carrier recombination was reduced. This resulted in a significant increase in V_{OC} and FF, leading to a device efficiency of 13.19%.

1.5.3 Absorber band-gap engineering

The controllable preparation of double gradient band-gap CZTSSe absorber was successfully achieved, in this work, by simply spin-coating K_2S solution at different stages of precursor film preparation. This strategy enables the preparation of absorber

with different notch positions and front gradient sizes, which greatly improves the carrier transport performance of CZTSSe absorber. At the same time, the existence of potassium avoids the deeper defects that may result from the introduction of additional S. Our study comprehensively investigated the impact of K_2S on the microscopic morphology, band structure, electrical properties, and defect characteristics of CZTSSe devices. Meanwhile, K_2S can react with Sn during selenization to form wide band-gap $K_2Sn_2S_5$ with reduced carrier recombination at the grain boundary. It is believed that the introduction of K_2S at an optimized stage could obtain CZTSSe devices with double gradient band-gap. A novel and cost-effective approach has been used in this work to obtain the highest power conversion efficiency (13.70%) for CZTSSe devices based on gradient band-gap absorber.

1.6 Conclusions and motivations

The objective of this PhD work is to prepare CZTSSe thin films and solar cell devices based on a non-hydrazine method, using the ethylene glycol methyl ether (2-Me) as solvent. The following aspects have been specially optimized: Mo/CZTSSe interface, CZTSSe/CdS interface, and CZTSSe absorber layer band-gap structure. In order to reduce the severe open-circuit voltage deficit of the devices, attentions have been particularly put on the understanding of thin film grain growth mechanism, on the improvement of carrier transport performance, and on the absorber conduction band and valence band modulation. A controlled fabrication method for obtaining high-quality CZTSSe thin films based on ethylene glycol methyl ether solution and double-gradient band-gap absorber layer, was developed, leading to a CZTSSe solar cell with an efficiency of 13.7%.

REFERENCES

[1] https://www.iea.org/energy-system/renewables/solar-pv

[2] https://www.nrel.gov/pv/interactive-cell-efficiency.html

[3] Green M. A., Bremner S. P., Energy conversion approaches and materials for high-efficiency photovoltaics. *Nature materials*, **2016**, 16, 23.

[4] Murakami T. N., Koumura N., Development of Next-Generation Organic-Based Solar Cells: Studies on Dye-Sensitized and Perovskite Solar Cells. *Adv. Energy Mater.*, **2018**, 9,

[5] Liu F., Zeng Q., Li J., Hao X., Ho-Baillie A., Tang J., Green M. A., Emerging inorganic compound thin film photovoltaic materials: Progress, challenges and strategies. *Mater. Today*, **2020**, 41, 120.

[6] Polman A., Knight M., Garnett E. C., Ehrler B., Sinke W. C., Photovoltaic materials: Present efficiencies and future challenges. *Science*, **2016**, 352, aad4424.

[7] Ribeyron P.-J., Crystalline silicon solar cells: Better than ever. *Nat. Energy*, **2017**, 2,

[8] Green M. A., Dunlop E. D., Yoshita M., Kopidakis N., Bothe K., Siefer G., Hao X., Solar cell efficiency tables (Version 63). *Prog. Photovolt: Res. Appl.*, **2023**, 32, 3.

[9] Moon S., Kim K., Kim Y., Heo J., Lee J., Highly efficient single-junction GaAs thin-film solar cell on flexible substrate. *Scientific reports*, **2016**, 6, 30107.

[10] Ramanujam J., Bishop D. M., Todorov T. K., Gunawan O., Rath J., Nekovei R., Artegiani E., Romeo A., Flexible CIGS, CdTe and a-Si:H based thin film solar cells: A review. *Prog. Mater. Sci.*, **2020**, 110, 100619.

[11] Ramanujam J., Singh U. P., Copper indium gallium selenide based solar cells – a review. *Energy Environ. Sci.*, **2017**, 10, 1306.

[12] Gong J., Sumathy K., Qiao Q., Zhou Z., Review on dye-sensitized solar cells (DSSCs): Advanced techniques and research trends. *Renewable Sustainable Energy Rev.*, **2017**, 68, 234.

[13] Kaur N., Singh M., Pathak D., Wagner T., Nunzi J. M., Organic materials for photovoltaic applications: Review and mechanism. *Synthetic Metals*, **2014**, 190, 20.

[14] Wehrenfennig C., Eperon G. E., Johnston M. B., Snaith H. J., Herz L. M., High charge carrier mobilities and lifetimes in organolead trihalide perovskites. *Adv. Mater.*, **2014**, 26, 1584.

[15] Giraldo S., Jehl Z., Placidi M., Izquierdo-Roca V., Perez-Rodriguez A., Saucedo E., Progress and perspectives of thin film kesterite photovoltaic technology: a critical review. *Adv. Mater.*, **2019**, 31, e1806692.

[16] Kumar M., Dubey A., Adhikari N., Venkatesan S., Qiao Q., Strategic review of secondary phases, defects and defect-complexes in kesterite CZTS–Se solar cells. *Energy Environ. Sci.*, **2015**, 8, 3134.

[17] He M., Yan C., Li J., Suryawanshi M. P., Kim J., Green M. A., Hao X., Kesterite solar cells: insights into current strategies and challenges. *Adv. Sci.*, **2021**, 8, 2004313.

[18] Minbashi M., Ghobadi A., Yazdani E., Ahmadkhan Kordbacheh A., Hajjiah A., Efficiency enhancement of CZTSSe solar cells via screening the absorber layer by examining of different possible defects. *Scientific reports*, **2020**, 10, 21813.

[19] Siebentritt S., Why are kesterite solar cells not 20% efficient? *Thin Solid Films*, **2013**, 535, 1.

[20] Pal K., Singh P., Bhaduri A., Thapa K. B., Current challenges and future prospects for a highly efficient (>20%) kesterite CZTS solar cell: A review. *Sol. Energy Mater. Sol. Cells*, **2019**, 196, 138.

[21] Gürel T., Sevik C., Çağın T., Characterization of vibrational and mechanical properties of quaternary compounds Cu_2ZnSnS_4 and $Cu_2ZnSnSe_4$ in kesterite and stannite structures. *Phys. Rev. B*, **2011**, 84,

[22] Chen S., Walsh A., Yang J.-H., Gong X. G., Sun L., Yang P.-X., Chu J.-H., Wei S.-H., Compositional dependence of structural and electronic properties of $Cu_2ZnSn(S,Se)_4$ alloys for thin film solar cells. *Phys. Rev. B*, **2011**, 83, 125201.

[23] Ito K., Nakzawa T., Electrical and Optical Properties of Stannite-Type Quaternary Semiconductor Thin Films. *Jpn. J. Appl. Phys.*, **1998**, 27, 2094.

[24] Hironori Katagiri, Nobuyuki Sasaguchi, Shima Hando, Suguro Hoshino, Jiro Ohashi, Yokota T., Preparation films by and evaluation of Cu_2ZnSnS_4 thin sulfurization of E-B evaporated precursors. *Sol. Energy Mater. Sol. Cells*, **1997**, 49, 407.

[25] Th.M. Friedlmeier, N. Wieser, Th. Walter, H. Dittrich, H.W. Schock, Proc. *14th European PVSEC and Exhibition* **1997**, P4B.10.

[26] Katagiri. H., Jimbo K., Development of rare metal-free CZTS-based thin film solar cells. *37th IEEE Photovoltaic Specialists Conference*, **2011**, 003516.

[27] Katagiri H., Jimbo K., Maw W. S., Oishi K., Yamazaki M., Araki H., Takeuchi A., Development of CZTS-based thin film solar cells. *Thin Solid Films*, **2009**, 517, 2455.

[28] Guo Q., Hillhouse H. W., Agrawal R., Synthesis of Cu_2ZnSnS_4 Nanocrystal Ink and Its Use for Solar Cells. *J. Am. Chem. Soc.*, **2009**, 131, 11672.

[29] Guo Q., Ford G. M., Yang W.-C., Walker B. C., Stach E. A., Hillhouse H. W., Agrawal R., Fabrication of 7.2% Efficient CZTSSe Solar Cells Using CZTS Nanocrystals. *J. Am. Chem. Soc.*, **2010**, 132, 17384.

[30] Todorov T. K., Reuter K. B., Mitzi D. B., High-efficiency solar cell with Earth-abundant liquid-processed absorber. *Adv. Mater.*, **2010**, 22, E156.

[31] Barkhouse D. A. R., Gunawan O., Gokmen T., Todorov T. K., Mitzi D. B., Device characteristics of a 10.1% hydrazine-processed $Cu_2ZnSn(Se,S)_4$ solar cell. *Prog. Photovolt: Res. Appl.*, **2011**, 20, 6.

[32] Todorov T. K., Tang J., Bag S., Gunawan O., Gokmen T., Zhu Y., Mitzi D. B., Beyond 11% Efficiency: Characteristics of State-of-the-Art Cu2ZnSn(S,Se)4Solar Cells. *Adv. Energy Mater.*, **2013**, 3, 34.

[33] Wang W., Winkler M. T., Gunawan O., Gokmen T., Todorov T. K., Zhu Y., Mitzi D. B., Device characteristics of CZTSSe thin-film solar cells with 12.6% efficiency. *Adv. Energy Mater.*, **2014**, 4, 1301465.

[34] Son D.-H., Kim S.-H., Kim S.-Y., Kim Y.-I., Sim J.-H., Park S.-N., Jeon D.-H., Hwang D.-K., Sung S.-J., Kang J.-K., Yang K.-J., Kim D.-H., Effect of solid-H2S gas reactions on CZTSSe thin film growth and photovoltaic properties of a 12.62% efficiency device. *J. Mater. Chem. A*, **2019**, 7, 25279.

[35] Cong J., He M., Jang J. S., Huang J., Privat K., Chen Y. S., Li J., Yang L., Green M. A., Kim J. H., Cairney J. M., Hao X., Unveiling the Role of Ge in CZTSSe Solar Cells by Advanced Micro-To-Atom Scale Characterizations. *Adv. Sci.*, **2024**, 11, e2305938.

[36] Gong Y., Qiu R., Niu C., Fu J., Jedlicka E., Giridharagopal R., Zhu Q., Zhou Y., Yan W., Yu S., Jiang J., Wu S., Ginger D. S., Huang W., Xin H., Ag incorporation with controlled grain growth enables 12.5% efficient kesterite solar cell with open circuit voltage reached 64.2% shockley–queisser limit. *Adv. Funct. Mater.*, **2021**, 31, 2101927.

[37] Zhao Y., Chen S., Ishaq M., Cathelinaud M., Yan C., Ma H., Fan P., Zhang X., Su Z., Liang G., Controllable Double Gradient Band-gap Strategy Enables High Efficiency Solution-Processed Kesterite Solar Cells. *Adv. Funct. Mater.*, **2023**, 34, 2311992.

[38] Yan C., Huang J., Sun K., Johnston S., Zhang Y., Sun H., Pu A., He M., Liu F., Eder K., Yang L., Cairney J. M., Ekins-Daukes N. J., Hameiri Z., Stride J. A., Chen

S., Green M. A., Hao X., Cu_2ZnSnS_4 solar cells with over 10% power conversion efficiency enabled by heterojunction heat treatment. *Nat. Energy*, **2018**, 3, 764.

[39] Li J., Huang J., Ma F., Sun H., Cong J., Privat K., Webster R. F., Cheong S., Yao Y., Chin R. L., Yuan X., He M., Sun K., Li H., Mai Y., Hameiri Z., Ekins-Daukes N. J., Tilley R. D., Unold T., Green M. A., Hao X., Unveiling microscopic carrier loss mechanisms in 12% efficient $Cu_2ZnSnSe_4$ solar cells. *Nat. Energy*, **2022**, 7, 754.

[40] Giraldo S., Placidi M., Saucedo E., Kesterite: New Progress Toward Earth-Abundant Thin-Film Photovoltaic. *Advanced Micro- and Nanomaterials for Photovoltaics. Elsevier*, **2019**, 93.

[41] Li J., Sun K., Yuan X., Huang J., Green M. A., Hao X., Emergence of flexible kesterite solar cells: progress and perspectives. *npj Flexible Electron.*, **2023**, 7,

[42] Huang P.-c., Huang C.-h., Lin M.-y., Chou C.-y., Hsu C.-y., Kuo C.-g., The Effect of Sputtering Parameters on the Film Properties of Molybdenum Back Contact for CIGS Solar Cells. *Int. J. Photoenergy*, **2013**, 2013, 1.

[43] Fu J., Tian Q., Zhou Z., Kou D., Meng Y., Zhou W., Wu S., Improving the Performance of Solution-Processed $Cu_2ZnSn(S,Se)_4$ Photovoltaic Materials by Cd^{2+} Substitution. *Chem. Mater.*, **2016**, 28, 5821.

[44] Beggas A., Benhaoua B., Attaf A., Aida M. S., Growth study of CdS thin films deposited by chemical bath. *Optik*, **2016**, 127, 8423.

[45] Jeong H., Nandi R., Cho J. Y., Pawar P. S., Lee H. S., Neerugatti K. E., Kim J. H., Heo J., CZTSSe/Zn(O,S) heterojunction solar cells with 9.82% efficiency enabled via $(NH_4)_2S$ treatment of absorber layer. *Prog. Photovolt: Res. Appl.*, **2021**, 29, 1057.

[46] Valla A., Carroy P., Ozanne F., Muñoz D., Understanding the role of mobility of

ITO films for silicon heterojunction solar cell applications. *Sol. Energy Mater. Sol. Cells*, **2016**, 157, 874.

[47] Katz E., Electrochemical contributions: Sir William Robert Grove (1811–1896). *Electrochem. Sci. Adv.*, **2023**, 3,

[48] Xinchen Li, Daming Zhuang, Ning Zhang, Ming Zhao, Xinping Yu, Peng Liu, Yaowei Wei, Ren G., Achieving 11.95% efficient $Cu_2ZnSnSe_4$ solar cells fabricated by sputtering a Cu-Zn-Sn-Se quaternary compound target with a selenization process. *J. Mater. Chem. A*, **2019**, 7, 9948.

[49] Tripathi S., Kumar B., Dwivedi D. K., Study on formation and characterization of kesterite CZTSSe thin films deposited by thermal evaporation technique for solar cell applications. *J. Mater. Sci.: Mater. Electron.*, **2020**, 31, 8308.

[50] Jiang M., Lan F., Yan X., Li G., Cu2ZnSn(S1–xSex)4 thin film solar cells prepared by water-based solution process. *Phys. Status Solidi RRL*, **2013**, 8, 223.

[51] Sun Y., Qin S., Ding D., Gao H., Zhou Q., Guo X., Gao C., Liu H., Zhang Y., Yu W., Promoting carrier collection by DMF/DMSO binary solvent for efficient kesterite solar cells. *Chem. Eng. J.*, **2023**, 455, 140596.

[52] Fu J., Zhang A., Kou D., Xiao Z., Zhou W., Zhou Z., Yuan S., Qi Y., Zheng Z., Wu S., Defect engineering enabling p-type $Mo(S,Se)_2$:TM (TM = V, Nb, Ta) towards high-efficiency kesterite solar cells. *Chem. Eng. J.*, **2023**, 457, 141348.

[53] Fan P., He Y., Liang G., Xie Z., Yu Z., Lin J., Chen S., Zheng Z., Luo J., Su Z., Enhancing Ag-alloyed Cu_2ZnSnS_4 solar cell performance by interfacial modification via In and Al. *J. Mater. Chem. A*, **2021**, 9, 25196.

[54] Gansukh M., Li Z., Rodriguez M. E., Engberg S., Martinho F. M. A., Marino S. L., Stamate E., Schou J., Hansen O., Canulescu S., Energy band alignment at the heterointerface between CdS and Ag-alloyed CZTS. *Scientific reports*, **2020**, 10,

18388.

[55] Xu Z., Gao Q., Cui C., Yuan S., Kou D., Zhou Z., Zhou W., Meng Y., Qi Y., Ishaq M., Shah U. A., Wu S., Gradient conduction band energy engineering driven high-efficiency solution-processed $Cu_2ZnSn(S,Se)_4/Zn_xCd_{1-x}S$ solar cells. *Adv. Funct. Mater.*, **2022**, 33, 2209187.

[56] Lee J., Enkhbat T., Han G., Sharif M. H., Enkhbayar E., Yoo H., Kim J. H., Kim S., Kim J., Over 11 % efficient eco-friendly kesterite solar cell: Effects of S-enriched surface of $Cu_2ZnSn(S,Se)_4$ absorber and band-gap controlled (Zn,Sn)O buffer. *Nano Energy*, **2020**, 78, 105206.

[57] Wang Z., Meng R., Guo H., Sun Y., Liu Y., Zhang H., Cao Z., Dong J., Xu X., Liang G., Lou L., Li D., Meng Q., Zhang Y., Toward high efficient $Cu_2ZnSn(S_x,Se_{1-x})_4$ solar cells: Break the limitations of V_{OC} and FF. *Small*, **2023**, 19, e2300634.

[58] Y. Ji, X. Zhao, Y. Pan, Z. Su, J. Lin, E. M. Akinoglu, Y. Xu, H. Zhang, P. Zhao, Y. Dong, X. Wei, F. Liu, Mulvaney P., CuSCN modified back contacts for high performance CZTSSe solar cells. *Adv. Funct. Mater.*, **2023**, 33, 2211421.

[59] Zhao Y., Yu Z., Hu J., Zheng Z., Ma H., Sun K., Hao X., Liang G., Fan P., Zhang X., Su Z., Over 12% efficient kesterite solar cell via back interface engineering. *J. Energy Chem.*, **2022**, 75, 321.

[60] Wang J., Zhou J., Xu X., Meng F., Xiang C., Lou L., Yin K., Duan B., Wu H., Shi J., Luo Y., Li D., Xin H., Meng Q., Ge bidirectional diffusion to simultaneously engineer back interface and bulk defects in the absorber for efficient CZTSSe solar cells. *Adv. Mater.*, **2022**, 34, e2202858.

[61] Y hou Y., Xiang C., Dai Q., Xiang S., Li R., Gong Y., Zhu Q., Yan W., Huang W., Xin H., 11.4% efficiency kesterite solar cells on transparent electrode. *Adv. Energy*

Mater., **2023**, 13, 2300253.

[62] Cui C., Kou D., Zhou W., Zhou Z., Yuan S., Qi Y., Zheng Z., Wu S., Surface defect ordered $Cu_2ZnSn(S,Se)_4$ solar cells with efficiency over 12% via manipulating local substitution. *J. Energy Chem.*, **2022**, 67, 555.

[63] Enkhbat T., Enkhbayar E., Otgontamir N., Sharif M. H., Mina M. S., Kim S. Y., Kim J., High efficiency CZTSSe solar cells enabled by dual Ag-passivation approach via aqueous solution process. *J. Energy Chem.*, **2023**, 77, 239.

[64] Sun Y., Qiu P., Yu W., Li J., Guo H., Wu L., Luo H., Meng R., Zhang Y., Liu S. F., N-type surface design for p-Type CZTSSe thin film to attain high efficiency. *Adv. Mater.*, **2021**, 33, e2104330.

[65] Yin K., Lou L., Wang J., Xu X., Zhou J., Shi J., Li D., Wu H., Luo Y., Meng Q., Lanthanum-induced synergetic carrier doping of heterojunction to achieve high-efficiency kesterite solar cells. *J Mater Chem A*, **2023**, 11, 9646.

[66] Deng Y., Zhou Z., Zhang X., Cao L., Zhou W., Kou D., Qi Y., Yuan S., Zheng Z., Wu S., Adjusting the Sn_{Zn} defects in $Cu_2ZnSn(S,Se)_4$ absorber layer via Ge^{4+} implanting for efficient kesterite solar cells. *J. Energy Chem.*, **2021**, 61, 1.

[67] Zhang X., Zhou Z., Cao L., Kou D., Yuan S., Zheng Z., Yang G., Tian Q., Wu S., Liu S., Suppressed interface defects by $GeSe_2$ post-deposition treatment enables high-efficiency kesterite solar cells. *Adv. Funct. Mater.*, **2022**, 33, 2211315.

[68] Kim S., Kim K. M., Tampo H., Shibata H., Niki S., Improvement of voltage deficit of Ge-incorporated kesterite solar cell with 12.3% conversion efficiency. *Appl. Phys. Express*, **2016**, 9, 102301.

[69] He M., Huang J., Li J., Jang J. S., Suryawanshi U. P., Yan C., Sun K., Cong J., Zhang Y., Kampwerth H., Suryawanshi M. P., Kim J., Green M. A., Hao X., Systematic efficiency improvement for $Cu_2ZnSn(S,Se)_4$ solar cells by double cation

incorporation with Cd and Ge. *Adv. Funct. Mater.*, **2021**, 31, 2104528.

[70] He M., Zhang X., Huang J., Li J., Yan C., Kim J., Chen Y. S., Yang L., Cairney J. M., Zhang Y., Chen S., Kim J., Green M. A., Hao X., High efficiency $Cu_2ZnSn(S,Se)_4$ solar cells with shallow Li_{Zn} acceptor defects enabled by solution-based Li post-deposition treatment. *Adv. Energy Mater.*, **2021**, 11, 2003783.

[71] Zhou J., Xu X., Duan B., Wu H., Shi J., Luo Y., Li D., Meng Q., Regulating crystal growth via organic lithium salt additive for efficient kesterite solar cells. *Nano Energy*, **2021**, 89, 106405.

[72] Du Y., Wang S., Tian Q., Zhao Y., Chang X., Xiao H., Deng Y., Chen S., Wu S., Liu S., Defect engineering in earth-abundant $Cu_2ZnSn(S,Se)_4$ photovoltaic materials via Ga^{3+}-doping for over 12% efficient solar cells. *Adv. Funct. Mater.*, **2021**, 31, 2010325.

[73] Farooq U., Ali Shah U., Ishaq M., Hu J.-G., Ahmed S., Chen S., Zheng Z.-H., Su Z.-H., Fan P., Liang G.-X., Defects passivation by solution-processed titanium doping strategy towards high efficiency kesterite solar cells. *Chem. Eng. J.*, **2023**, 451, 139109.

[74] Chen X.-Y., Ishaq M., Ahmad N., Tang R., Zheng Z.-H., Hu J.-G., Su Z.-H., Fan P., Liang G.-X., Chen S., Ag, Ti dual-cation substitution in $Cu_2ZnSn(S,Se)_4$ induced growth promotion and defect suppression for high-efficiency solar cells. *J. Mater. Chem. A*, **2022**, 10, 22791.

[75] Cui Y., Wang M., Dong P., Zhang S., Fu J., Fan L., Zhao C., Wu S., Zheng Z., DMF-based large-grain spanning $Cu_2ZnSn(S_x,Se_{1-x})_4$ device with a PCE of 11.76%. *Adv. Sci.*, **2022**, 9, e2201241.

[76] Yin K., Xu X., Wang M., Zhou J., Duan B., Shi J., Li D., Wu H., Luo Y., Meng Q., A high-efficiency (12.5%) kesterite solar cell realized by crystallization growth

kinetics control over aqueous solution based $Cu_2ZnSn(S,Se)_4$. *J. Mater. Chem. A*, **2022**, 10, 779.

[77] Geng H., Wang M., Wang S., Kou D., Zhou Z., Zhou W., Qi Y., Yuan S., Han L., Meng Y., Wu S., Two-step cooling strategy for synergistic control of Cu_{Zn} and Sn_{Zn} defects enabling 12.87% efficiency $(Ag,Cu)_2ZnSn(S,Se)_4$ solar cells. *Adv. Funct. Mater.*, **2022**, 33, 2210551.

[78] Guo H., Meng R., Wang G., Wang S., Wu L., Li J., Wang Z., Dong J., Hao X., Zhang Y., Band-gap-graded $Cu_2ZnSn(S,Se)_4$ drives highly efficient solar cells. *Energy Environ. Sci.*, **2022**, 15, 693.

[79] Gong Y., Zhu Q., Li B., Wang S., Duan B., Lou L., Xiang C., Jedlicka E., Giridharagopal R., Zhou Y., Dai Q., Yan W., Chen S., Meng Q., Xin H., Elemental de-mixing-induced epitaxial kesterite/CdS interface enabling 13%-efficiency kesterite solar cells. *Nat. Energy*, **2022**, 7, 966.

[80] Zhou J., Xu X., Wu H., Wang J., Lou L., Yin K., Gong Y., Shi J., Luo Y., Li D., Xin H., Meng Q., Control of the phase evolution of kesterite by tuning of the selenium partial pressure for solar cells with 13.8% certified efficiency. *Nat. Energy*, **2023**, 8, 526.

[81] Li W., Han X., Zhao Y., Yang S., Pre-annealing induced oxide barrier to suppress the over-selenization of Mo contact. *J. Mater. Sci.: Mater. Electron.*, **2016**, 27, 11188.

[82] Zhang X., Kobayashi M., Yamada A., Comparison of Ag(In,Ga)Se2/Mo and Cu(In,Ga)Se2/Mo Interfaces in Solar Cells. *ACS Appl. Mater. Interfaces*, **2017**, 9, 16215.

[83] Scragg J. J., Watjen J. T., Edoff M., Ericson T., Kubart T., Platzer-Bjorkman C., A detrimental reaction at the molybdenum back contact in Cu2ZnSn(S,Se)4 thin-film

solar cells. *J. Am. Chem. Soc.*, **2012**, 134, 19330.

[84] Liu F., Huang J., Sun K., Yan C., Shen Y., Park J., Pu A., Zhou F., Liu X., Stride J. A., Green M. A., Hao X., Beyond 8% ultrathin kesterite Cu_2ZnSnS_4 solar cells by interface reaction route controlling and self-organized nanopattern at the back contact. *NPG Asia Mater.*, **2017**, 9, e401.

[85] Yu Q., Shi J., Guo L., Duan B., Luo Y., Wu H., Li D., Meng Q., Eliminating multilayer crystallization of Cu2ZnSn(S,Se)4 absorber by controlling back interface reaction. *Nano Energy*, **2020**, 76, 105042.

[86] Kim S. Y., Son D. H., Kim S. H., Kim Y. I., Kim S., Ahn K., Yang K. J., Kang J. K., Kim D. H., Effect of Cu–Sn–Se Liquid Phase on Grain Growth and Efficiency of CZTSSe Solar Cells. *Adv. Energy Mater.*, **2020**, 10, 1903173.

[87] Shibayama N., Zhang Y., Satake T., Sugiyama M., Modelling of an equivalent circuit for Cu2ZnSnS4- and Cu2ZnSnSe4-based thin film solar cells. *RSC Adv.*, **2017**, 7, 25347.

[88] Just J., Sutter-Fella C. M., Lutzenkirchen-Hecht D., Frahm R., Schorr S., Unold T., Secondary phases and their influence on the composition of the kesterite phase in CZTS and CZTSe thin films. *Physical chemistry chemical physics : PCCP*, **2016**, 18, 15988.

[89] Wang R., Lan M., Zheng Y., Yang J., Li B., Wei S. H., Interface Engineering of Cu(In,Ga)Se2 Solar Cells by Optimizing Cd- and Zn-Chalcogenide Alloys as the Buffer Layer. *ACS Appl. Mater. Interfaces*, **2021**, 13, 15237.

[90] Park G. S., Chu V. B., Kim B. W., Kim D. W., Oh H. S., Hwang Y. J., Min B. K., Achieving 14.4% Alcohol-Based Solution-Processed Cu(In,Ga)(S,Se)2 Thin Film Solar Cell through Interface Engineering. *ACS Appl. Mater. Interfaces*, **2018**, 10, 9894.

[91] Ahmad N., Zhao Y., Ye F., Zhao J., Chen S., Zheng Z., Fan P., Yan C., Li Y., Su Z., Zhang X., Liang G., Cadmium-Free Kesterite Thin-Film Solar Cells with High Efficiency Approaching 12%. *Adv. Sci.*, **2023**, 10, e2302869.

[92] Chen S., Walsh A., Gong X. G., Wei S. H., Classification of lattice defects in the kesterite Cu_2ZnSnS_4 and $Cu_2ZnSnSe_4$ earth-abundant solar cell absorbers. *Adv. Mater.*, **2013**, 25, 1522.

[93] Jung S., Ahn S., Yun J. H., Gwak J., Kim D., Yoon K., Effects of Ga contents on properties of CIGS thin films and solar cells fabricated by co-evaporation technique. *Curr. Appl. Phys.*, **2010**, 10, 990.

[94] Pistor P., Zahedi-Azad S., Hartnauer S., Wägele L. A., Jarzembowski E., Scheer R., Real time observation of phase formations by XRD during Ga-rich or In-rich Cu(In, Ga)Se2growth by co-evaporation. *Phys. Status Solidi A*, **2015**, 212, 1897.

[95] Avancini E., Carron R., Bissig B., Reinhard P., Menozzi R., Sozzi G., Di Napoli S., Feurer T., Nishiwaki S., Buecheler S., Tiwari A. N., Impact of compositional grading and overall Cu deficiency on the near-infrared response in Cu(In, Ga)Se2 solar cells. *Prog. Photovolt: Res. Appl.*, **2017**, 25, 233.

[96] Kato T., Cu(In,Ga)(Se,S)2solar cell research in Solar Frontier: Progress and current status. *Jpn. J. Appl. Phys.*, **2017**, 56, 04CA02.

[97] Fan Q., Tian Q., Wang H., Zhao F., Kong J., Wu S., Regulating the starting location of front-gradient enabled highly efficient $Cu(In,Ga)Se_2$ solar cells via a facile thiol–amine solution approach. *J. Mater. Chem. A*, **2018**, 6, 4095.

[98] Wang D., Wu J., Liu X., Wu L., Ao J., Liu W., Sun Y., Zhang Y., Formation of the front-gradient band-gap in the Ag doped CZTSe thin films and solar cells. *J. Energy Chem.*, **2019**, 35, 188.

Chapter II: Efficient CZTSSe solar cell with improved minority carrier diffusion length via back interface engineering

2.1 Introduction

The kesterite $Cu_2ZnSn(S,Se)_4$ (CZTSSe) thin film solar cells have attracted considerable interest as potential alternatives for the commercialized high-efficiency solar devices such as $Cu(In,Ga)Se_2$ (CIGS) and CdTe. This material family enjoys its compelling features of optimal band-gap (E_g), remarkable absorption coefficients ($>10^4 cm^{-1}$), abundant and nontoxic elemental components, and thermodynamically stable structure.[1] However, the highest CZTSSe solar cell efficiency is stagnated at relatively low level, compared than those of CIGS and CdTe.[2] The major bottleneck restricting the development of kesterite-based CZTSSe is the large open-circuit voltage deficit (Voc-def) and the low fill factor (FF), which mainly attributes to the unfavorable absorber and interface quality.[3] Back interface engineering is one of the important directions to obtain high absorber and interface quality. This is because the poor back interface leading to decomposition reactions, which form secondary phases and voids that seriously deteriorate the quality of the absorber and interface.[4]

Thermodynamic calculations show that CZTSSe readily decomposes into secondary phase [such as Zn(S,Se), Sn(S,Se) and $Cu_2(S,Se)$] and forms thick $Mo(S,Se)_2$ layers and voids during the high temperature selenization.[5, 6]

$$Cu_2ZnSn(S,Se)_4+Mo \rightarrow Cu_2(S,Se) + Zn(S,Se) + Sn(S,Se) + Mo(S,Se)_2 \quad (2\text{-}1)$$

Typically, the nucleation process of CZTSSe begins at the surface due to the relatively high selenium partial pressure during selenization. However, relevant studies show that the Mo back electrode plays a vital role in inducing the bottom nucleation of absorber, so crystal growth occurs simultaneously at the surface and back interface. This bidirectional grain growth process results in a typical double layer structure with poor crystallinity, resulting in a short minority carrier diffusion length in CZTSSe devices.[7, 8] In addition, the over thick $Mo(S,Se)_2$ at the back interface is another serious problem

commonly existing in kesterite devices prepared by spin-coating and selenization process. Too thick $Mo(S,Se)_2$ at the back interface can significantly reduce the thickness of Mo back electrode, worsen the electrical contact between absorber and electrode, leading to significant increase of the series resistance (R_s) and back interface contact barrier height (Φ_B) of the device significantly.[9]

One of the effective methods to solve the problem of poor absorber crystallization and thick $Mo(S,Se)_2$ is to introduce an intermediate layer at Mo/CZTSSe back interface to control the harmful back interface reaction. For example, Cui et al. deposited 20 nm Ag on Mo electrode to improve CZTS/Mo contact and achieved a device efficiency of 4.42% (**Figure 2-1**a).[10] The thin layer is found to inhibit the formation of SnS_2, MoS_2, and other defects especially voids at the back contact; therefore, reduces the series resistance and recombination leading to substantially higher J_{SC}, FF, V_{OC}, and efficiency in comparison to the controlled reference Mo. Shin et al. used the TiN diffusion barrier and demonstrated 8.9% efficiency CZTSe solar cells with an improved carriers lifetime (Figure 2-1b).[11] They have examined $Cu_2ZnSnSe_4$ (CZTSe) solar cells prepared by thermal co-evaporation on Mo-coated glass substrates followed by post-deposition annealing under Se atmosphere. They show that the control of an interfacial $MoSe_2$ layer thickness and the introduction of an adequate Se partial pressure (P_{Se}) during annealing are essential to achieve high efficiency CZTSe solar cells—a reverse correlation between device performance and $MoSe_2$ thickness is observed, and insufficient P_{Se} leads to the formation of defects within the band-gap as revealed by photoluminescence measurements. Meng et al. obtained 11.68% efficiency in preparing high quality CZTSSe single-layer crystals by introducing MoO_3 isolating layer (Figure 2-1c).[7] The formation mechanism of the multi-layer crystallization is revealed, that is, the well-known reaction between CZTS and Mo may give the secondary phase, which subsequently acts as crystal nucleus to facilitate the CZTSSe crystal growth at back

interface (Mo/CZTSSe), leading to multi-layer crystallization. By introducing MoO_3 isolating layer, this undesired reaction can be well prevented, and high quality single-layer crystals are obtained. This absorber film with fewer defects and secondary phases exhibits better semiconductor properties. By introducing WO_3 intermediate layer at back interface, Yao et al. obtained CZTSSe devices with thin $Mo(S,Se)_2$ and good absorber crystallinity, demonstrating the potential of WO_3 intermediate layer for obtaining high performance CZTSSe device (Figure 2-1d).[12] They designed and prepared CZTSSe-based solar cells with a new structure of Al/ITO/ZnO/CdS/CZTSSe/WO_3/Mo/SLG (called "S1-5") by depositing about 4-nm-thick WO_3 layer with monoclinic structure on the back electrode Mo/SLG of solar cells, in comparison with the convention structure of Al/ITO/ZnO/CdS/Mo/CZTSSe/SLG (called "S2"). It is found that the average Voc increases from 346.7 mV of the S2 cells to 400.9 mV of the S1-5 cells, the average Jsc from 26.4 mA cm^{-2} to 32.1 mA cm^{-2} and the FF from 33.8 to 40.0% by addition of the WO_3 layer, which results in that the average PCE increases from 3.10% of the S2 cells to 5.14% of the S1-5 cells. The average increasing percent of the PCE is 65.8%. They believe that the increase in Voc, Jsc and FF of the S1-5 cells compared to the S2 cells is attributed to that the WO_3 layer prevent the Se coming from Se atmosphere and CZTSSe to react with the Mo to form $MoSe_2$ and other second phases, which makes the shunt resistance (R_{sh}) of the S1-5 increase and the series resistance and reverse saturation current density (J_0) decrease compared to the S2 cells. The decreased J_0 is a main factor of improvement of the PCE. An influence mechanism of the R_{sh}, R_s and J_0 on the PCE is also revealed. Their result demonstrates that addition of the WO_3 layer with a reasonable thickness can be a promising technical route for improving the PCE of the CZTSSe-based solar cell.

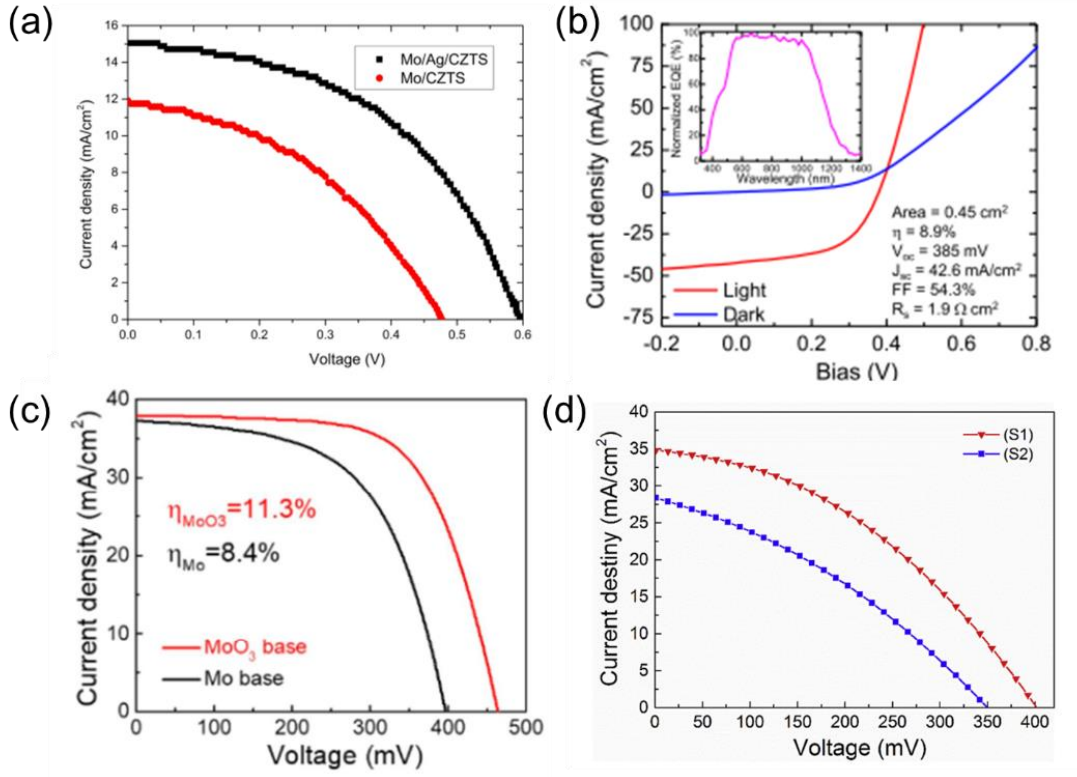

Figure 2-1 *(a) J-V curves for Ag intermediate layer containing devices,[10] (b) J-V curves for TiN intermediate layer containing devices,[11] (c) J-V curves for MoO_3 intermediate layer devices,[7] (d) J-V curves for WO_3 intermediate layer devices.[12]*

However, although the experimental studies have proved the positive effect of the WO_3 intermediate layer on effectively inhibiting the interface decomposition reaction, the fundamental mechanism of efficiency improvement has not been fully revealed and needs further study. More importantly, the effect of the WO_3 layer on the grain growth mechanism of the absorber, on the formation of $Mo(S,Se)_2$, on the minority carriers diffusion length and on the contact barrier at the back interface have not been fully studied. Hence, the effect of WO_3 layer on CZTSSe absorber needs to be re-investigated to provide guidance to improve grain growth of CZTSSe absorber, in order to suppress carrier recombination of CZTSSe absorber and to enhance CZTSSe device performance.

In this work, a WO_3 intermediate layer was introduced to solve the problem of poor crystallinity of CZTSSe absorber and the unfavorable front and back interface contact.

We systematically investigated the effects of WO_3 intermediate layer on the microstructure, electrical and defects property of CZTSSe for the first time, with the objective to obtain high efficiency photovoltaic devices.

2.2 CZTSSe solar cells preparation

Se powder, $CdSO_4$, thiourea, ammonia, $Cu(CH_3COO)_2·H_2O$, $SnCl_2·2H_2O$, $ZnCl_2$, $Zn(CH_3COO)_2·2H_2O$ and 2-methoxyethanol were purchased from Shanghai Aladdin Reagent Co. $SnCl_4·5H_2O$ and CuCl were purchased from Shanghai McLean Biochemical Technology Co. All the above chemicals and reagents were used directly during the experiment without any purification. The schematic illustration of the fabrication process of CZTSSe thin-film solar cells is shown in **Figure 2-2**.

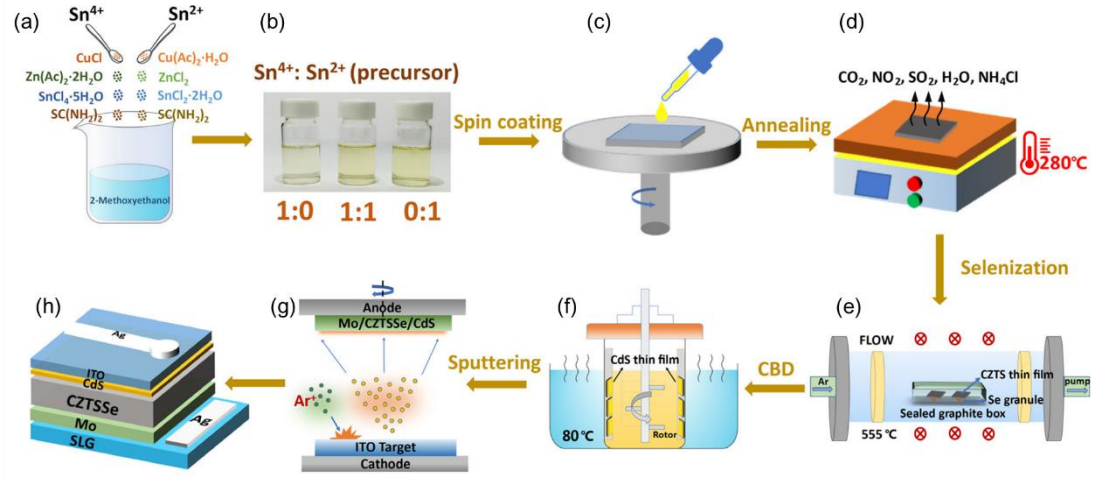

Figure 2-2 *Schematic illustration of the fabrication process of CZTSSe solar cells.*

2.2.1 Precursor solution preparation

The Sn^{4+} and Sn^{2+} precursor solutions have been obtained by dissolving respectively CuCl, $Zn(CH_3COO)_2·2H_2O$, $SnCl_4·5H_2O$, $SC(NH_2)_2$ into 2-methoxyethanol and $Cu(CH_3COO)_2·H_2O$, $ZnCl_2$, $SnCl_2·2H_2O$, $SC(NH_2)_2$ into 2-methoxyethanol. A deep yellow solution was prepared by stirring them at 60°C for one hour. The ratio of

Cu/(Zn+Sn) was 0.775 and the ratio of Zn/Sn was 1.2 (Figure 2-2a). The solutions containing Sn^{4+} and Sn^{2+} were evenly mixed 1:1 and diluted to half of the original concentration to obtain precursor solution (Figure 2-2b). The solution was stirred at room temperature for three hours until the final solution was pale yellow.

2.2.2 Back interface layer

Molybdenum (Mo)-coated soda lime glass (SLG) was employed as the substrate for solar cells and cleaned with detergent and deionized water. WO_3 films with thickness of 10, 15 and 20 nm were evaporated on Mo-coated soda-lime glass substrate using TEMD500 evaporator.

2.2.3 Precursor film preparation

The CZTS precursor solution was spin-coated on Mo-SLG substrates with 3000 rpm for 20 s to prepare reference sample (Figure 2-2c). Except for the reference sample, the films were spin-coated on Mo-SLG prepared with WO_3 layers of different thicknesses. And the wet film was immediately annealed at 280 ^oC for 2 min on a hot plate (Figure 2-2d). The coating-annealing-cooling cycle was repeated 10 times. The preparation of CZTS precursor films was operated in air.

2.2.4 Absorber preparation

Then, the precursor films and Se powder were placed into a graphite box for selenization at 520 ^oC for 15 min in an argon-filled rapid thermal process (RTP) furnace to form the CZTSSe absorber films (Figure 2-2e). The details of the RTP are as follows: the graphite box containing the sample is closed and placed in a quartz tube furnace, which is then pumped with a mechanical pump to evacuate the air from the tube to a residual pressure of 5.0×10^{-2} Pa, then filled with Argon gas to atmospheric pressure. The pumping and filling cycle is repeated three times to ensure the evacuation of air in

the tube. An argon flow with a rate of 120 sccm is maintained in the quartz tube during the selenization. The furnace is rapidly heated up from room temperature to 555 °C in 1 minute and then kept at this temperature for 15 minutes, before cooling naturally to room temperature.

2.2.5 CZTSSe device preparation

CdS buffer layer was deposited on the absorber by chemical bath deposition method (CBD), and the buffer layer thickness is about 50-80 nm (Figure 2-2f). The CBD process lasted 9 min at 80 °C in a solution containing $CdSO_4$ (0.015 M, 20 mL), thiourea (0.75 M, 20 mL), ammonia (14.8 M, 20 mL), and deionized water (140 mL). Then ITO window was later sputtered on CdS by magnetron sputtering under suitable O_2/Ar ratio (O_2/Ar≈2%) atmosphere (Figure 2-2g). The Ag electrode (70 nm) was deposited onto the ITO (Figure 2-2h).

2.3 Device characterization

The morphology of CZTSSe films were observed by SEM (SUPRA 55). Illuminated and dark J-V measurement were performed by a Keithley 2400 SourceMeter and a Zolix SS150 solar simulator (100 mW/cm^2, 25 ^{o}C, AM 1.5 G). Atomic force microscopy (AFM) was carried out by using an equipment from Bruker. Capacitance-voltage (C-V) and drive-level capacitance profiling (DLCP) were tested by a Keithley 4200A-SCS system with JANIS cryogenic platform. Admittance characterization was realized using a Lakeshore 325 temperature controller and the device was cooled with liquid nitrogen. Steady state photoluminescence (PL) and time-resolved photoluminescence (TRPL) were performed using time correlated single photon counting (TCSPC) system (FluoTime 300, PicoQuant Gmbh). Temperature-dependent dark J-V (J-V-T) measurements were carried out using a Lakeshore 325 temperature controller. External quantum efficiency (EQE) was carried out by a Zolix solar cell

QE/IPCE measurement system (Solar Cell Scan 100). The reflection spectrum data were analyzed by UV-3600Plus UV–VIS-NIR (SHIMADZU) spectrophotometer.

2.4 Device performance

For clarity, CZTSSe absorbers with 0, 10, 15 and 20 nm WO_3 intermediate layer were defined as W0, W10, W15 and W20, respectively. For W0 absorber, the microstructures of CZTSSe films exhibited large amount of voids (**Figure 2-3**a).

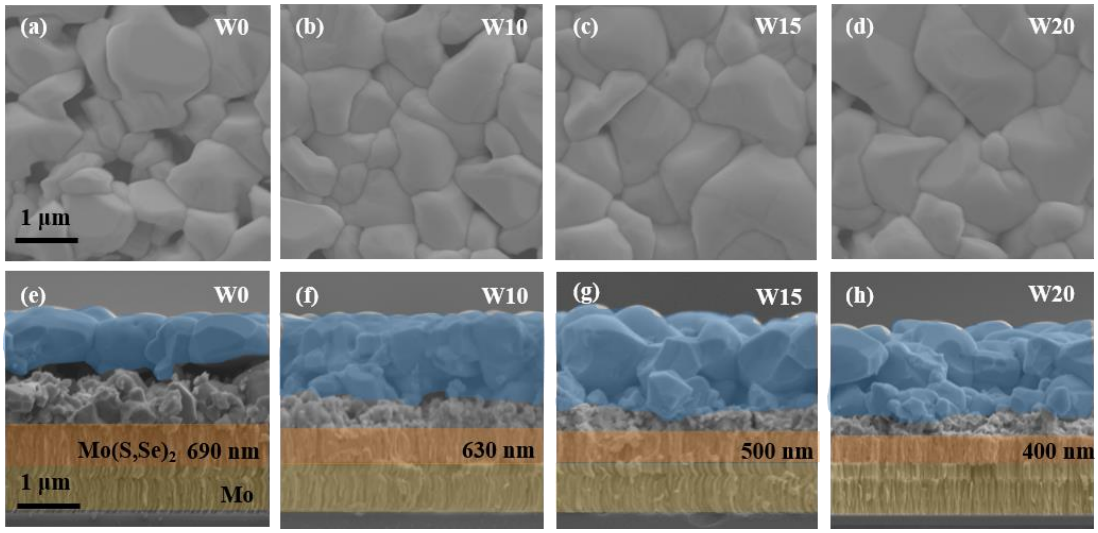

Figure 2-3 *Top view (a-d) and cross-section (e-h) SEM micrographs of W0, W10, W15 and W20 CZTSSe films.*

The introduction of WO_3 layer in Mo/CZTSSe substantially facilitated the grain growth and the film densification. The SEM measurements show that the selenized CZTSSe absorber has a typical double-layer structure, in which the upper layer is large grain layer and the lower layer is fine grain layer (Figure 2-3e-h). Fine grain layers was usually due to unwanted impurity residue of organic solvents and inadequate selenization, and it will degrade cell efficiency.[13] A thick $Mo(S,Se)_2$ is presented between absorber and back electrode, which has been observed in previous studies.[14] With the increase of WO_3 layer thickness, the thickness of large grain layer of CZTSSe absorber increases gradually and fine grain layer decreases. In addition, compared with

W0 sample, the large voids in the middle of CZTSSe film with WO_3 layer are almost invisible. Besides, it can be clearly seen from Figure 2-3(h) that the $Mo(S,Se)_2$ thickness decreases radically from 690 to 400 nm after the insertion of 20 nm WO_3 at the back interface. These results confirm that the WO_3 layer does increase the crystal size, improve the crystallization of CZTSSe and reduce the $Mo(S,Se)_2$ formation.

CZTSSe devices were fabricated and the effect of WO_3 layer thickness on device performance was investigated. **Figure 2-4**a shows the conventional structure of CZTSSe solar cells with a WO_3 intermediate layer. The optimal *J-V* curve of devices with different WO3 thicknesses are shown in Figure 2-4b, and the device parameters are listed in **Table 2-1**.

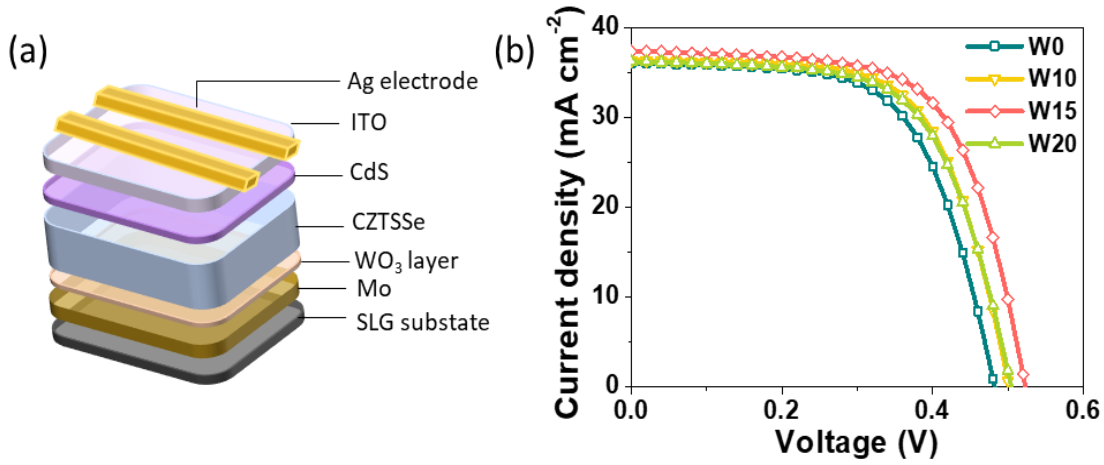

Figure 2-4 *(a) Structure of CZTSSe devices with WO_3 intermediate layer. (b) The J-V curves of the W0-W20 devices.*

Table 2-1 *CZTSSe devices parameters with different thickness of WO_3 intermediate layer.*

	J_{SC} [mA/cm^2]	V_{OC} [mV]	FF [%]	PCE [%]	J_0 [mA/cm^2]	A	R_s [Ω•cm^2]	R_{sh} [Ω•cm^2]	$V_{OC\text{-}def}$
W0	36.20 (35.85±1.31)	0.483 (0.488±0.08)	62.75 (63.12±2.32)	10.87 (10.82±0.04)	6.58×10^{-3}	2.96	1.13	638	0.422
W10	36.49 (37.19±1.49)	0.502 (0.506±0.09)	64.44 (63.60±1.86)	11.73 (11.69±0.03)	2.22×10^{-4}	1.83	1.02	862	0.403
W15	37.46 (37.32±1.72)	0.524 (0.516±0.010)	65.12 (65.57±2.76)	12.66 (12.30±0.36)	7.23×10^{-5}	1.72	0.70	1030	0.381
W20	36.24 (36.31±1.56)	0.505 (0.506±0.016)	63.57 (64.68±4.78)	11.54 (11.51±0.03)	1.19×10^{-3}	1.93	1.05	777	0.385

Ten devices were constructed for each thickness of intermediate layer. The statistic values of J_{SC}, V_{OC}, FF and PCE are shown in **Figure 2-5**a-d, the specific values are shown in Table 2-1. The W0 device without WO_3 achieved a PCE of 10.87% with V_{OC} of 483 mV, J_{SC} of 36.2 mA/cm^2 and FF of 62.75%. The best CZTSSe solar cell was obtained with optimized WO_3 thickness of 15 nm (W15), demonstrating a PCE of 12.66%, V_{OC} of 524 mV, J_{SC} of 37.46 mA/cm^2, and FF of 65.12%. When the WO_3 layer (W20) was too thick, the average performance was decreased (11.54%), probably because the WO_3 layer was too thick to form good back interface contact. The ideality factor (A) and reverse saturation current density (J_0) values of W15 device were the lowest, indicating the lower recombination in the depletion region and absorber, and the improved heterojunction quality.[15] Besides, compared with the W0, the W15 showed lager shunt resistance (R_{sh}) and small series resistance (R_s) (Table 2-1), which contribute to the increased FF.[16] In this work, the only difference between W0 W15

device was the existence of WO_3 layer in W15, while other film preparation and device fabrication process were the same. Therefore, the improvement must be due to the optimization of the back interface.

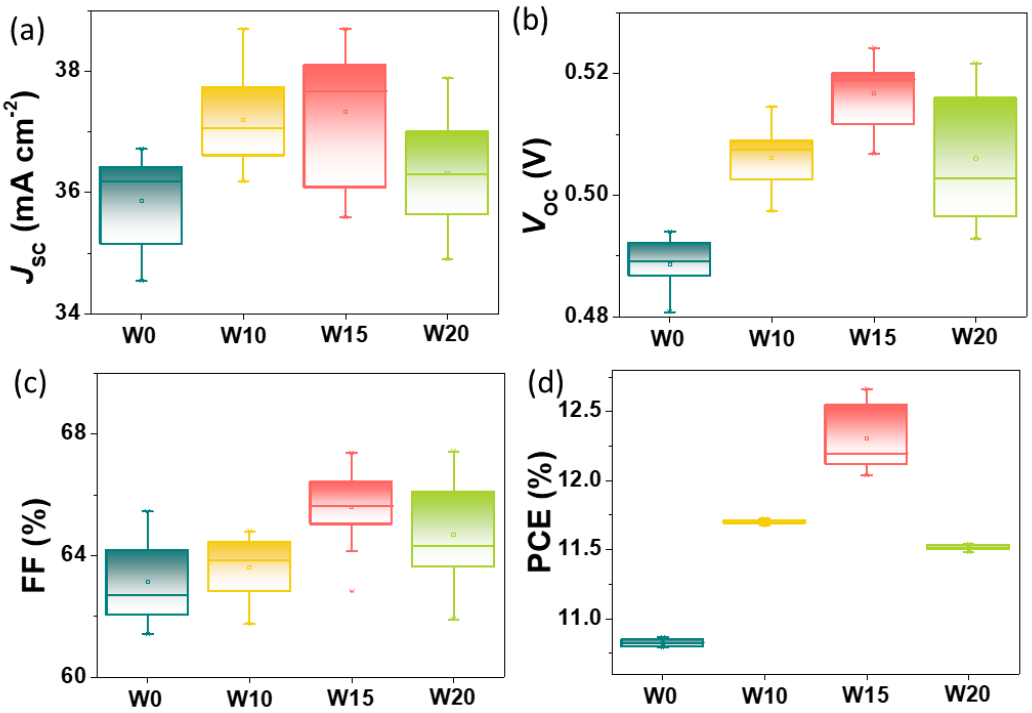

Figure 2-5 *Statistical box diagrams of photovoltaic parameters of Device W0-W20: (a)J_{SC}, (b)V_{OC}, (c)FF, (d)PCE. Ten cells were selected for each sample for analysis.*

The R_s of the W15 device (**Figure 2-6**, 0.70 Ω·cm^2) is significantly smaller than that of the W0 device (1.13 Ω·cm^2). Therefore, an appropriate WO_3 leads also to the reduction of R_s, which is favorable for achieving higher fill factors.[17]

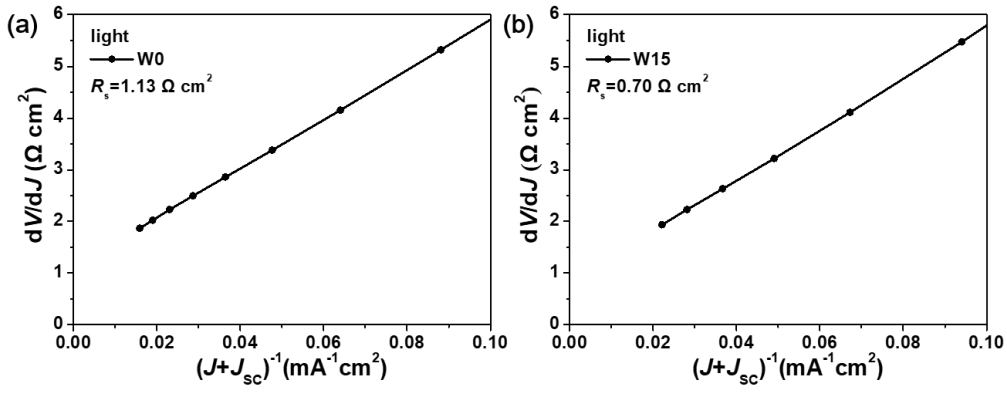

Figure 2-6 *dV/dJ versus $(J+J_{SC})^{-1}$ of W0 and W15 devices.*

2.5 Grain growth mechanism

To explore the WO_3 layer influence on the reaction path and the grain growth mechanism of CZTSSe, W0 and W15 precursor films were selenized and characterized by SEM at different selenization stages (0 s/300 s/600 s/900 s), as shown in **Figure 2-7**. Films at different selenization stage were labelled as WX_t to simplify the details, where X is the thickness of WO_3, t indicates the selenization time. For example, $W15_{300}$ stands for W15 film underwent selenization for 300s. The precursor films of W0 show amorphous structures (Figure 2-7a $W0_0$).

When the W0 film was selenized at 555 ºC for 300 s, larger grains appear at both the surface of the film and back interface, and grow bilaterally (identified as blue crystal of $W0_{300}$ in Figure 2-7b). Figure 2-7a shows the presence of crystals on the film surface accompanied by numerous voids when the W0 film was selenized at 555ºC for 300 s. As the selenization time is prolonged, the grain size gradually increases and crystal grows from both the top and bottom of CZTSSe film simultaneously ($W0_{600}$ in Figure 2-7a). SEM images show that the thin film has a typical double-layer structure. Once the two layers come into contact, the competition for maturity begins. It is obvious that the fine grain layer at the bottom can be merged by the top large grain layer, but with

the extension of selenization time, this merging behavior cannot continue indefinitely.[7] The direct result of composition competition between the top and bottom layers is that the absorber has large voids with low surface coverage rate, because the competition greatly restricts the lateral growth of the top layer crystals (Figure 2-7a $W0_{900}$). It can be seen from Figure 2-7b ($W0_{900}$) that the thickness of the upper large grains of W0 is about 650 nm and there are lots of voids on the surface and in the middle of the absorber.

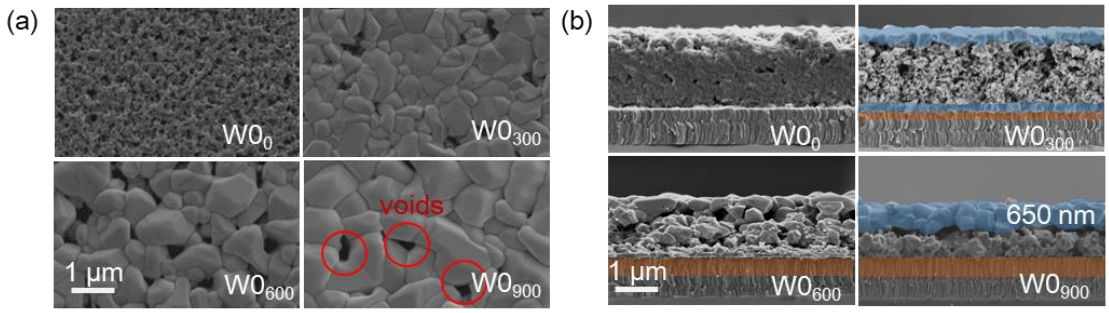

Figure 2-7 *Surface images (a) and cross-sections (b) SEM of W0 film at different selenization stage.*

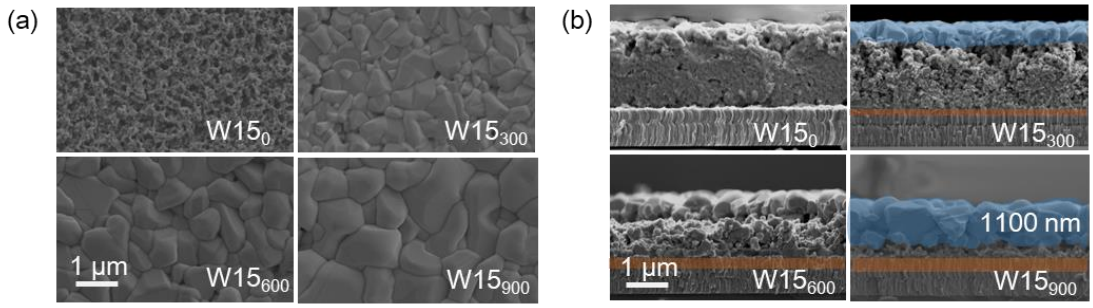

Figure 2-8 *SEM surface images (a) and cross-sections (b) of W15 film at different selenization stage.*

In the case of W15, the precursor films of W15 show similar amorphous structures like W0 (**Figure 2-8**a $W15_0$). When the selenization time was 300s, grains appeared on the upper surface of W15 film only (Figure 2-8b, $W15_{300}$). The SEM image of the cross section proved that no nucleation reaction occurred at the back interface at this time

(blue crystal of $W15_{300}$ in Figure 2-8b). This indicates that the presence of WO_3 intermediate layer inhibits the grain growth at the back interface at the initial selenization stage. The crystal size increases with the extension of selenization time, and the large grain layer of W15 absorber is about 1.1 micron, and the crystals are closely bonded without obvious voids (Figure 2-8b $W15_{900}$). Besides, as shown in the orange part of Figure 2-7b and Figure 2-8b, the $Mo(S,Se)_2$ thickness at back interface gradually increases with the extension of selenization time, while the $Mo(S,Se)_2$ thickness of W15 sample at each stage is significantly thinner than that of W0.

The significant improvement in the absorber crystallization and the decrease in $Mo(S,Se)_2$ were obviously due to the presence of WO_3 layer, which inhibited the reaction between the absorber and Mo at the back interface during selenization, as illustrated in **Figure 2-9**.

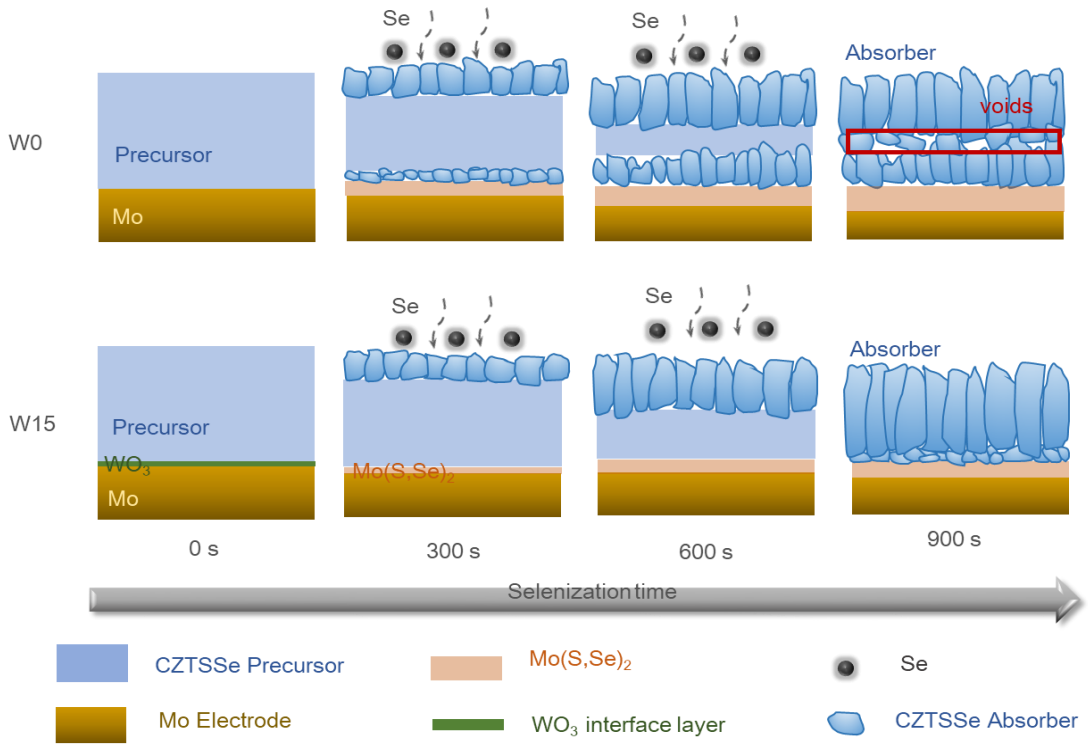

Figure 2-9 *Schematic illustration of the proposed grain growth mechanism for W0 and W15 film.*

The nucleation process starts from the CZTSSe surface due to the relatively high partial pressure of selenium on the surface. Besides, the small holes and cracks in the amorphous precursor film can facilitate Se penetrating the film. In the W0 case, where the precursor film is in direct contact with the Mo back electrode, reactions (2-1) can occur due to its negative Gibbs Energy at high temperature and high pressure during the selenization process.[18] This reaction can induce precursor film decomposition into some secondary phases [$Cu_2(S,Se)$, Zn(S,Se), Sn(S,Se)] and the formation of $MoSe_2$.[19] Then the $Cu_2(S,Se)$ compound reacts with Sn(S,Se) to form $Cu_2Sn(S,Se)_3$, and $Cu_2Sn(S,Se)_3$ reacts with Zn(S, Se) to form $Cu_2ZnSn(S,Se)_4$. Liquid-phase Cu-SSe can lead to liquid-assisted grain growth, so that the formation of $Cu_2(S,Se)$ at the back interface could induce and promote back interface crystallization.[20] The reactions of the above two steps are shown below.[21]

$$Cu_2(S,Se)+Sn(S,Se)\rightarrow Cu_2Sn(S,Se)_3 \quad (2\text{-}2)$$

$$Cu_2Sn(S,Se)_3+Zn(S,Se)\rightarrow Cu_2ZnSn(S,Se)_4 \quad (2\text{-}3)$$

Hence, initial nucleation in the W0 film occurs at the surface and the back interface of the absorber. With prolonged selenization time, the top and bottom crystal nucleus grow together and generate compositional competition. This competition between multilayers will inevitably lead to compositional non-uniformity during grain growth. For the W15 film, nucleation starts from the CZTSSe surface in the initial stage of selenization. The Se vapor diffuses into the back interface through the small holes and cracks in the precursor film, but the WO_3 layer blocks the contact between precursor and Mo, inhibiting the progress of reaction (2-1). The existence of WO_3 therefore inhibits the formation of $Cu_2(S,Se)$, Zn(S,Se) and Sn(S,Se) at the back interface. The absence of these secondary phases, especially $Cu_2(S,Se)$, prevents reactions (2-2) and (2-3). The existence of WO_3 layer inhibits the grain growth at the Mo/CZTSSe interface of the W15 film, the CZTSSe is formed from the top and its formation mechanism can

be described as a top-to-down process. The thickness of the upper large grain layer increases as the upper large grain layer merges with the bottom fine grain layer. With the extension of selenization time, the unidirectional crystal growth eventually forms the crystal structure with good crystallinity and compact grain arrangement. Besides, the formation of $Mo(S,Se)_2$ was mainly limited by Se vapor diffusion in the absorber, which is a rate-determining step.[6] The grain boundary (GB) of the absorber provides a pathway for the diffusion of selenium vapor. It is obvious that the crystallinity of W0 film is worse than that of W15 film, with more grain boundaries and holes. These grain boundaries and holes provide more favorable pathways for Se vapor diffusion to the back interface, resulting in over thick $Mo(S,Se)_2$ of W0 sample.

The topography was further studied by AFM (**Figure 2-10**). The surface of W15 film is smoother and has a smaller root-mean-square (RMS) roughness (40.2 nm) than that of the W0 film (53.0 nm). The same results were obtained by linear scanning of the surface roughness of the two films (Figure 2-10c). The grain size and height distribution of W15 films were more uniform. Larger surface roughness may results in incomplete coverage of CdS on the absorber, thus increasing the shunt path between window layer and absorber.[22] The relatively smooth surface of W15 film is beneficial to improve the quality of heterojunction and to reduce the carriers recombination at the heterojunction interface in order to decrease both the dark current and interface states.[14]

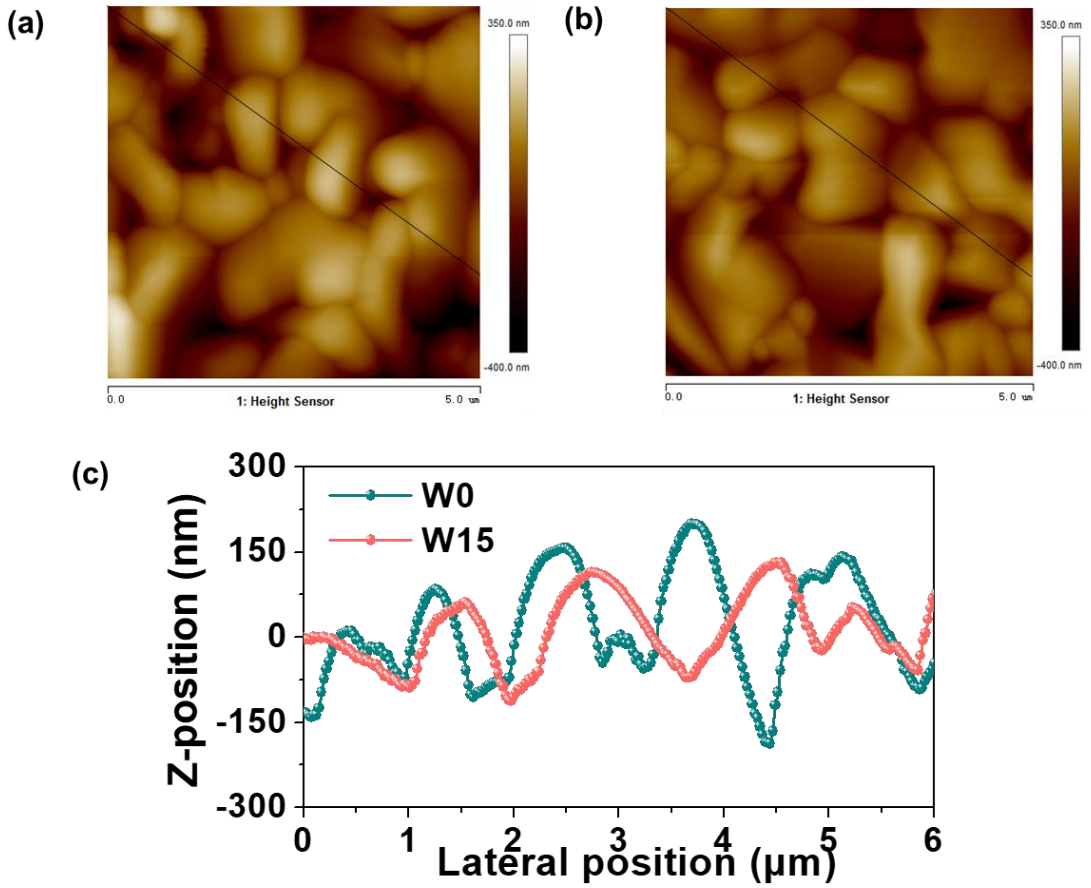

Figure 2-10 *AFM images of (a) W0 films and (b) W15 film, (c) surface roughness line scans along the solid black lines drawn in (a) and (b).*

2.6 Defect property

To evaluate the defect density of CZTSSe absorbers and the recombination properties of the devices, C-V and DLCP measurements were performed. The obtained profiles are shown in **Figure 2-11**a and the results are summarized in **Table 2-2**. The carrier concentration of the device calculated by DLCP measurement was $1.61\times10^{16}cm^{-3}$ and $8.70\times10^{15}cm^{-3}$ without and with WO_3 layer, respectively. In CZTSSe, the free carriers are usually provided by acceptor defects (V_{Cu}, Cu_{Zn}). The decrease in carrier concentration may be due to a reduction in defects, which will be discussed in detail later.[23] The measured depletion width (W_d) for W15 device (0.192 μm) is significantly

higher than that of W0 device (0.111 μm). A larger depletion width is beneficial to the collection and separation of photogenerated carriers.[24] Compared with that of W0 device (340 mV), the built-in potential (V_{bi}) of W15 device is increased to 561 mV (Figure 2-11b). Larger V_{bi} can form an enhanced built-in electric field, which reduces charge accumulation at the heterojunction and thus increases V_{OC}.[25] In general, C-V measurement is more sensitive to interface defects than DLCP, CV response (N_{CV}) includes the contribution of free carriers, bulk defects and interface defects, while DLCP results (N_{DL}) only reflect the contribution of free carriers and bulk defects, thus the difference between them is the interface defect density of the device.[26] This defects density for W15 CZTSSe device ($1.38\times10^{15}cm^{-3}$) was lower than that of W0 device ($5.56\times10^{15}cm^{-3}$), confirming the much less defective surface of W15 absorber. This may be attributed to the fact that the absorber of W15 with improved crystallinity, as discussed earlier, has a smoother surface, which can give better heterojunction quality and reduce the interface defect density. The decrease of the interface defects density means that the recombination and performance degradation caused by the surface state have been attenuated.

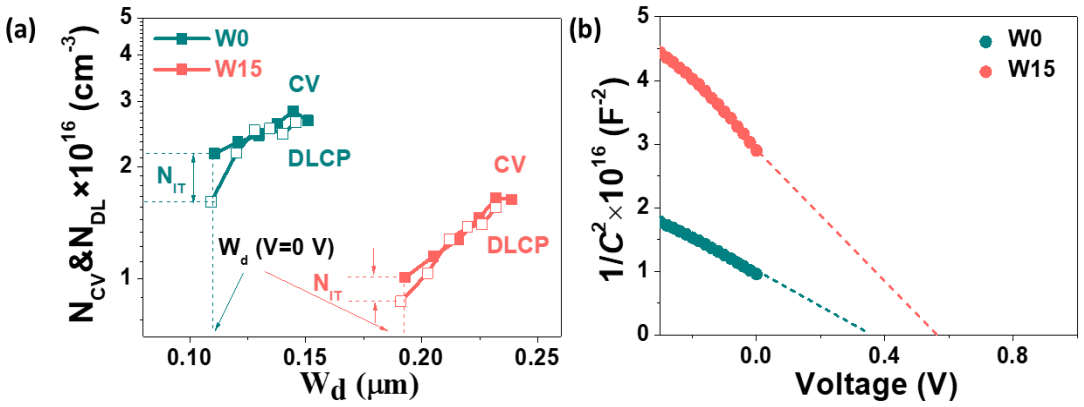

Figure 2-11 *(a) The profile of C-V and DLCP of W0 and W15 devices, (b) $1/C^2$ versus V curves of W0 and W15 CZTSSe devices.*

Table 2-2 *Summary of relevant parameters of AFM, C-V, DLCP and TRPL measurements.*

	RMS [nm]	N_{CV} [cm^{-3}]	N_{DLCP} [cm^{-3}]	Interface state	V_{bi} [mV]	W_d [µm]	τ [ns]	L_d [µm]
W0	53.0	2.16×10^{16}	1.61×10^{16}	5.56×10^{15}	340	0.111	0.71	0.8
W15	40.2	1.00×10^{16}	8.70×10^{15}	1.38×10^{15}	561	0.192	2.05	1.2

Root-mean-square (RMS); CV response (N_{CV}); DLCP response (N_{DL}); built-in potential (V_{bi}); depletion width (W_d); decay time (τ); carrier diffusion length (L_d).

To determine the defect character of CZTSSe absorber with and without WO_3 layer, admittance spectroscopy (AS) measurements were performed on the W0 and W15 devices. The capacitance-frequency (C-f) spectra from 10^2 Hz to 10^6 Hz in the temperature range of 300-120 K are shown in **Figure 2-12**a and b. The high-frequency capacitance response obtained by admittance is mainly caused by free carrier density, while the low-frequency capacitance represents the response caused by free carrier and deep traps.[27] The capacitance of W0 showed a larger variation in the low frequency region compared with W15 device. This significant frequency dependence of capacitance in W0 indicates higher defect density in the absorber.[26]

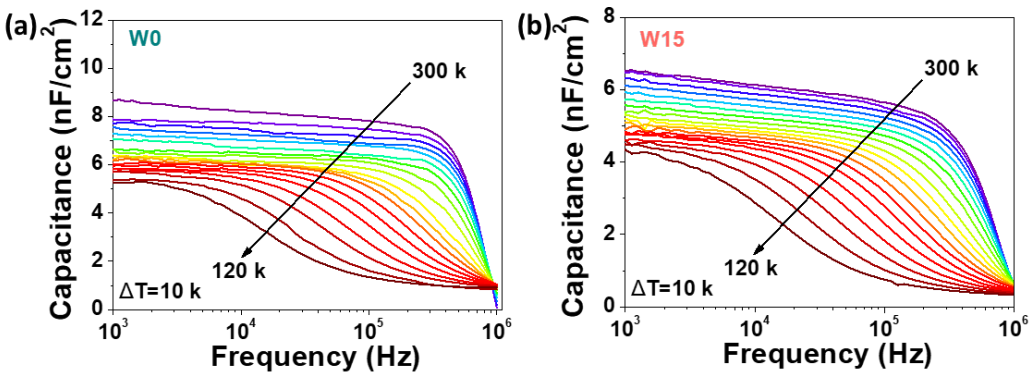

Figure 2-12 *Admittance spectroscopy results for (a) W0 and (b) W15 CZTSSe solar cells.*

The angular frequency corresponding to the maximum of the peak in the -fdC/df plot yields the inflection point ω_0.[28] We constructed an Arrhenius plot of $\ln(\omega_0/T^2)$ vs. 1000/T for W0 and W15 device, shown in **Figure 2-13**a. The Arrhenius plot was constructed using the following equation:

$$\omega_0 = 2\pi v_0 T^2 e^{-\frac{E_a}{kT}} \quad (2\text{-}4)$$

Where E_a is the electronic state level of defect, v_0 is the emission factor.[29] The trap energy levels of W0 and W15 were calculated to be 119 meV and 94 meV, respectively. First-principle calculations suggest that the energy level of the deep acceptor level of Cu_{Zn} is 100-120 meV.[30] The W0 defects with Ea of 119 meV and the W15 defects with Ea of 94 meV can be assigned as Cu_{Zn}. The W15 device has a lower Ea value, which means a higher barrier of defect creation and a lower effective recombination center concentration.[24] Therefore, the WO_3 layer between Mo and CZTSSe could effectively reduce carrier recombination.

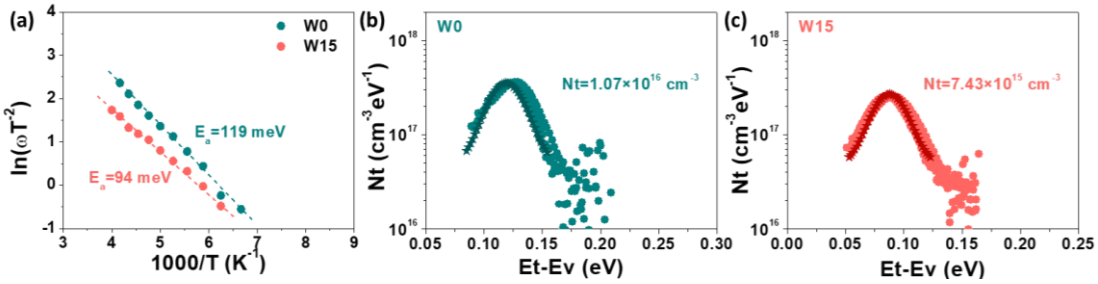

Figure 2-13 *The Arrhenius plots of* $\ln(\omega_0/T^2)$ for *W0 and W15 (a), the defect density of states for (b) W0 and (c) W15.*

The defect spectra are shown in Figure 2-13b, c. The calculation formula was as follows:

$$E_{(\omega)} = kT\ln\left(\frac{2\pi v_0 T^2}{\omega}\right) \quad (2\text{-}5)$$

$$N_t\left(E_{(\omega)}\right) = -\frac{V_{bi}}{W_d}\cdot\frac{dC}{d\omega}\cdot\frac{\omega}{kT} \quad (2\text{-}6)$$

The line composed of pentagons is a Gaussian fit of the corresponding defect energy

levels. Notably, the N_t of Cu_{Zn} (N_t =7.43×$10^{15}$$cm^{-3}$) in W15 is lower than that (N_t=1.07×$10^{16}$$cm^{-3}$) in W0, which contributes to the low free carrier density. This is consistent with the C-V and DLCP measurement. Lower carrier densities may limit V_{OC} increase by reducing the quasi Femi level splitting in the quasi neutral region.[31] On the other hand, lower and shallower acceptor defects could effectively reduce the non-radiative recombination at the interface by reducing the carrier density of the absorber and increasing the interface hole lifetime. According to the recombination model of heterogeneous junction interface established by Li et al., the band bending is enhanced.[32] In brief, the reduced N_t and E_a of acceptor defects induced by the introduction of WO_3 layer at Mo/CZTSSe interface may significantly improve the carrier collection efficiency and may also greatly contribute to the increase of V_{OC} by reducing non-radiative interface recombination. The decrease of both defect level and defect density reveals the great advantage of the transition from double layer to single layer formation mechanism in fabricating high quality kesterite-based material.

To further clarify the low FF associated with the high R_S, we measured the J-V-T within the temperature interval of 180-300 K in dark condition for devices without and with WO_3 intermediate layer (**Figure 2-14**).

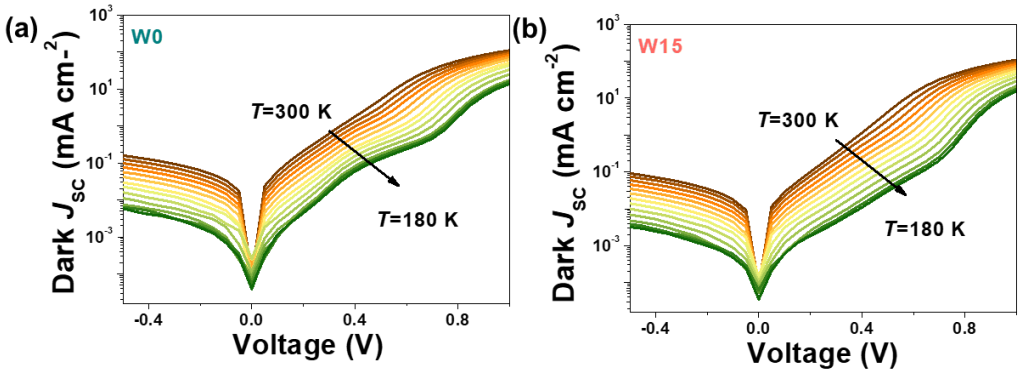

Figure 2-14 *J-V-T plots of (a) W0 device and (b) W15 device*

The devices R_S and back contact diode barrier heights can be estimated from the J-V-

T.[24] In **Figure 2-15**a, the calculated dark R_S is represented as function of temperature. It can be seen that from 300 to 180 K, R_S of W0 increases as much as 4 times, while R_S of W15 increases only 2 times. The existence of the blocking contact barrier Φ_B at the back interface is likely the main reason for the divergent behavior of series resistors versus low temperature. This barrier may exist at the CZTSSe and Mo interfaces and reduce the transport of majority carrier holes. At lower temperature, the back contact diode term will dominate. By replotting ln(R_ST) versus 1/T (Figure 2-15b), , W15 has a lower Φ_B (94 meV) in comparison with W0 (265 meV), suggesting a small barrier in W15 device, which may be related to a thinner $Mo(S,Se)_2$. Obviously, W0 device showed a higher barrier and therefore had larger series resistance.

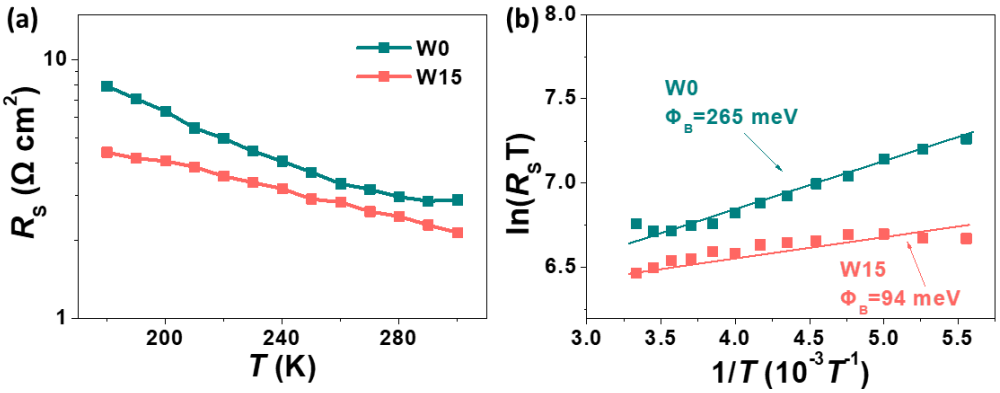

Figure 2-15 *(a) R_S-T curves. (b) ln(R_ST) vs 1/T plot for back contact barrier height determination.*

The presence of such Schottky barrier results in the crossover behavior of the light and dark J-V curves besides double diode performance (**Figure 2-16**a).[33] This crossover behavior occurs at lower current density of the W0 device, corresponding to the higher barrier height in the device. In conclusion, the WO_3 layer significantly reduces $Mo(S,Se)_2$ thickness and the height of contact barrier in the back contact region, and ultimately improves the hole carrier transport of CZTSSe devices.

In addition, J-V-T measurement is one of the most useful methods to determine the main

composite paths in CZTSSe devices by plotting the relationship between Aln(J_0) and 1/kT (A is the diode ideality factor), using the following equation:

$$Aln(J_0) = Aln(J_{00}) - \frac{E_A}{kT}$$

where A is an ideality factor, J_0 is a reverse saturation current density, J_{00} is a prefactor dependent on recombination paths, E_A is a recombination activation energy, k is Boltzmann constant, and T is a temperature. According to the equation, Aln(J_0) versus 1/kT data should yield a straight line and extrapolate to activation energy of interface recombination (E_A) at the temperature of 0 K, as shown in Figure 2-16b.[24] The estimated E_A for the W0 device is 0.86 eV while that for the W15 device is 1.04 eV. The band-gap E_g of CZTSSe films is 1.15 eV for both W0 and W15 cases which was determined by the EQE analysis (Figure 2-16c). The E_A value of W0 was significantly lower than E_g, indicating that the recombination mechanism of W0 was greatly affected by interface recombination, which also limited V_{OC} at room temperature. The E_A value of W15 was close to E_g, indicating that the introduction of WO_3 intermediate layer could passivate the interface recombination significantly, which is attributed to better P-N junction quality and lower back contact barrier.

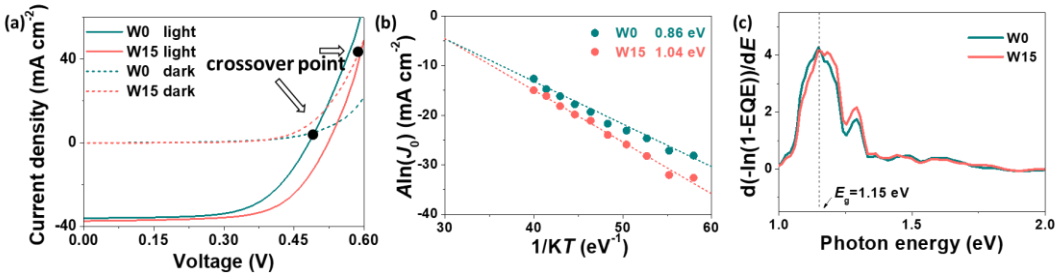

Figure 2-16 *(a) J-V curves of device under light and dark state. (b) Aln(J_0) vs 1/kT plot of W0 and W15 CZTSSe devices. (c) The extraction of band-gap fluctuations of the absorbers from the EQE.*

Further, to investigate the charge carrier recombination behavior and charge carrier

dynamics in CZTSSe films, photoluminescence PL and time-resolved photoluminescence TRPL were conducted and the results are shown in **Figure 2-17(**a) and Figure 2-17(b), respectively. The PL signal of W15 device is significantly increased due to the decrease of non-radiative recombination. The decay time measured by TRPL of W15 device (2.05 ns) is much larger than that of W0 device (0.71 ns). The prolongation of carrier lifetime also indicates that WO_3 layer can significantly inhibit the non-radiative recombination of CZTSSe films, which may be related to improved crystallinity and decreased defects density of CZTSSe films.

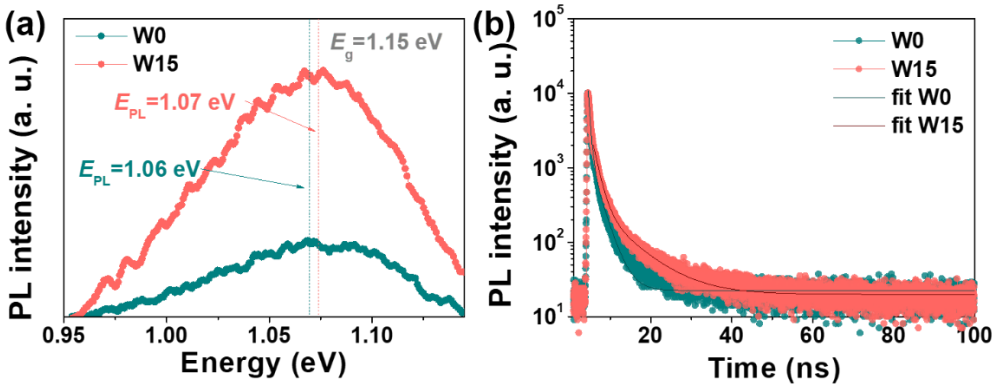

Figure 2-17 *(a) PL and (b) TRPL of W0 and W15 devices.*

2.7 Carrier diffusion length

The EQE and reflection (R) spectra of W0 and W15 sample are shown in **Figure 2-18**a and b. It can be seen that in the long wavelength range, the EQE response of W15 device reflects better carrier collection efficiency than that of W0 device, confirming that W15 device has higher J_{SC}. This improvement can be related to better crystal quality, longer carrier lifetime and decreased $Mo(S,Se)_2$ thickness, which also contribute to FF improvement. WO_3 intermediate layer reduces $Mo(S,Se)_2$ thickness and voids in W15 absorber, thus the recombination at the back interface is reduced and the carrier collection ability is improved. The E_g was determined by plotting d(-ln(1-EQE)) vs dE (Figure 2-16c). E_g of W0 and W15 sample was both 1.15 eV, and the presence of WO_3

layer does not change the band-gap width. In addition, the calculated J_{SC} from EQE were 35.04 and 36.14 mA/cm^2, which was in good agreement with the J-V results.

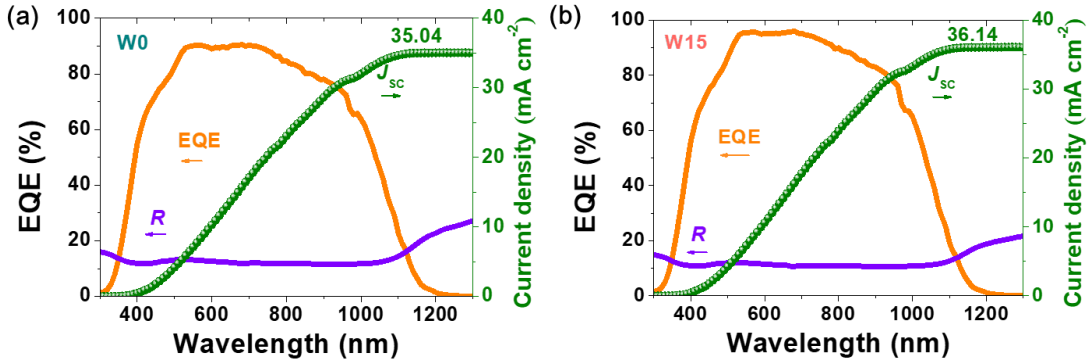

Figure 2-18 *EQE (orange curve) and reflection (R, violet curve) spectra of the W0 device (a) and W15 device (b), the green curve is the EQE integrated current.*

We have also performed minority carrier diffusion length (L_d) measurement by the bias-dependent EQE (**Figure 2-19**), C-V (**Figure 2-20**), and reflectance measurements.[34, 35]

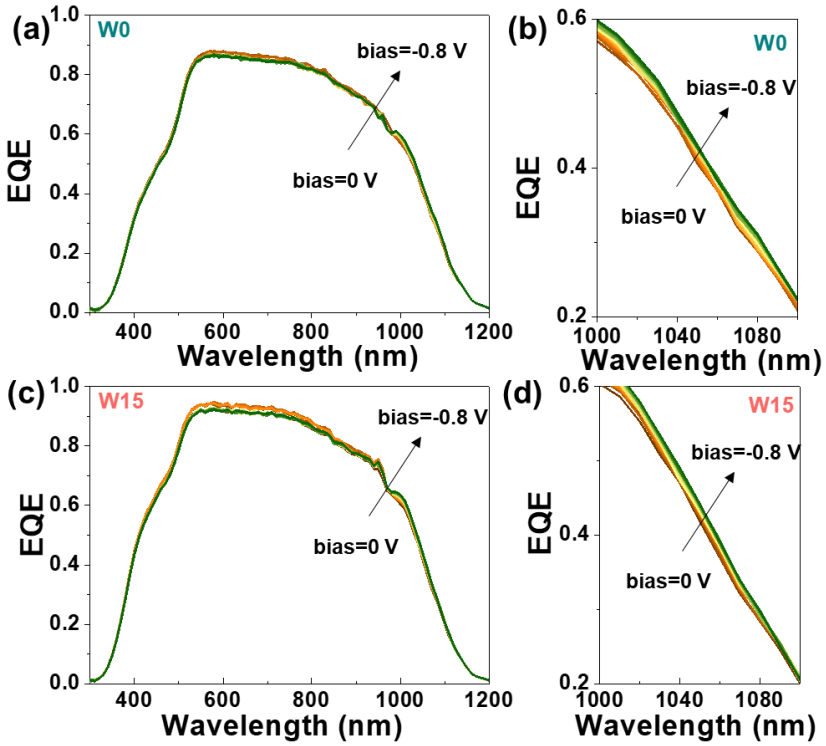

Figure 2-19 *EQE characteristics for a bias range of approximately 0 to -0.8V for (a) W0 device and (c) W15 device. (b) and (d) are the partial enlargement of (a) and (c) respectively.*

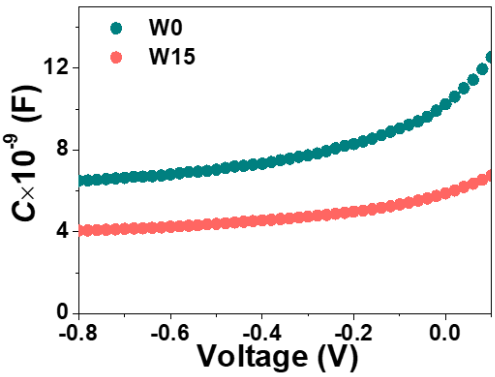

Figure 2-20 *C-V curves of W0 and W15 CZTSSe devices.*

The calculation formula was as follows:

$$\mathrm{IQE}(\lambda, \mathrm{V}) = \frac{\mathrm{EQE}(\lambda,\mathrm{V})}{1-\mathrm{R}(\lambda)} \qquad (2\text{-}7)$$

where EQE(λ,V) is measured as function of wavelength (λ) and voltage bias (V), R(λ) is determined by the reflectivity as function of wavelength, W_d(V) (the voltage dependence of the W_d) is deduced from the separate C-V measurement (**Figure 2-21**).

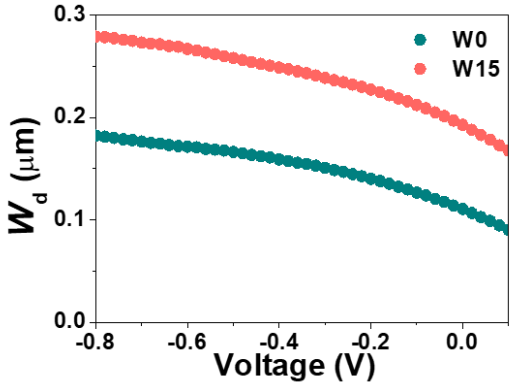

Figure 2-21 *The curves of voltage dependence of the depletion width of W0 and W15 CZTSSe devices.*

Then using the $W_d(V)$, the W_d dependence of IQE at each λ, [IQE(λ,V)→IQE(λ,Wd)] is obtained. The array of IQE(λ,Wd) data are integrated into the analytical expression given by Eq.(2-8) to extract the L_d and the absorption coefficient (α) at each λ:

$$\mathrm{IQE}(\lambda, W_d) = 1 - \frac{\exp(-\alpha(\lambda)W_d)}{1+\alpha(\lambda)L_d} \qquad (2\text{-}8)$$

Figure 2-22a and b show the internal quantum efficiency (IQE) versus W_d at various wavelengths. When the value of IQE changes between 0.2 and 0.8, the dependence of IQE on W_d is most obvious, as shown in Figure 2-22a and b for both samples. The minority carrier diffusion length of absorber estimated from the Figure 2-22 were 0.8 μm for W0 and 1.2 μm for W15, and this may be one of the reasons for the increase of V_{OC}. The fine grain layer obstructs charge transport in the absorber, and defects at grain boundaries, on the surfaces and/or in the interface between these layers provide various charge recombination pathways. Therefore, the thinning of fine grain layer is beneficial to the increase of carrier diffusion length. Besides, the calculation results show that the presence of WO_3 intermediate layer increases the minority carrier diffusion length from 0.8 μm to 1.2 μm, which is consistent with the SEM measurement showing that the thickness of large grain layer increases from 650 nm to 1100 nm. The results show that the W15 device has better carrier collection efficiency. Moreover, the back interface recombination is highly dependent on the carrier diffusion length, the increase of minority carrier diffusion length is also beneficial to reduce back interface recombination.

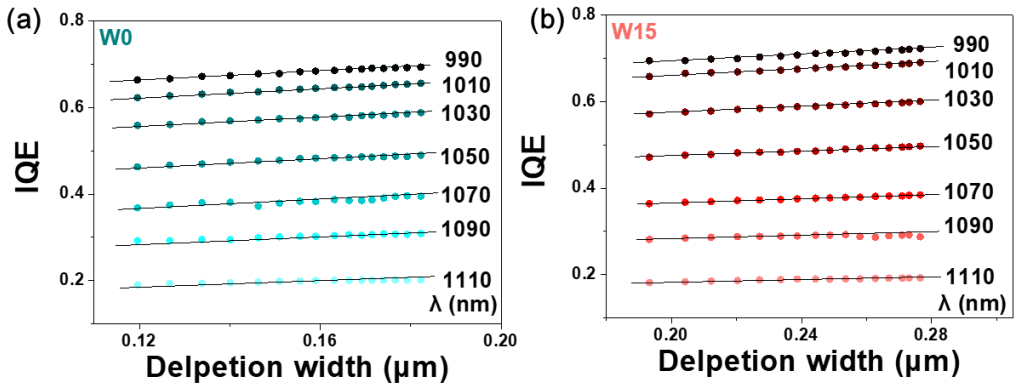

Figure 2-22 *IQE at different W_d (voltage biases) and at different wavelengths near the band edge for (c) W0 and (d) W15.*

Figure 2-23 illustrates the energy band alignment and cross-section schematic diagram for W0 and W15 devices. Apparently the WO_3 layer inhibits the unfavorable interface reaction between CZTSSe and Mo in the initial stage of selenization, and high quality crystals and better interface contact are obtained. The improved crystallization could help to improve the heterojunction quality and maximize the minority carrier diffusion length, and the thin $Mo(S,Se)_2$ layer could reduce the width of the Schottky barrier and carriers can be transported more easily by the tunneling effect, which was believed to promote the CZTSSe device performance.

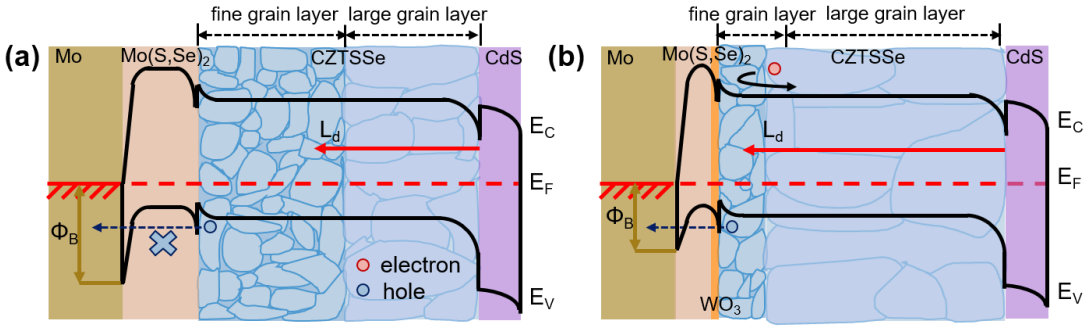

Figure 2-23 *The band diagrams of (a) W0 and (b) W15 CZTSSe devices*

2.8 Conclusions

In summary, we systematically improve the CZTSSe device performance by introducing WO_3 intermediate layer to optimize the crystal growth process. WO_3 layer successfully inhibits the adverse reaction between Mo and CZTSSe, which resulted in poor crystallinity and thick $Mo(S,Se)_2$ layer. And finally, high quality CZTSSe crystal with low defect density and good charge transfer ability is obtained, and the smooth absorber surface also improves the quality of P-N junction. Besides, the inhibition of the back interface reaction effectively reduces the thickness of $Mo(S,Se)_2$, lowers the back interface contact barrier and significantly increases the fill factor. The introduction of WO_3 layer not only improves the minority carrier diffusion length, but also reduces the deep acceptor defects, which greatly inhibits the non-radiative recombination of devices and thus reduces the open circuit voltage deficit. As a result, we demonstrated efficiency improvement from 10.87% to 12.66% in CZTSSe solar cell with a pronounced increase in V_{OC} and FF and a slight increase in J_{SC}. This work provides an effective pathway to regulate selenization process and crystal growth by introducing WO_3 layer as isolation layer for highly efficient CZTSSe solar cells.

REFERENCES

[1] He M., Yan C., Li J., Suryawanshi M. P., Kim J., Green M. A., Hao X., Kesterite solar cells: insights into current strategies and challenges. *Adv. Sci.*, **2021**, 8, 2004313.

[2] Green M. A., Dunlop E. D., Yoshita M., Kopidakis N., Bothe K., Siefer G., Hao X., Solar cell efficiency tables (Version 63). *Prog. Photovolt: Res. Appl.*, **2023**, 32, 3.

[3] Zhao Y., Chen S., Su Z., Luo J., Zhang X., Liang G., Research progress of kesterite solar cells. *Chin. Sci. Bull.*, **2023**, 68, 4662.

[4] Guo H., Meng R., Wang G., Wang S., Wu L., Li J., Wang Z., Dong J., Hao X., Zhang Y., Band-gap-graded $Cu_2ZnSn(S,Se)_4$ drives highly efficient solar cells. *Energy Environ. Sci.*, **2022**, 15, 693.

[5] Scragg J. J., Watjen J. T., Edoff M., Ericson T., Kubart T., Platzer-Bjorkman C., A detrimental reaction at the molybdenum back contact in Cu2ZnSn(S,Se)4 thin-film solar cells. *J. Am. Chem. Soc.*, **2012**, 134, 19330.

[6] Karade V., Lokhande A., Babar P., Gang M. G., Suryawanshi M., Patil P., Kim J. H., Insights into kesterite's back contact interface: A status review. *Sol. Energy Mater. Sol. Cells*, **2019**, 200, 109911.

[7] Yu Q., Shi J., Guo L., Duan B., Luo Y., Wu H., Li D., Meng Q., Eliminating multi-layer crystallization of Cu2ZnSn(S,Se)4 absorber by controlling back interface reaction. *Nano Energy*, **2020**, 76, 105042.

[8] López-Marino S., Placidi M., Pérez-Tomás A., Llobet J., Izquierdo-Roca V., Fontané X., Fairbrother A., Espíndola-Rodríguez M., Sylla D., Pérez-Rodríguez A., Saucedo E., Inhibiting the absorber/Mo-back contact decomposition reaction in $Cu_2ZnSnSe_4$ solar cells: the role of a ZnO intermediate nanolayer. *J. Mater. Chem. A*, **2013**, 1, 8338.

[9] Liu F., Huang J., Sun K., Yan C., Shen Y., Park J., Pu A., Zhou F., Liu X., Stride J. A., Green M. A., Hao X., Beyond 8% ultrathin kesterite Cu_2ZnSnS_4 solar cells by interface reaction route controlling and self-organized nanopattern at the back contact. *NPG Asia Mater.*, **2017**, 9, e401.

[10] Cui H., Liu X., Liu F., Hao X., Song N., Yan C., Boosting Cu_2ZnSnS_4 solar cells efficiency by a thin Ag intermediate layer between absorber and back contact. *Appl. Phys. Lett.*, **2014**, 104, 041115.

[11] Shin B., Zhu Y., Bojarczuk N. A., Jay Chey S., Guha S., Control of an interfacial MoSe2 layer in Cu2ZnSnSe4 thin film solar cells: 8.9% power conversion efficiency with a TiN diffusion barrier. *Applied Physics Letters*, **2012**, 101, 053903.

[12] Kun Shi, Bin Yao, Yongfeng Li, Zhanhui Ding, Rui Deng, Yingrui Sui, Zhenzhong Zhang, Haifeng Zhao, Zhang L., Modification of back electrode with WO_3 layer and its effect on $Cu_2ZnSn(S,Se)_4$-Based Solar Cells. *Superlattices Microstruct.*, **2018**, 113, 328.

[13] Du Y., Tian Q., Huang J., Zhao Y., Chang X., Zhang A., Wu S., Heterovalent Ga^{3+} doping in solution-processed $Cu_2ZnSn(S,Se)_4$ solar cells for better optoelectronic performance. *Sustainable Energy Fuels*, **2020**, 4, 1621.

[14] Fan P., He Y., Liang G., Xie Z., Yu Z., Lin J., Chen S., Zheng Z., Luo J., Su Z., Enhancing Ag-alloyed Cu_2ZnSnS_4 solar cell performance by interfacial modification via In and Al. *J. Mater. Chem. A*, **2021**, 9, 25196.

[15] Zhao Y.-H., Gao Q.-Q., Yuan S.-J., Chang Q.-Q., Liang T., Su Z.-H., Ma H.-L., Chen S., Liang G.-X., Fan P., Zhang X.-H., Wu S.-X., Defects passivation and crystal growth promotion by solution-processed K doping strategy toward 16.02% efficiency $Cu(In,Ga)(S,Se)_2$ solar cells. *Chem. Eng. J.*, **2022**, 436, 135008.

[16] Yuan S., Wang X., Zhao Y., Chang Q., Xu Z., Kong J., Wu S., Solution Processed $Cu(In,Ga)(S,Se)_2$ Solar Cells with 15.25% Efficiency by Surface Sulfurization. *ACS Appl. Energy Mater.*, **2020**, 3, 6785.

[17] Zhao Y., Zhao J., Chen X., Cathelinaud M., Chen S., Ma H., Fan P., Zhang X., Su Z., Liang G., Suppressing surface and bulk effect enables high efficiency solution-processed kesterite solar cells. *Chem. Eng. J.*, **2024**, 479, 147739.

[18] Li J., Zhang Y., Wang H., Wu L., Wang J., Liu W., Zhou Z., He Q., Sun Y., On the growth process of $Cu_2ZnSn(S,Se)_4$ absorber layer formed by selenizing Cu–ZnS–SnS precursors and its photovoltaic performance. *Sol. Energy Mater. Sol. Cells*, **2015**, 132, 363.

[19] Liu F., Zeng F., Song N., Jiang L., Han Z., Su Z., Yan C., Wen X., Hao X., Liu Y., Kesterite $Cu_2ZnSn(S,Se)_4$ Solar Cells with beyond 8% Efficiency by a Sol-Gel and Selenization Process. *ACS Appl. Mater. Interfaces*, **2015**, 7, 14376.

[20] Kim S. Y., Son D. H., Kim S. H., Kim Y. I., Kim S., Ahn K., Yang K. J., Kang J. K., Kim D. H., Effect of Cu–Sn–Se Liquid Phase on Grain Growth and Efficiency of CZTSSe Solar Cells. *Adv. Energy Mater.*, **2020**, 10, 1903173.

[21] Fairbrother A., Fontané X., Izquierdo-Roca V., Espíndola-Rodríguez M., López-Marino S., Placidi M., Calvo-Barrio L., Pérez-Rodríguez A., Saucedo E., On the formation mechanisms of Zn-rich Cu_2ZnSnS_4 films prepared by sulfurization of metallic stacks. *Sol. Energy Mater. Sol. Cells*, **2013**, 112, 97.

[22] Sun Y., Guo H., Qiu P., Zhang S., Wang S., Wu L., Ao J., Zhang Y., Na-doping-induced modification of the CuZnSn(S,Se)/CdS heterojunction towards efficient solar cells. *J. Energy Chem.*, **2020**,

[23] Chen S., Walsh A., Gong X. G., Wei S. H., Classification of lattice defects in the kesterite Cu_2ZnSnS_4 and $Cu_2ZnSnSe_4$ earth-abundant solar cell absorbers. *Adv. Mater.*, **2013**, 25, 1522.

[24] Zhao Y., Yuan S., Chang Q., Zhou Z., Kou D., Zhou W., Qi Y., Wu S., Controllable Formation of Ordered Vacancy Compound for High Efficiency Solution Processed Cu(In,Ga)Se_2 Solar Cells. *Adv. Funct. Mater.*, **2020**, 31, 2007928.

[25] Ohnesorge B., Weigand R., Bacher G., Forchel A., Riedl W., Minority-carrier lifetime and efficiency of Cu(In,Ga)Se_2 solar cells. *Appl. Phys. Lett.*, **1998**, 73, 1224.

[26] Duan H.-S., Yang W., Bob B., Hsu C.-J., Lei B., Yang Y., The role of sulfur in solution-processed $Cu_2ZnSn(S,Se)_4$ and its Effect on defect properties. *Adv. Funct. Mater.*, **2013**, 23, 1466.

[27] Tang R., Zheng Z.-H., Su Z.-H., Li X.-J., Wei Y.-D., Zhang X.-H., Fu Y.-Q., Luo J.-T., Fan P., Liang G.-X., Highly efficient and stable planar heterojunction solar cell based on sputtered and post-selenized Sb_2Se_3 thin film. *Nano Energy*, **2019**, 64, 103929.

[28] Li J., Huang Y., Huang J., Liang G., Zhang Y., Rey G., Guo F., Su Z., Zhu H., Cai L., Sun K., Sun Y., Liu F., Chen S., Hao X., Mai Y., Green M. A., Defect control for 12.5% efficiency $Cu_2ZnSnSe_4$ kesterite thin-film solar cells by engineering of local chemical environment. *Adv. Mater.*, **2020**, 32, e2005268.

[29] Fan P., Xie Z., Liang G., Ishaq M., Chen S., Zheng Z., Yan C., Huang J., Hao X., Zhang Y., Su Z., High-efficiency ultra-thin Cu_2ZnSnS_4 solar cells by double-pressure sputtering with spark plasma sintered quaternary target. *J. Energy Chem.*, **2021**, 61, 186.

[30] Yang K.-J., Sim J.-H., Jeon B., Son D.-H., Kim D.-H., Sung S.-J., Hwang D.-K., Song S., Khadka D. B., Kim J., Kang J.-K., Effects of Na and MoS_2 on Cu_2ZnSnS_4 thin-film solar cell. *Prog. Photovolt: Res. Appl.*, **2015**, 23, 862.

[31] Li J., Kim S., Nam D., Liu X., Kim J., Cheong H., Liu W., Li H., Sun Y., Zhang Y., Tailoring the defects and carrier density for beyond 10% efficient CZTSe thin film solar cells. *Sol. Energy Mater. Sol. Cells*, **2017**, 159, 447.

[32] Li J., Huang J., Huang Y., Tampo H., Sakurai T., Chen C., Sun K., Yan C., Cui X., Mai Y., Hao X., Interface Recombination of Cu2ZnSnS4 Solar Cells Leveraged by High Carrier Density and Interface Defects. *Solar RRL*, **2021**, 5, 2100418.

[33] Dario Cozza, Carmen M. Ruiz, David Duché, Jean Jacques Simon, Escoubas L., Modeling the Back Contact of Cu2ZnSnSe4 Solar Cells. *IEEE Journal of photovoltaics*, **2016**, 6, 1292

[34] Gokmen T., Gunawan O., Mitzi D. B., Minority carrier diffusion length extraction in $Cu_2ZnSn(Se,S)_4$ solar cells. *J. Appl. Phys.*, **2013**, 114, 114511.

[35] Lee Y. S., Gershon T., Gunawan O., Todorov T. K., Gokmen T., Virgus Y., Guha S., $Cu_2ZnSnSe_4$ thin-film solar cells by thermal co-evaporation with 11.6% efficiency and improved minority carrier diffusion Length. *Adv. Energy Mater.*, **2015**, 5, 1401372.

Chapter III: Suppressing front interface and bulk effect enables high efficiency solution-processed CZTSSe solar cells

3.1 Introduction

As discussed earlier, the power conversion efficiency (PCE) of CZTSSe (14.9%) is still far below the highest performance of CIGS solar cells (23.6%).[1, 2] Among the many factors constraining the improvement of device efficiency, carrier recombination at the heterojunction interface and in the absorber bulk should be the key limiting factor. Interface and bulk defects lead to increased Shockley-Reed-Hall recombination (i.e., trap-assisted recombination), which inevitably results in larger open-circuit voltage deficit ($V_{OC\text{-}def}$).[3, 4] Meanwhile, a series of secondary phases are inevitably generated during the selenization process, which affects the adhesion between the buffer layer and absorber and reduces the filling factor (FF).[5] Besides, Sn(S,Se) is commonly used to suppress Sn loss during the selenization process, excess Sn(S,Se) may condense on absorber surface during the cooling.[6, 7] The deep level defects in the absorber can be effectively passivated by cation (Ag, Cd, Ge, et al.) doping, and changing the selenization process to control the chemical environment during the crystallization process can also obtain absorber with lower defect density.[8, 9] However, it is very difficult to improve the absorber bulk as well as the heterojunction interface properties by one strategy at the same time. It is necessary to find a way to solve both the defect and the interface problems to further increase the V_{OC} and FF. Electroactive defect reduction and secondary phase elimination at the CZTSSe/CdS interface by surface treatment is an effective way to improve the quality of the heterojunction interface.[10]

Among the various guiding interface treatment strategy, sulfurization of the CZTSSe absorber has proven to be a simple and effective method.[10] It consists of two main approaches: sulfur-containing vapor treatment and solution treatment. Post-annealing treatment at elevated temperatures under H_2S gas or S vapor atmosphere can effectively

increase the V_{OC}, and the increase is usually attributed to the activation energy transfer of the interface state at the CZTSSe/CdS interface.[11] In this case, the electron transport barrier formed on the surface of the S-rich component deteriorates the device efficiency, so it is essential to control the additional sulfur content introduced by the sulfurization treatment.[12] However, it is very difficult to accurately regulate sulfur doping in CZTSSe film during sulfurization treatment because of the high activity of sulfur at high temperature. Besides, due to the decomposition of kesterite film at high temperatures, elements such as Sn are easily lost. Sulfur-containing solution soaking, such as $(NH_4)_2S$ and Na_2S treatments could take out the secondary phase on the absorber surface and improve the surface wettability of the absorber.[13] However, the appropriate treatment time is crucial for the solution sulfurization treatment, and the absorber needs to be washed immediately after the treatment. The sulfurization activity is closely related to the reaction temperature, which makes it difficult to achieve the passivation of defects by this method. In order to achieve an effective sulfurization effect and at the same time a good control of the degree of sulfurization, a new sulfurization process needs to be explored.

3.2 Sulfurization process

In the present contribution, we report on an effective and simple solution treatment method that can be applied on the surface of sulfur-based thin films and achieve vapor sulfurization, being able to adjust simultaneously the surface property as well as the internal defect of the absorber. This method is based on the use of vapor from ammonium sulphide ($(NH_4)_2S$, abbreviated here AS) as a sulfur source. AS is a salt of a weak alkali and a weak acid and thermally decomposes at 280 °C to release H_2S as follows,[14, 15]

$(NH_4)_2S \leftrightharpoons NH_3+H_2S$ (3-1)

compared with the solution soaking sulfurization process alone, the H_2S released at 280 °C is expected to obtain higher reactivity, while the benign treatment temperature of 280 °C promotes the diffusion of S elements, which can effectively passivate the interface defects as well as bulk defects. Therefore, AS sulfurization treatment is expected to suppress interface and bulk recombination synergistically and well control the elemental distribution, thus further improving the heterojunction quality and device performance.

The surface sulfurization process was the following. The AS solution was coated on the CZTSSe absorber and kept for 2 min, then spinning was performed to obtain thin AS layer on the absorber surface. The thin layer was finally sintered at 280 °C under inert atmosphere. The synergistic effect of surface etching and surface sulfurization can be obtained simultaneously by this method. After the surface sulfurization treatment, the sulfur content of the absorber was slightly increased.

3.2.1 Surface treatment method and its characterization

Ammonium sulfide solution was purchased from Shanghai Aladdin Reagent Co (Ammonium sulfide solution, 20%-26% in H_2O). The precursor solution was prepared in the same way as in Chapter II.

The CZTSSe absorber was prepared using the same experimental method as in Chapter II. Then sulfurization treatment was carried out and we use two sulfurization methods, the traditional treatment method A and the novel treatment method B to compare its influence.

Method A: Soak the CZTSSe absorber in ammonium sulphide solution, use a

stopwatch to accurately calculate the soaking time, and rinse the film with deionised water immediately after the soaking. The rinsed film was dried in an oven at 60°C.

Method B: Place the CZTSSe absorber in the spin coater machine and use a dropper to draw ammonium sulphide solution onto the absorber surface so that the surface is completely covered by the ammonium sulphide solution. The infiltration time was accurately calculated using a stopwatch, and the spin coater machine was started immediately after the timing to rotate the film. The CZTSSe absorber covered with ammonium sulphide (AS) layer were then annealed on a hot plate at 280 ℃. The same spin-coating parameters were used for the CTZS film and the AS layer. The solution was spin-coated with 3000 rpm for 20 s. The whole process was carried out in a glove box under nitrogen atmosphere.

Next, device preparation was performed according to the steps detailed in Chapter II: The CdS buffer layer was prepared by chemical bath deposition on absorber. The ITO window layer was sputtered by magnetron sputtering on the buffer layer. Ag electrodes were deposited by thermal evaporation.

Compared with the characterization methods described in Chapter II, we have used other characterization techniques to observe the influence of the two methods of sulfurization. The new experimental instruments include: Ultraviolet photoelectron spectroscopy (UPS) obtained by using PHI 5000 VersaProbe III with He I source (21.22 eV). The X-ray photoelectron spectroscopy (XPS) was measured by PHI 5000 VersaProbe III with a monochromatic Al Kα X-ray source. The topography and surface potential were measured by Kelvin Electrostatic Force Microscopy (KPFM, Dimension Icon, Bruker). Electrochemistry impedance spectroscopy (EIS) was measured by frequency response analysis (FRA) equipped PGSTAT-30 from Autolab (AUT302N).

The transient photovoltage (TPV) spectra were collected by Agilent B1500A semiconductor characterization system. Admittance spectral measurement was collected through Lakeshore 325 temperature controller and the devices were mounted inside a Janis VPF-100 cryostat and the system was cooled with liquid nitrogen. The device was put into a SEM vacuum chamber to implement EBIC (Electron Beam Induced Current) measurements (Gatan, Inc.).

3.3 Effect of the sulfurization method on the secondary phase

The **Figure 3-1** illustrates the preparation of CZTSSe thin films treated by AS solution sulfurization. The conventional AS solution sulfurization method usually selects a suitable soaking time to soak the CZTSSe absorber in AS solution at room temperature, and then the film is placed in deionized water, and finally dried to obtain the treated film. The film prepared by the traditional method is called as sample A. The soaking time of AS solution corresponding to sample A1 and A2 is 1 and 2 min, respectively. Such a treatment removes secondary phase and passivates the defect of the absorber surface to some extent. Overall, this method is convenient but cannot improve the internal property (e.g., bulk defect) of the absorber, and thus the improvement of PCE is limited. Therefore, we chose a new treatment method: firstly, drop the AS solution on the CZTSSe absorber surface, so that the AS solution completely covers the whole film surface, stay for a few minutes to remove the secondary phase of the surface. Then the spin coater is turned on, and a high-speed rotation makes the AS solution transformed into a thin AS layer. Finally, the samples are placed on a hot plate at 280 ℃ for annealing, the whole process was carried out in a glove box. The samples prepared

using this method are called sample B, and the AS solution infiltration time of sample B1, B2 and B3 corresponds to 1, 2 and 3 min, respectively. The H_2S released from the decomposition of AS at 280°C has higher reactivity, and the favorable sulfurization temperature of 280°C is conducive to promoting the diffusion of S into the interior of the absorber, which can effectively passivate the defect on the surface as well as in the bulk.

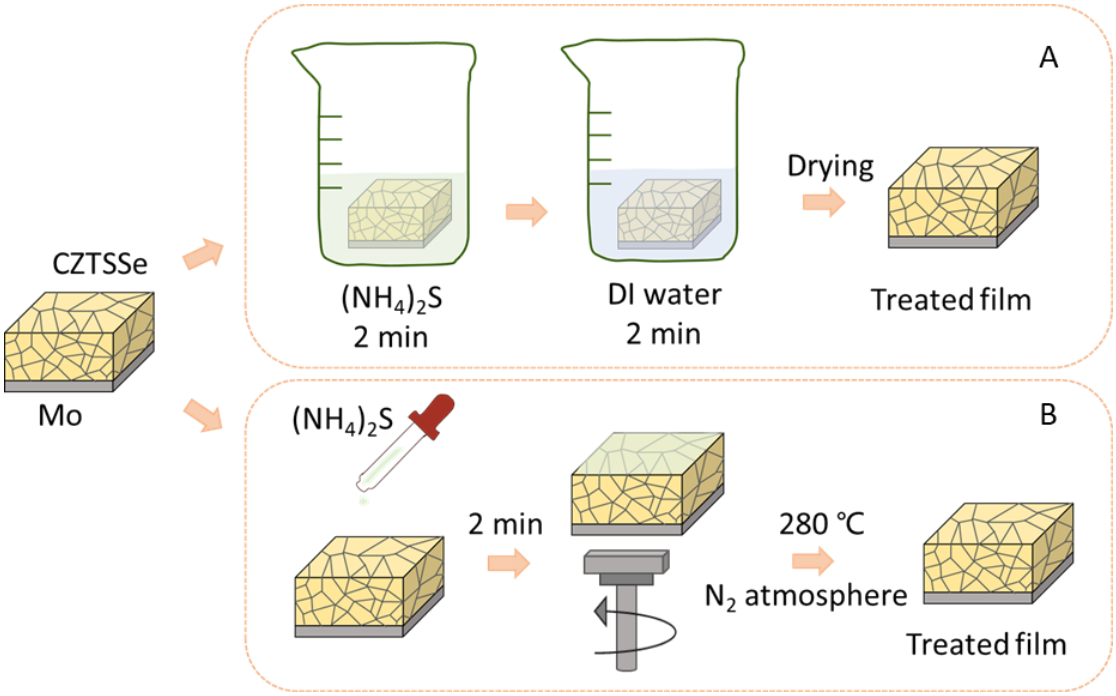

Figure 3-1 *Illustration of different AS sulfurization treatment processes.*

The XRD spectra and partial magnification of the reference sample and samples A, B are shown in **Figure 3-2**a and b, respectively. The XRD spectra indicate that the crystal structure of the samples is kesterite CZTSSe, and the bulge located on the right side of the (112) peak is assigned to the secondary phase Sn(S, Se).[16] The Sn(S, Se) peak intensity of the thin film treated with AS solution was significantly weakened than reference (Figure 3-2b), indicating that the secondary phase in the absorber was effectively reduced. Moreover, the Sn(S,Se) peak intensity of A2 sample is lower than

that of A1, and the Sn(S,Se) peak intensity of B1, B2 and B3 are weakened in turn, which means that the longer the AS solution stays on the absorber, the better the remove effect of the secondary phase is.

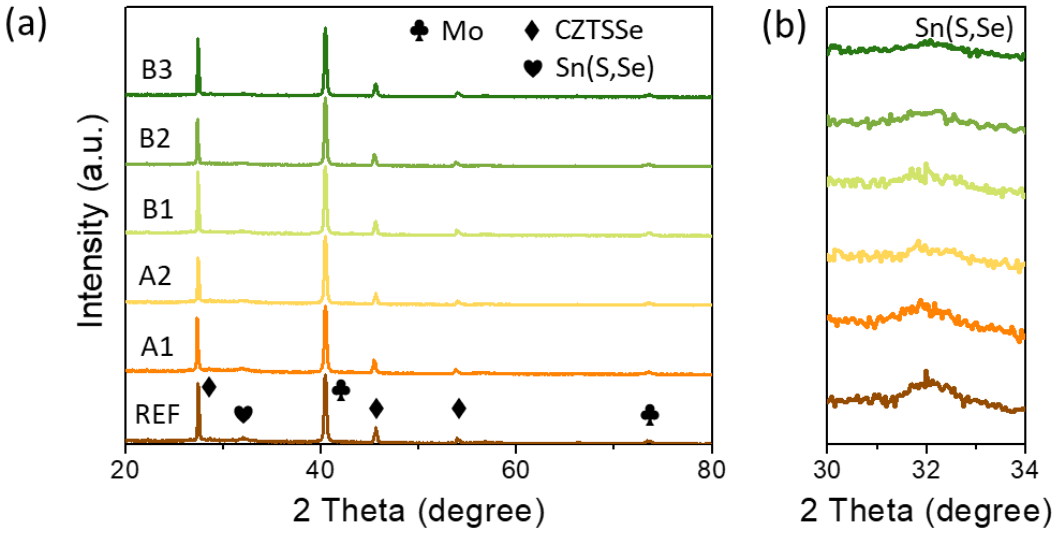

Figure 3-2 *(a) XRD patterns of the reference sample, sample A and sample B, (b) The enlarged characteristic of (112) peak.*

3.4 Influence of sulfurization on the device efficiency

To investigate the effect of AS solution treatment on the device efficiency, the PCE of the reference sample and sample A, B are summarized in **Table 3-1**. The results show a negligible slight enhancement in short-circuit current density (J_{SC}) and V_{OC} and a small increase in FF, hence a slight enhancement in efficiency for the sample treated by method A. AS solution soaking removes the secondary phase of absorber surface, which favors better heterojunction quality, and therefore the FF is enhanced. The increase in V_{OC} and FF in the samples treated with method B was quite significant. Residence of the AS solution on the surface of the absorber dissolves the secondary phase, and subsequent rotation of the spin coater removes the secondary phase dissolved in the AS

solution. Annealing at 280 °C in an inert gas atmosphere enhances the reactivity of the sulfurization and promotes elemental diffusion, and the AS decomposes into NH_3 and H_2S, which effectively passivates the electroactive defects on the surface and in the bulk of the absorber. The improvement of the heterojunction quality and the reduction of the defects lead to the enhancement of the FF and the V_{OC}, which resulted in an efficiency of 13.19%. The 2 minutes residence time of AS solution gives the best result.

Table 3-1 *Photovoltaic parameters of reference, A and B solar cells.*

	REF	**A1**	**A2**	**B1**	**B2**	**B3**
J_{SC} **(mA/cm²)**	37.27	37.82	37.54	37.34	37.47	37.35
V_{OC} **(V)**	0.494	0.493	0.495	0.510	0.531	0.514
FF (%)	63.10	63.29	63.74	64.37	66.30	65.55
PCE (%)	11.26	11.80	11.84	11.98	13.19	12.32

In the following, the reference device and the optimal device B2 will be referred to as W/O AS and With AS respectively for ease of expression. **Figure 3-3** illustrates the box statistics of the PV parameters, where the average efficiency of the With AS device increases from 11.15% to 12.76%. The enhancement of J_{SC} may originate from the reduction of recombination loss at the heterojunction interface and the enhancement of charge carrier collection.[17]

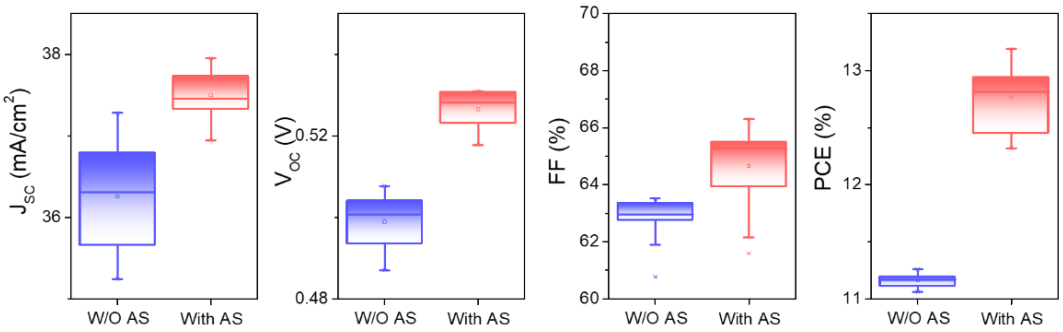

Figure 3-3 *Statistical boxplot of J_{SC}, V_{OC}, FF and PCE for W/O AS and With AS devices.*

Figure 3-4 shows the J-V curves of the W/O AS and With AS devices. The V_{OC} and FF of the With AS device demonstrates a significant enhancement, which may originate from the passivation of defects. The series resistance (R_s), shunt resistance (R_{sh}), ideality factor (A), and reverse saturation current (J_0) calculated from the J-V curves are summarized in **Table 3-2**.

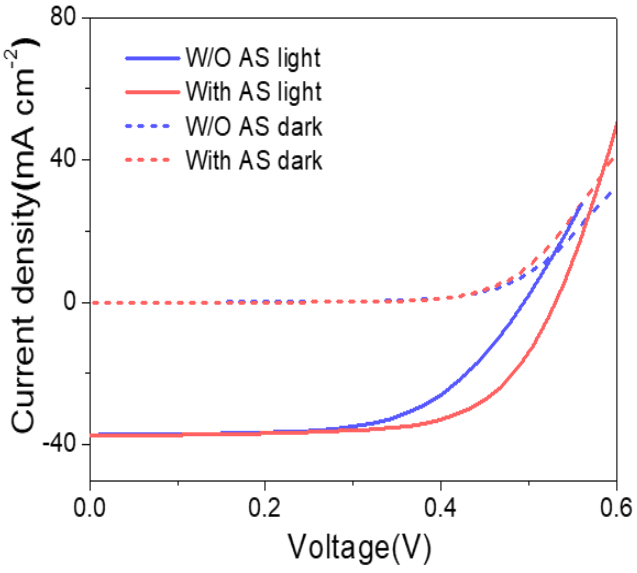

Figure 3-4 *Light-state and dark-state J-V curves for W/O AS and With AS devices.*

Table 3-2 *Diode parameters, band-gap, defect recombination activation energy and deep defect density for W/O AS and With AS devices*

	R_s (Ω)	R_{sh} (Ω)	A	J_0 (mA cm^{-2})	E_g (eV)	E_a (meV)	N_T (cm^{-3})
W/O AS	1.41	383	1.64	2.70×10^{-5}	1.14	308	3.10×10^{16}
With AS	0.71	441	1.50	1.57×10^{-5}	1.15	147	1.10×10^{16}

The diode parameters (**Figure 3-5** and **Figure 3-6**) of the solar cell help us to analyze the performance loss mechanism of the device. The With AS device have smaller R_s and larger R_{sh}, which is beneficial to enhance the FF. The A and J_0 of With AS devices are 1.5 and 1.57×10^{-5} mA cm^{-2}, respectively, which are smaller than that of the W/O AS devices.[20] It implies that there is a significant reduction of carrier recombination in the With AS devices, which could be due to the sulfurization treatment, leading to passivated defects thereby reducing the number of carrier recombination centers.

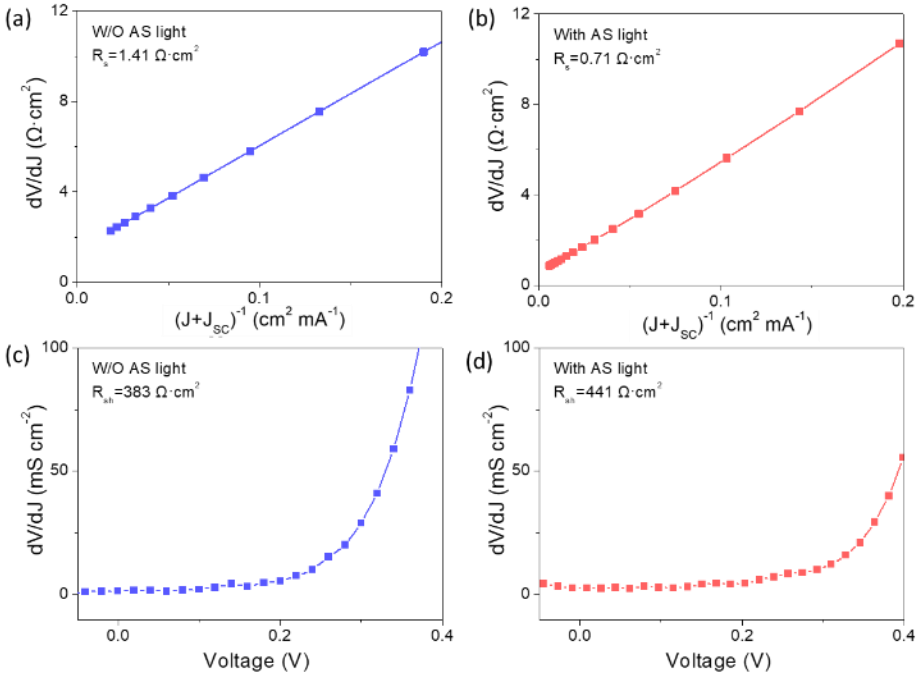

Figure 3-5 *Series resistance (a, b) and parallel resistance (c, d) for W/O AS and With AS devices. (a) and (c) correspond to W/O AS device, (b) and (d) correspond to With AS device.*

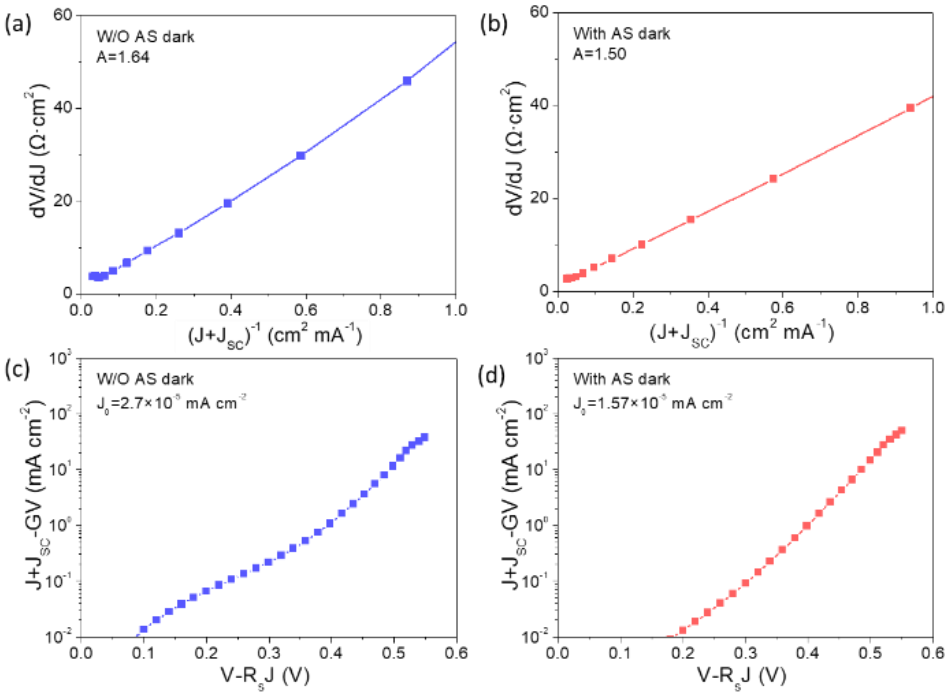

Figure 3-6 *Diode ideality factor (a, b) and reverse saturation current (c, d) for W/O AS and With AS devices. (a) and (c) correspond to W/O AS devices, (b) and (d) correspond to With AS devices.*

The EQE curve are shown in **Figure 3-7**a. Consistent with J_{SC}, the AS sulfurization treatment slightly improves the EQE in the broad spectral range of 400-1000 nm, presumably due to the sulfurization treatment passivating the recombination centers in the absorber and enhancing the carrier collection efficiency.[21] Notably, the EQE response of the treated devices starts to decrease around 1000 nm, which is related to the decrease in long-wavelength absorption due to the S content increase in the absorber of the processed device.[22] The band-gap (E_g) was determined from EQE curve by

linear extrapolation of $(\ln(1\text{-EQE}))^2$ versus wavelength (Figure 3-7b).[23] The E_g of the W/O AS and With AS devices are 1.14 eV and 1.15 eV, respectively, and the E_g of the treated device increases slightly due to the increase in S content.[24]

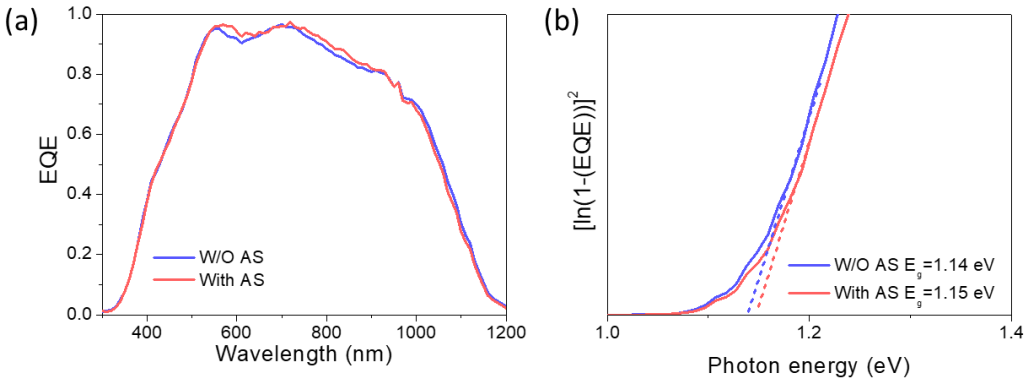

Figure 3-7 *(a) EQE of W/O AS and With AS device, (b) Band-gap of W/O AS and With AS devices calculated from EQE curves.*

The integral current density calculated from the EQE spectral response is displayed in **Figure 3-8**. The integral current density of the W/O AS and With AS devices are 34.68 and 34.95 mA cm^{-2}, respectively, which are in good agreement with the J_{SC} in the *J-V* curves. The UPS analysis can obtain the work function and valence band of the semiconductor materials, which can be combined with the band-gap values to obtain the band alignment of the heterojunctions.

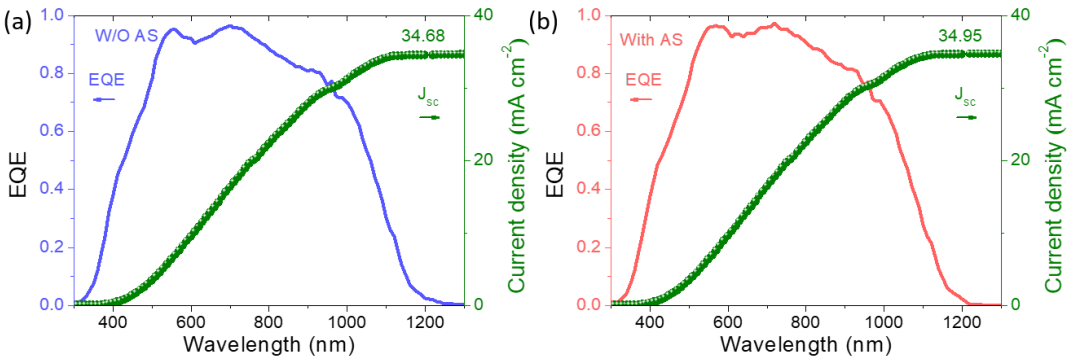

Figure 3-8 *Integral current density of W/O AS (a) and With AS (b) devices*

calculated from EQE curve.

3.5 Sulfurization effects on the elemental content

SEM mapping tests were performed on the surface of W/O AS and With AS absorber to investigate the effect of AS treatment on the elemental content of the absorber surface, and the result is displayed in **Figure 3-9**a, b. The S content of the With AS absorber surface increases obviously, the Se content changes insignificantly, and the Sn content decreases slightly, which coincides with the result that the Sn-related secondary phases are removed after the sulfurization treatment.

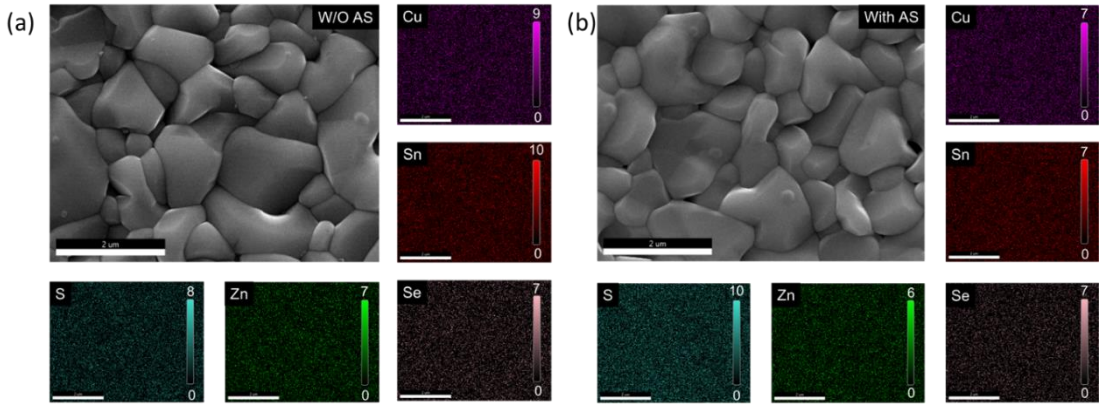

Figure 3-9 *(a) SEM image and EDS mapping of the W/O AS film, (b) SEM image and EDS mapping of the With AS film.*

The EDS elemental line scan shows a slight increase of S content in the near-surface region (400 nm) of the absorber after sulfurization treatment (**Figure 3-10**a). Figure 3-10b demonstrates the changes of S/Se in the films before and after the sulfurization treatment and the corresponding band-gap changes. The band-gap values of $Cu_2ZnSn(S_{1-x}Se_x)_4$ for different Se contents can be calculated using the sophisticated hybrid functional HSE (Heyd-Scuseria-Ernzerhof) reported by Chen et al. with the following formula:[18]

$$E_g(x)=(1-x)E_g(\mathrm{CZTS})+xE_g(\mathrm{CZTSe})-bx(1-x) \quad (3\text{-}2)$$

where Se content is x, S content is 1-x, E_g(CZTS) is 1.5 eV, E_g(CZTSe) is 0.96 eV, and b denotes band-gap bending with a value of 0.07 eV. The With AS films possess a larger value of S/Se near the surface and the surface band-gap is larger than that of the W/O AS films. The V_{OC} is proportional to the band-gap, and a slightly larger band-gap at the surface favors the enhancement of the V_{OC}.

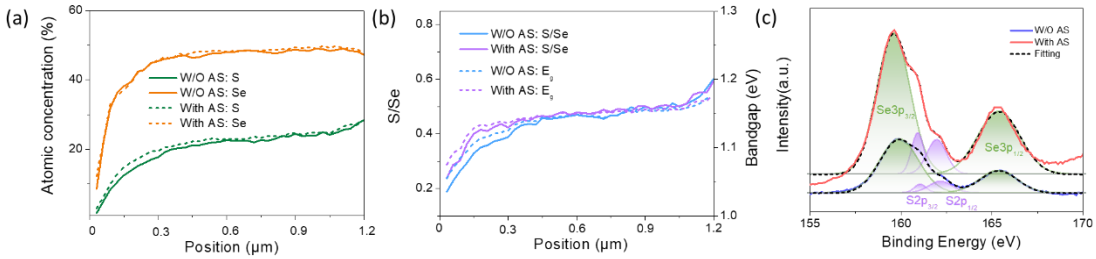

Figure 3-10 *(a) S and Se elemental line scans of W/O AS and With AS films, (b) S/Se profiles and band-gap profiles of W/O AS and With AS films, (c) XPS analysis of Se 3p for the W/O AS and With AS film.*

XPS is very sensitive to the elemental components of the sample surface, and the surface composition of the W/O AS and With AS CZTSSe absorber was investigated using XPS. Figure 3-10c illustrates the S 2p peak of both samples. Four peaks were observed in the S 2p spectra, the peaks at 161.0 and 162.2 eV belong to the S 2p core, consistent with the sulphide state S located at 160-164 eV, while the peak at 159.7 and 165.4 eV belong to the Se 3p core.[19] The sulfurization treatment greatly affects the surface S peak intensity, which is significantly increased for the treated film surface, compared to the W/O AS film, indicating a higher S content. It is in agreement with the results of SEM-Mapping.

3.6 Band alignment

Ultraviolet Photoelectron spectroscopy (UPS) is a technique for measuring the energies of the valence states, in particular for semiconductors. This technique has been applied for the buffer layer CdS (E_g=2.40 eV) and for the W/O AS and With AS CZTSSe absorber.

The UPS curves of CdS, W/O AS film and With AS film are shown in **Figure 3-11** and **Figure 3-12**, respectively. The work function (φ) is obtained from the following equation:[18]

$$\varphi = h\upsilon - E_{\text{cut off}} \qquad (3\text{-}3)$$

where $h\upsilon$ is 21.22 eV (He I source) and $E_{\text{cut off}}$ is based on the extrapolation of the linear region of high binding energy.

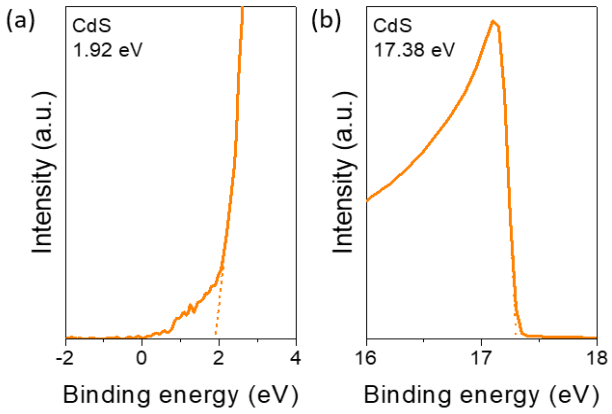

Figure 3-11 *UPS curve for CdS. (a) correspond to low binding energy, (b) correspond to high binding energy.*

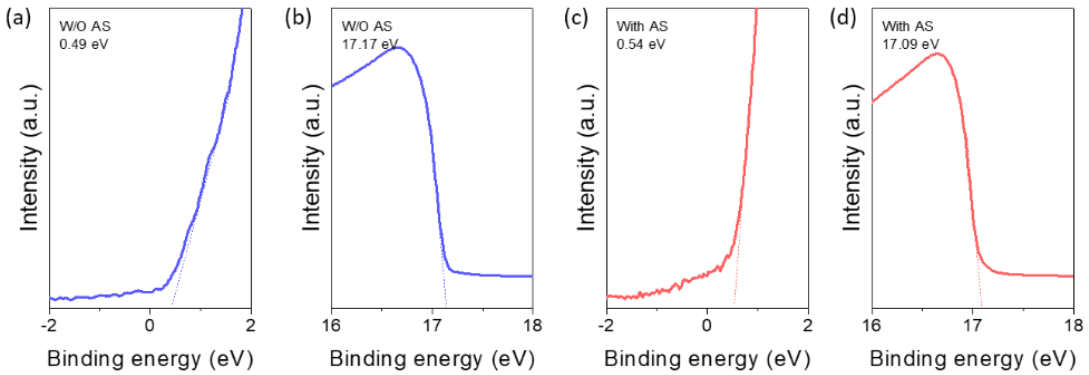

Figure 3-12 *UPS curves for W/O AS (a, b) and With AS films (c, d). (a) and (c) correspond to low binding energy, (c) and (d) correspond to high binding energy.*

The calculation results show that the conduction band of CdS is higher than that of W/O AS film and With AS film (the band alignment schematic is shown in **Figure 3-13**), which proves that the p-n junctions of both devices are spike structures that are favorable for carrier transport. The band alignment at the heterojunction contains both spike-type and cliff-type. When the electron affinity energy of the buffer layer is larger than that of the absorber, the CBO at the heterojunction is negative, and the band alignment at this time is cliff-type. The cliff-type band alignment will strongly increase the interface recombination and decrease the V_{OC}. And when the electron affinity energy of the buffer layer is smaller than that of the absorber, the CBO at the heterojunction is positive, and the band alignment is spike-type in this case. Spike-type band alignment is favorable to prevent electron return and reduce interface recombination, but excessive spike (too large CBO) affects the electron tunneling effect at the interface thus deteriorating the device performance. Relevant literatures show that CBO is optimal between 0-0.4 eV, in which larger CBO is more favorable to reduce interface recombination. In this work, the CBO at the heterojunction of the With AS device is slightly increased due to the sulfurization treatment that improves the S/Se

content in the near-surface region of the absorber layer, favoring the reduction of heterojunction interface recombination.

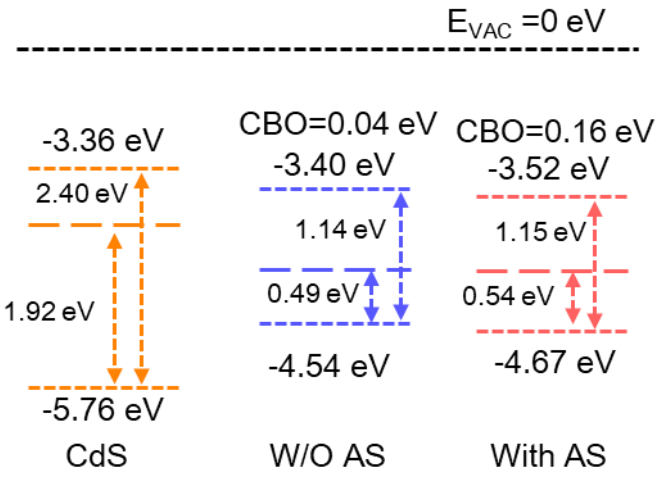

Figure 3-13 *heterojunction band alignment schematic for W/O AS and With AS devices.*

The CBO of the heterojunction is 0.04 eV for the W/O AS device and 0.16 eV for the With AS device. The slightly increased CBO of the With AS device is more conductive to the reduction of interface recombination and does not affect the electron tunneling, which improves the performance of the device.

3.7 Surface potential

AFM and KPFM measurements are widely used in solar cells to analyze the spatial morphology and the potential distribution around the grain boundary (GB) of the samples. The 2D morphology and surface potential maps of the CZTSSe absorber are shown in **Figure 3-14**. The surface morphology of the two samples is in good agreement with the SEM images. The surface potentials of the W/O AS and With AS sample are shown in Figure 3-14b and 3-14e. The brightness of the grain boundary of the two samples is significantly higher than that of the grain interior (GI), which means that the

contact potential difference (CPD) of the grain boundary is higher than grain interior. Higher CPD at grain boundary lead to downward bending of the bands, which attracts electrons and repels holes.[10, 18. 25] This downward bending phenomenon can promote the separation of electrons and holes, leading to a reduction in carrier recombination and an enhancement of carrier separation.

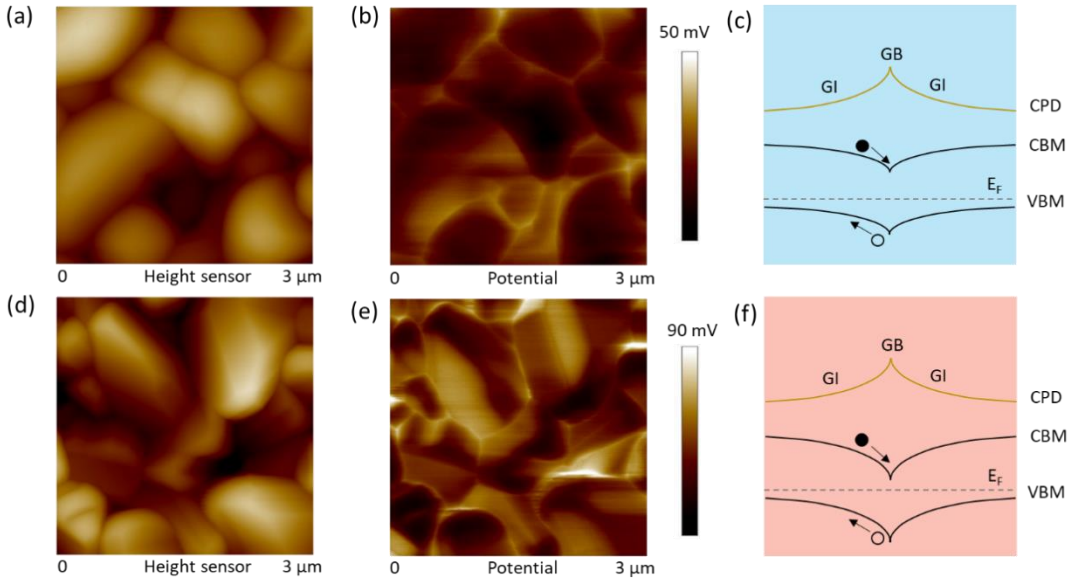

Figure 3-14 *AFM and KPFM of the (a, b) W/O AS film and (d, e) With AS film. Schematic of the band diagram and contact potential difference near grain boundary of (c) W/O AS film and (f) With AS film.*

In addition, the average potential difference of W/O AS and With As samples between the GB and GI is 26 and 73 mV, respectively (**Figure 3-15**a and b). KPFM is used to determine the electrostatic potential change between the probe and the sample due to the localized surface potential change. The brightness of the grain boundary (GB) of both samples is significantly higher than that of the grain interior (GI), and the potential difference between GI and GB can be expressed by the following equation:

$$\Delta CPD=\varphi_{GI}-\varphi_{GB}=eV_{CPD(GB)}-eV_{CPD(GI)} \quad (3\text{-}4)$$

where φ_{GI} and φ_{GB} are the potentials at the GI and GB, respectively. It suggests that the AS sulfurization treatment increases the band bending at the grain boundary.[26] Larger band bending facilitates enhanced carrier separation and collection at grain boundary, suggesting that the higher carrier separation efficiency after surface sulfurization treatment is one of the reasons for the increase in V_{OC}.

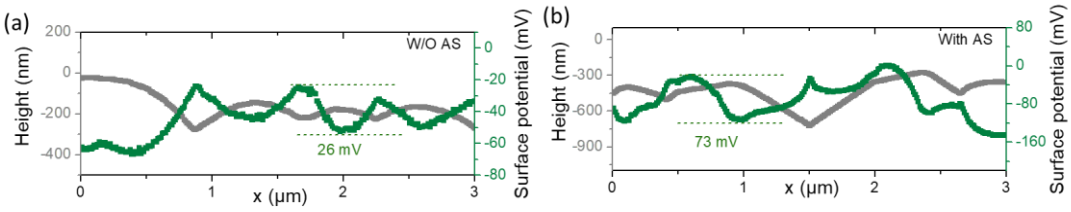

Figure 3-15 *The potential variation of (a) W/O AS film and (b) With AS film.*

3.8 Defect property

The PCE of kesterite devices is limited by the level of deep traps at the interface and in the absorber bulk. Since annealing of the treated devices at 280 ℃ leads to ion exchange between the CZTSSe and AS layer, the defect property of the absorber may change accordingly. In order to gain insight into the correlation between interdiffusion and deep-trap states, we performed admittance spectral measurements on W/O AS devices and With AS devices. The results are shown in **Figure 3-16**a, c, the capacitance of the W/O AS device varies greatly with frequency, while the capacitance of the With AS content device varies less between high and low frequency. The significant frequency dependence of the capacitance in the W/O AS device suggests that there are moretraps in the absorber.[27]

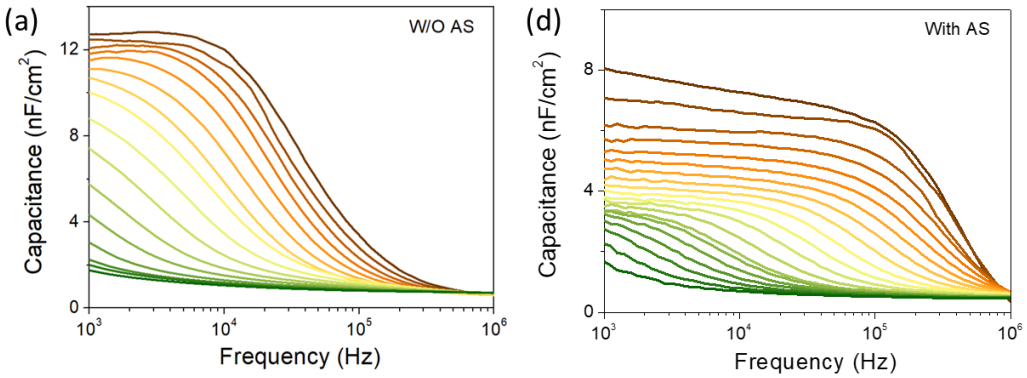

Figure 3-16 *Admittance spectral results for (a) W/O AS, (d) With AS*

Admittance spectral measurements are used to estimate the defect level within the band-gap. The inflection frequency ω_0 of each admittance spectral curve is determined by the corner frequency point at the maximum of the $-\omega dC/d\omega$ plot (**Figure 3-17**). The fitting equation for the Arrhenius plot is:[28]

$$\omega_0 = 2\pi v_0 T^2 e^{-\frac{E_a}{kT}} \qquad (3\text{-}5)$$

where ω_0 is the inflection frequency, E_a is the depth of the defect relative to the edge of the valence band, and υ_0 is a prefactor (Hz K^{-2}).

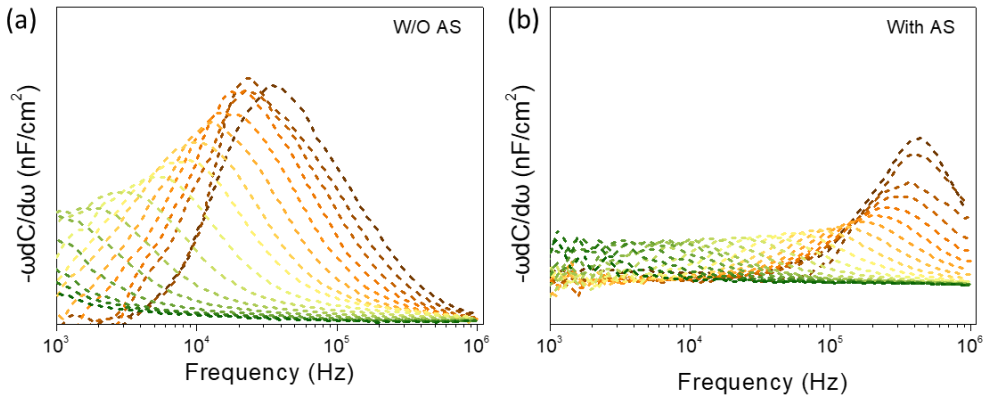

Figure 3-17 *Plots of $-\omega dC/d\omega$ vs. frequency at different temperature for W/O AS (a) and With AS devices (b).*

In this case, the activation energy E_a determined from the Arrhenius diagram is approximated as the energy difference between the defect energy level and the valence band edge. The defect density obtained from the *C-f* scan is calculated as follows:[28]

$$E_a = kTln(\frac{2\pi v_0 T^2}{\omega}) \quad (3\text{-}6)$$

$$N_t = -\frac{V_{bi}}{W_d} \cdot \frac{dC}{d\omega} \cdot \frac{\omega}{kT} \quad (3\text{-}7)$$

where N_T is the defect density, W_d is depletion width and V_{bi} is the built-in voltage

Figure 3-18a and c shows the Arrhenius plots of the W/O AS and With AS device, the activation energy (E_a) determined from the Arrhenius plots approximates the difference between the defect level and the edge of the valence band.

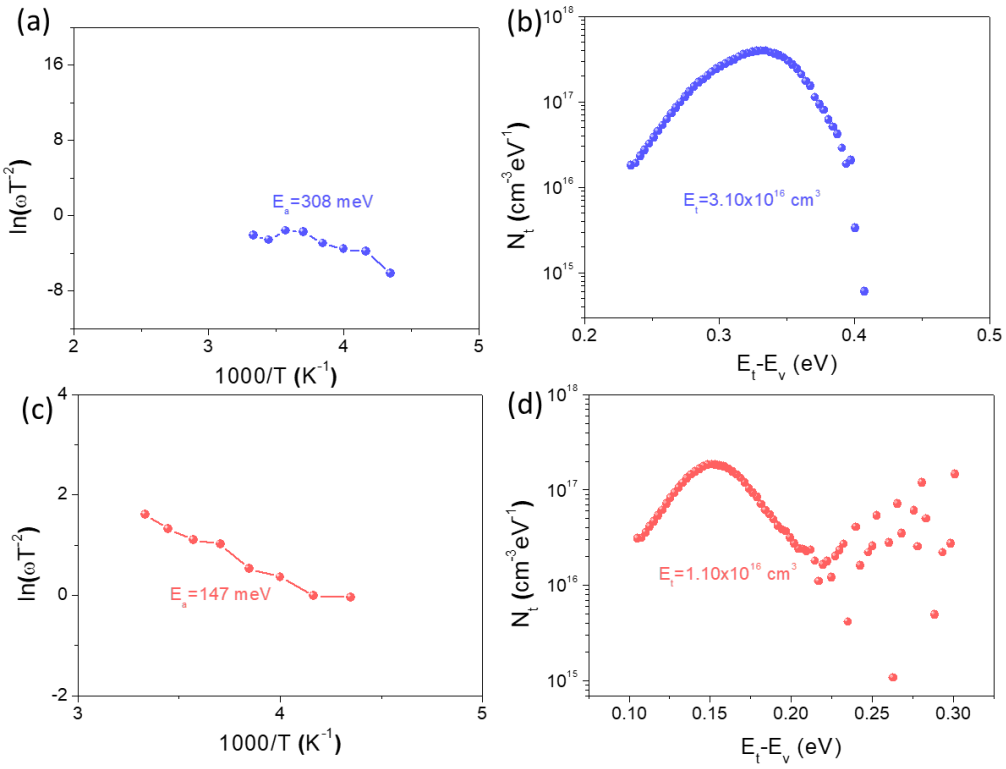

Figure 3-18 *From the inflection points of the C-f-T results, the Arrhenius plots of (a) W/O AS, (c) With AS, the defect density of states for (b) W/O AS, (d) With AS.*

The E_a for the W/O AS and the With AS device is about 308 meV and 147 meV, respectively. A larger E_a value usually indicates a slower hole emission rate, so defects with larger activation energy are more likely to become more efficient recombination centers. In the CZTSSe, the deeper energy level that are located at about 300 meV above the valence band defects include the acceptor defect Cu_{Sn} and the donor defect V_{Se}, while another defect level 150 meV away from the valence band can be attributed to the Cu_{zn} defect.[4] For the With AS devices, the annealing at 280 °C promotes ion exchange, and the S elements in the AS layer can diffuse into the absorber to a greater extent, which can passivate the V_{Se} defect on the absorber surface as well as in the bulk at the same time.[29] Therefore, the dominant deep-energy level defects in the With AS device are converted from V_{Se} to Cu_{Zn}, which is the main reason for the V_{OC} enhancement in the With AS device. In contrast to V_{Se}, which deteriorates the device performance by trapping carriers as a deep energy level recombination center, ionization of the acceptor defect Cu_{Zn} generates a large number of hole carriers and leads to a good p-type conductivity.[29]

3.9 Device carrier transport capacity

Temperature-dependent J-V tests (J-V-T) are widely used to analyze carrier transport mechanism in thin-film solar cells. **Figure 3-19** shows the J-V-T curves of W/O AS and With AS devices from 120 k to 300 k under dark conditions. The diode-like behavior (dashed circle) of the W/O AS device is largely suppressed at 220 k, whereas the J-V curves of the With AS device show good diode characteristics even when the temperature drops to 160 K, proving that the With AS device has a low transport barrier.[30]

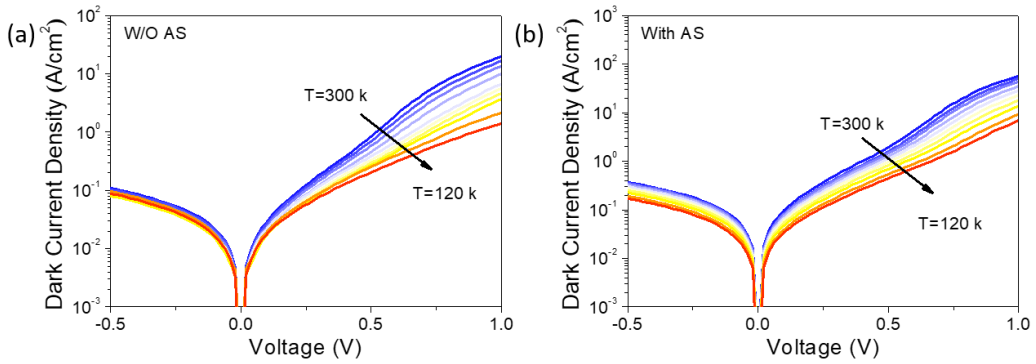

Figure 3-19 *Temperature-dependent dark J–V curves of W/O AS device (a) and With AS device (b).*

The reverse saturation current (J_0) and ideality factor (A) were extracted from the J-V curves. The A of the With AS device showed lower temperature dependence, indicating the dominance of Shockley-Read-Hall recombination in the depletion region (**Figure 3-20**a). The A of the W/O AS device was much larger and strongly correlated with the temperature, suggesting that unfavorable tunneling-enhanced recombination was dominant.[31] The dominant recombination paths can be found by plotting Aln(J_0) against 1/kT and calculating the slope E_A (Interface recombination activation energy, Figure 3-20b). E_A close to E_g indicates that bulk recombination dominates; whereas E_A less than E_g implies that interface recombination is dominant.[32] The E_A of the W/O AS and With AS devices are 0.79 eV and 0.95 eV, respectively. The E_A values of With AS devices are close to the band-gap, indicating that the AS sulfurization treatment significantly passivates the interface recombination.

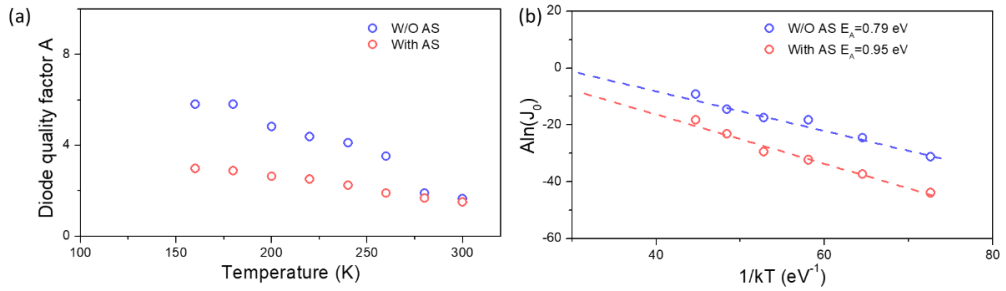

Figure 3-20 *(a) Temperature dependence of ideality factor of W/O AS and With AS device, (b) Aln(J₀) versus 1/kT plot of W/O AS and With AS device.*

The carrier concentration of absorber and recombination property of heterojunction were investigated by capacitance–voltage (C–V) and Drive Level Capacitance Profiling (DLCP) characterizations. **Figure 3-21** is the CV and DLCP data for the W/O AS and the With AS device.

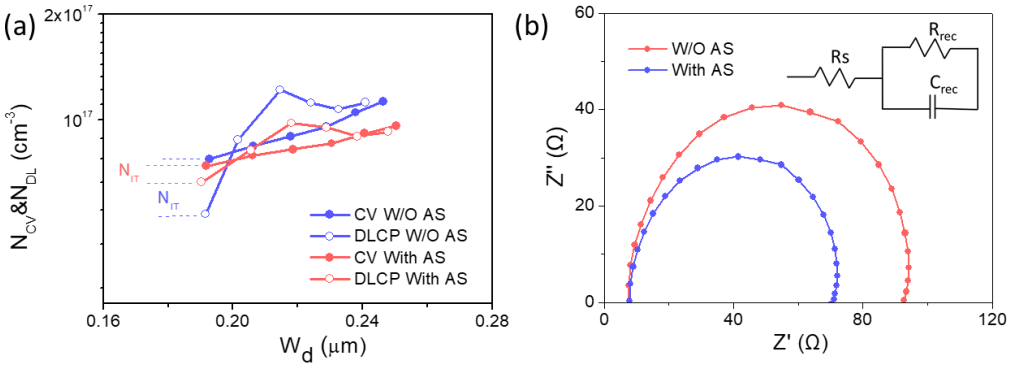

Figure 3-21 *(a) The plot of CV and DLCP for devices W/O AS and With AS, (b) The EIS curves for the W/O AS and With AS devices, inset shows the equivalent circuit diagram.*

CV and DLCP are often used to analyze carrier concentration and depletion width in thin film solar cells. The formulas for the calculations are as follows:[33]

$$N_{CV} = \frac{C^3}{qA^2\varepsilon_0\varepsilon}\left(\frac{dC}{dV}\right)^{-1} \qquad (3\text{-}8)$$

$$W_{d-CV} = \frac{\varepsilon_0 \varepsilon A}{C} \quad (3\text{-}9)$$

$$N_{DL} = -\frac{C_0^3}{2q\varepsilon_0 \varepsilon A^2 C_1} \quad (3\text{-}10)$$

$$W_{d-DL} = \frac{\varepsilon_0 \varepsilon A}{C_0} \quad (3\text{-}11)$$

Where ε and ε_0 stand for the dielectric constant of the CZTSSe and vacuum dielectric constant, respectively; C, A and q is the measured capacitance, the active area of the cell, and elementary charge, C_0 a capacitance and C_1 a coefficient which are used to fit parameters derived from the DLCP. Besides, The CV measurement is more sensitive to the interface state (N_{IT}) than the DLCP, so the interface state density can be obtained from the difference between the CV and the DLCP:

$$N_{IT}=N_{CV}-N_{DL} \quad (3\text{-}12)$$

The carrier density (N_{CV} amd N_{DL}) and the width of depletion region (W_d) derived from the DLCP data are shown in **Table 3-3**. The W_d is similar for both samples, but that the carrier density (zero bias) is larger for the With AS device. The carrier density of With AS device increases from 5.40×10^{16} to 6.66×10^{16} cm^3, which is attributed to the transformation of the dominant defect from V_{Se} to Cu_{Zn}. In general, DLCP only includes bulk defects, the CV also includes interface defects.[34] Therefore, the interface defect density (N_{IT}) can be obtained by comparing N_{CV}-N_{DLCP}. The N_{IT} value estimated for the W/O AS and With AS device was 3.34×10^{16} and 4.70×10^{15} cm^3, respectively. The interface defects were reduced by an order of magnitude after the sulfurization treatment. Such a considerable decrease in N_{IT} strongly confirms the superiority of the heterojunction interface of the With AS devices, which reduces the carrier recombination of the heterojunction and accelerates the carrier transport at the interface.

Table 3-3 *Calculated results of CV, DLCP, EIS and TPV analysis.*

	N_{CV} (cm^{-3})	N_{DL} (cm^{-3})	W_d (μm)	N_{IT} (cm^3)	R_{rec} (Ω)	R_s* (Ω)	C_{rec} (nF)	τ (μs)	τ_{TPV} (μs)
W/O AS	8.74×10^{16}	5.40×10^{16}	0.191	3.34×10^{16}	30.36	25.14	19.43	0.59	10.38
With AS	7.13×10^{16}	6.66×10^{16}	0.190	4.70×10^{15}	46.85	71.33	49.73	2.33	12.89

The carrier transport characteristics of the devices were analyzed by EIS at V=0.5V in the dark, and the correlation curves and fitting results are displayed in Figure 3-21b and Table 3. The inset of Figure 3-21b shows the equivalent circuit diagram of the CZTSSe solar cell, and the EIS curves were fitted to obtain the series resistance (R_s*), recombination resistance (R_{rec}), and chemical capacitance (C_{rec}). EIS can be used to determine minority carrier (electron) recombination to characterize carrier transport behavior. The EIS data were fitted using an equivalent circuit model, which consists of a chemical capacitor (C_{rec}) connected by a shunt composite resistor (R_{rec}) and a series resistor (R_s*), and the measured carrier lifetimes corresponded to the carrier transport behavior within the absorber layer close to the CdS/CZTSSe interface. According to the diffusion-recombination model, the minority carrier lifetime can be calculated according to the following equation:[35]

$$\tau=R_{rec}\times C_{rec} \qquad (3\text{-}13)$$

The minority carrier lifetimes are respectively 0.59 and 2.33 ns for the W/O-AS and With-AS devices, indicating that the sulfurization treatment significantly improves the carrier transport dynamics of the devices.

To further evaluate the carrier lifetime in fully working devices, the W/O AS and With AS device were tested by measuring the Transient Photovoltage (TPV), where

photocarriers are generated under pulsed light irradiation, free electrons and holes are produced and a photovoltage is generated. Once the incident light is switched off, the voltage starts to decay due to transient non-radiative recombination of electrons and holes at possible defect locations.[36] **Figure 3-22** shows the TPV results for the W/O AS and the With AS device. Based on the results of the single-exponential model fitting, it is found that the TPV lifetime (τ_{TPV}) of the With AS device increases from 10.38 μs to 12.89 μs. The longer decay time provides more opportunity for carriers to be extracted from the absorber to the electrodes, which greatly reduces the carrier recombination. We know that a relatively long decay time means fewer non-radiative recombination sites in the intact device. Therefore, the AS sulfurization treatment reduces the defects in the CZTSSe, which reduces the recombination of free carriers and facilitates carrier collection and cell performance.

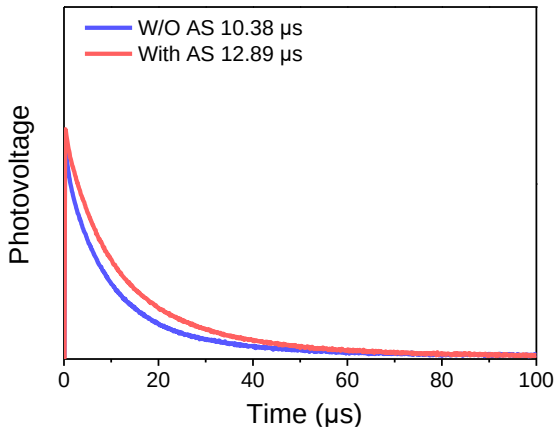

Figure 3-22 *TPV spectra of the W/O AS and With AS device,*

The improvement in charge transport induced by sulfurization-enhanced carrier collection and separation at grain boundary may be the direct cause of the enhanced electrical property of the devices. Electron-beam-induced current (EBIC) can help us to further investigate the transport of electrons across grain boundary at microscopic

level. The SEM cross-section, EBIC mapping is shown in **Figure 3-23** a, b. Figure 3-23c shows the normalized EBIC signals of the W/O AS and With AS device along the grey dashed line. Bright regions in the EBIC image imply high carrier collection efficiency, and the depths represent minority carrier diffusion lengths.[37] Near the CdS/CZTSSe interface, both samples show strong carrier collection, and the reason for the strong EBIC signal near the interface is the strong electric field in the region. It indicates high carrier collection efficiency near the heterojunction. The EBIC signal is significantly weaker away from the p-n junction, which was limited by the possible presence of significant recombination and/or carrier transport barriers. Compared to W/O AS device. With AS device have stronger EBIC signal at the heterojunction interface (Figure 3-23d, non-normalized EBIC line scan), implying that the With AS device has stronger built-in electric field, as reflected in the KPFM data. Meanwhile, the EBIC signal of the With-AS device decreases more slowly and has higher intensity near the back interface (Figure 3-23c, normalized EBIC line scan), indicating that the AS sulfurization treatment effectively improves the carrier collection capability, the carrier diffusion length is extended and the charge collection process is improved.

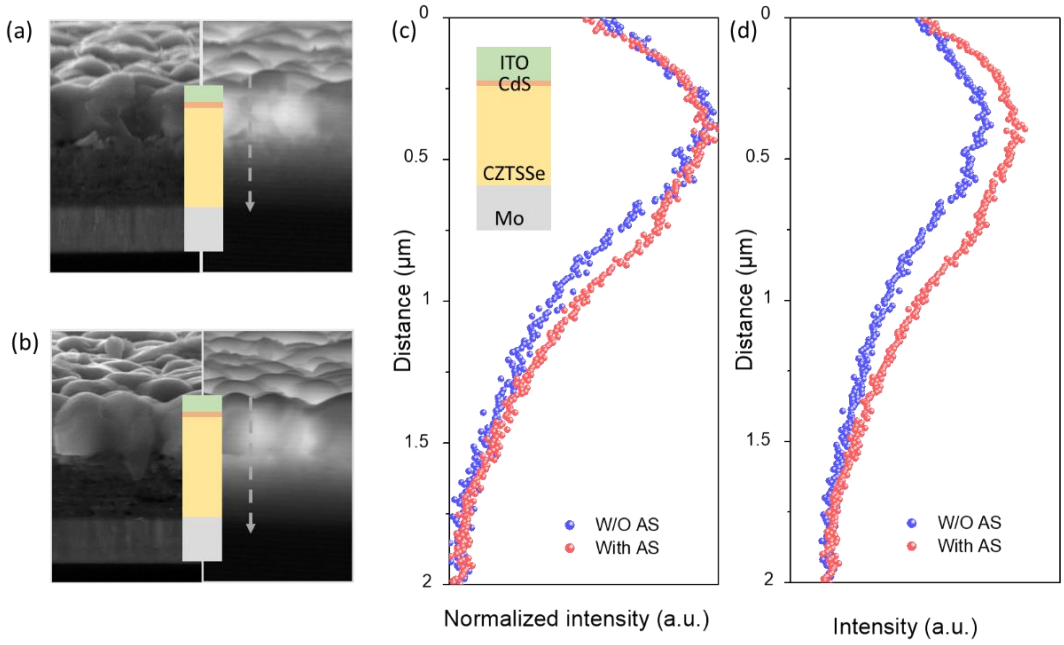

Figure 3-23 *Cross-sectional SEM and EBIC images for (a) W/O AS device and (b) With AS device, (c) the intensity profiling of the dashed line in EBIC images, (d) W/O AS and With AS device non-normalized EBIC signal line scanning.*

3.9 Conclusions

This chapter proposes, for the first time, a simple and effective method to simultaneously treat the surface and the bulk of CZTSSe device by a pre-soaking and spin-coating-annealing sulfurization. The best CZTSSe device based on the optimal AS solution sulfurization treatment duration has a PCE of 13.19%. This strategy adds an annealing step to the surface sulfurization process, which promotes elemental diffusion and passivates surface and bulk defects of CZTSSe devices. The removal of secondary phase from the absorber surface facilitates better p-n junction quality and reduces interface carrier recombination. Further study shows that the band bending at grain boundary of the treated samples is larger, which is more favorable for the carrier

separation and collection. The conversion of the dominant deep energy level defect from V_{Se} to Cu_{Zn} reduces the recombination of free carriers. Stronger EBIC signals and slower decay rates indicate that the AS sulfurization treatment effectively improves the carrier collection, extends the carrier diffusion length and improves the charge collection process. This work provides a new idea and easy-to-handle method for removing the bulk defects and the secondary phase on the absorber layer surface.

REFERENCES

[1] Zhou J., Xu X., Wu H., Wang J., Lou L., Yin K., Gong Y., Shi J., Luo Y., Li D., Xin H., Meng Q., Control of the phase evolution of kesterite by tuning of the selenium partial pressure for solar cells with 13.8% certified efficiency. *Nat. Energy*, **2023**, 8, 526.

[2] Green M. A., Dunlop E. D., Yoshita M., Kopidakis N., Bothe K., Siefer G., Hao X., Solar cell efficiency tables (version 62). *Prog. Photovolt: Res. Appl.*, **2023**, 31, 651.

[3] Lou L., Gong Y., Zhou J., Wang J., Xu X., Yin K., Duan B., Wu H., Shi J., Luo Y., Li D., Xin H., Meng Q., A feasible and effective solution-processed PCBM electron extraction layer enabling the high V_{OC} and efficient $Cu_2ZnSn(S, Se)_4$ devices. *J. Energy Chem.*, **2022**, 70, 154.

[4] Chen S., Walsh A., Gong X. G., Wei S. H., Classification of lattice defects in the kesterite Cu_2ZnSnS_4 and $Cu_2ZnSnSe_4$ earth-abundant solar cell absorbers. *Adv. Mater.*, **2013**, 25, 1522.

[5] Buffière M., Mel A.-A. E., Lenaers N., Brammertz G., Zaghi A. E., Meuris M., Poortmans J., Surface Cleaning and Passivation Using $(NH_4)_2S$ Treatment for $Cu(In,Ga)Se_2$ Solar Cells: A Safe Alternative to KCN. *Adv. Energy Mater.*, **2015**, 5, 1401689.

[6] Xie H., Sanchez Y., Lopez-Marino S., Espindola-Rodriguez M., Neuschitzer M., Sylla D., Fairbrother A., Izquierdo-Roca V., Perez-Rodriguez A., Saucedo E., Impact of Sn(S,Se) secondary phases in $Cu_2ZnSn(S,Se)_4$ solar cells: a chemical route for their selective removal and absorber surface passivation. *ACS Appl. Mater. Interfaces*, **2014**, 6, 12744.

[7] Buffiere M., Brammertz G., Sahayaraj S., Batuk M., Khelifi S., Mangin D., El Mel A. A., Arzel L., Hadermann J., Meuris M., Poortmans J., KCN Chemical Etch for Interface Engineering in $Cu_2ZnSnSe_4$ Solar Cells. *ACS Appl. Mater. Interfaces*, **2015**, 7, 14690.

[8] Gong Y., Qiu R., Niu C., Fu J., Jedlicka E., Giridharagopal R., Zhu Q., Zhou Y., Yan W., Yu S., Jiang J., Wu S., Ginger D. S., Huang W., Xin H., Ag incorporation with controlled grain growth enables 12.5% efficient kesterite solar cell with open circuit voltage reached 64.2% shockley–queisser limit. *Adv. Funct. Mater.*, **2021**, 31, 2101927.

[9] He M., Huang J., Li J., Jang J. S., Suryawanshi U. P., Yan C., Sun K., Cong J., Zhang Y., Kampwerth H., Suryawanshi M. P., Kim J., Green M. A., Hao X., Systematic efficiency improvement for $Cu_2ZnSn(S,Se)_4$ solar cells by double cation incorporation with Cd and Ge. *Adv. Funct. Mater.*, **2021**, 31, 2104528.

[10] Yuan S., Wang X., Zhao Y., Chang Q., Xu Z., Kong J., Wu S., Solution Processed $Cu(In,Ga)(S,Se)_2$ Solar Cells with 15.25% Efficiency by Surface Sulfurization. *ACS Appl. Energy Mater.*, **2020**, 3, 6785.

[11] Liu W. C., Guo B. L., Wu X. S., Zhang F. M., Mak C. L., Wong K. H., Facile hydrothermal synthesis of hydrotropic Cu_2ZnSnS_4 nanocrystal quantum dots: band-gap engineering and phonon confinement effect. *J. Mater. Chem. A*, **2013**, 1, 3182.

[12] Yu L., Dong X., Yang F., Sun X., Chen J., Zhang X., Zhao Y., Li Y., $(NH_4)_2S$-induced improvement of interfacial wettability for high-quality heterojunctions to boost the chloride-assembled CZTSSe solar cells. *J. Chem. Phys.*, **2022**, 157, 134706.

[13] Zhong J., Xia Z., Luo M., Zhao J., Chen J., Wang L., Liu X., Xue D. J., Cheng Y. B., Song H., Tang J., Sulfurization induced surface constitution and its correlation to the performance of solution-processed $Cu_2ZnSn(S,Se)_4$ solar cells. *Scientific reports*, **2014**, 4, 6288.

[14] Taskesen T., Pareek D., Hauschild D., Haertel A., Weinhardt L., Yang W., Pfeiffelmann T., Nowak D., Heske C., Gutay L., Steep sulfur gradient in CZTSSe solar cells by H_2S-assisted rapid surface sulfurization. *RSC Adv.*, **2021**, 11, 12687.

[15] Wang K.-C., Hsu H.-R., Chen H.-S., Study of surface sulfurization of $Cu_2ZnSn(S, Se)_4$ thin film solar cell by sequential H_2Se-selenization/H_2S-sulfurization. *Sol. Energy Mater. Sol. Cells*, **2017**, 163, 31.

[16] Deng Y., Zhou Z., Zhang X., Cao L., Zhou W., Kou D., Qi Y., Yuan S., Zheng Z., Wu S., Adjusting the Sn_{Zn} defects in $Cu_2ZnSn(S,Se)_4$ absorber layer via Ge^{4+} implanting for efficient kesterite solar cells. *J. Energy Chem.*, **2021**, 61, 1.

[17] Danilson M., Altosaar M., Kauk M., Katerski A., Krustok J., Raudoja J., XPS study of CZTSSe monograin powders. *Thin Solid Films*, **2011**, 519, 7407.

[18] Yu Z., Li C., Chen S., Zheng Z., Fan P., Li Y., Tan M., Yan C., Zhang X., Su Z., Liang G., Unveiling the Selenization Reaction Mechanisms in Ambient Air-Processed Highly Efficient Kesterite Solar Cells. *Adv. Energy Mater.*, **2023**, 13, 2300521.

[19] Kim M., Park G. D., Kang Y. C., Investigation of the potassium-ion storage mechanism of nickel selenide materials and rational design of nickel selenide-C yolk-shell structure for enhancing electrochemical properties. *Int. J. Energy Res.*, **2021**, 46, 5800.

[20] Zhao Y., Yuan S., Kou D., Zhou Z., Wang X., Xiao H., Deng Y., Cui C., Chang Q., Wu S., High efficiency CIGS solar cells by bulk defect passivation through Ag substituting strategy. *ACS Appl. Mater. Interfaces*, **2020**, 12, 12717.

[21] Duan H.-S., Yang W., Bob B., Hsu C.-J., Lei B., Yang Y., The role of sulfur in solution-processed $Cu_2ZnSn(S,Se)_4$ and its Effect on defect properties. *Adv. Funct. Mater.*, **2013**, 23, 1466.

[22] Tang R., Chen S., Zheng Z. H., Su Z. H., Luo J. T., Fan P., Zhang X. H., Tang J., Liang G. X., Heterojunction Annealing Enabling Record Open-Circuit Voltage in Antimony Triselenide Solar Cells. *Adv. Mater.*, **2022**, 34, e2109078.

[23] Haass S. G., Diethelm M., Werner M., Bissig B., Romanyuk Y. E., Tiwari A. N., 11.2% Efficient Solution Processed Kesterite Solar Cell with a Low Voltage Deficit. *Adv. Energy Mater.*, **2015**, 5, 1500712.

[24] Wu T., Hu J., Chen S., Zheng Z., Cathelinaud M., Ma H., Su Z., Fan P., Zhang X., Liang G., Energy Band Alignment by Solution-Processed Aluminum Doping Strategy toward Record Efficiency in Pulsed Laser-Deposited Kesterite Thin-Film Solar Cell. *ACS Appl. Mater. Interfaces*, **2023**,

[25] Zhou J., Xu X., Duan B., Wu H., Shi J., Luo Y., Li D., Meng Q., Regulating crystal growth via organic lithium salt additive for efficient kesterite solar cells. *Nano Energy*, **2021**, 89, 106405.

[26] Cao Q., Gunawan O., Copel M., Reuter K. B., Chey S. J., Deline V. R., Mitzi D. B., Defects in Cu(In,Ga)Se_2 Chalcopyrite Semiconductors: A Comparative Study of Material Properties, Defect States, and Photovoltaic Performance. *Adv. Energy Mate.*, **2011**, 1, 845.

[27] Tang R., Zheng Z.-H., Su Z.-H., Li X.-J., Wei Y.-D., Zhang X.-H., Fu Y.-Q., Luo J.-T., Fan P., Liang G.-X., Highly efficient and stable planar heterojunction solar cell based on sputtered and post-selenized Sb_2Se_3 thin film. *Nano Energy*, **2019**, 64, 103929.

[28] Luo Y.-D., Tang R., Chen S., Hu J.-G., Liu Y.-K., Li Y.-F., Liu X.-S., Zheng Z.-H., Su Z.-H., Ma X.-F., Fan P., Zhang X.-H., Ma H.-L., Chen Z.-G., Liang G.-X., An effective combination reaction involved with sputtered and selenized Sb precursors for efficient Sb2Se3 thin film solar cells. *Chem. Eng. J.*, **2020**, 393, 124599.

[29] Siebentritt S., Avancini E., Bär M., Bombsch J., Bourgeois E., Buecheler S., Carron R., Castro C., Duguay S., Félix R., Handick E., Hariskos D., Havu V., Jackson P., Komsa H. P., Kunze T., Malitckaya M., Menozzi R., Nesladek M., Nicoara N., Puska M., Raghuwanshi M., Pareige P., Sadewasser S., Sozzi G., Tiwari A. N., Ueda S., Vilalta-Clemente A., Weiss T. P., Werner F., Wilks R. G., Witte W., Wolter M. H., Heavy Alkali Treatment of Cu(In,Ga)Se_2 Solar Cells: Surface versus Bulk Effects. *Adv. Energy Mater.*, **2020**, 10, 1903752.

[30] Williams B. L., Smit S., Kniknie B. J., Bakker K. J., Keuning W., Kessels W. M. M., Schropp R. E. I., Creatore M., Identifying parasitic current pathways in CIGS solar cells by modelling dark J-V response. *Prog. Photovoltaics*, **2015**, 23, 1516.

[31] Park G. S., Chu V. B., Kim B. W., Kim D. W., Oh H. S., Hwang Y. J., Min B. K., Achieving 14.4% Alcohol-Based Solution-Processed Cu(In,Ga)(S,Se)2 Thin Film Solar Cell through Interface Engineering. *ACS Appl. Mater. Interfaces*, **2018**, 10, 9894.

[32] Zhao Y., Yuan S., Chang Q., Zhou Z., Kou D., Zhou W., Qi Y., Wu S., Controllable Formation of Ordered Vacancy Compound for High Efficiency Solution Processed Cu(In,Ga)Se_2 Solar Cells. *Adv. Funct. Mater.*, **2020**, 31, 2007928.

[33] Jennifer T. Heath, J. David Cohen, William N. Shafarman; Bulk and metastable defects in $CuIn_{1-x}Ga_xSe_2$ thin films using drive-level capacitance profiling. *J. Appl. Phys*. **2004**; 95, 1000.

[34] Chen X.-Y., Ishaq M., Ahmad N., Tang R., Zheng Z.-H., Hu J.-G., Su Z.-H., Fan P., Liang G.-X., Chen S., Ag, Ti dual-cation substitution in $Cu_2ZnSn(S,Se)_4$ induced growth promotion and defect suppression for high-efficiency solar cells. *J. Mater. Chem. A*, **2022**, 10, 22791.

[35] Lin Y.-R., Tunuguntla V., Wei S.-Y., Chen W.-C., Wong D., Lai C.-H., Liu L.-K., Chen L.-C., Chen K.-H., Bifacial sodium-incorporated treatments: Tailoring deep traps and enhancing carrier transport properties in Cu_2ZnSnS_4 solar cells. *Nano Energy*, **2015**, 16, 438.

[36] Wang W., Winkler M. T., Gunawan O., Gokmen T., Todorov T. K., Zhu Y., Mitzi D. B., Device characteristics of CZTSSe thin-film solar cells with 12.6% efficiency. *Adv. Energy Mater.*, **2014**, 4, 1301465.

[37] Zhao X., Chang X., Kou D., Zhou W., Zhou Z., Tian Q., Yuan S., Qi Y., Wu S., Lithium-assisted synergistic engineering of charge transport both in GBs and GI for Ag-substituted $Cu_2ZnSn(S,Se)_4$ solar cells. *J. Energy Chem.*, **2020**, 50, 9.

Chapter IV: Double gradient band-gap absorber for high efficiency CZTSSe solar cells

4.1 Introduction

Since CZTSSe and CIGS have similar crystal structures and the same device structure, the mature technology and optimization strategies of CIGS are worthy of reference. Reviewing the development history of CIGS, the rapid improvement of CIGS efficiency can be attributed to three strategies: (1) Replacing partially In with similar Ga. The introduction of Ga facilitates the increase of the V_{OC} due to the fact that the E_g is proportional to the V_{OC}.[1, 2] Researchers have tried adding Ga to CZTSSe and found that it reduced defects, increased minority carrier lifetime and improved the electrical property of CZTSSe.[3] (2) Alkali post-deposition treatment. Light alkali metals (Li, Na) tend to enter the grains and heavy alkali metals (Rb, Cs) are often distributed at the grain boundaries. For CZTSSe, the performance enhancement due to alkali metal incorporation is usually attributed to better crystallinity, the reduced grain boundary recombination and the increased P-type doping.[4, 5] (3) Double gradient band-gap absorber. In the preparation of the CIGS absorber, the evaporation rate of different elements in the co-evaporation process can be finely regulated to obtain double gradient band-gap from the Mo electrode to the heterojunction, where the band-gap first decreases and then increases, which is called "V-shape double gradient band-gap structure".[6]

The shrinking band-gap (E_g) from the back electrode to the absorber forms a back surface field (BSF), assisting electron transport to the p-n junction. It diminishes the probability of recombination of carriers at Mo electrode and boosts the short-circuit current density (J_{SC}). The minimum value of E_g (the notch) in the middle of the absorber can ensure the light absorption of CIGS and promote the J_{SC}. The gradually increasing E_g from the notch to the p-n junction can ensure a large E_g value at the heterojunction

interface, so as to obtain high V_{OC}.[7] This double gradient band-gap structure enables the absorber to obtain both good electron transport characteristics and high V_{OC}, which results in a significant increase in CIGS device efficiency and is instructive for CZTSSe. Besides, it has been shown that the appropriate notch location and depth are crucial for efficiency improvement. A large front gradient (the gradient band-gap structure from the notch position to the CdS front interface) forms an electron barrier, and the electrons generated inside the notch and deep in the absorber do not have enough thermal energy to overcome this barrier, resulting in carrier recombination that reduces V_{OC} and FF.[8]

Till now, the most efficient CZTSSe device are obtained by solution method, a rapid high temperature selenization process is required to convert amorphous precursor film into crystalline absorber. This high-temperature selenization process exhibits a rapid element diffusion to obtain a uniform elemental distribution, making it challenging to finely regulate the element flux and to obtain a gradient band-gap structure as in CIGS.[9] At the same time, the fine grain layer caused by residual organic impurity during the process of selenization is an inherent shortcoming of the solution process. Recently, researchers have sightseen the gradient band-gap of CZTSSe, signifying that CZTSSe absorber films with single gradient band-gap (either in the front or back) can be achieved through the selenization-sulfurization process.[10] However, the selenization-sulfurization progress generally requires the simultaneous supply of sulfur and selenium powders, which have different reactivity and therefore can be difficult to control. Some cation doping can change the band-gap to obtain absorber with gradient band-gap structure. For example, Ge doping can yield absorber with a back gradient because Ge tends to accumulate at the bottom of the absorber.[11] Recently, it has been found that Cu^{+} and Cd^{2+} can undergo solid-state ion-exchange reaction by

heterojunction annealing, and the absorber with front gradient can be obtained.[9] These strategies can alleviate the carrier recombination at the front interface or back interface to a certain extent. By preparing a nano-CZTS layer on the surface of the absorber, Du et al. obtained a CZTSSe device with a U-shape gradient band-gap structure with an efficiency of 9.9%;[12] by spin-coating CZTSSe precursor solutions with different Ag contents, Wu et al. obtained V-shape gradient band-gap CZTSSe devices with an efficiency of 11.2%, demonstrating the potential of CZTSSe devices with double gradient band-gap structure.[13] However, these processes are relatively complicated. To be competitive in the photovoltaic market, a simpler process must be found to reduce costs and labor. More importantly, it is vital to develop a controllable formation methodology to control the notch position and the front gradient size to obtain the ideal double gradient band-gap structure. Herein, we assert the development of a non-toxic and facile treatment method, which not only regulate the notch position and the front gradient size to obtain a double gradient band-gap absorber but also improve the grain growth process.

In this chapter the introduction of K_2S at an optimized stage is considered in view to obtain CZTSSe devices with double gradient band-gap.

4.2 Preparation of absorber with double composition gradient

In this paragraph, the influence of K_2S inserted at different positions in the bulk of CZTSSe is considered. The CZTSSe has been prepared as mentioned in chapter II and the K_2S solution was obtained by dissolving K_2S powder in ethanol. Three different K_2S solution concentrations were selected 0.01M, 0.05M and 0.1M, respectively.

The CZTS precursor film was prepared by spin-coating process. This process of Reference sample was repeated ten times to obtain a thickness of about 1.2 μm. K_2S samples were obtained by inserting K_2S layers at different locations in the CZTSSe precursor films: 0L-K_2S samples were obtained by spin-coating the K_2S solution on the Mo substrate followed by 10 layers of CZTS solution. 10L-K_2S samples were obtained by spin coating 10 layers of CZTS solution followed by K_2S solution. 3L-K_2S and 6L-K_2S samples were obtained by inserting K_2S layers after spin-coating 3 and 6 layers of CZTS precursor solution, respectively. The same spin-coating parameters were used for the CTZS film and the K_2S layer. In all cases, the solution was spin-coated with 3000 rpm for 20 s, and the wet film was immediately annealed at 280 °C for 2 min on a hot plate. The prepared films were seleniated in a rapid thermal processing (RTP) furnace as mentioned in chapter II to obtain xL-K_2S CZTSSe absorber.

For devices, the buffer layer CdS and ITO window are deposited respectively on the surface of the xL-K_2S CZTSSe absorber as described in the chapter II and III.

Figure 4-1a illustrates the schematic of the preparation process for both the reference and the K_2S sample. Three different K_2S solution concentrations were selected, the K_2S layer were inserted at different positions in the precursor film, which are described in detail in the experimental section. For the convenience of expression, samples with K_2S layer were abbreviated as xL-K_2S. For example, 3L-K_2S represents inserted K_2S layer between the third and fourth CZTSSe precursor layer.

Different photovoltaic devices, with K_2S at different positions in the absorber have been prepared and characterized. The results are summarized in **Table 4-1**. It can be seen that the best performance is obtained by inserting K_2S layer between the sixth and seventh precursor films (6L-K_2S).

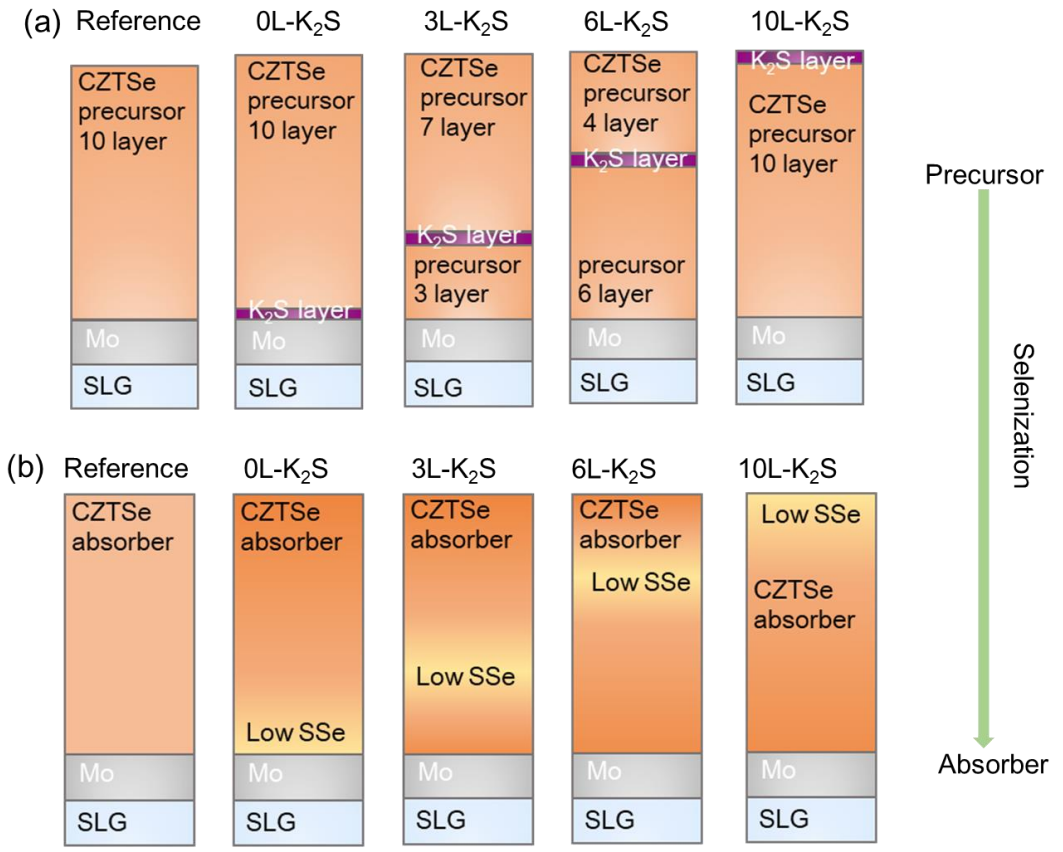

Figure 4-1 *(a) Schematic representation of different samples with K_2S precursor at different positions. (b) Schematic distribution of S/(S+Se) after selenization of different absorbers.*

To investigate the intrinsic reasons affecting the device performance upon inserting K_2S layer at different positions, the elemental distribution profile of samples A-M was analyzed by SEM-EDS. The K_2S layer was found significantly affecting the S distribution as the K_2S layer provides additional S. On the other hand, K combines with Se easily in presence of excess Se atmosphere so that the location of K_2S layer is relatively Se-rich and S-poor (Low S/(S+Se) ratio, as illustrated in Figure 4-1b, the S/(S+Se) is abbreviated as SSe).[14] The SSe profile of sample A-M is shown in Figure 4-2a-c.

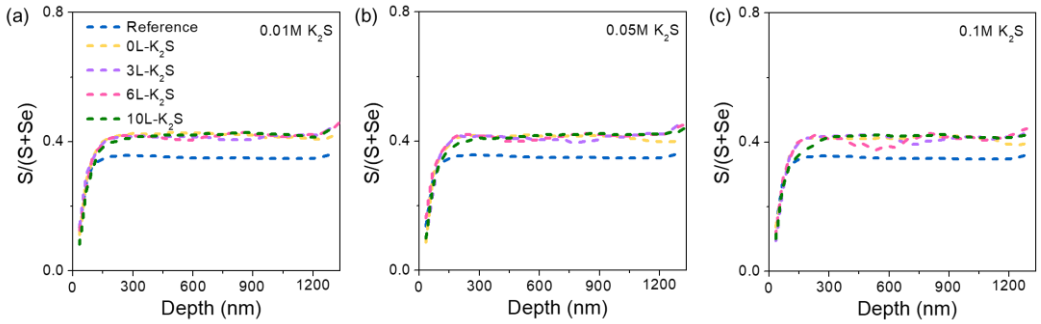

Figure 4-2 *S/(S+Se) atomic concentration depth profiles of the Reference (blue), 0L-K_2S (yellow), 3L-K_2S (violet), 6L-K_2S (pink) and 10L-K_2S (green) films detected by EDS, the concentration of K_2S solution is 0.01 M (a, 0.05 M (b) and 0.1 M (c).*

The front side (left part) of the SSe profile corresponds to the surface of absorber, and the other side corresponds to the interface with Mo. After selenization, all samples showed a decrease in SSe near the position of the K_2S layer. Obviously, higher the concentration of the K_2S solution is, the more obvious decrease in SSe will be. The SSe profile of sample B, F, J (the yellow curves, *0L-K_2S*) obtained by spin-coating the K_2S solution on Mo back electrode are smaller at the back interface compare to sample A; the sample E, I, M (the green curves, 10L-K2S) which obtained by spin-coating K_2S solution on the precursor film surface show earlier depletion of SSe at the front surface. The SSe profile of sample C, G, K (the violet curve, *3L-K_2S*) obtained by inserting K_2S layer between the third and fourth layer of the precursor film and sample D, H, L (the pink curve, *6L-K_2S*) obtained by inserting K_2S layer between the sixth and seventh layer of the precursor film show obvious notch near the position of K_2S layer. In this case (*6L-K_2S*), SSe is higher at the surface and bottom of the absorber and lower in the middle of the absorber, demonstrating a V-shape double gradient distribution of SSe. The double gradient distribution of SSe indicates that the band-gap of absorber is

double gradient structure. The EDS analysis demonstrated that the change of the SSe gradient profile of the absorber is the result of the varying K_2S solution concentration and spin coating position. With the upward shift of the K_2S spin-coating position, the notch is brought closer to the surface; higher K_2S solution concentration led to an increased degree of localized S poor, corresponding to more obvious SSe notch. Thus, the shape of double gradient band-gap and notch depth can be controlled simply by changing the position of K_2S layer and the concentration of K_2S solution. This modification is attributed to the adjustment of elemental distribution of Se and S in the absorber by K_2S layer. Since the reaction of Se with K is prioritized compared to that of S with K during the film growth, the high affinity energy of K-Se can accelerate the selenization and lead to Se rich and S poor locally near the K_2S layer, and thus the SSe profile changes.[15] This reaction sequence results in the front and back side of the film holding high SSe ratio when the K_2S layer is inserted in the middle of the absorber, while the middle of the film has a characteristic notch with low SSe ratio, so that the absorber possesses a composition distribution of double gradient of SSe.

The performance of the CZTSSe solar cells with K_2S layer was all enhanced, benefiting from the gradient composition structure. It can be seen from **Table 4-1** that no matter whether the concentration of K_2S solution is high or low, the device efficiency is higher when the K_2S layer is inserted between the sixth and seventh layer of the precursor film, signifying the formation of double composition gradient, leading to double gardient band-gap structure.

Table 4-1 *The comparison of photovoltaic parameters of cells A-M.*

	REF	**0.01**	**0.01**	**0.01**	**0.01**	**0.05**	**0.05**	**0.05**	**0.05**	**0.1**	**0.1**	**0.1**	**0.1**
Layer	-	0L	3L	6L	10L	0L	3L	6L	10L	0L	3L	6L	10L

Device	A	B	C	D	E	F	G	H	I	J	K	L	M
J_{SC} (mA/cm^2)	35.19	36.43	36.31	36.37	36.44	36.61	36.49	36.73	36.38	36.03	36.65	36.42	36.51
V_{OC} (mV)	0.512	0.519	0.525	0.532	0.511	0.543	0.526	0.544	0.524	0.527	0.523	0.529	0.519
FF (%)	62.27	61.78	64.64	68.30	63.23	63.33	65.40	68.48	64.14	61.67	63.85	65.34	63.53
PCE (%)	11.23	11.68	12.33	13.20	11.76	12.58	12.57	13.70	12.23	11.72	12.24	12.60	12.06

The experimental results demonstrate that increasing the concentration of the K_2S solution from 0.01 to 0.05 M leads to a more pronounced local Se-rich and S-poor region. As a result, the sample H with a deeper SSe notch obtains a device efficiency of 13.70%. However, when the concentration of the solution is increased to 0.1 M, the SSe notch of the corresponding sample L is further deepened and the device efficiency decreases instead. For Cu-based thin-film solar cells, p-n junctions are formed between absorber and buffer layer, leading to valence band and conduction band bending (**Figure 4-3**a).[15]

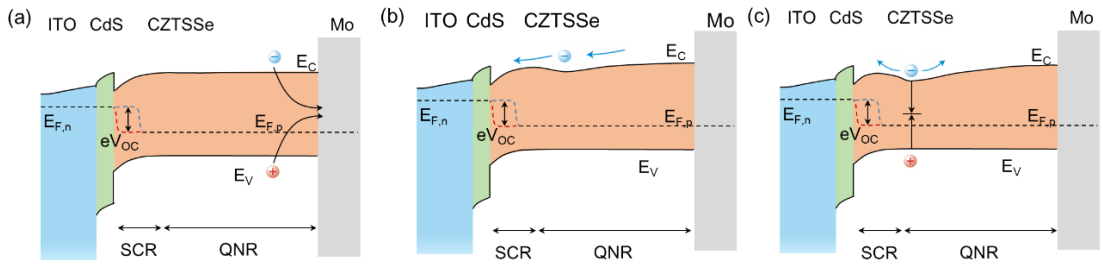

Figure 4-3 *(a) The band diagram of CZTSSe solar cell. (b) Schematic band diagram of an optimized grading profile. (c) Schematic band diagrams of too pronounced grading profile.*

The CZTSSe is divided into majority carrier depletion space charge region (SCR) and

quasi-neutral region (QNR). Incident light is absorbed and generates electron-hole pairs that are separated by the built-in electric field within the SCR. Electrons collection from the CZTSSe absorber is critical for maximizing conversion efficiency. However, the band alignment at the heterojunction interface is often unsatisfactory, and the dynamics of electron diffusion into the ITO shrinks in the QNR near the back interface. As a result, electrons and holes tend to recombine at the front and back interface eventually leading to significant open circuit voltage deficit ($V_{OC\text{-}def}$). The existence of K_2S layer adjusts the S and Se distribution in the absorber resulting in a double gradient band-gap structure (Figure 4-3b): the gradually decreasing E_g from Mo electrode to the notch provided additional back surface field (BSF) to help electron transport to the p-n junction, thus reducing the probability of carriers recombination at back interface; the notch of band-gap can ensure the light absorption of CZTSSe and enhance the J_{SC}; the gradually increasing band-gap from the notch to the front surface ensures a large band-gap value at the p-n junction interface, which results in a high V_{OC}.[16] Therefore, the device performance of sample H is substantially improved. Normally, electrons generated in the SCR can be collected efficiently due to the strong electric field. Yet, the width of SCR is significantly reduced when the solar cell is operating, so that a large front gradient will lead to the existence of an electron barrier.[13] This potential barrier does not significantly affect the device performance at room temperature, since the thermal energy is sufficient for most electrons to overcome it.[17] Nevertheless, it still increases the carrier recombination and reduces the V_{OC} and FF of the device, which is one of the main reasons why sample L is not as good as sample H. This means that excessively pronounced gradient (Figure 4-3c) can lead to a large notch at the conduct band edge (E_C) and become an electronic potential barrier. Electrons generated within the notch and deep in the absorber cannot hold enough thermal energy to overcome this

barrier. Thus the too deep notch becomes a trap for capturing electrons and leads to enhanced recombination with holes in the valence band. Therefore, tuning the appropriate band-gap gradient profile of CZTSSe is essential to reduce the recombination and achieve high efficiency.

In addition, inserting K_2S layer after third layer also exhibited a gradient band-gap, but the inappropriate notch position prevented the transport of photogenerated electrons, thus limiting the PCE **(Figure 4-4**).

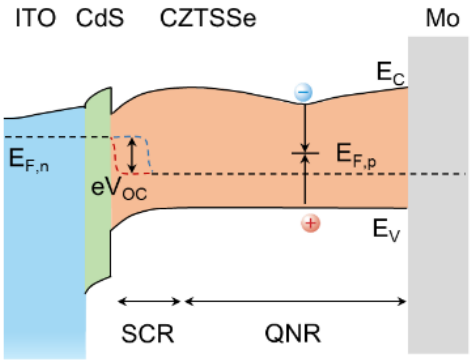

Figure 4-4 *Schematic band diagram of an inappropriate double gradient band-gap with the front gradient starting from the quasi neutral region.*

If the front gradient starts at the edge of the SCR (where the band-gap notch is located), it eliminates the potential barrier at zero bias by forming an electron barrier at positive bias. This affects electron transport and hamper device performance.[8] Conversely, the front gradient originated at QNR (where the band-gap notch is situated) creates an electron transfer barrier at any bias voltage. This significantly reduces electron collection capability, leading to a decline in J_{SC}, *FF*, and overall PCE.[18] For sample C, G and K (*3L-K_2S)*, the band-gap notch is closer to the back interface, suggesting that the notch is located in the QNR, and the presence of the electronic barrier in this case hinders the device efficiency, so that the PCE can only be improved to a certain extent

despite the double gradient band-gap structure.

4.3 Analysis of the optimal double gradient band-gap structure

4.3.1 Characterization by SIMS and XRD

Table 1 confirms that sample H has the highest device efficiency, and the depth profile of S and Se of sample A and sample H were analyzed using secondary ion mass spectrometry (SIMS) with more accuracy. The elemental depth composition curves were obtained by the TOF SIMS 5 secondary ion mass spectrometry (SIMS) workstation (IONTOF GmbH). For the convenience of expression, sample A and sample H (*6L-K_2S with 0.05M)* are abbreviated as REF and K_2S sample onward. As shown in **Figure 4-5a**, the distribution of S for both samples have a similar trend while the K_2S sample has a higher S concentration due to the contribution of K_2S layer. The absorber film is Se-rich at the bottom of REF sample, due to the higher Se content in the fine grain layer. This bottom Se-rich phenomenon is diminished in the K_2S film, where the Se distribution in the K_2S film is more uniform compared to the REF film. The acceleration of selenization is caused by the high chemical affinity between K and Se, therefore the distribution of Se in the absorber is changed.[14] The SSe distribution was extracted from the atomic concentration depth distribution of Figure 4-5a and displayed in Figure 4-5b. The distribution of SSe from CdS interface to the back electrode (Mo) of the REF sample is relatively uniform, signifying a relatively uniform band-gap profile. The SSe profile of the K_2S sample, on the other hand, exhibits a V-shape double gradient distribution trend, lowering first and then ascending, from the CdS interface to the Mo electrode. The band-gap of the CZTSSe absorber is positively

correlated with the SSe ratio, this double gradient SSe profile imply that the K_2S sample has a double gradient band-gap absorber.

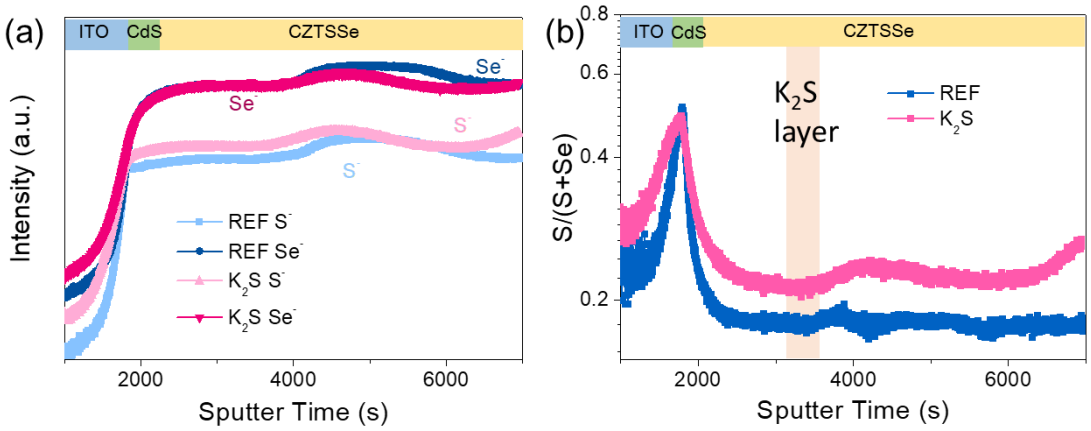

Figure 4-5 *(a) The depth distribution of S and Se in REF and K_2S device detected by SIMS, (b) S/(S+Se) depth profile of the REF and K_2S device along the film depth.*

To investigate the film structure and the band-gap variation at different depths, we etched the REF and K_2S absorber film to different thicknesses, and controlled the thickness of the etched film by controlling the sputtering power and sputtering time (the thickness of the original REF and K_2S absorber is about 1.2 μm).

The step profiler was used to quantify the thickness of the etched samples, which were designated R1-R10 and K1-K10. Each sample's thickness difference for R1-R10 was around 100 nm, and the same is true for K1-K10. The principle of the step profiler is that the probe in direct contact with the sample is deformed by the undulation of the surface, and the sensor transforms this deformation into an electrical signal that is sent to a computer for analysis, and ultimately outputs the change of sample thickness. The instrument is mainly used to test the thickness of thin films, and can also be used for three-dimensional mapping of the undulations of the sample. **Table 4-2** displays the correlation between sample counts and thicknesses.

Table 4-2. *Summary of result REF, R1-R10, K_2S, K1-K10 samples derived from step profiler, XRD.*

Sample	REF/K_2S	R1/K1	R2/K2	R3/K3	R4/K4	R5/K5	R6/K6	R7/K7	R8/K8	R9/K9	R10/K10
Thickness (μm)	1.2	1.1	1.0	0.9	0.8	0.7	0.6	0.5	0.4	0.3	0.2
(112) peak position (2 Theta (degree))	27.38/27.48	-	27.37/27.43	-	-	27.38/27.46	-	27.36/27.47	-	-	27.37/27.48

To investigate the structural depth profile for CZTSSe absorber, REF/K_2S, R2/K2, R5/K5, R7/K7 and R10/K10 films were selected for X-ray diffraction (XRD) (**Figure 4-6**). The essence of XRD is the scattering of electrons by high-frequency electromagnetic waves. As a high-frequency electromagnetic wave, X-rays are extremely penetrating. When it strikes a lattice atom, it is scattered by the electrons outside the nucleus of the atom, and the scattered waves from these periodically arranged atoms interfere with each other, resulting in the intensity of the scattered X-rays being enhanced in certain directions and diminished in other directions. Bragg's law summarizes well the mathematical relationship between the direction of incidence and diffraction of X-rays. Based on the Bragg equation, the lattice spacing can be calculated and thus the ratio of S/Se in CZTSSe. In the field of CZTSSe, XRD can be used to determine the major phases within the precursor and selenide films, and $Sn(S, Se)_x$ and $Cu_x(S, Se)_y$ can also be identified. S/Se can be deduced from the position of

the diffraction peaks of the Kesterite phase CZTSSe(112) in the spectral lines.

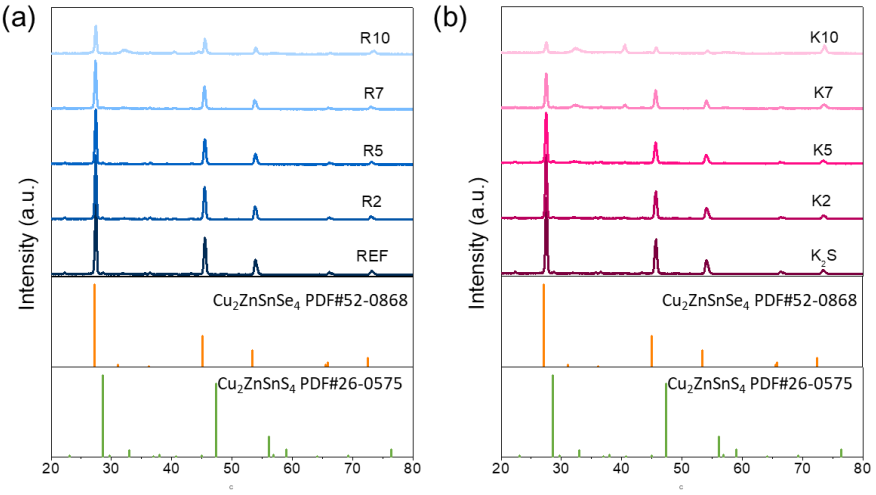

Figure 4-6 *XRD of REF films (a) and K_2S films (b) with different thickness.*

The (112) diffraction peak of all samples were enlarged and shown in **Figure 4-7**a, b and c to observe the changes. Both type of samples showed a similar diffraction pattern, however the (112) diffraction peak position of K_2S samples exhibited a right shift due to the addition S provided by K_2S (Figure 4-7b).

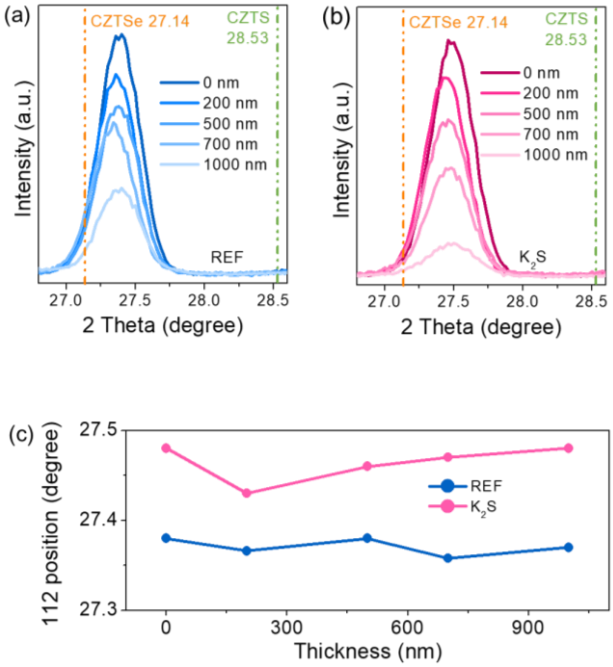

Figure 4-7 *The enlarged view of XRD patterns (112) peak of etched REF (a) and*

K_2S (b) films. (c) The position of (112) crystal plane.

For K_2S samples, the (112) peak position of the un-etched film and K2 film is 27.48 and 27.43, with a left shift. As the etching depth deepens, the (112) peak position of the K5, K7 and K10 films is shifted to larger angle. Initially the left and then the rightward shift of (112) diffraction peak of the etched K_2S samples along the depth indicated a decreasing and then increasing SSe ratio profile. These findings authenticated that the SSe of the surface and bottom of the K_2S sample is higher than that the middle, indicating the formation of SSe gradient upon K_2S layer insertion (Figure 4-7c). These results are consistent with the SEM-EDS and SIMS results.

4.3.2 Characterization by UPS of a double gradient band-gap absorber

The UV photoelectron spectroscopy (UPS) is a common method used to test the positions of valence bands and Fermi energy levels of semiconductor films. When UV photons with energies in the range of 16-41 eV irradiate the sample under test, these photons cause the electrons in the sample to gain enough energy to escape from the surface, this process follows Einstein's law of photoelectricity. During the escape process, the relationship between the kinetic energy of the photoelectrons (E_k) and the energy of the incident photons (hν) and the binding energy of the electrons (E_b) can be expressed as follows: $E_k = h\nu - E_b - \Phi sp$, where Φsp is the escape work of the spectrometer. By measuring the energy of these photoelectrons, information about the energy band structure of the electrons in the sample can be obtained, especially the valence electronic states near the Fermi energy level.

In this part, the measurements by UPS were performed by PHI5000 VersaProbe III with

He I source (21.22 eV) under an applied negative bias of 9 volts. The UPS data for REF, K_2S, and CdS films are illustrated in **Figure 4-8** and **Figure 4-9**a, b, and the calculation shows the conduction band offset (CBO) value at the p-n junction interface (CBO_{REF}=0.563 eV, CBO_{K2S}=0.354 eV). In this case, it is assumed know the band-gap (Eg) obtained by EQE (see below figure 4-14) for REF and K_2S films. The optimal range of CBO is 0-0.4 eV and an electronic barrier is formed when the CBO is greater than 0.4 eV which deteriorates the device efficiency.[19] The reduction of CBO due to the upward shift of the E_C of the K_2S sample favors the improvement of the electron transport at the heterojunction and the reduction of the interface recombination (Figure 4-9c).

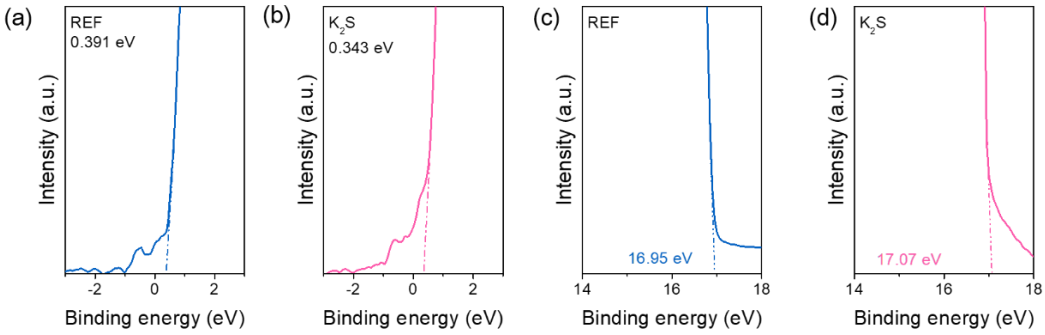

Figure 4-8 *UPS spectra of REF film (a, c) and K_2S film (b, d).*

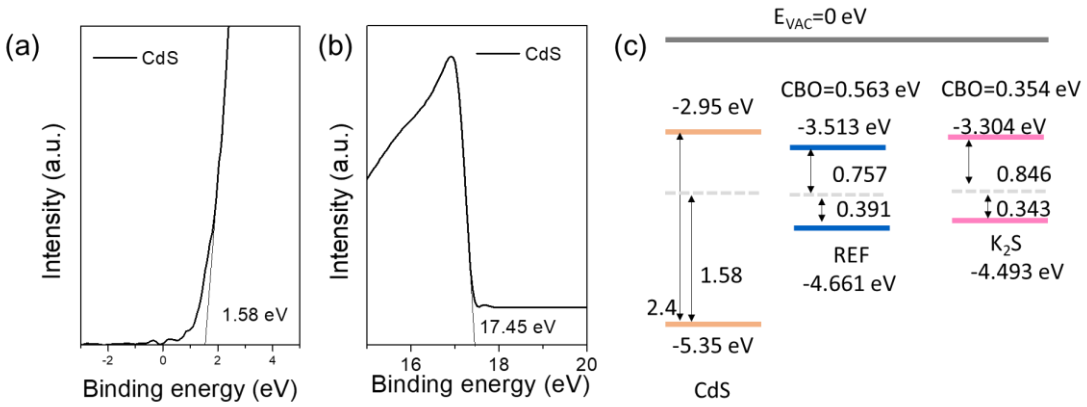

Figure 4-9 *UPS spectra of CdS. (a, b) and (c) herojunction band alignment schematic for REF and K_2S (Eg_{REF}=1.148 eV and Eg_{K2S}=1.189 eV see figure 4-14).*

Both SIMS and XRD data confirm that SSe is higher at the surface and bottom and lower in the middle of K_2S absorber. The shorter Sn-S bond moves the CBM higher by generating stronger repulsion than the Sn-Se bond, so the S/(S+Se)-based double gradient implies that most likely the conduction band has also a double gradient.[20] To verify this conclusion, UPS measurements were performed on the R1-R10 and K1-K10 films to obtain the value of their valence band. The results are shown in **Figure 4-10** and **4-11**.

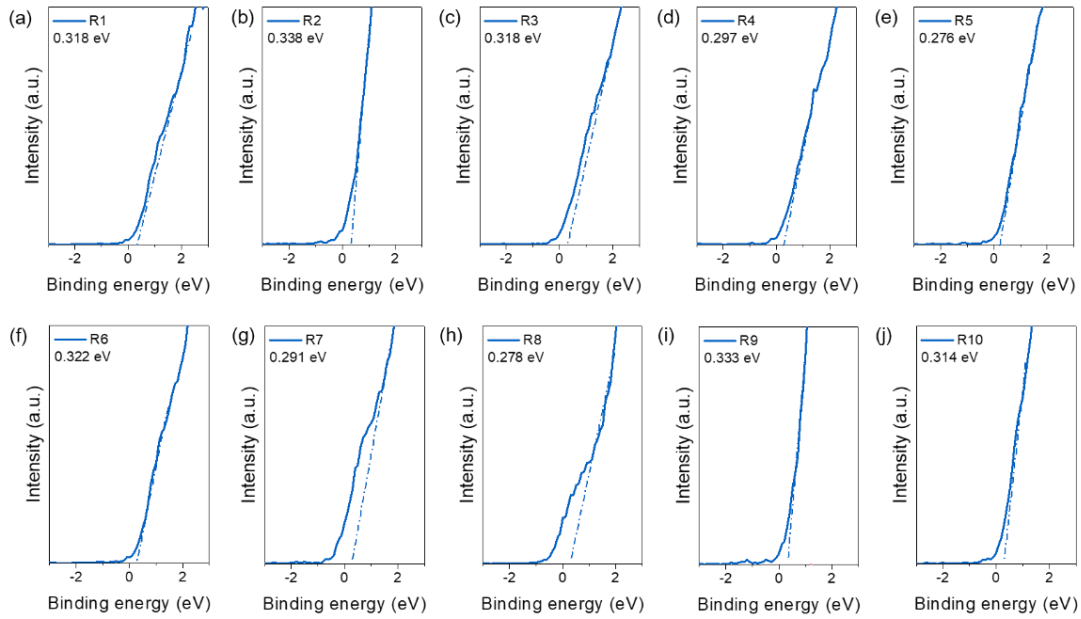

Figure 4-10 *Valence band edge of R1-R10 films tested using UPS.*

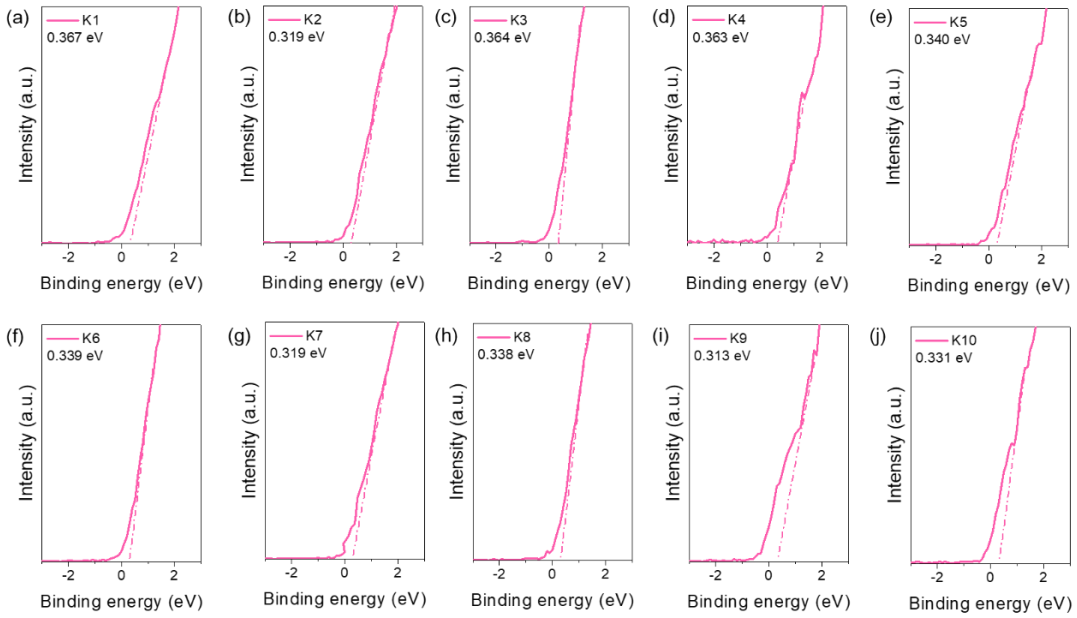

Figure 4-11 *Valence band edge of K1-K10 films tested using UPS.*

4.3.3 Characterizations by EQE

The R1-R10 and K1-K10 films were assembled into solar cells and the EQE were measured to obtain the E_g to show the whole band-gap profiles of the absorber more thoroughly (**Figure 4-12, Figure 4-13**). The external quantum efficiency (EQE) was measured using a Zolix solar cell QE/IPCE measurement system (solar cell Scan 100).

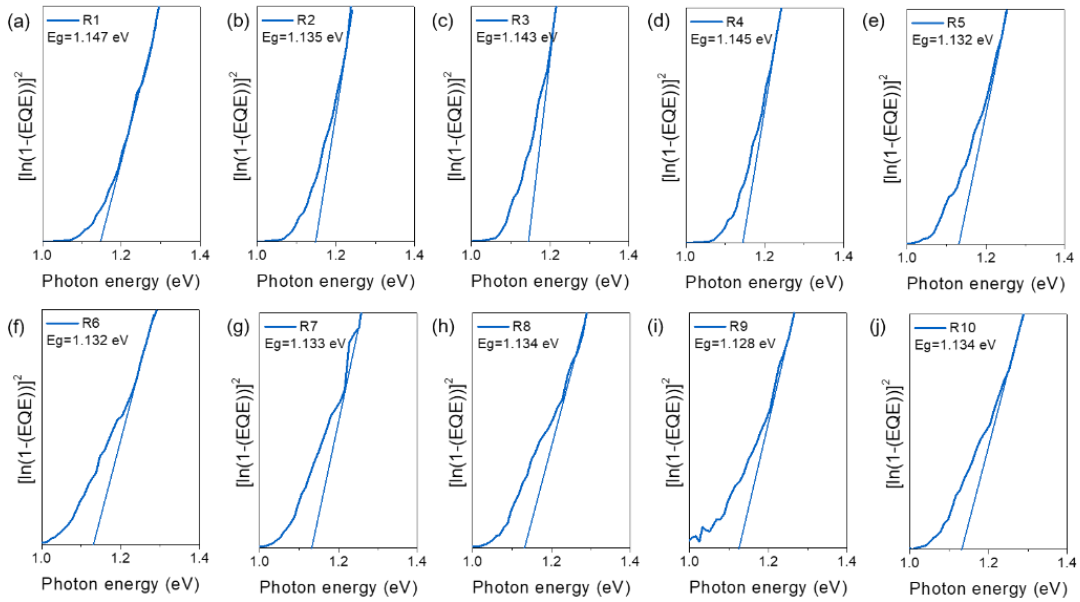

Figure 4-12 *Band-gap of R1-R10 devicesobtained from the measured EQE.*

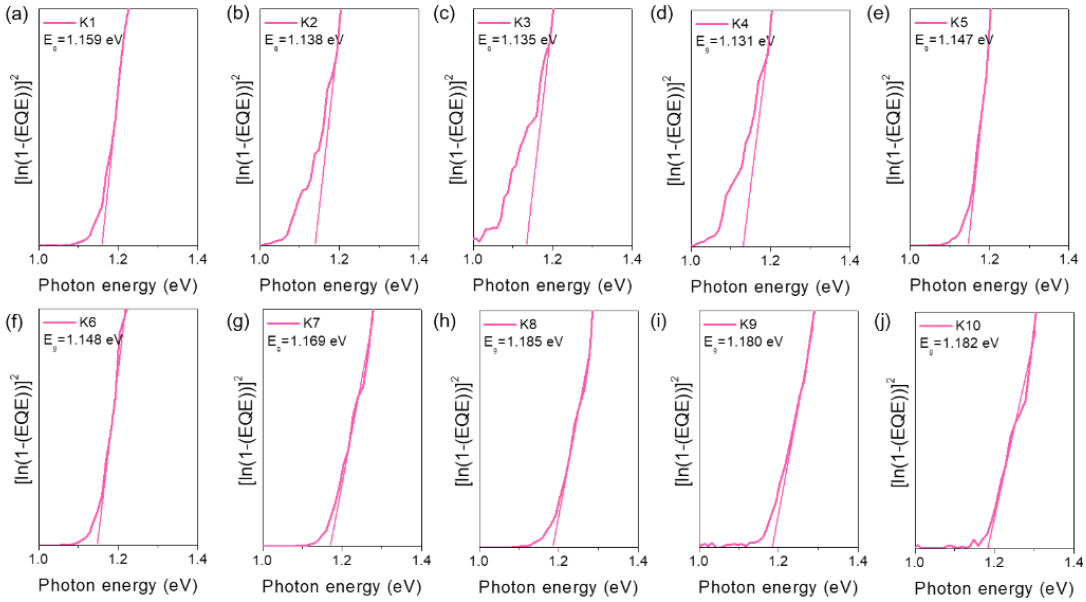

Figure 4-13 *Band-gap of K1-K10 devices tested using EQE.*

Figure 4-14a shows the band-gap of REF and K2S device and Figure 4-14b shows the profile of REF and K_2S sample. The band-gap profiles coincide with the XRD and SIMS results, demonstrating that the band-gap of the REF device does not change significantly and the absorber of the K2S device has a double-gradient band-gap

structure.

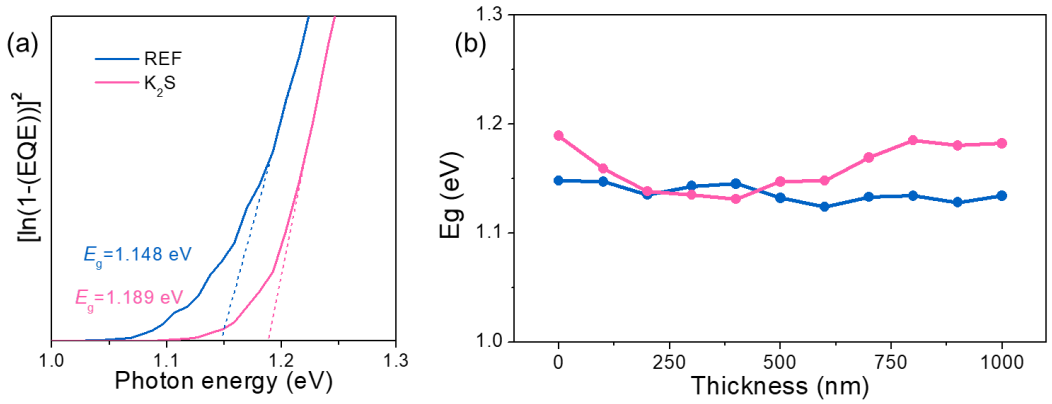

Figure 4-14 *The extraction of band-gap from [(-ln(1-EQE))]^2 versus E plots. (a) In pink the REF sample and in blue the K2S sample. (b) Profile distribution of the band-gap E_g.*

Figure 4-15a and b show the fluctuations of the E_C and E_V of REF and K_2S sample. The band-gaps at different location of REF did not reveal significant fluctuations, which is consistent with the results of the SSe profile in SIMS analysis. In contrast, the band-gap of the K_2S sample initially diminishes as the thickness of the film decreases, with a minimum value near about 200-500 nm from the upper surface of the absorber, and then the E_g of the film increases slightly as the thickness decreases. This result is consistent with the notch in the SSe near CdS interface in the SIMS analysis and also with the variation of the (112) peak position at the crystal plane in the XRD analysis. The band structure diagram illustrates the presence of a double gradient band-gap in the K_2S sample. The varying conduction band in double gradient and then the conduction band gradient near the back interface is able to create an additional electric field to help the free electrons drift toward the front junction. This contributes to the efficient collection of carriers, especially for carrier generated with near-infrared photon

energy.[17] Meanwhile, there is a notch in the conduction band position near the front interface, which improves the absorption of low-energy photons. The conduction band front gradient located within the space charge region helps to reduce the CBO and increase the V_{OC}.

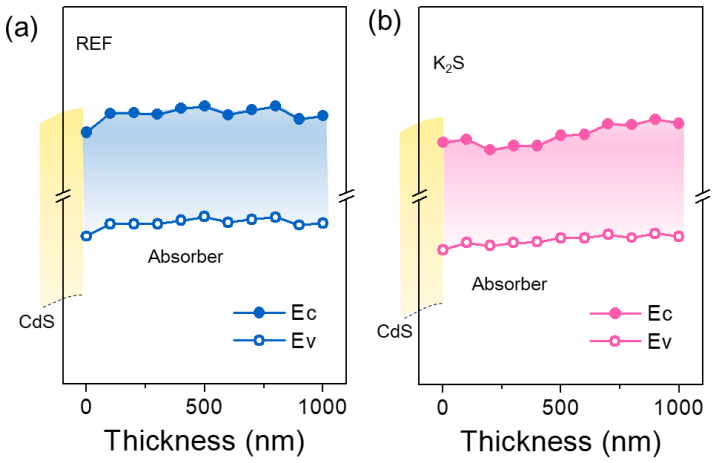

Figure 4-15 *Valence and conduction bands depth profile of the REF (a) and K_2S (b) device along the CZTSSe film depth.*

Figure 4-16a show the comparison of the performance of REF device and K_2S device. It is clear that the EQE response of the K_2S device is significantly increased in the 700-900 nm range compared to the REF sample (Figure 4-16b), implying lower recombination of photogenerated carriers in the K_2S absorber bulk.[21] The K_2S device displays comparatively lower EQE response in the long wavelength range due to the degradation of long wavelength absorption owing to high S content in the absorber.[22] For CZTSSe devices, V_{OC} usually increases with increasing band-gap, which coincides with the higher V_{OC} of K_2S devices.

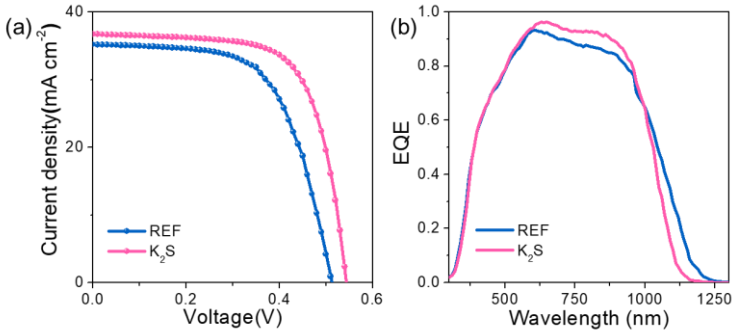

Figure 4-16 *(a) J−V curves of the reference and champion device. (b) EQE curves of reference and champion device.*

The EQE decays exponentially in the long wavelength range, while the Urbach energy (E_U) is one of the parameters describing the extent of the band-tail state that leads to such a decay. Thus, we also analyzed the Urbach energy of both the devices (Figure 4-17a). E_U values reduced from 35.7 meV (REF) to 30.5 meV (K_2S), indicating the decreasing tailing state of the K_2S absorber and reducing the $V_{OC\text{-}def}$. The presence of intrinsic deep defects as recombination centers or band tails contributing to Shockley-Read-Hall recombination limits the useful energy of photogenerated carriers and their transport.[19] Typically for kesterite material, the band-tailed state is caused by two known fundamental mechanisms: a high concentration of deep defects with a high degree of compensation, leading to electrostatic potential fluctuation; or inhomogeneity in the crystalline or composition, leading to band and band-gap fluctuations. The band-gap fluctuation (σ_g) and the electrostatic potential fluctuation (γ_{opt}) can be extracted by redrawing EQE as a function of energy in the long wavelength range according to literature (Figure 4-17b, c).[23] The σ_g were 142 meV for the REF device and 101 meV for K_2S device. The potential fluctuations in polycrystalline CZTSSe materials usually act as potential traps for carriers, which is a key factor limiting the carrier transport/diffusion performance in the devices. The formation of charged defects (for

example [Cu_{Zn}^{-}+Zn_{Cu}^{+}] is the most abundant because it has the lowest formation energy) and the magnitude of the dielectric constant are the main factors that determine the fluctuation of electrostatic potential.[24] The γ_{opt} of the REF and K_2S devices are 34.2 meV and 28.4 meV, respectively, indicating that K_2S devices have fewer defect complexes, which may be related to the reduction of [Cu_{Zn}^{-}+Zn_{Cu}^{+}] due to the substitution of K^+ for Cu^+.

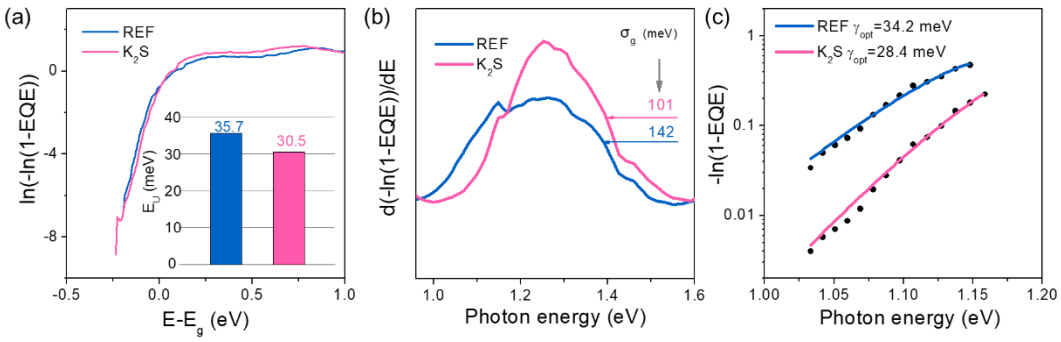

Figure 4-17 *(a) Calculated Urbach energy. (b) The extraction of band-gap fluctuation. (c) The extraction of electrostatic potential fluctuation.*

4.3.4 Other optical characterizations

Firstly, Transient Photovoltage Decay (TPV) measurements were used to investigate the carrier recombination dynamics in CZTSSe devices.[25] The TPV measurement was performed using 355nm pulsed laser (Quantel Brilliant Easy, BRILEZ/IR-10) as the light soure to excite the films and an oscilloscope (Tektronix TDS 3054C, 500MHz) was used to record the voltage signal. As shown in **Figure 4-18**, the transient photovoltage decay lifetime (τ_{TPV}) of the REF device is 3.36×10^{-5} s, whereas the τ_{TPV} of the K_2S device is 8.19×10^{-5} s, indicating significantly suppressed nonradiative charge recombination in the K_2S device.

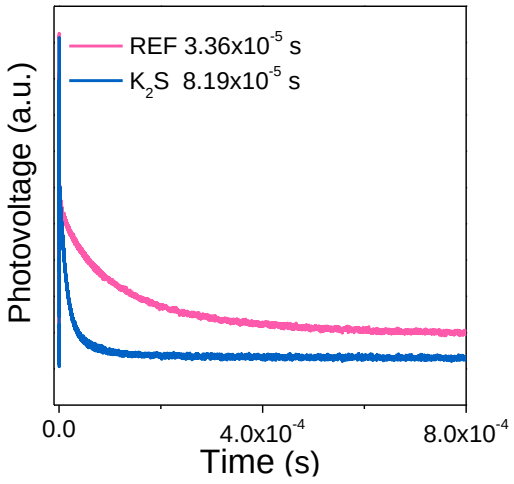

Figure 4-18 *TPV spectra of reference and champion device.*

Secondly, a fluoTime 300 spectrometer with an excitation wavelength of 532 nm was used to measure photoluminescence (PL). The PL spectroscopy is a powerful optical method to characterize solar cells. PL emission of CZTSSe involving tail-state transition usually presents asymmetric PL bands. **Figure 4-19** shows the normalized photoluminescence spectra of REF and K_2S films. The difference between the PL peak and band-gap is large and is mainly due to band tailing caused by γ_{opt}, associated with the V_{OC}-def. The PL peaks are shifted toward lower energy relative to $E_{g,EQE}$ and the value of $E_{g,EQE}$-$E_{g,PL}$ can be used to characterize the energy band fluctuation. **Table 4-3** shows the $E_{g,EQE}$-$E_{g,PL}$ difference for REF and K_2S films. Due to the different band-gap, the difference is 103 meV for the K_2S film, which is smaller than that of the REF film (129 meV). It means that the defects in K_2S film are reduced and the potential fluctuations are minimized, which is beneficial to reduce the V_{OC}-def.[26]

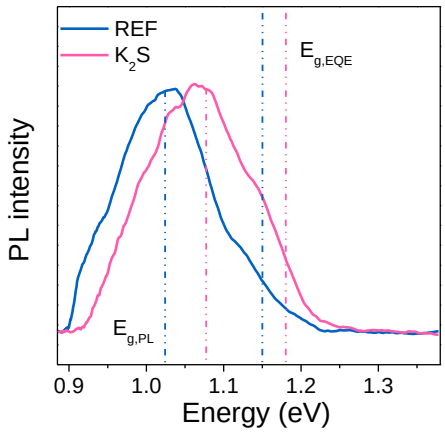

Figure 4-19 *PL spectra of REF film and K_2S film.*

Table 4-3 *Summary of result derived from EQE, PL and TPV.*

	$E_{g,EQE}$ (eV)	E_U (meV)	σ_g (meV)	γ_{opt} (meV)	$E_{g,PL}$ (eV)	$E_{g,EQE}$-$E_{g,PL}$(meV)	σ_{total} (meV)	τ_{TPV} (s)
REF	1.148	35.7	142	34.2	1.019	129	146	3.36×10^{-5}
K_2S	1.189	30.5	101	28.4	1.086	103	104	8.19×10^{-5}

The Gaussian fit to the PL curves of both the main peak (peak 1) and the secondary peaks (peaks 2 and 3) are present in (**Figure 4-20**). According to theoretical calculations, the formation energy of the vacancy V_{Cu} (20-50 meV) and the antisite C u_{Zn} (120-200 meV) are lower than the other acceptor and donor defects which lead to the electrons and holes recombination in the conduction and valence band respectively. Thus, the CZTSSe films also exhibit an inherent p-type conductivity.[24]

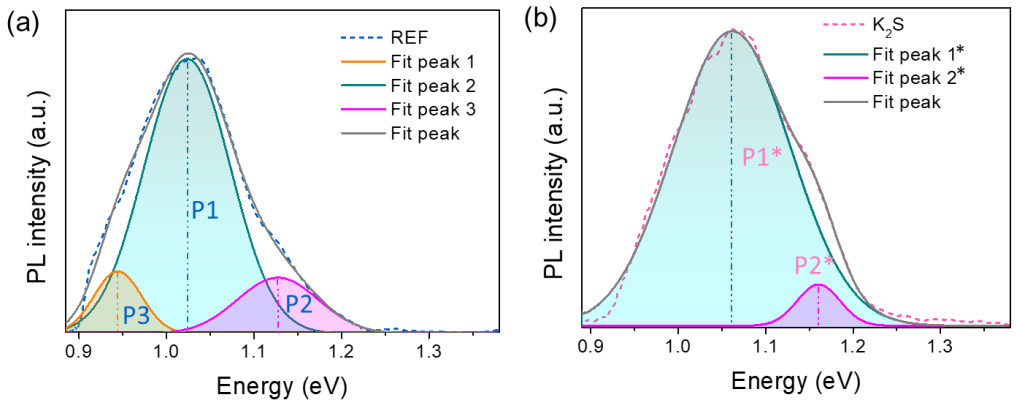

Figure 4-20 *The peak analysis of the PL spectrum of (a) REF film and (c) K_2S film.*

Figure 4-21a and d shows a schematic diagram of the band electron structure. P1 (1.021 eV, REF film) and P1* (1.063 eV, K_2S film) are assigned as FB1 (FB stands for free carrier-band transition), involving the most abundant shallow defect Cu_{Zn} in CZTSSe. P2 (1.127 eV) and P2* (1.159 eV) are again matched with the FB transition, assigned as FB2, involving valence band and V_{Cu} vacancy site defects. This can also be considered as band-band (BB) transitions due to their small difference from the CZTSSe band-gap, indicating recombination of the free electrons in the conduction band with the holes in the E_V.[37] The P3 peak of the REF film (0.944 eV) is assigned as FB3 with respect to V_{Sn}.

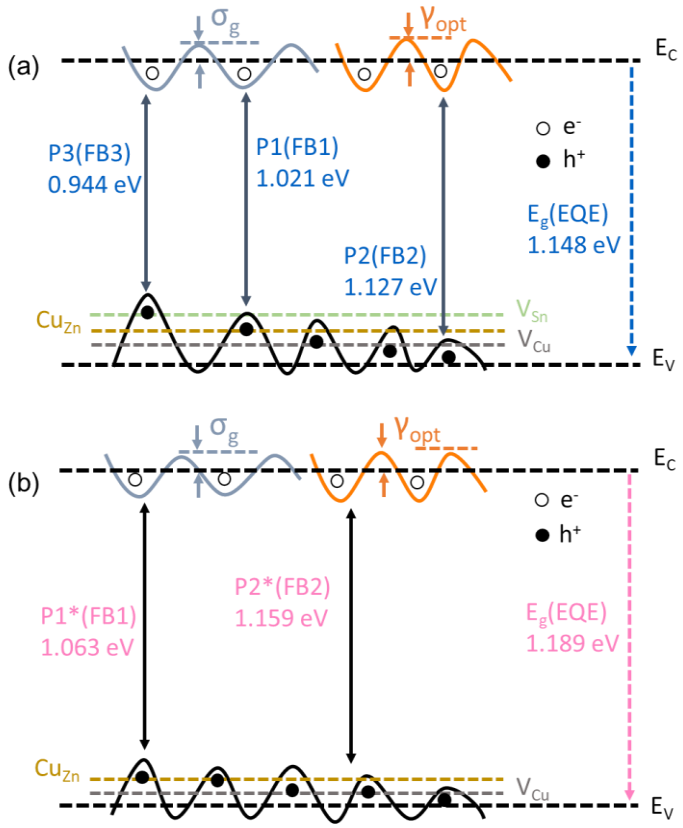

Figure 4-21 *Schematics of transitions for each peak designated of (a) REF film and (b) K_2S film including band-gap and electrostatic potential fluctuations.*

An interesting difference in the PL spectra of the two samples is the almost complete quenching of P3* in the K_2S film, leaving P1* and P2*. This PL shows that K_2S can effectively passivate the acceptor defect (V_{Sn}), and it has been demonstrated that K is able to reduce Sn-related defects by promoting elemental diffusion to stabilize the Sn content.[27] Therefore, the supply of K_2S modified the defect chemistry of CZTSSe by reducing the transition path passing through the defects and passivating the non-radiative defects in CZTSSe. In multi-crystalline CIGS and CZTSSe materials, potential fluctuation usually can act as traps for carriers to hinder carrier transport and diffusion. The non-uniformity of electrons and the energy depth of potential fluctuations are the key factors limiting the carrier transport/diffusion properties, the

superposition of σ_g and γ_{opt} is able to describe any spatial variation in the E_C and E_V. Both fluctuations occur simultaneously in the actual absorber, leading to a total variation width $\sigma_{total}=\sqrt{{\sigma_g}^2+{\gamma_{opt}}^2}$, with $\sigma_{total,\ K2S}$ (104 meV) reduced by 1/3 compared to $\sigma_{total,\ REF}$ (146 meV).

4.4 Oxidation state of the elements

In order to clarify the elemental changes on the absorber surface of REF and K_2S device, X-ray photoelectron spectroscopy (XPS) tests were performed. XPS measurements was performed by PHI 5000 VersaProbe III with a monochromatic Al Kα X-ray source. As shown in **Figure 4-22**a-c, the binding energy in the Cu 2p, Zn 2p and Sn 3d regions can be determined as Cu^+, Zn^{2+} and Sn^{4+}. A shoulder peak located at 495.8 eV is observed near the Sn 3d3/2 peak of the REF film (Figure 4-22c), which belongs to the Zn-Auger peak, possibly originating from Zn-based secondary phases or Zn-related defects. The peak does not appear in the K_2S film, implying that the K_2S layer suppresses the Zn related defects.[28]

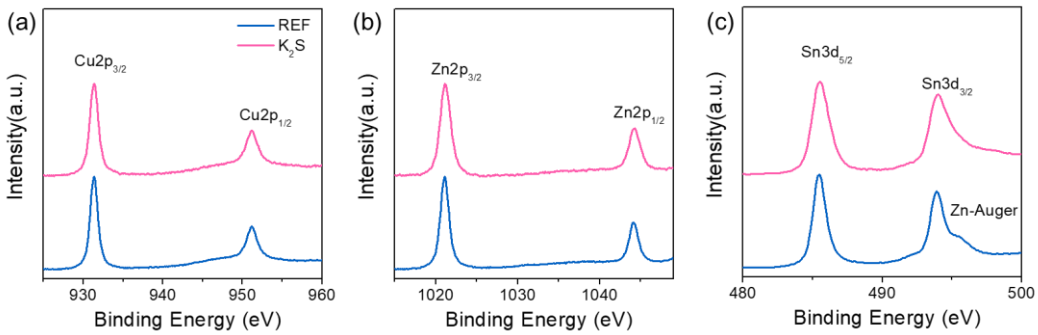

Figure 4-22 *The (a) Cu 2p, (b) Zn 2p, (c) Sn 3d XPS spectra of the REF and K_2S films;*

Four peaks were present in the S 2p spectrum (**Figure 4-23**a, b), and the BE peaks at 160.9 and 162.1 eV belonged to S 2p, while the 159.6 eV and 165.3 eV belongs to the

Se 3p core.[29] Figure 4-23f, g shows the Se 3d XPS data for REF and K_2S films. Se-1 XPS peaks were observed in both samples (at 53.4 eV and 54.3 eV, respectively), which is assigned to the kesterite CZTSSe. For the K_2S film, it can be found an additional Se 3d contribution (Se-2) which is not assigned to CZTSSe at higher binding energy than Se-1.[30] The peaks at lower binding energies of 52.8 eV and 53.6 eV were assigned to the K_2Se_3 phase, confirming the presence of the K-Se phase.[31] Figure 4-23e, f shows the XPS spectra of the Se Auger-K 2p region. For the K_2S film, a shoulder peak on the Se Auger peak is observed at the low binding energy (292.6 and 249.8 eV) side, which is attributed to the K 2p response.[32]

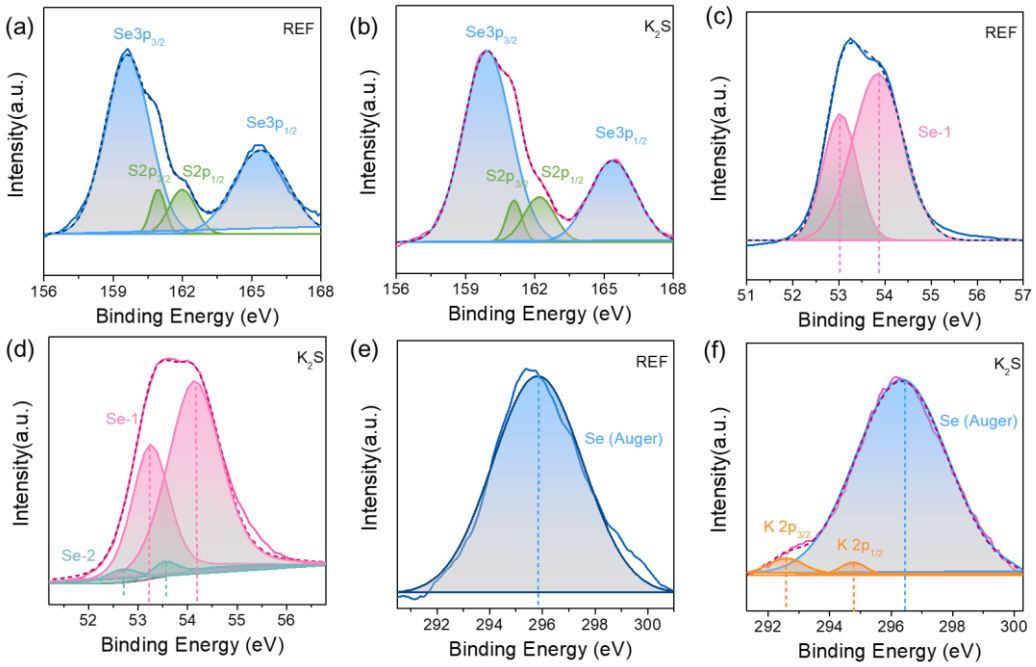

Figure 4-23 *(a, b) S2p and (c, d) Se 3d XPS spectra of the REF and K_2S films; (e, f) K 2p photoelectron transitions of REF and K_2S films.*

4.5 Grain growth mechanism

The SEM image of REF film and K_2S film cross-sections in **Figure 4-24** revealed a

dual layer of large grains on the top and fine grains at the bottom. This double-layer structure is commonly observed in solution progress CZTSSe absorbers.[33] The fine grain layer is caused by residual organic solvent impurity under selenization, which reduces the PCE. The crystallinity of K_2S sample is obviously improved and the fine grain layer is thinned. This is contrary to the usual conclusion that high S content deteriorates the crystallinity.[15]

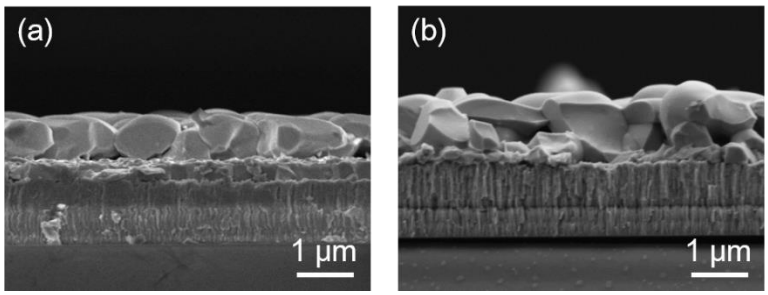

Figure 4-24 *The cross sectional image of (a) REF film and (b) K_2S film.*

To further investigate the effect of the K_2S layer on the grain growth mechanism, SEM analysis of REF samples and K_2S samples at different selenization stages (0 s/300 s/600 s/900 s) was carried out, as shown in **Figure 4-25**. Figures 5a-d and e-h show the surface and cross morphology of REF and K_2S samples at different selenization, respectively. As shown in Figure 4-25b and f, when the selenization time is 300 s, large grain appears on the surface and some fine grain formed at the back interface of REF sample; there are large grain on the surface and back interface of K_2S sample. When the selenization time was extended to 600s, the upper layer grain of REF sample increased significantly but the change of fine grain at the back interface was not obvious (Figure 4-25c). However, the upper and lower grain of K_2S sample increased visibly and the two layers were in contact with each other (Figure 4-25g). When the selenization time was further extended to 900 s, the size of the upper large grain of REF sample increased and formed a typical double layer structure, while two large grain layers of K_2S sample fused with

each other and further grew into single large grain. The above results confirm that the grain growth rate of the K_2S film is faster than REF film with the same selenization time, and the K_2S led to enhance the grain size and improve the CZTSSe crystallization. The significant improvement in grain growth rate is attributed to the formation of K-Se phase during selenization.[34] The band-gap fluctuation and electrostatic potential fluctuation were slightly higher for REF than for K_2S, which is consistent with the relatively good homogeneity due to the grain growth mechanism of the K-Se liquid phase.[35]

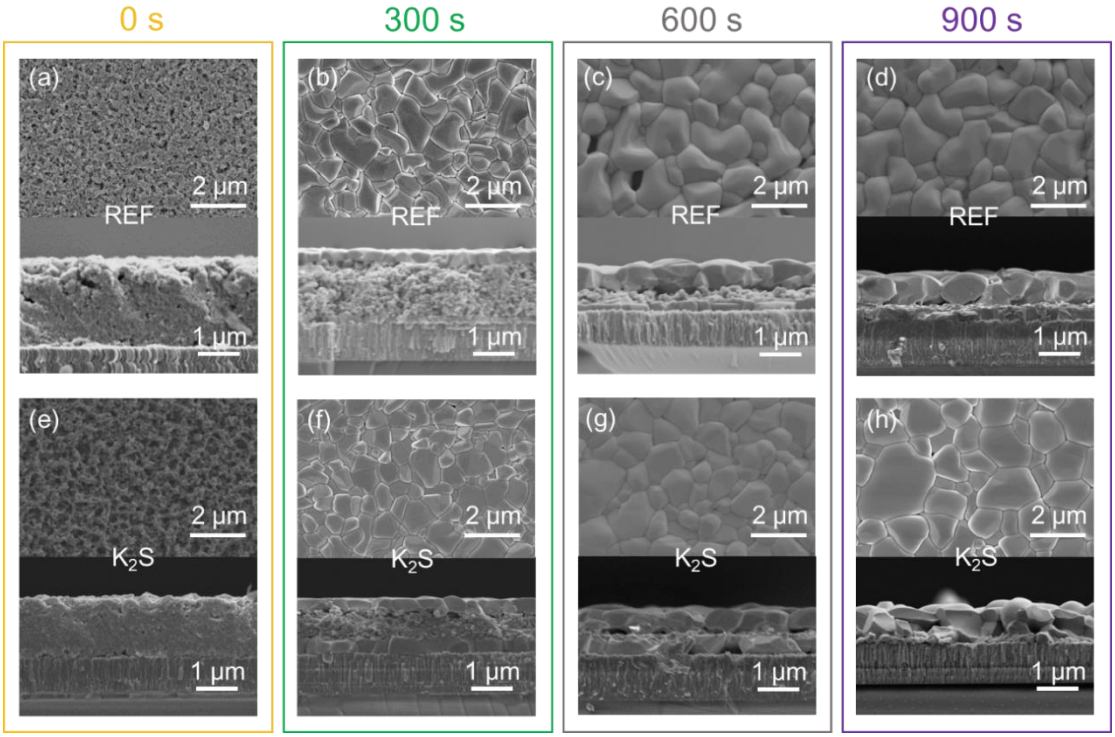

Figure 4-25 *Top and cross SEM images of (a)-(d) REF and (e)-(h) K_2S films at the selenization process of 0, 300, 600, and 900s.*

During the selenization of CZTSSe, the diffusion of K ions in CZTSSe films consists of two ways: the first one is the movement of K ions through vacancy defects,[4]

$$2V_{Cu}+K_2S\ (s) \rightarrow 2K_{Cu}+S\ (g) \qquad (4\text{-}1)$$

Several theoretical calculations have demonstrated that K_{Cu} does not form as easily thermodynamically as Na_{Cu}.[4] Therefore K atoms prefer the second type of diffusion: diffusion through gaps, voids and particles in CZTSSe films. The high affinity energy of K for Se at high temperatures and with an excess supply of selenium vapor leads to the formation of a series of selenium rich K-Se phases,[35]

$K_2S+5Se \rightarrow K_2Se_5+S$ (Starting temperature: 195 ℃) (4-2)

$K_2S+2Se \rightarrow 2KSe_2+S$ (Starting temperature: 206 ℃) (4-3)

$K_2S+3Se \rightarrow K_2Se_3+S$ (Starting temperature: 375 ℃) (4-4)

In Figure 4-23d, the peaks located at higher affinity energy (52.8 eV and 53.6 eV) belong to the K_2Se_3 phase, confirming the presence of the K-Se phase. After the selenization temperature reaches 375 ℃, the liquid K_2Se_3 phase flows between grain boundary (**Figure 4-26**), lowering the melting point and leading to rapid crystallization at lower temperatures.[36]

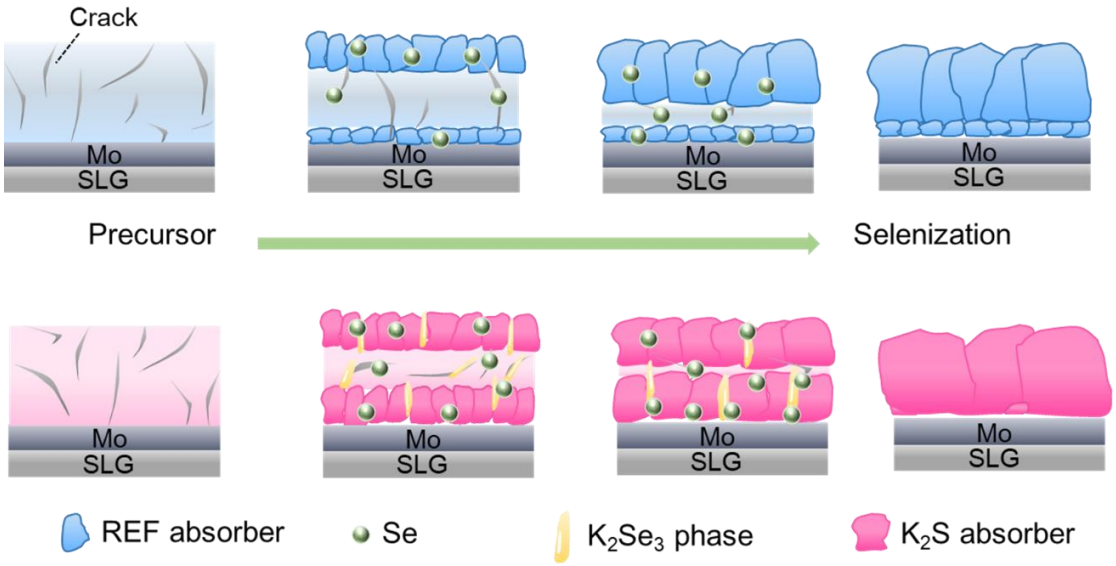

Figure 4-26 *Schematic illustration of growth mechanism for the REF and K_2S film during selenization process.*

Moreover, the flow of K_2Se_3 liquid phase is accompanied by the supply of Se. Placing the K_2S layer in the middle of the CZTSSe film facilitates the downward diffusion of the generated K_2Se_3 to the rest of the film, which is the key reason why the film is able to form two layers of microcrystals when selenization time is 600 s.

In addition, K_2S readily reactivates with Sn to form wide band-gap alkali metal compound ($K_2Sn_2S_5$) as follow,[38]

$$K_2S+Sn+S \rightarrow K_2Sn_2S_5 \text{ (Starting temperature: 275 ℃)} \quad (4\text{-}6)$$

The Sn in this reaction comes from the formation and decomposition of $SnSe_2$,[19]

$$SnS+Se_2 \rightarrow SnSe_2+S \quad (4\text{-}7)$$

$$SnSe_2 \rightleftharpoons SnSe+Se\ (g) \text{ (Starting temperature: 340 ℃)} \quad (4\text{-}8)$$

$$3SnSe \rightleftharpoons 2Sn+SnSe_3 \text{ (Starting temperature: above 400 ℃)} \quad (4\text{-}9)$$

Theoretical calculations show that the formation energy of $K_2Sn_2S_5$ is very low (-7.36 eV) during the formation of K-doped kesterite.[39] This wide band-gap alkali compound has a substantially smaller VBM because the alkali metal atoms lack the 3d orbital necessary to hybridize with the S 3p orbital. As a result, it can introduce hole barriers at grain boundaries and surfaces to prevent electron-hole recombination. This property reflects the specificity and superiority of the choice of K_2S material to treat the absorber.

4.6 Electrical characterization

To further investigate the carrier density and collection characteristic of the CZTSSe absorber, the *Capacitance-voltage (C-V) profile and the Driver level capicitance Profiling (DLCP)* are shown in **Figure 4-27**a. The carrier density N_{CV} and N_{DL} are obtained by the equations given in the chaper III.[13] The DLCP allows more accurate

assessment of the free carriers and deep defect states than *C-V* measurement, while the *C-V* also include the effect of the interface state in kesterite-based cells. Thus the contribution of the interface state can be extracted by subtracting the DLCP result from the C-V result.[19] The reduction in N_{CV}-N_{DL} (zero bias) imply a reduction in interface traps. The K_2S device, by virtue of its low interface defect density (5.60×10^{14} cm^{-3} for the K_2S device and 9.06×10^{14} cm^{-3} for the REF device), makes interface recombination easier to control. In addition, the defects cannot respond effectively at high frequency, only free carriers contribute to the DLCP signal at high frequency. In contrast, the low-frequency capacitance represents the response of the total of free carriers and deep traps, which means that the DLCP is able to observe the response of free carriers and deep defects at low frequency. Therefore, the difference between the high and low frequency DLCP responses is mainly related to the bulk defect density.[40] The bulk defect density of REF device and K_2S device is 1.31×10^{15} and 6.80×10^{14} cm^{-3}, respectively. Normally CZTSSe devices with high S content exhibit higher bulk defect density while K_2S device with higher sulfur content but lower bulk defect density is attributed to the existence of alkali metal K which plays a major role in passivating the defects.

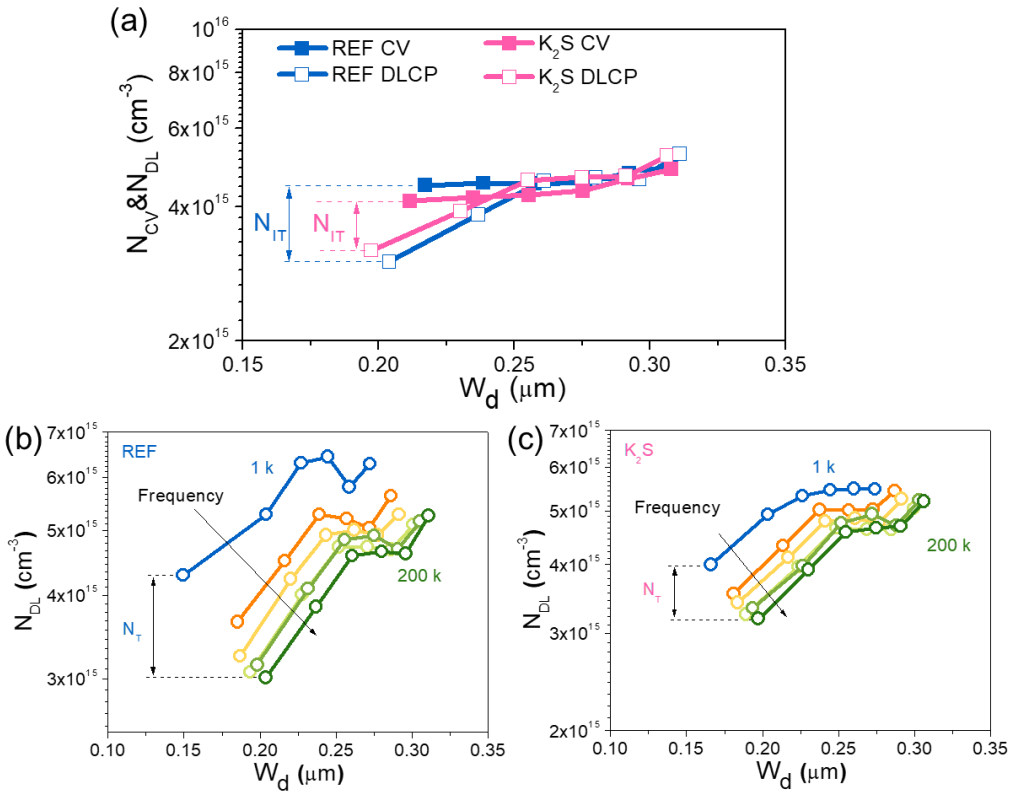

Figure 4-27 *(a) The C–V and DLCP profiles of REF and K_2S device. N_{DL} of (b) REF device and (c) K_2S device measured at frequencies from 1 to 200 kHz.*

The minority carrier diffusion length (L_d) is one of the important parameters affecting the collection efficiency, bias-dependent EQE (**Figure 4-28**), reflectivity (**Figure 4-29**a and b) and *C-V* measurements (Figure 4-29c) were performed to investigate the L_d of REF and K_2S devices.[41]

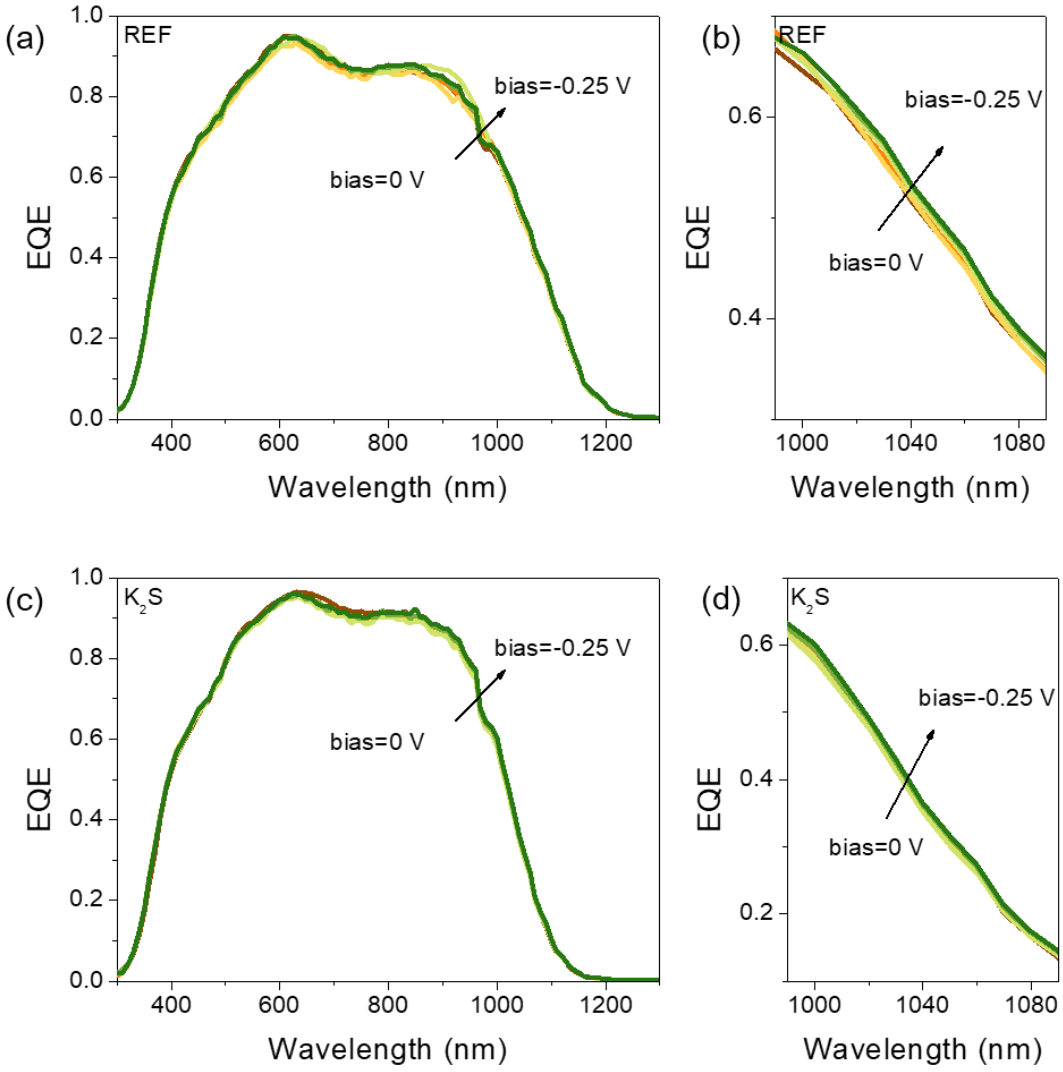

Figure 4-28 *EQE characteristics for a bias range of approximately 0 to -0.25V for (a) REF device and (c) K_2S device. (b) and (d) are the partial enlargement of (a) and (c) respectively.*

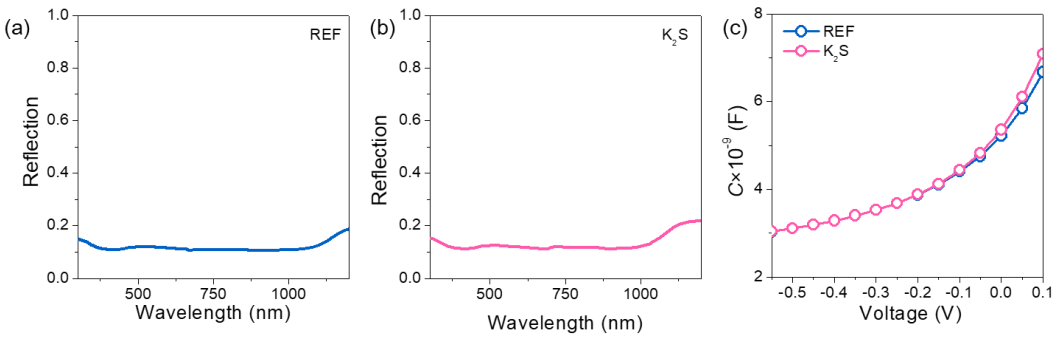

Figure 4-29 *Reflection curves of (a) REF film and (b) K_2S film. (c) C-V curves of REF device and K_2S device.*

The calculation process and equations are already given in the chapter II to obtain minority carrier diffusion length. The REF device has a strong depletion region width (W_d) dependence (large slope) and the L_d value obtained is 0.77 μm (**Figure 4-30**). The derived L_d value is estimated from Figure 4-30 to be about 1.38 μm for K_2S devices with a small W_d dependence (small slope). Since the extracted L_d value exceeds the thickness of the sample, the true L_d is expected to be larger than the thickness of the absorber (1.2 μm).[41] In fact, this phenomenon has been observed in high performance CIGS solar cells, and it is assumed that the generation of L_d values larger than the absorber thickness is related to the back surface field. For K_2S devices, the back gradient can provide a stronger back surface field to drive electron transport to the p-n junction compared to REF devices, thus increasing the minority carrier diffusion length and facilitating the reduction of back interface recombination. The optimization of the band-tailed state can also effectively improve the L_d. In addition, the carrier mobility is calculated from the equation $L_d = \sqrt{\mu_e k_b T/q}$ (where k_b is Boltzmann constant, T is temperature, and q is the elementary charge).[41] The electron mobility (μ_e) of REF and K_2S devices are 23 and 74 $cm^2 V^{-1}s^{-1}$, respectively. The large grains of the K_2S absorber reduces grain boundary scattering, which is more favorable for minority carrier diffusion. Also, the band-gap fluctuation caused by charge compensation can lead to small mobility, and the smaller band-gap fluctuations and electrostatic potential fluctuations of K_2S device are favorable for carrier mobility.[42]

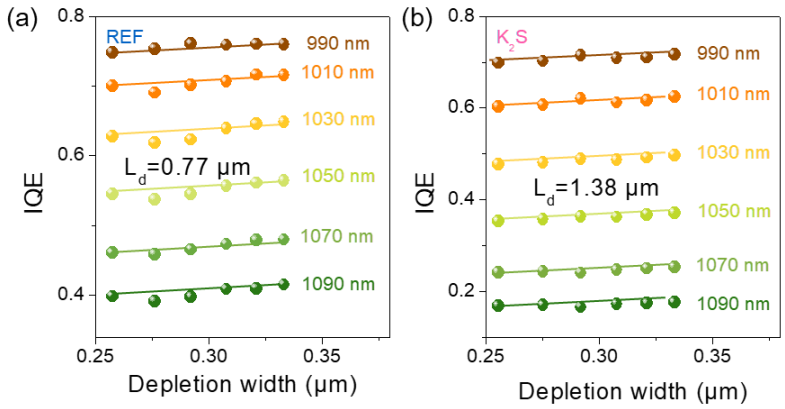

Figure 4-30 *Minority carrier diffusion length extraction of (d) REF device and (e) K_2S device.*

The defect property of semiconductor materials largely determines the transport characteristics of photogenerated carriers, which in turn affects the performance parameters of photovoltaic devices. Therefore the longer L_d means the shallower defect energy level and the smaller defect density. Defect formation is highly dependent on the reaction process, crystallinity and absorber composition. To further evaluate the defect energy level and defect density of REF device and K_2S device, the property of defects was investigated using Deep Level Transient Spectroscopy (DLTS). **Figure 4-31** shows the DLTS signal in the temperature range of 120-350 K. It can be seen that two negative peaks (H1 and H2) appear in both samples, indicating the detection of two defects, the negative peak being assigned to the acceptor defect in the kesterite film. One (peak 1) is close to 220 K and the other (peak 2) is close to 270 K, indicating similar defect characteristics for both absorbers.

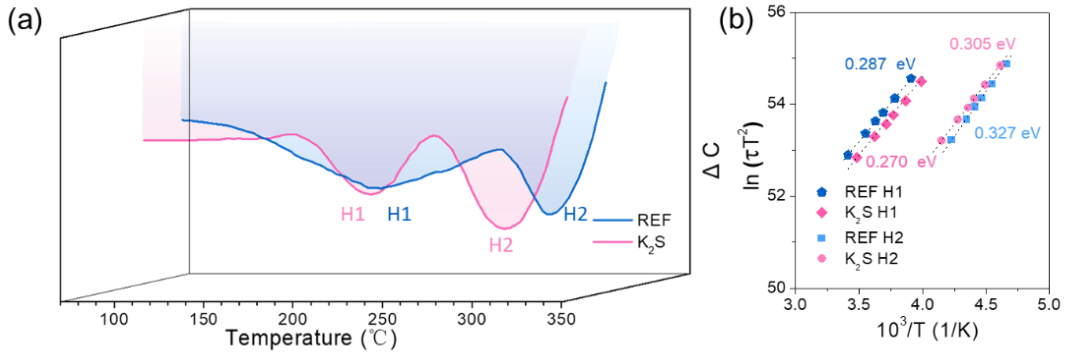

Figure 4-31 *(a) C-DLTS spectra of REF and K_2S samples and (b) the corresponding Arrhenius curves.*

The data in the DLTS are extracted from the current transient state at each temperature. The values of E_a and N_t can be calculated on an Arrhenius plot by linearly fitting the points near the DLTS peaks.

The defect activation energy (E_a), defect density (N_t), and capture cross section (σ) of the defects can be extracted from the Arrhenius plot (Figure 4-31b) and summarized in **Table 4-4**. The defects of both devices have similar E_a, which means that they have similar origins. Among them, defects H1 and H2 are located 0.27-0.29 and 0.30-0.33 eV above the E_V, and combined with theoretical calculations, the H1 and H2 defects are identified as V_{Sn} and Cu_{Sn} deep energy level acceptor defects, respectively.[24] In deep trap centers, a lower E_a value denotes a faster carrier emission. H1 and H2 defects in the K_2S device have a lower activation energy than those in the REF device, decreasing their likelihood of functioning as efficient recombination centers.

Table 4-4 *Summary of result derived from DLTS.*

	Peak ID	E_a (eV)	N_t (cm^{-3})	σ (cm^2)	$\sigma \times N_t$	Possible defect level
REF	H1	0.287	3.79×10^{13}	6.92×10^{-18}	2.62×10^{-4}	V_{Sn}
	H2	0.327	3.97×10^{14}	3.46×10^{-18}	1.37×10^{-3}	Cu_{Sn}
K_2S	H1	0.270	6.32×10^{12}	4.72×10^{-18}	2.98×10^{-5}	V_{Sn}
	H2	0.305	1.68×10^{14}	1.57×10^{-18}	2.64×10^{-4}	Cu_{Sn}

A schematic diagram in **Figure 4-32**a and b clearly show the defect concentration and energy level of these defects. It is clear that both V_{Sn} and Cu_{Sn} are deep energy level defects and close to the middle of the band-gap, which are difficult to ionize at room temperature due to their high activation energy. Instead of affecting the doping type (n/p type) and carrier concentration, the deep defects typically operate as recombination centers, impairing carrier transit and lifetime. It is worth noting that the concentration of the V_{Sn} defect in K_2S device further reduced 6 times (from 3.79×10^{13} to 6.32×10^{12} cm^{-3}) compared to the REF device, confirming that the defects are sufficiently suppressed. The relatively small decrease in the Cu_{Sn} defect (2.3 times) compared to the sharp decrease in the V_{Sn} defect (6 times) is justified by the much higher formation energy of Cu_{Sn}. Agreeing with PL and DLCP results, the DLTS analysis demonstrates that K_2S devices have a lower defect density than REF devices. Typically, sulfur-rich devices with higher defect density and deeper defect energy levels lead to stronger recombination, contrary to our conclusions.[22] The decrease in the density of Sn-related deep defect states may be due to the existence of element K in the absorber layer of the K_2S device which enhances the element diffusion rate, allowing a larger fraction of the

absorber to participate in the evaporation and inclusion during selenization, stabilizing the Sn content.[27] This demonstrates the necessity of selecting K_2S material for CZTSSe, where the presence of K_2S is able to passivate deep energy level defects, thus reducing the defect problems that may result from the increased S content. Further calculations of $\sigma \times N_t$ to evaluate the trap lifetime are shown in figure 4-32c. It can be found that the two defects in the K_2S device have shorter lifetimes therefore the photo-generated holes and electrons are more likely to be trapped by the defects in the REF device, leading to severe trap-assisted recombination.

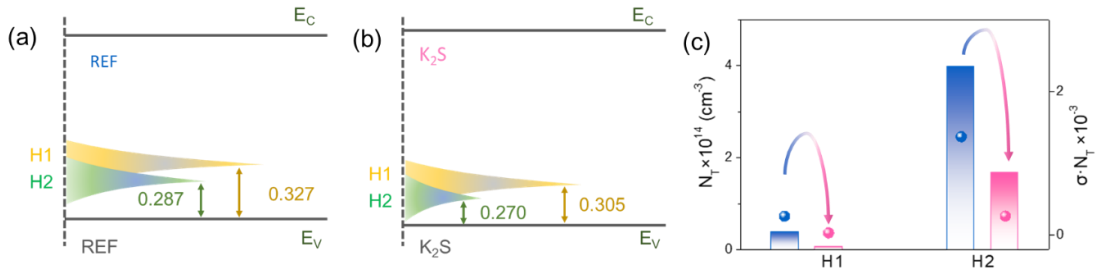

Figure 4-32 *The schematic diagram of E_a and N_t of (a) REF device and (b) K_2S device. (c) The values of N_t and ($\sigma \cdot N_t$) at H1 (Cu_{Sn}) and H2 (V_{Sn}) defects.*

4.9 Conclusions

This chapter presents a simple and effective method for obtaining double gradient band-gap by inserting a K_2S layer into the CZTSSe precursor film to modulate the S/(S+Se) profile of the absorber for the first time. The efficiency of the best CZTSSe devices based on the optimal double gradient band-gap structure is as high as 13.70%. The characterization results obtained by EDS, SIMS, EQE and XPS clearly demonstrate the formation of an ideal double gradient band-gap in CZTSSe solar cell. It is shown that K_2S provided additional S to the absorber and the high affinity of K-Se optimized the Se profile and makes the K_2S layer locally Se rich and S poor during selenization. It

means that during the high temperature selenization process, the S and Se distribution in the absorber was adjusted and the S/(S+Se) notch appeared at the location of K_2S layer, implying that the band-gap was distributed in similar double gradient. In addition, the K-Se liquid phase (K_2Se_3) formed during selenization contributes to lowering of the melting point to promote grain growth, which helps to increase the minority carrier diffusion length. At the same time, the presence of K^+ stabilizes the Sn content by enhancing the elemental diffusion rate, thereby reducing the transition path through defects, passivating non-radiative defects and suppressing band-gap fluctuation and electrostatic potential fluctuation. This method of obtaining a double-gradient band-gap absorber does not require additional equipment or change of equipment, which makes it easy to introduce into the CZTSSe solar cells preparation process with strong production applicability. These highly encouraging results and the associated innovative process for obtaining double band-gap gradient absorber may open up further opportunities for further improving CZTSSe solar cell performance.

REFERENCES

[1] Zhang X., Zhou Z., Cao L., Kou D., Yuan S., Zheng Z., Yang G., Tian Q., Wu S., Liu S., Suppressed interface defects by $GeSe_2$ post-deposition treatment enables high-efficiency kesterite solar cells. *Adv. Funct. Mater.*, **2022**, 33, 2211315.

[2] Jung S., Ahn S., Yun J. H., Gwak J., Kim D., Yoon K., Effects of Ga contents on properties of CIGS thin films and solar cells fabricated by co-evaporation technique. *Curr. Appl. Phys.*, **2010**, 10, 990.

[3] Du Y., Wang S., Tian Q., Zhao Y., Chang X., Xiao H., Deng Y., Chen S., Wu S., Liu S., Defect engineering in earth-abundant $Cu_2ZnSn(S,Se)_4$ photovoltaic materials via Ga^{3+}-doping for over 12% efficient solar cells. *Adv. Funct. Mater.*, **2021**, 31, 2010325.

[4] Yuan Z.-K., Chen S., Xie Y., Park J.-S., Xiang H., Gong X.-G., Wei S.-H., Na-Diffusion Enhanced p-type Conductivity in $Cu(In,Ga)Se_2$: A New Mechanism for Efficient Doping in Semiconductors. *Adv. Energy Mater.*, **2016**, 6, 1601191.

[5] Zhou J., Xu X., Duan B., Wu H., Shi J., Luo Y., Li D., Meng Q., Regulating crystal growth via organic lithium salt additive for efficient kesterite solar cells. *Nano Energy*, **2021**, 89, 106405.

[6] Avancini E., Carron R., Bissig B., Reinhard P., Menozzi R., Sozzi G., Di Napoli S., Feurer T., Nishiwaki S., Buecheler S., Tiwari A. N., Impact of compositional grading and overall Cu deficiency on the near-infrared response in Cu(In, Ga)Se2 solar cells. *Prog. Photovolt: Res. Appl.*, **2017**, 25, 233.

[7] Fan Q., Tian Q., Wang H., Zhao F., Kong J., Wu S., Regulating the starting location of front-gradient enabled highly efficient $Cu(In,Ga)Se_2$ solar cells via a facile thiol–amine solution approach. *J. Mater. Chem. A*, **2018**, 6, 4095.

[8] Chirila A., Buecheler S., Pianezzi F., Bloesch P., Gretener C., Uhl A. R., Fella C., Kranz L., Perrenoud J., Seyrling S., Verma R., Nishiwaki S., Romanyuk Y. E., Bilger G., Tiwari A. N., Highly efficient Cu(In,Ga)Se2 solar cells grown on flexible polymer films. *Nature materials*, **2011**, 10, 857.

[9] Guo H., Meng R., Wang G., Wang S., Wu L., Li J., Wang Z., Dong J., Hao X., Zhang Y., Band-gap-graded $Cu_2ZnSn(S,Se)_4$ drives highly efficient solar cells. *Energy Environ. Sci.*, **2022**, 15, 693.

[10] Kauk-Kuusik M., Li X., Pilvet M., Timmo K., Mikli V., Kaupmees R., Danilson M., Grossberg M., Nano-scale sulfurization of the Cu2ZnSnSe4 crystal surface for photovoltaic applications. *J. Mater. Chem. A*, **2019**, 7, 24884.

[11] Márquez J., Stange H., Hages C. J., Schaefer N., Levcenko S., Giraldo S., Saucedo E., Schwarzburg K., Abou-Ras D., Redinger A., Klaus M., Genzel C., Unold T., Mainz R., Chemistry and Dynamics of Ge in Kesterite: Toward Band-Gap-Graded Absorbers. *Chem. Mater.*, **2017**, 29, 9399.

[12] Zhang Z., Qi Y., Zhao W., Liu J., Liu X., Cheng K., Du Z., Nanoscale sharp band-gap gradient for efficiency improvement of $Cu_2ZnSn(S, Se)_4$ thin film solar cells. *J. Alloys Compd.*, **2022**, 910, 164665.

[13] Qi Y.-F., Kou D.-X., Zhou W.-H., Zhou Z.-J., Tian Q.-W., Meng Y.-N., Liu X.-S., Du Z.-L., Wu S.-X., Engineering of interface band bending and defects elimination via a Ag-graded active layer for efficient $(Cu,Ag)_2ZnSn(S,Se)_4$ solar cells. *Energy Environ. Sci.*, **2017**, 10, 2401.

[14] Kim J. H., Kim M. K., Gadisa A., Stuard S. J., Nahid M. M., Kwon S., Bae S., Kim B., Park G. S., Won D. H., Lee D. K., Kim D. W., Shin T. J., Do Y. R., Kim J., Choi W. J., Ade H., Min B. K., Morphological-Electrical Property Relation in $Cu(In,Ga)(S,Se)_2$ Solar Cells: Significance of Crystal Grain Growth and Band Grading by Potassium Treatment. *Small*, **2020**, 16, e2003865.

[15] Muzzillo C. P., Review of grain interior, grain boundary, and interface effects of K in CIGS solar cells: Mechanisms for performance enhancement. *Sol. Energy Mater. Sol. Cells*, **2017**, 172, 18.

[16] Uhl A. R., Katahara J. K., Hillhouse H. W., Molecular-ink route to 13.0% efficient low-band-gap CuIn(S,Se)2 and 14.7% efficient Cu(In,Ga)(S,Se)2 solar cells. *Energy Environ. Sci.*, **2016**, 9, 130.

[17] Thomas Feurer, Patrick Reinhard, Enrico Avancini, Benjamin Bissig, Johannes Löckinger, Peter Fuchs, Romain Carron, Thomas Paul Weiss, Julian Perrenoud, Stephan Stutterheim, Stephan Buecheler, Tiwari A. N., Progress in thin film CIGS photovoltaics – Research and development, manufacturing, and applications. *Prog. Photovolt: Res. Appl.*, **2017**, 25, 645.

[18] Gong Y., Zhu Q., Li B., Wang S., Duan B., Lou L., Xiang C., Jedlicka E., Giridharagopal R., Zhou Y., Dai Q., Yan W., Chen S., Meng Q., Xin H., Elemental de-mixing-induced epitaxial kesterite/CdS interface enabling 13%-efficiency kesterite solar cells. *Nat. Energy*, **2022**, 7, 966.

[19] Yu Z., Li C., Chen S., Zheng Z., Fan P., Li Y., Tan M., Yan C., Zhang X., Su Z., Liang G., Unveiling the Selenization Reaction Mechanisms in Ambient Air-Processed Highly Efficient Kesterite Solar Cells. *Adv. Energy Mater.*, **2023**, 13, 2300521.

[20] Kim S., Rana T. R., Kim J., Son D.-H., Yang K.-J., Kang J.-K., Kim D.-H., Limiting effects of conduction band offset and defect states on high efficiency CZTSSe solar cell. *Nano Energy*, **2018**, 45, 75.

[21] Zhao Y., Yuan S., Kou D., Zhou Z., Wang X., Xiao H., Deng Y., Cui C., Chang Q., Wu S., High efficiency CIGS solar cells by bulk defect passivation through Ag substituting strategy. *ACS Appl. Mater. Interfaces*, **2020**, 12, 12717.

[22] Duan H.-S., Yang W., Bob B., Hsu C.-J., Lei B., Yang Y., The role of sulfur in solution-processed $Cu_2ZnSn(S,Se)_4$ and its Effect on defect properties. *Adv. Funct. Mater.*, **2013**, 23, 1466.

[23] Hadke S., Levcenko S., Sai Gautam G., Hages C. J., Márquez J. A., Izquierdo-Roca V., Carter E. A., Unold T., Wong L. H., Suppressed deep traps and band-gap fluctuations in Cu_2CdSnS_4 solar cells with ≈8% efficiency. *Adv. Energy Mater.*, **2019**, 9, 1902509.

[24] Chen S., Walsh A., Gong X. G., Wei S. H., Classification of lattice defects in the kesterite Cu_2ZnSnS_4 and $Cu_2ZnSnSe_4$ earth-abundant solar cell absorbers. *Adv. Mater.*, **2013**, 25, 1522.

[25] Duan B., Guo L., Yu Q., Shi J., Wu H., Luo Y., Li D., Wu S., Zheng Z., Meng Q., Highly efficient solution-processed CZTSSe solar cells based on a convenient sodium-incorporated post-treatment method. *J. Energy Chem.*, **2020**, 40, 196.

[26] Lee H., Jang Y., Nam S. W., Jung C., Choi P. P., Gwak J., Yun J. H., Kim K., Shin B., Passivation of Deep-Level Defects by Cesium Fluoride Post-Deposition Treatment for Improved Device Performance of $Cu(In,Ga)Se_2$ Solar Cells. *ACS Appl. Mater. Interfaces*, **2019**, 11, 35653.

[27] Tao S., Dong L., Han J., Wang Y., Gong Q., Wei J., Zhao M., Zhuang D., Efficiency enhancement of CZTSe solar cells based on in situ K-doped precursor. *J. Mater. Chem. A*, **2023**, 11, 9085.

[28] Tong Z., Yan C., Su Z., Zeng F., Yang J., Li Y., Jiang L., Lai Y., Liu F., Effects of potassium doping on solution processed kesterite Cu2ZnSnS4 thin film solar cells. *Appl. Phys. Lett.*, **2014**, 105, 223903.

[29] Danilson M., Altosaar M., Kauk M., Katerski A., Krustok J., Raudoja J., XPS study of CZTSSe monograin powders. *Thin Solid Films*, **2011**, 519, 7407.

[30] Harel S., Arzel L., Lepetit T., Zabierowski P., Barreau N., Influence of Sulfur Evaporation during or after KF-Post Deposition Treatment On Cu(In,Ga)Se2/CdS Interface Formation. *ACS Appl. Mater. Interfaces*, **2020**, 12, 46953.

[31] Kim J.-H., Bae S., Min B. K., Impact of Absorber Layer Morphology on Photovoltaic Properties in Solution-Processed Chalcopyrite Solar Cells. *ACS Applied Materials & Interfaces*, **2020**,

[32] Alruqobah E. H., Agrawal R., Potassium Treatments for Solution-Processed $Cu(In,Ga)(S,Se)_2$ Solar Cells. *ACS Appl. Energy Mater.*, **2020**, 3, 4821.

[33] Zhao Y., Yu Z., Hu J., Zheng Z., Ma H., Sun K., Hao X., Liang G., Fan P., Zhang X., Su Z., Over 12% efficient kesterite solar cell via back interface engineering. *J. Energy Chem.*, **2022**, 75, 321.

[34] Zhao Y.-H., Gao Q.-Q., Yuan S.-J., Chang Q.-Q., Liang T., Su Z.-H., Ma H.-L., Chen S., Liang G.-X., Fan P., Zhang X.-H., Wu S.-X., Defects passivation and crystal growth promotion by solution-processed K doping strategy toward 16.02% efficiency $Cu(In,Ga)(S,Se)_2$ solar cells. *Chem. Eng. J.*, **2022**, 436, 135008.

[35] Maeda T., Kawabata A., Wada T., First-principles study on alkali-metal effect of Li, Na, and K in Cu_2ZnSnS_4 and $Cu_2ZnSnSe_4$. *Phys. Status Solidi C*, **2015**, 12, 631.

[36] Kim M., Park G. D., Kang Y. C., Investigation of the potassium-ion storage mechanism of nickel selenide materials and rational design of nickel selenide-C yolk-shell structure for enhancing electrochemical properties. *Int. J. Energy Res.*, **2021**, 46, 5800.

[37] Sun Y., Lin S., Li W., Cheng S., Zhang Y., Liu Y., Liu W., Review on alkali element doping in Cu(In,Ga)Se_2 thin films and solar cells. *Engineering*, **2017**, 3, 452.

[38] Klepp K. O., Darstellung und Kristallstruktur von $K_2Sn_2S_5$ und $K_2Sn_2Se_5$/Preparation and Crystal Structure of $K_2Sn_2S_5$ und $K_2Sn_2Se_5$. *Z. Naturforsch.*, **1992**, 47, 197.

[39] Zhang X., Han D., Chen S., Duan C., Chu J., First-principles study on the alkali chalcogenide secondary compounds in Cu(In,Ga)Se2 and Cu2ZnSn(S,Se)4 thin film solar cells. *J. Energy Chem.*, **2018**, 27, 1140.

[40] Handick E., Reinhard P., Alsmeier J. H., Kohler L., Pianezzi F., Krause S., Gorgoi M., Ikenaga E., Koch N., Wilks R. G., Buecheler S., Tiwari A. N., Bar M., Potassium Postdeposition Treatment-Induced Band-gap Widening at Cu(In,Ga)Se(2) Surfaces--Reason for Performance Leap? *ACS Appl. Mater. Interfaces*, **2015**, 7, 27414.

[41] Wang D., Wu J., Liu X., Wu L., Ao J., Liu W., Sun Y., Zhang Y., Formation of the front-gradient band-gap in the Ag doped CZTSe thin films and solar cells. *J. Energy Chem.*, **2019**, 35, 188.

[42] Guo J., Mao Y., Ao J., Han Y., Cao C., Liu F., Bi J., Wang S., Zhang Y., Microenvironment Created by SnSe(2) Vapor and Pre-Selenization to Stabilize the Surface and Back Contact in Kesterite Solar Cells. *Small*, **2022**, 18, e2203354.

GENERAL CONCLUSIONS

CZTSSe solar cells are one of the most promising new thin-film solar cells with many advantages such as abundant raw material reserves and low cost. The main obstacle to its industrialization is the relatively low conversion efficiency. Poor front and back interface quality and the absorber bulk properties are the main limiting factors for efficiency improvement. This PhD thesis is devoted to the preparation of CZTSSe absorber layers by ethylene glycol methyl ether solution method, with the goal of overcoming the severe open-circuit voltage deficit (V_{OC}-def) of the device from three perspectives: improvement of the quality of Mo/CZTSSe back interface, optimization of the quality of CZTSSe/CdS front interface, and the construction of an absorber with double-gradient bandgap structure. Under the core idea of "improving device performance", this doctoral work has carried out a series of complementary research work on interface engineering and gradient bandgap construction. The major results are summarized here.

(1) Mo/CZTSSe back interface engineering

To address the problem that the Mo/CZTSSe back interface is prone to unfavorable reactions, leading to the interface quality deterioration, we introduced a WO_3 intermediate layer by thermal evaporation. This layer successfully suppressed the undesirable reaction between Mo and CZTSSe, resulting in the reduction of the undesirable products. As a result, high-quality CZTSSe crystals with low defect density and good charge transfer ability were obtained, and the smooth absorber surface is also favorable for improving the quality of P-N junction. The suppression of the interface reaction effectively reduces the thickness of $Mo(S,Se)_2$, decreases the back interface contact barrier, and significantly improves the filling factor. The introduction of the WO_3 not only improves the short carrier diffusion length, but also reduces the deep dominant defects, which greatly minimizes the nonradiative recombination of the

charge carriers, thus decreasing the open-circuit voltage loss. The results show that the efficiency of the CZTSSe solar cell is increased from 10.87% to 12.66% thank to back interface engineering.

(2) CZTSSe/CdS front interface engineering

We have also tried to simultaneously deal with the surface and bulk defects of the CZTSSe absorber by treating the CZTSSe absorber with ammonium sulfide solution with a subsequent thermal annealing. This method has been revealed efficient and the power conversion efficiency of treated CZTSSe devices was as high as 12.78%. This process introduced an additional annealing step to the surface sulfurization process, which promotes elemental diffusion and reduces defects on the surface as well as in the bulk of the absorber. It has also been demonstrated that the energy band bending at the grain boundaries of the treated samples is larger, which is more favorable for the separation and the collection of electrons and holes. The sulfurization treatment improves significantly the charge collection process.

(3) Construction of absorber with gradient bandgap

An innovative technique has been developed to modulate the S/(S+Se) profile of the absorber by inserting a K_2S layer into the CZTSSe precursor film in order to obtain a dual-gradient bandgap structure. The analytical results show that K2S provides additional S to the absorber, and the selenization process favorize the formation of K-Se so that the K_2S layer is locally Se-enriched. The S/(S+Se) value is therefore lower at the position of the K_2S layer, leading to the narrowing of the band gap. The K-Se liquid phase (K_2Se_3) formed during selenization contributes to the lowering of the melting point and promotes grain growth. Meanwhile, the presence of K^+ stabilizes the Sn content by increasing the diffusion rate of the element, thus reducing the probability of non-radiative defects. The efficiency of the CZTSSe device based on the optimal double-gradient bandgap structure is as high as 13.70%.

However, this high efficiency still needs to be improved before real commercial application. Potential ways to enhance the efficiency include improved defect modulation, device structure optimization and post-annealing strategies. Future works could include the following aspects:

(1) Identification and mitigation of intrinsic defects

Identification and mitigation of complex intrinsic defects in CZTSSe material and device are the most difficult and important research directions at present. There is an urgent need to establish a new theory of defects in multi-element compounds and to develop more advanced defect characterization tools to elucidate the fundamental causes of severe non-radiative recombination. The combination of theoretical calculations and experimental confirmations is necessary to understand the formation mechanism of intrinsic defects, to identify the defect types which are most detrimental to the device performance. The final objective is to finely regulate and to passivate the defects during the film growth process to reduce the concentration of harmful defects.

(2) Cadmium sulfide/device post-annealing

Relevant studies have shown that after depositing cadmium sulfide, the post annealing process is very important to improve the device quality through elemental interdiffusion. This process needs to be further investigated/improved.

Additional information

C-V

Capacitance-Voltage (C-V) spectroscopy is used to detect the concentration distribution of defects within the device. The depletion region of p-n junction in the semiconductor device consists of anions and cations formed by point defects or impurities that have lost carriers, and the free carriers are distributed in the material on both sides of the depletion region. When the device is loaded with reverse bias voltage, the depletion region width increases and changes the junction capacitance by an amount which is determined by both the doping and defect concentration and the reverse bias voltage. For CdS/CZTSSe, which is a one-sided heavily doped n^+p junction, the depletion region is mainly located on the relatively lightly doped CZTSSe side, and therefore the doping concentration can be calculated by measuring the spectral lines of capacitance and voltage.

DLCP

Most of the light absorbers of thin-film cells are polycrystalline materials with significant defect states in the bandgap. Due to the capacitive contribution of the defect states, C-V test results may overestimate the doping concentration, leading to the development of drive-level capacitance analysis (DLCP), a capacitance characterization technique mainly used to study amorphous as well as polycrystalline semiconductors. Compared to C-V testing, DLCP testing is less susceptible to interface states and therefore produces more accurate doping concentrations. The technique of DLCP yields the density of states responding dynamically to the alternating current (AC) bias. In addition, DLCP data at high frequency yields an N_{DL} value only equal to the free-carrier density because the defects cannot effectively respond to the excitation signals at high frequencies. It means that DLCP data at low frequency yield an N_{DL}

value equal to the sum of free-carrier density and the bulk defect density. DLCP data at high frequency yields an N_{DL} value only equal to the free-carrier density.

Admittance spectrum

Applying an AC signal to the cells in AC testing is equivalent to applying a certain amount of test energy to the cells at a certain angular frequency and temperature. At this time, the hole defects (or electron defects) will have a charge/discharge effect with the external energy, trapping/releasing holes (or electrons) into the valence band (or conduction band). For p-type semiconductors, hole defects respond to an AC signal (charge/discharge) when they are close to the valence band E_V and the activation energy is less than the test energy. The response of a circuit element to an AC signal can be characterized by two physical quantities: impedance and conductance. Impedance is a collective term for the resistance, inductance, and capacitance in a circuit that impedes an alternating current, and admittance is defined as the reciprocal of impedance. Utilizing the sample's AC capacitance and conductance with frequency and temperature changes and the development of test methods, can detect defects in semiconductor samples related information. The admittance spectrum is mainly concerned with the capacitance-frequency (C-f) curve characteristics.

DLTS

Deep energy level transient spectroscopy (DLTS) is an experimental technique used to investigate deep energy level impurities, defects and interface states in semiconductors. The principle is based on applying a reverse bias voltage to a semiconductor sample and superimposing a periodic pulse voltage. During the pulse, the junction barrier decreases and the width of the space charge region decreases, leading to filling of certain deep energy levels with electrons. At the end of the pulse, the junction bias returns to its original state, the space charge region widens, and the electrons filling the deep energy levels emit into the conduction band, forming a capacitive transient. The

capacitance transient waveform can effectively reflect the information of the deep energy level. The DLTS technique utilizes the "emissivity window" technique to form the DLTS spectrum through the temperature scanning, where different deep centers appear at different temperatures. The height of the peaks corresponds to the concentration of the deep centers, and the positive and negative peaks correspond to the minority traps and majority traps. This method is capable of detecting trace impurities, defects, and interface states in semiconductors with high detection sensitivity.

PL

Photoluminescence (PL) is a physical phenomenon. When a substance absorbs energy from an external light source, electrons are excited to higher energy levels in the excited state, and then these electrons release energy in the form of photons when they return to a lower energy or ground state. This process involves electrons transition between different energy levels and can be divided into the following three main stages: ① Absorption. Substances absorb the energy of photons (or electromagnetic waves), causing electrons to transfer from the ground state to the excited state. ② Energy transition. In the excited state, electrons may transfer energy by interacting with phonons in the lattice or with other electrons. ③Photoemission. The return of an electron from the excited state to the ground state or a lower energy level with the release of a photon, a process that may be accompanied by a loss of energy, usually in the form of heat energy. In cases where the excitation light energy is not very high, PL testing is a non-destructive test method to quickly and easily characterize semiconductor materials for defects, impurities, and the luminescent properties of the material.

TRPL

Time-resolved photoluminescence spectroscopy (TRPL) involves excitation of a sample by a laser pulse, measuring the luminescence signals generated by the sample

under the action of the excitation light pulse, and analyzing the time evolution of the luminescence signals. TRPL technique can achieve high temporal and spectral resolution, and provide accurate measurements of the lifetimes and evolutionary processes of the photogenerated carriers of the sample as well as information about the carrier recombination, transportation, and lifetimes. TRPL is one of the important methods to study the kinetic behavior of photogenerated carriers, which enables accurate measurements of the lifetimes and evolutionary processes of photogenerated carriers in solar cells. It can reveal important information about the recombination, transportation and lifetime of photogenerated carriers in solar cells, and provide important references for the performance optimization and material design of solar cells.

TPV

The Transient Photovoltage (TPV) test is a method that focuses on the in-depth study and analysis of carriers. The test provides a comprehensive and effective analysis and measurement of carrier mobility in solar cells and semiconductors. The principle of the TPV test is based on the voltage change at the semiconductor surface after light irradiation, and the carrier behavior inside the semiconductor is reflected through the measurement of this change. Specifically, when light strikes the semiconductor surface, photogenerated carriers are generated, and the migration and recombination of these carriers within the semiconductor causes changes in the semiconductor surface voltage. By testing the change of the semiconductor surface voltage before and after the light exposure, the carrier mobility, lifetime, recombination rate and other important parameters can be obtained inside the semiconductor. TPV test is one of the important ways to study the carrier characteristics and transient processes of semiconductor devices, which is of great significance for understanding the working principle of semiconductor devices and optimizing the design of the devices.

KPFM

Kelvin Probe Force Microscopy (KPFM) is an instrument that utilizes AFM techniques to measure the surface potential and work function of a sample. It works based on the Tap and Nap modes and is mainly used to study surface charge distribution and potential maps. We have already mentioned that the AFM detects the morphology of the sample surface by means of a microcantilever that is extremely sensitive to weak forces. In KPFM, the microcantilever is not only used to detect the morphology, but also the electrical potential of the sample surface. This is done by applying an AC voltage to the microcantilever to generate vibrations and simultaneously applying a DC bias to compensate for the potential difference between the sample and the microcantilever to minimize the amplitude of the microcantilever. By detecting the desired DC bias voltage, the potential distribution on the surface of the sample can be inferred. Nap mode is a special mode in KPFM that is achieved by scanning twice in the same row. The first scan uses a tap mode to obtain height information about the sample surface, and on the second scan the probe is lifted a certain height and maintains a constant height difference with the sample, but does not touch the sample surface. In this mode, the vibration of the probe is driven by a piezoelectric motor and is no longer dependent on the contact force between the tip and the sample. The vibration of the probe and the compensation of the potential difference can be precisely controlled by applying an AC voltage and a DC bias.

EBIC

Electron Beam Induced Current (EBIC) is a technique for characterizing nanomaterials. The EBIC principle refers to the current induced by scanning an electron beam over the surface of a material to study the electron transport properties of the material. The method is a non-contact, non-destructive material characterization technique that is widely used in the research and fabrication of nanomaterials and semiconductor devices. The basic process of the EBIC principle consists of the following steps. ① Electron

Beam Incidence: An electron beam is emitted by an electron gun and focused onto the surface of the nanomaterial. By adjusting the beam intensity and focusing conditions, the probing area can be accurate down to the nanometer or sub-nanometer scale. ② Electron-hole pair generation: When the electron beam interacts with the material, a number of electron-hole pairs are excited. The electrons are excited as part of the electron beam, while the holes remain in the material. ③ Electron transportation: Excited electrons are transported inside the material while holes move toward the surface. ④ Separation and collection of electron-hole pairs: When a hole moves to a position that coincides with the scanning path of the electron beam, the hole is attracted to the electron beam and re-injected into the material. During this process, some electrons are attracted to the surface of the material by the electron beam and form an electron beam induced current. ⑤ Current Detection: Using an induced current detection system, the current signal induced by the electron beam can be measured, and the electron transport properties of the material can be obtained from the magnitude of the signal and the change in the position of the hole injection. The EBIC principle has a wide range of applications, especially in the research and manufacture of nanomaterials and semiconductor devices. Conventional EBIC measurements can be used to determine carrier diffusion length (L_d), if the depletion width is known. However, this is a destructive technique as the device itself needs to be cleaved before the measurement.

Bias EQE

In addition to EBIC, there is a non-destructive technique for Ld extraction, the Ld extraction method relies on a sequence of measurements and twodimensional (2D) curve fitting techniques: ① First, EQE (λ, V) as function of wavelength (λ) and voltage bias (V) is measured. ② Then, the reflectivity as function of wavelength, R(λ), is determined. ③ Combining steps 1 and 2, the internal quantum efficiency, IQE(λ,V), of

the cell is deduced as function of λ and V using the relation IQE(λ,V)= EQE (λ,*V*)/[1-R(λ)]. ④ From a separate capacitance-voltage (C-V) measurement, the voltage dependence of the depletion width, Wd(V), is deduced. ⑤ Using the voltage dependence of Wd, the Wd dependence of IQE at each λ is obtained [i.e., IQE(λ,V)→ IQE(λ, Wd)]. ⑥ The array of IQE(λ, Wd) data is fit to the analytic expression given by the equation to extract a single Ld value and the absorption coefficient (α) at each λ: IQE(λ, Wd)=1-exp(-α(λ)Wd)/[1+α(λ)Ld]. The derivation of this equation can be found in literature with the main assumptions being that: (1) The photo-generated carriers are created with an exponentially decaying function, where the length scale is defined by the absorption coefficient. (2) All the carriers generated within the depletion region are collected with 100% probability. (3) The carriers generated in the neutral region are collected with an exponentially decaying probability, where the minority carrier diffusion length defines the length scale.

Titre : Ingénierie de l'interface et absorbeur avec gradient de composition pour les cellules solaires en Kesterite à haut rendement ....

Mots clés : CZTSSe, cellules solaires, mécanisme d'amélioration de l'efficacité, recombinaison des porteurs

Résumé : Dans cette thèse, les propriétés de transport des porteurs de charge, le processus de croissance des grains, le mécanisme de perte de V_{OC} et les possibilités d'amélioration du rendement des cellules solaires de CZTSSe ont été étudiés.

L'importante perte de V_{OC} et le faible facteur de remplissage des cellules solaires CZTSSe sont les principaux défis pour l'amélioration du rendement. Cela est principalement dû à la mauvaise qualité de l'interface arrière, à l'alignement non optimisé des bandes et à la présence des phases secondaires dans l'absorbeur. Trois approaches ont été utilisées dans ce travail pour améliorer le rendement de ce cellules PV. Premièrement, une couche intermédiaire de WO_3 a été introduite dans l'interface arrière pour inhiber la réaction indésirable entre la couche d'tungsten et l'absorbeur. Deuxièmement, l'alignement des bandes et la présence de phases secondaires à l'interface avant ont été améliorés en même temps par un traitement de sulfuration à basse température.

Enfin, la conception et la réalisation d'une couche absorbeure à double gradient de band-gap en CZTSSe ont facilité la séparation et l'extraction des porteuirs de charge. Des cellules solaires en CZTSSe avec un rendement de conversion photovoltaïque de 13,7% ont été obtenues. Ces très bons résultats, obtenus grâce à une meilleure comprehnsion du mécanisme de pertes, pourraient être une excellente base pour des améliorations futures.

Title : Interface engineering and absorber with composition gradient for high-efficiency Kesterite solar cells..... ....

Keywords : CZTSSe, solar cells, efficiency improvement mechanism, carrier recombination

Abstract : In this thesis, the transport properties of charge carriers, grain growth process, V_{OC} loss mechanism and efficiency improvement possibilities of CZTSSe solar cells were investigated.

The large V_{OC} loss and low FF of CZTSSe solar cells are the main challenges for efficiency improvement. This is mainly due to the poor quality of the rear interface, the non-optimized alignment of the bandgaps and the secondary phases in the absorber. Three approaches were used in this work to improve the performance of this type of PV cells. First, an interlayer of WO_3 was introduced into the back interface to inhibit the unwanted reaction between the WO_3 layer and the absorber. Second, the alignment of the bands and the presence of secondary phases at the front interface have been improved at the same time by a low temperature sulfurization treatment.

Finally, the design and production of a double band-gap gradient absorber layer in CZTSSe facilitated the separation and extraction of charge carriers. CZTSSe solar cells with a photovoltaic conversion efficiency of 13.7% were obtained. These very good results, obtained thanks to a better understanding of the loss mechanism, could be an excellent basis for future improvements.